RESEARCH ON THE STRUCTURAL VIBRATION ATTENUATION CHARACTERISTICS OF LOCALLY RESONANT METAMATERIAL

Submitted by Cong GAO, MSc, BEng

A thesis submitted to The University of Nottingham
for the degree of Doctor of Philosophy,
July 2020

The University of Nottingham
UNITED KINGDOM · CHINA · MALAYSIA

TABLE OF CONTENTS

LIST OF FIGURES

LIST OF TABLES

ABSTRACT

Low frequency structural vibration is a common issue in engineering applications. In recent decades, the local resonant type metamaterial concept was proposed as a potential solution to the vibration control problems. In particularly, the membrane-type metamaterial (MemM) is widely studied for its extraordinary sound isolation performance. As a lightweight metamaterial, the related research works mainly focus on MemM's acoustic property yet its structural vibration absorption capability is not fully investigated. Researches about some problems and research gaps, such as the development of analytical model for bandgap property prediction, investigation of bandgap formation mechanism, confirmation of key design parameters and the corresponding effect on bandgap property and development semi-active control algorithm, are still limited in the MemM research area.

Therefore, to further investigate the MemM, the main research contents and novelty of this study are:

1. Based on the local resonant phenomenon, this study proposes a novel design of elastic metamaterial (EM) for the purpose of investigating the bandgap formation mechanism. Modal analysis is conducted to help understanding the relationship between local resonant phenomenon and bandgap formation. Also, we study the tuning of bandgap properties through geometrical structure adjustment. The structural vibration absorption capability and bandgap tunability of the EM is verified through numerical simulation and experiment.

2. This study proposes a modified Plane Wave Expansion (PWE) model for predicting the bandgap property of MemM applied on a thin plate. Further modification is made to allow the bandgap calculation for bilayer MemM. The accuracy of the analytical model is verified by numerical simulation. It is the first analytical model derived specifically for the application of MemM. The tensile stress of membrane is contained in the model as an independent variable. In order to reveal the effect of the design parameters – such as tensile stress attached mass magnitude – on the bandgap property, parametric analysis can be conducted by using this analytical model.
3. This study also proposes an analytical model that can predict the bandgap property and bandgap tunability of MemM equipped with polyvinylidene difluoride (PVDF) membrane. It is the first analytical model integrates the piezoelectric material properties into MemM model for bandgap prediction.
4. The MemM's thin plate vibration suppression performance is investigated experimentally.
5. This study combines the analytical model of membrane-type resonator (MemR) with the thin plate – resonator coupling model. The integrated model allows the prediction and investigation of a thin plate structure's vibration response when MemRs are attached. Different from the modified PWE model, this analytical model allows the adjustment of resonator settings individually. Therefore, optimisation of resonator allocation and distribution can be achieved through this model.

6. Preliminary derivation of semi-active control algorithm for the PVDF MemM is conducted. It provides solid concept proof and support for the future application of PVDF MemM and realisation of semi-active control MemM.

In conclusion, this study has investigated the structural vibration absorption capability of metamaterial and examined the local resonant phenomenon's effect on bandgap forming. It develops the bandgap property prediction method of MemM, constructs analytical model for the MemM that applied to thin plate structure and builds up the control system model for PVDF MemM's semi-active control algorithm. It enriches the analytical foundation of the MemM, and will encourage the design, optimisation and application of MemM.

ACKNOWLEDGEMENTS

I would like to express my deepest gratitude to my supervisor Dr Dunant Halim for his constructive suggestions, patient guidance, inspiring encouragement and thoughtful kindness. He has been so generous in spending time for guiding my research work and it is very much appreciated. It would be impossible for me to finish this Ph.D. degree without his acceptance and support during my tough time.

I would also like to thank my second supervisor Professor Yi Xiaosu for supporting my experimental work. I would take this opportunity to express my gratitude to the Graduate School faculty, especially Ms Jessica Wang, for their assistant.

My grateful thanks also extended to Mr Li Xuan, for his help in analytical work, for the sleepless nights writing together, and for the friendship. It is a privilege and great fortune to be able to work together with him.

My sincere thanks goes to Mr Li Lucen and Ms Tang Yuxin for their kindness and precious friendship in the last four years. I would also like to thank my friend Mr Li Hui for his support and encouragement.

Special thanks should be given to my beloved wife Ms Cheng Moyi, for her trust and comfort during my hard moments, for her enlightening words that inspired me and toleration of all my bad moods.

For all those people that loved and supported me, I will always be grateful.

Chapter 1

1. INTRODUCTION

1.1 Research Background and Motivation

Mechanical vibration is a widely acknowledged phenomenon that can jeopardise structures and human health by causing fatigue, noise pollution and structural failure. Different techniques have been developed for vibration control and suppression in different applications [1, 2, 3, 4]. A most traditional way of suppressing vibration is to apply passive damping layer that composed by viscoelastic materials to the primary system [5], and such measure is effective in eliminating high frequency (<2000 Hz) the vibration. However, the damping layer cannot effectively control the low frequency vibration. As a result, measures for controlling low frequency vibration are in demand. A commonly used method is by adding a tuned mass damper (TMD) to the primary system. The TMD is able to absorb the vibration kinetic energy of the primary system and dissipate it by transforming the kinetic into other forms of energy (heat, field energy etc.). Hartog [6] demonstrates in his book that a TMD comprised of a mass, spring and damper can effectively control the vibration of the primary structure that under harmonic excitation. However, the TMD also has assignable disadvantages: First, for the vibration absorption satisfactory, the TMD should have certain mass which is proportional to the primary structure; second, it brings extra difficulties in design and installation for the primary structure; third, it has a narrow operation frequency band [7]. In practical situations, the disturbance signal may have a wide frequency range. In order to achieve wide frequency range absorption, usage of multiple TMDs simultaneously is proposed for application [8]. Yet this solution leads to the first disadvantage and therefore, a new effective solution for vibration control that with small mass and wide frequency range is needed.

Phononic Crystal (PnC), which is a manually engineered composite material that has spatial periodicity, was proposed in 1993 [8, 9]. The concept of phononic crystal was originally developed from photonic crystal. In 1987, John [10] proposed the concept of photonic crystal, and pointed out that the refractive index within the material was designed artificially in a periodic pattern, so optical waves can propagate in an analogous way as electrons in real crystals. Such phenomenon can be described as possessing band structure characteristics. Similar to photonic crystals [11], PnC is able to attenuate or manipulate the elastic waves over certain frequencies, and such frequency regions are called bandgaps. The bandgap generating mechanism of PnC is based on the Bragg Scattering phenomenon [12]. When periodic structure of the PnC is in wavelength scale, interference to the acoustic wave in corresponding wavelength will be generated and as a result, the acoustic wave propagation can be manipulated [13, 14, 15]. However, since the lattice constant of the PnC needs to be in the same order as the affected wavelength, the application of PnC in low frequency range is limited by the size requirement. As the main noise and vibration facing in daily lives and industrial fields are in low frequency regions [16], and the low frequency waves have a better penetrating ability than the high frequency ones, therefore PnC is not the best choice for the low frequency vibration control.

Acoustic metamaterials (AM), which can also generate bandgaps, are proposed later for attenuating of the elastic wave propagation. Different from PnC, AM bandgap mechanism is based on localized resonant phenomenon [17].

Metamaterials are manually engineered structures that formed by one or several kinds of materials. They possess material properties that are not available in natural [18], such as negative Poisson's ratio and negative modulus. AM is a subwavelength structure, which means it can affect the elastic waves that have larger wave lengths than the metamaterial structure's size. It can thus work effectively in low frequency range without requiring a considerable space. While the main focus of AM's function is on acoustic wave attenuation or control [19], elastic metamaterial (EM), the focus of which is the attenuation of elastic wave and structural vibration, has also come to researchers' attention. The theoretical basis of AM and EM are similar to each other, so in this thesis, both will be mentioned and reviewed. Many different kinds of AMs/EMs have been designed and proposed in the past decades, yet the actual application are rare. Further researches about factors that influence metamaterial's bandgap property, geometry structure optimisation and analytical models for rapid design are required to enable the application. In particularly, the broadening of bandgap width, investigation of controllable bandgap and a convenient method for metamaterial design in accordance with the application environment are 3 key elements that drive the metamaterial from labs to engineering fields.

These deficiency in metamaterial's research and its lack of engineering application motivate the author to conduct this study. The work mainly focus on the membrane-type metamaterial (MemM), though an elastic metamaterial is also designed preliminary for concept proof and study.

The MemM consists a supporting frame that fixed with membrane decorated with mass. Tensile stress is applied to the membrane for the purpose of stiffening [20]. For deeper understanding of the metamaterial vibration absorption mechanism, the author intends to find out the key factors that influence the bandgap property of metamaterial through the design of a new elastic metamaterial structure. Also, to make the bandgap prediction of MemM more convenient, a modified theoretical model needs to be constructed.

The research can broaden the theoretical background of MemMs, and investigate the vibration control performance of a MemM under different conditions and fill the existing research gap. Otherwise, in this study, the feasibility of realising bandgap tuning through using piezoelectric material as the membrane is investigated. For a MemM with piezoelectric material membrane, the tuning of bandgap can be achieved through adjusting the applied electric field intensity [21] and thus allow the MemM to possess agile controllability. This work provides a detailed feasibility assessment for the usage of piezoelectric membrane and for the bandgap tuning ability. It demonstrates a potential development pathway for the MemM.

1.2 Aims and Objectives

The main aims of the research are:

Aim 1. Investigate the EM bandgap mechanism and possibility of forming a broad low frequency bandgap;

Aim 2. Reveal the performance and effect of MemM in structural vibration control;

Aim 3. Reveal the feasibility of enabling MemM to possess active tuning capability.

To accomplish these aims, corresponding objectives are planned as stage-gates.

For Aim1:

(i). Study the bandgap forming mechanism, vibration absorption of metamaterial;

(ii). Design a novel EM in accordance to the bandgap mechanism, and enable it to have broad bandgap;

(iii). Investigate the key design factors of the proposed EM through numerical simulation and examine the accuracy by experimental work.

For Aim 2:

(i). Study the bandgap mechanism of MemM structures and the key factors that affect the bandgap properties;

(ii). Study the vibration characteristics of membrane structures, develop a theoretical model for the estimation of MemM structure's bandgap properties and examine the key factors' effect;

(iii). Verify the accuracy of the model and effect of key factors through numerical simulation;

(iv). Conduct experimental work to support the findings.

For Aim 3:

(i). Study the characteristics of piezoelectric material and its constitutive equations;

(ii). Incorporate the proposed theoretical model for MemM structure with the piezoelectric constitutive equations and construct equations between applied voltage and MemM bandgap properties;

(iii). Simulate the effect of using piezoelectric material in MemM and the vibration control performance.

1.3 Research Significance

The general purpose of this research is to study the vibration absorption performance of metamaterial and to investigate the possibility of enhancing the metamaterial's bandgap property. Conducted research works mainly focus on: the analytical model development, vibration control performance and adjustability of metamaterial. The main contributions of this research are:

1. In this work, a novel elastic metamaterial (EM) structure that can generate low frequency bandgap in structural vibration is designed. The vibration absorption performance of the proposed EM when applied to a thin plate structure is investigated. This is different from the other EM researches which mainly focus on the vibration absorption of the EM structure itself, rather than applying it to a target structure. This research demonstrates the effectiveness of EM in vibration absorption for a thin plate, and thus encourage the actual application of EM.

2. This study derives a new analytical mode based on Plane Wave Expansion (PWE) model for the prediction of MemM bandgap properties. It is the first analytical model that can estimate the bandgap location and width of MemM attached to a thin plate and can reveal the influence of the tuning of MemR's design parameters – such as tensile stress and attached mass magnitudes – on bandgap properties.

3. It modifies the PWE model and integrate it with the piezoelectric constitutive equations for the first time. The model allows the bandgap prediction of membrane-type metamaterial (MemM) with polyvinylidene difluoride (PVDF) membrane. The relation between applied electric field intensity and

corresponding tensile stress can be derived through constitutive equations. In addition, the vibration absorption capability of the MemM equipped with piezoelectric material membrane was investigated. The accuracy of the model and effectiveness of adjustability of MemM with piezoelectric material were verified through numerical simulation.

4. It develops the semi-active control algorithm of the PVDF MemM. Based on the modified PWE model and thin plate – resonator coupling model, the basic analytical model of semi-active control system of the PVDF MemM attached on a thin plate structure is developed.

This research has systematically studied the MemM's structural vibration absorption performance and the feasibility of conducting bandgap tuning. Analytical models are developed to conduct bandgap prediction and to reveal the effect of design parameters. Numerical simulation and experimental works demonstrate the effectiveness of MemM in structural vibration control. Also, a design of EM that can generate a broad low frequency bandgap is proposed. The research outcomes can encourage the development and application of metamaterial in vibration control field.

1.4 Literature Review

1.4.1 Origin of metamaterial concept

Periodic structures can affect propagation of elastic waves, and the related researches about periodic materials' corresponding functions can be traced back to Sir Isaac Newton's work in 18th century, as illustrated by Brillouin [22]. The propagation of elastic wave in periodic structures then drew attention when researchers tried to find a way of assessing the laminated composite materials' integrity through non-destructive evaluation (NDE) methods [23]. Continuum theory was then developed for the analysis of laminated composite [24] and the harmonic wave propagation in periodic structures' formulations were given by Nemat-Nasser [25]. These works tried to find out the relationships among the stress, strain and displacement in the composite. By combining various layers' dynamic characteristics, the wave dispersion and propagation properties are revealed, as well as the equivalent stiffness and mass properties of the whole laminated structure. The transfer matrix approach is one of the first methods used for wave dispersion and propagation properties analysing, for example the method introduced in the work by Fahmy and Adler [26]. For estimating equivalent properties, some researchers tried to use mixture theories [27]. These studies provide theoretical basis and methods for the study of PnC and AM.

In 1968, Veselago first proposed a concept of metamaterial, in which it described a material having negative dielectric constant and permeability [28]. The validation of this concept demonstrates that through proper design, a manually created material can possessing properties that unavailable in nature. In 1993, Kushwaha et al. [9] proposed the concept of phononic crystal (PnC). As mentioned earlier, the PnC can form bandgaps within which the elastic wave propagation will be attenuated or manipulated. Since PnC's bandgap mechanism relies on Bragg scattering theorem, its lattice constant size should be in the same scale as the manipulated wavelength. Because of this characteristic, the dispersion relation of a PnC is sensitive to the lattice constant and therefore, a resonance cavity or waveguide pathway can be formed by creating a defect in the periodic structure [29]. However, because the necessity of relatively large structure size, utilisation of PnC in low frequency area is limited. Otherwise, the tuning of operation frequency of a PnC will require the changing of whole structure's periodicity, so it causes extra difficulty in application.

In 1995, the first experimental study of PnC material's wave attenuation capability was conducted by Mártinez-Sala et al. [30]. In their work, the sound attenuation traits of a sculpture that consists of periodically arranged steel cylinders was measured and a bandgap is found. However, the measured bandgap is later proved to be a pseudo-gap, which means it is not related with the vanishing of density of states [31]. In the next year, de Espinosa et al. [32] accomplished the experiment that observed full bandgap in a 2D periodic structures. The structure is formed by an array of cylindrical holes in aluminium alloy plate, and filled with mercury [32]. These experiments provide solid proof for the PnCs' bandgap existence. Since then, numerous studies have attempted to investigate the bandgap formation mechanism, key design factors and possibilities of PnC applications.

In 2000, Liu et al. published their work in which they describe a sonic crystal that can attenuate elastic wave propagation in subwavelength scale. The sonic crystal (shown in Figure 1) was composed of silicone rubber coated lead spheres, and a rigid epoxy frame. The spheres are located in an $8 \times 8 \times 8$ array whose lattice constant is 1.55cm, and the spheres are fixed on the rigid epoxy frame. In such structure, each of the lead spheres can be equivalent to a resonator, and therefore it will experience resonant vibration when under certain excitation. Thus, when the incident wave frequency is near the resonance frequency, the sonic crystal can exhibit negative elastic constants, and attenuate the wave propagation. Instead of Bragg scattering theorem, the working mechanism of this sonic crystal is based on the localized resonant phenomenon [17]. According to the results, two obvious bandgaps are found at about 400Hz and 1400Hz [17].The sonic crystal is considered as the original AM.

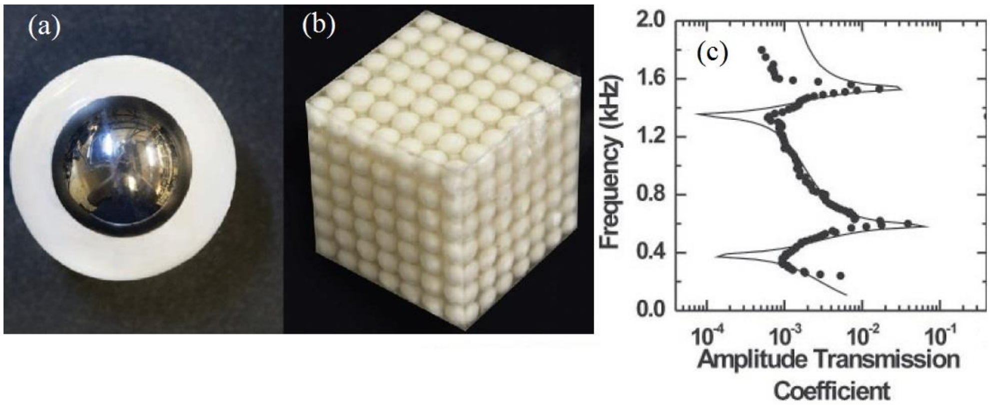

Figure 1. (a) Schematic figure of a sphere in the sonic crystal; (b)Sonic crystal in $8 \times 8 \times 8$ array; (c) Band structure of the sonic crystal in 0-2000Hz frequency range [17, 33].

Actually, there is not yet a commonly acknowledged definition about metamaterial, and whether PnC can be considered as AM. Yet it is widely acknowledged that metamaterials are artificial designed structures made from normal materials, and possess negative physical properties [18]. Fok et al. defined all materials generating bandgap relying on localized resonant phenomenon as AM, and those based on Bragg theory as PnC [34]. For clarity of the bandgap mechanism, classification method of Fok et al. is adopted in this work.

Currently, there are several different kinds of metamaterials, such as acoustic metamaterials [35], elastic metamaterials [3], hyper-damping metamaterials [36] and electromagnetic metamaterials [37] [38]. Since both the AMs and EMs are focusing on the propagation of elastic wave and the bandgap mechanisms are the same, so both AM and EM are reviewed in this chapter.

1.4.2 Research and development of acoustic metamaterial (AM) /elastic metamaterial (EM)

1.4.2.1 Negative material properties of metamaterial

A metamaterial is a subwavelength structure, which means the structure size is much smaller than the wavelength of the interfered waves, so the transmitting of elastic wave can be considered as travelling in a homogeneous medium. Therefore, effective material properties, such as effective bulk modulus, effective permittivity and effective mass density, are able to describe the characteristics of the metamaterial [39].

In AM/EM, negative effective mass density and bulk modulus are the most common properties attribute to generate bandgap. To illustrate the negative mass density effect, a mass-in-mass model is introduced in [33]. As given in Figure 2, mass M_2 is coupled with M_1 through spring. The system is under a sinusoidal excitation force F and the stiffness of the spring is K. Assume that there is no friction between M_1 and M_2 and consider the whole system as an effective mass M_e, then the equivalent mass is given by $M_e = M_1 + \frac{K}{\omega_0^2 - \omega^2}$, where $\omega_0 = \sqrt{\frac{K}{M_2}}$ is the resonance frequency of M_2. When tuning the frequency ω to a certain value, the equivalent mass will become negative and therefore one can find negative effective mass density ρ_e. With negative mass density, the system will experience out-of-phase motion with the incident force, and therefore help stabilizing the system and prevent wave transmitting. More details can be referred to [40, 41].

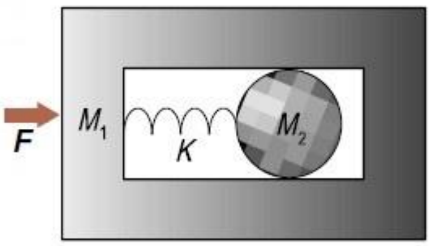

Figure 2. A mass-in-mass model that possess negative effective mass density.

The negative effective mass density is mainly attributing to the structures that allow relative displacements among components. In addition, for the motion in compression-extension mode, bulk modulus is adopted for description. The mechanism for negative bulk modulus derivation is similar, and more details can be reviewed at [42, 43].

Otherwise, similar to the electromagnetic metamaterial with negative permittivity and dielectric, the negative material properties can exist simultaneously for elastic or acoustic wave as well. Although negative properties are not necessarily appearing simultaneously when defining a metamaterial, AM with double negative properties (negative bulk modulus and effective mass density) was theoretically demonstrated to be feasible [43]. Zhou and Hu [44] identifies that the negative dynamic mass was caused by dipolar resonance, a phenomenon in which the total momentum of the system is in opposite direction to the macroscopic velocity, and the negative bulk modulus is caused by monopole resonance of microscopic structures. It is also verified by Ding and colleagues [45]. Instead of multiphase components, metamaterial made of solid materials was also reported to be able to achieve double negative properties [46]. Similarly, a structure shown in Figure 3 can reveal negative dynamic mass when the masses are performing translation motion and negative bulk modulus when performing centrifugal motions [47]. Therefore, the above introduced work demonstrate that the negative properties can be realised by geometric design.

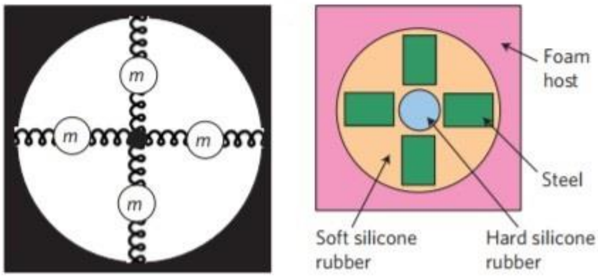

Figure 3. Microstructure model of metamaterial with double negative parameters [47]

Huang and Sun [48] analysed the wave attenuation mechanism of a metamaterial with negative effective mass density. The results explain that the transmitting elastic wave energy within the metamaterial is first absorbed and stored by the unit cells, then taken out by the external force when negative effect occurred. Thus the transmission of elastic wave is attenuated. Actually, damping of the structure materials is also able to dissipate the energy and achieve wave attenuation [49, 50].

Otherwise, negative bulk modulus can also be realized by Helmholtz resonator structure, as demonstrated by Fang et al. [42] . Instead of using combinations of different materials, the Helmholtz resonators creates a unique geometry structure that can allow the air/fluid within the resonator cavity to be simplified as mass-spring model [51]. The air/fluid in the neck is in small volume and thus assumed to be incompressible. It is considered as mass and the cavity provides equivalent stiffness [33]. The effective bulk modulus can be expressed as $\frac{1}{B_{eff}} = \frac{1}{B}(1 - \frac{\alpha\omega_n^2}{\omega^2 - \omega_n^2 + i\omega\gamma})$, where B is the bulk modulus of the air/fluid within cavity, ω is the excitation frequency, ω_n is the resonant frequency of the resonator, α is determined by $\omega_n < \omega < \omega_n\sqrt{1+\alpha}$, defining the bandgap width, and γ is the dissipation loss of resonating [52]. Therefore the effective bulk modulus can be negative under certain incident frequency.

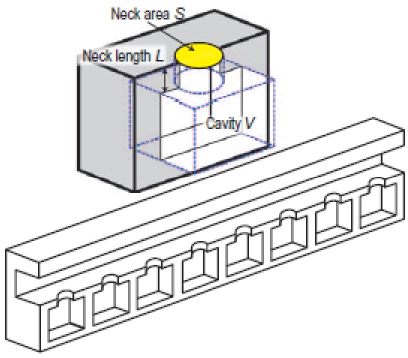

Figure 4. Configuration of Helmholtz resonator unit (upper) and the series of Helmholtz resonators connecter to a tube structure for wave absorption [33].

Actually, Helmholtz resonators have been adopted for noise control in different systems for many years [53, 54]. The bandgap property of the Helmholtz resonator composed AM can be effectively tuned by the geometric parameters, such as the neck length [55] and shape of the neck orifice [56].

1.4.2.2 Different designs of AM/EM

In the past two decades, AMs/EMs with various structure configurations have been proposed [33, 57, 58]. Most commonly used structures are reviewed.

The first kind is rigid inclusions wrapped by elastic materials and fixed onto square lattice structure. This is the first configuration of AM as proposed by Liu et al. [17]. Since then, numerous studies have been conducted to investigate the bandgap mechanism and key factors, such as periodicity, geometric size and shape of inclusions, that influencing the bandgap property of this structure. For example, Hirsekorn et al. conducted numerical simulation on a 2D sonic materials and concluded that the lattice constant has no effect on bandgap location, which means the bandgap frequency is entirely due to locally resonant phenomenon [59]. Another study published by Hirsekorn and Delsanto used finite element modal analysis (FEMA) to investigate the bandgap performance of a metamaterial with asymmetric inclusion [60]. The results demonstrate that the existence of bandgap is closely related with the resonant modes of the unit cell, and the break of symmetric in unit cell can lead to wider bandgap width. Otherwise, structure containing different inclusions were also studied by Qi et al. [61]. They reported a double local resonance mechanism, caused by two different types of rigid inclusion in the structure. It is found that the bandgap location and width are determined by the mass density, radius and elastic modulus of the inclusion bodies. The larger difference of the mass density and elastic modulus will lead to wider bandgap width.

These research works illustrated the importance of unit cell structures in bandgap properties. However, the configurations of such type of AMs/EMs are normally simple and in two-dimensional structure, the space for optimisation and modification of inclusion/coating material is insufficient. As a result, the second type of AM/EM structure is proposed as a transformation of the first kind.

The locally resonant mechanism of the rigid-elastic structure is realised by using the mass-spring resonator or equivalent system.

A metamaterial structure made by polyamide was reported as an innovative solution for noise and vibration problems in pipes [62]. As shown in Figure 5, in each of the unit cell, two relatively thin supporting beams are connected to the thick lump mass. The cell configuration can be simplified into a mass-spring system as the supporting beams are providing equivalent stiffness.

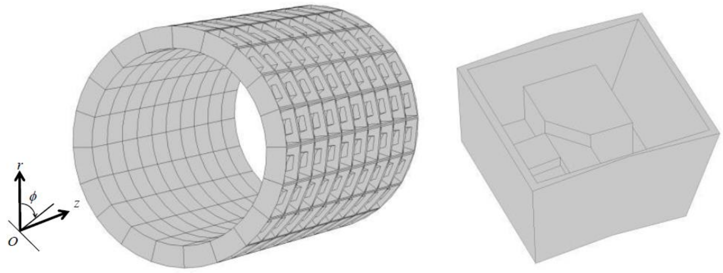

Figure 5. The configuration of the metamaterial pipe (left) and a unit cell (right) [62].

As this type of structure is more similar to mass-spring resonator, the application is mainly targeted at structural vibration rather than acoustical aspect. A metamaterial with slot-embedded local resonator was reported by He and Huang [63]. The structure is able to generate a complete low-frequency bandgap when applied to a thin plate and parametric studies indicated that the changing of mass and stiffness of the resonator can directly change the bandgap location or even eliminate the bandgap. Similar conclusion is also given by Huang et al. [64]. They introduced a novel structure as shown in Figure 6(a). Through adjusting the total size and ratio of h_1/h_2 on the stub, the bandgap location can be tuned effectively, as shown in Figure 6 (b)-(d). These research works demonstrated that in a specific type of AM/EM, the bandgap property, especially the bandgap location, can be tuned by adjusting the geometric structure. In practical, the external vibration or noise are normally combinations of waves in various frequencies, thus the AM/EM with a tunable and/or broad bandgap width is essential in application.

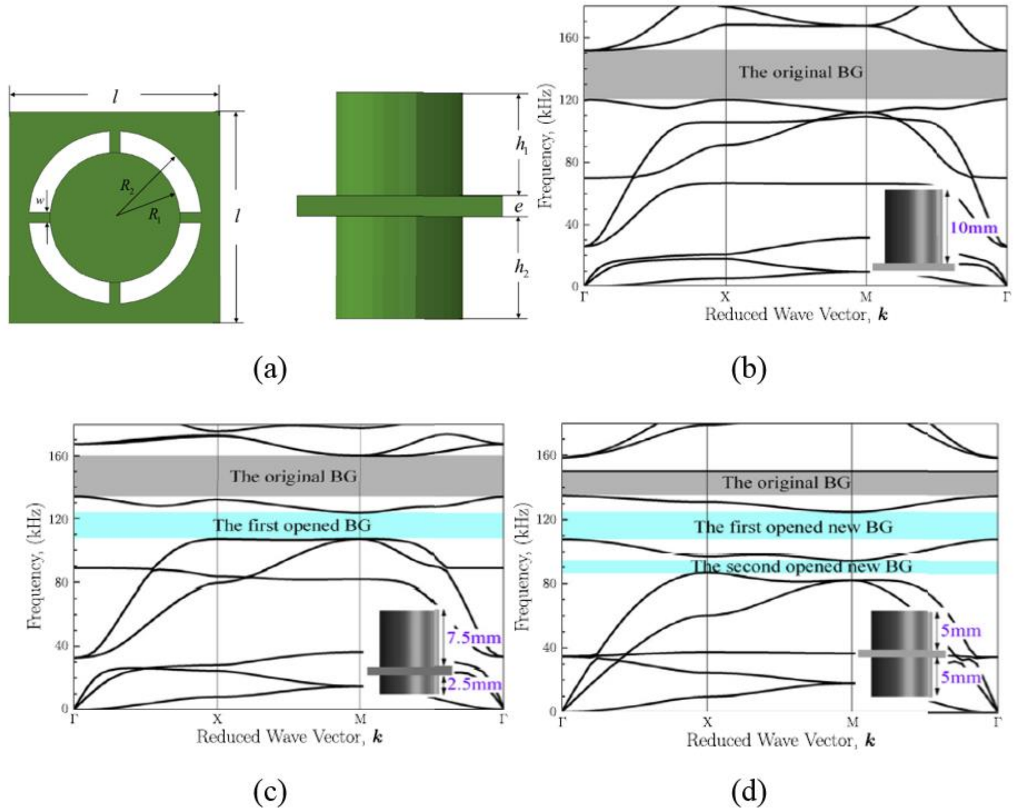

Figure 6. (a) Top view (left) and side view (right) of the configuration of the unit cell designed by Huang et al. [64]. The different bandgaps when the stub size ratio h_1/h_2 is adjusted are given in (b) (c) and (d).

The tuning of bandgap through geometric parameters are considered as a passive control method for bandgap. Matlack et al. constructed a tunable EM composed of elastic cubic lattice and rigid inclusion by 3D printing technique (Figure 7) [65]. By reducing the number of supporting beams for the steel cube, the equivalent stiffness of the unit cell is decreased simultaneously. As a result, the bandgap location will be changed accordingly, as shown in Figure 7(d). Similar works can be referred to [66].

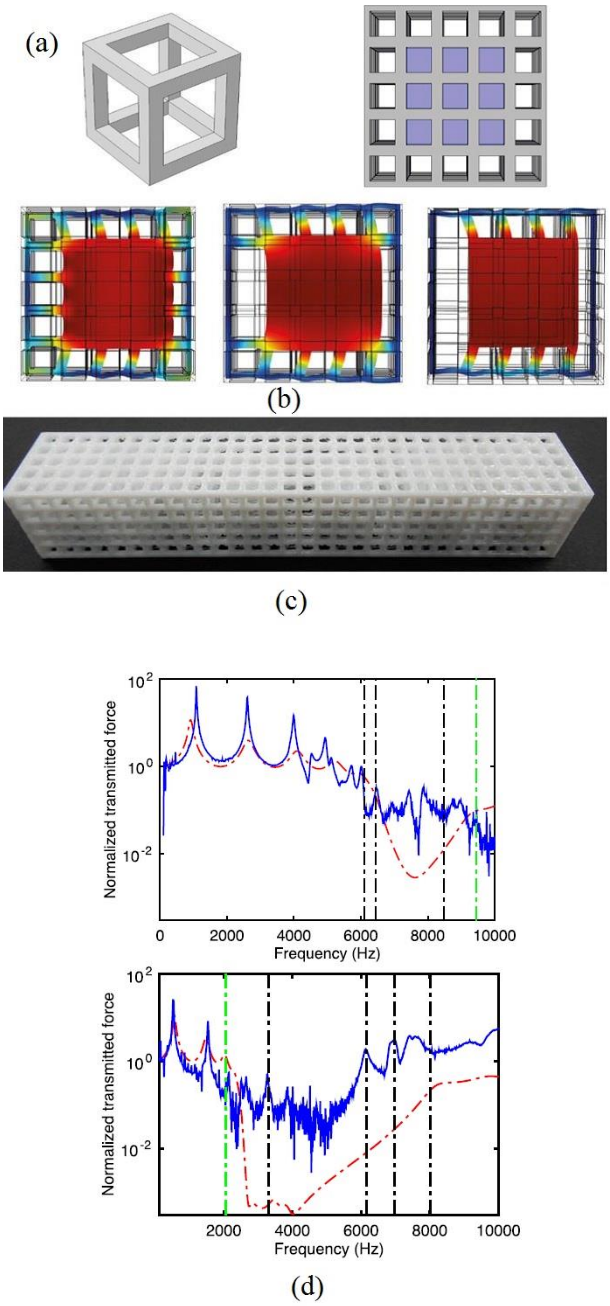

Figure 7. (a) Configuration of the cubic lattice and a unit cell of the metamaterial. (b) Locally resonant mode shapes of the unit cells with high, medium and low equivalent stiffness. (c) Sample of the designed metamaterial. (d) FEA simulation results (dashed red) and the experimental results (solid blue) for the high stiffness (upper) and low stiffness (lower) structure. [65]

The third type of metamaterial is composed of Helmholtz resonator, details about this type of metamaterial can be found in [53]-[56]. [53] [54] [55] [56].

The fourth type is the MemM and it will be discussed in **Section 1.4.3**.

1.4.2.3 Bandgap property calculation methods

In the study of AM/EM and PnC, the calculation methods for the band structure are developed. Band structure, which is also called dispersion relation, is originally a concept from solid state physics. It represents the relation between the energy and momentum of a system. For the elastic wave, the wave energy and momentum are directly proportional to the frequency and wave vector respectively. Therefore, the dispersion relation of elastic waves are revealed by the relation of frequency and wave vector [67]. Literature review have indicated that there are mainly 5 commonly used methods [68]:

1. Plane Wave Expansion (PWE) [9, 69, 70];
2. Transfer Matrices Method (TMM) [71, 72];
3. Multiple Scattering Theory (MST) [73, 74, 75];
4. Finite-Difference Time-Domain (FDTD) [76, 77];
5. Lump-mass method (LMM) [78].

Among these methods, the PWE is one of the mostly used. It is feasible for 1D, 2D and 3D periodical structures. Sigalas and Economous used PWE method for a 2D PnC applied on thin plate structure [69], and this method is extended to 3D structures [79]. In a periodical structure, by applying Bloch–Floquet theorem, the PWE method conducts Fourier series expansion of the displacement, density and modulus in the reciprocal lattice vector space and thus changes the dispersion relation problem into eigenvalue problem. Scan the wave vector on the Brillouin zone boundary of the structure, and work out the corresponding eigenfrequencies. The band structure can then be revealed by plotting the eigenfrequencies against the wave vector.

For example, the displacement $u(r,t)$ of a periodic structure at any point $r(x,y,z)$ can be expressed as [9]:

$$u(r,t) = e^{i(kr-\omega t)} \sum_G u_k(G) e^{iGr} \tag{1-1}$$

where k is the wave vector, G is the reciprocal-lattice, and t is time. By submitting this equation into the governing equation of motion of the system, and scan k along the area of the irreducible region, the equation of motion will become a set of equations for the eigenvectors $u_k(G)$ and eigenfrequencies $\omega(k)$. The solution of these equations will then give the dispersion relation of the system and reveal the band structures. Such as the example published in [9], the band structure is given in Figure 8. Each of the band curve along the wave vector is formed by the eigenfrequencies, and the resolution of the curve is decided by the step size of the wave vector whilst the number of plane waves is relying on the truncation number of the infinite expansion series [79].

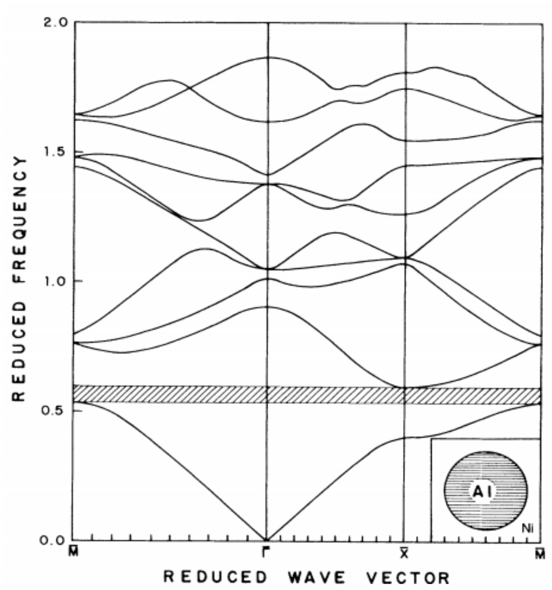

Figure 8. Band structure of a periodic array of aluminium alloy cylinders in a nickel alloy background [9].

There is research pointed out that the PWE method has the disadvantage of slow convergence because in order to ensure the accuracy, the truncation number needs to be relatively large for the Fourier series [80]. In addition, the PWE method cannot be applied to systems with complicated boundary conditions. Also, the Fourier series in the interface of different materials is slowing down the convergence. However, Cao et al. argued that the convergence problem is not caused by the interface but the inappropriate formulation that adopted for eigenvalue problem [81]. In the past few decades, PWE method was adopted in many research works that focused on photonic crystal and PnC, so its effectiveness is widely acknowledged [82, 83, 9, 84].

PWE method has the advantage that it has no assumption conditions introduced and the calculation programming is relatively simple. Therefore, in this work, PWE method is selected and modified for the calculation of bandgap structure. Detailed derivation and modification is presented in **Chapter 2**.

Otherwise, the FEA method is also widely used in the studies of metamaterial. It is convenience for the complicated structures. According to the Bloch theorem, the FEA can calculate the band structure of a metamaterial by applying periodic boundary condition to one unit cell and therefore dramatically reduced the calculation quantity. Moreover, the FEA is also utilised for the numerical simulation of finite metamaterial structures and for examining the accuracy of band structure estimation through the infinite structures.

1.4.3 Development of membrane-type metamaterial (MemM)

1.4.3.1 Study of MemM's bandgap property

In 2008, Yang et al. [85] introduced the design of MemM for sound reflection purpose for the first time. The MemM achieves a near total reflection of sound wave at 237Hz, and demonstrates the existence of negative dynamic mass. This result provides solid proof for the effectiveness of MemM in sound isolation. The proposed MemM consists of a circular elastic membrane with attached small mass, and a rigid grid the membrane is fixed on. Most of the MemMs have the same or similar configuration, therefore the MemMs have the advantages of easy manufacturing, low cost and lightweight. Especially, the thin thickness of the MemM makes it has relatively low requirement in space for installation and it is very suitable for application on plate structures.

The study of MemM bandgap property mainly focused on the bandgap location and bandgap mechanism. Similar to other locally resonant type metamaterial, the unit cell of a MemM, or so-called membrane-type resonator (MemR), can be simplified as a mass-spring model. The stiffness is provided by the prestressed elastic membrane, as a result of the stress stiffening phenomenon [21]. It is normally the fundamental resonant mode of the MemR that can generate bandgap [86], so the estimation of MemM's bandgap location relies on the membrane-with-mass system's resonant frequency. Otherwise, although generating bandgaps by locally resonant type metamaterial depends on the unit cell structure, the revealing of bandgap still requires certain periodic structure. It is because in most cases, the size of one unit cell is relatively small and the energy dissipation is not sufficient. Hence, to predict the band structure, the unit cell structure's equivalent properties, such as equivalent stiffness, need to be obtained and then substitute into existing methods.

Zhang et al. simplified a MemM beam as a beam structure with periodic resonator attached and established the equation of motion for the system based on the Kirchhoff theory [87]. Through this model, they calculated the bandgap location and the influence of membrane equivalent stiffness on effective mass density. However, instead of explaining the acquisition process of membrane equivalent stiffness, it is assumed directly in the study. Nouh et al. adopted the TMM and FEA method for the calculation of MemM formed beam and plate structures' bandgap [88]. They also carried out experimental works to validate the prediction of the proposed finite element model and results are found consistent with each other. The configuration of the tested plate structures and corresponding experiment setting is shown in Figure 9. According to the results, the plate with MemRs effectively attenuated the vibration from the shaker.

Dong et al. used FEA method to calculate the resonant frequencies of the membrane attached with mass model and explored the relation between resonant frequencies and membrane thickness under different level of tensile stress [89]. They found that with the same tensile stress applied, the increase of membrane thickness will reduce the resonant frequencies. Zhang et al. studied a beam structure composed of MemRs, and by using FEA software COMSOL Multiphysics, they revealed the bandgap property of the structure when applied with various tensile stress [90]. The resonant frequencies of the MemR are obtained directly in the FEA.

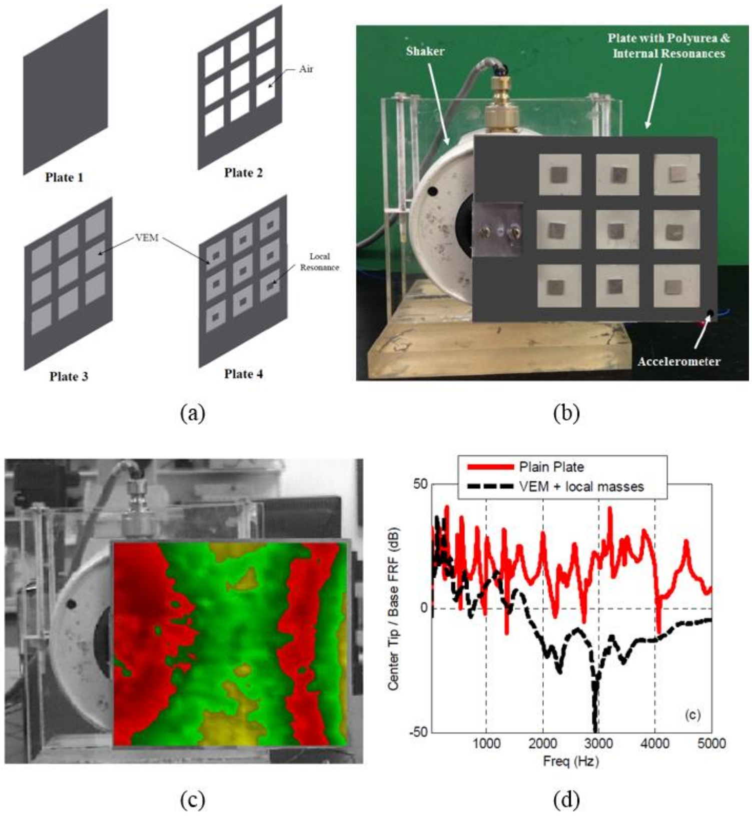

Figure 9. (a) Configurations of the tested plates. (b) Experiment setting for the testing of MemM Plate 4. (c) Mode shape of the MemM Plate 4 measured by Laser Doppler Vibrometer. (d) Frequency response of the MemM plate's tip deflection as a ration of the base excitation measured by the accelerometer. [88]

In these research works, the defining or acquisition method of the equivalent stiffness of the MemRs are not explained. The equivalent stiffness of the MemR system is either assumed directly [87] or calculated through FEA [90].

Several papers have introduced the calculation process of membrane-with-mass system's resonant frequency. Nagaya and Poltorak solved the boundary value problem of circular outer boundary membrane with eccentric circular inner boundaries that described by the Helmholtz equation [91]. It adopts the point-matching approach representing the inner boundary. It presents an effective solution for the problem that similar to membrane-with-mass system, but as it is mainly focusing on the mathematical aspect, it's usage in the physical field is not explored.

Kopmaz and Telli presented an analytical method of finding the eigenfrequencies of a rectangular plate carrying a uniformly distributed mass [92]. In their work, the area attached with mass is defined by the Heaviside function. It was mainly focusing on the plate structure. However, a membrane structure has similar equation of motion as a plate structure, but only ignored the bending stiffness of the membrane. Therefore, similar to this model, Zhang et al. proposed an analytical model for the fast calculation of sound transmission loss of MemM. In this model, they considered the inertia forces of the attached mass on membrane as a concentrated force, and with the application of Heaviside functions, the area of the attached mass was defined [93]. According to their work, the equation of motion of a membrane-with-mass system can be given by:

$$\rho_s \frac{\partial^2 w}{\partial t^2} + \rho_{mass} h\left(x, y, x_0, y_0, l_x, l_y\right) \frac{\partial^2 w}{\partial t^2} - T\nabla^2 w = 0 \qquad (1\text{-}2)$$

In this equation, w is the displacement, ρ_s and ρ_{mass} are the density per unit area of the membrane and mass respectively, T is tension per unit length, and $h\left(x, y, x_0, y_0, l_x, l_y\right)$ is a combination of four Heaviside functions that outlining the mass area. With incident sound wave, the equation of motion can then be changed to:

$$\rho_s \frac{\partial^2 w}{\partial t^2} + \rho_{mass} h\left(x, y, x_0, y_0, l_x, l_y\right) \frac{\partial^2 w}{\partial t^2} + 2\rho_1 c_1 \frac{\partial w}{\partial t} - T\nabla^2 w = 2Ae^{i\omega t} \qquad (1\text{-}3)$$

where A, ρ_1 and c_1 are the amplitude of the incident pressure, mass density and sound speed of the air. By using the superposition theory the mode function of the displacement w can be expanded into series and the above equation will transfer into a matrix form. With a proper truncation of the mode number, the displacement amplitude can be derived, and therefore the transmission coefficient. Also, the eigenfrequencies of the membrane-with-mass structure can be obtained by solving the eigenvalue problem.

However, in this method, the bending stiffness of the membrane is ignored and the mass attached area is allowed to bend. In actual, the membrane's bending stiffness is relatively small, however will still affect vibration of the system. In addition, the attached mass is normally a rigid platelet so the mass area is not able to bend. The allowing of bending will affect the accuracy of the mode function of assumption. Therefore, when the attached mass is relatively big or thick in geometric size if compared with the membrane area, the accuracy of this method may be weaken.

Chen et al. used the Rayleigh method for the resonant frequency prediction of membrane-with-mass model [86]. According to their work, the maximum strain and kinetic energy of the membrane-with-mass model are given as:

$$U_{max} = \frac{1}{2}\iint D\{(\frac{\partial^2 w}{\partial x^2} + \frac{\partial^2 w}{\partial y^2})^2 - 2(1-v)[\frac{\partial^2 w}{\partial x^2}\frac{\partial^2 w}{\partial y^2} - (\frac{\partial^2 w}{\partial x \partial y})^2]\}dxdy + \frac{1}{2}\iint T[(\frac{\partial^2 w}{\partial x^2})^2 + (\frac{\partial^2 w}{\partial y^2})^2]dxdy \quad (1\text{-}4)$$

$$T_{max} = \frac{\omega^2}{2}\{\iint m_s w^2(x,y)dxdy + M(q,h)\, w^2(q,h)\} \quad (1\text{-}5)$$

where $D = \frac{Et^3}{12(1-v^2)}$ is the bending stiffness of the membrane, E, t and v are the Young's modulus, thickness and Poisson's ratio of the membrane respectively. T is the tension stress per unit length on membrane, $M(q,h)$ is the mass located at coordinate (q,h). $w(x,y)$ and $w(q,h)$ are the transverse displacement of the membrane and mass and ω^2 is the natural frequency. By solving the equations, the resonance frequencies of the system can be obtained. The dispersion relation was then worked out by using FEA method. In this method, the bending stiffness of membrane, applied tensile stress, location of the mass, and membrane material properties are considered, but the mass attached was assumed to be a concentrated point mass rather than an area. Therefore certain error is expected when the size of mass is increased. However, when the attached mass size is small, the accuracy will be in an acceptable range.

These research works have explained the method that calculating the resonant frequencies of membrane-with-mass system. The equivalent stiffness of the structure can be derived when the MemR is considered as a mass-spring model. However, in Chen et al.'s work, the dispersion relation is still worked out by FEA method and Zhang et al's work did not focus on the dispersion relation but only the sound transmission loss spectrum.

Calculation of band structure in FEA model is time consuming and especially in the optimisation process, repeating calculation is required for various parameter settings. Therefore, an analytical method that can directly relate the MemR's properties with the bandgap property and provide capability of fast prediction will be very helpful in the design and optimisation of a MemM.

Otherwise, most of the MemM related research works were focusing on the acoustic aspect, and its performance in the structural vibration control field was rarely paid attention to. Sun et al. experimentally investigated the MemR's structural vibration control capability by attaching two dampers with 28mm diameter and 1.78g weight onto an aluminium beam [94]. The results (Figure 10) suggested that the two attached dampers can effectively reduce the host structure's vibration.

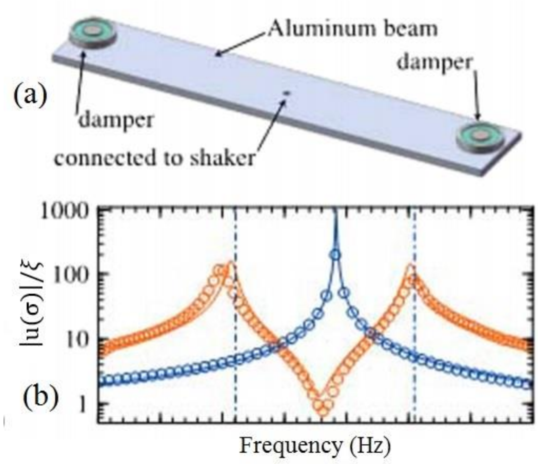

Figure 10. (a) The schematic of the tested aluminium beam with attached MemRs. (b) Normalized displacement $u(\sigma)$ at the end of the beam. ξ is the amplitude of shaker. Orange line represents the beam attached with damper and blue line stands for the bare beam. Circles are results tested from experiment whilst the solid line is from theoretical estimation. Adapted from [94].

Later on, Sun continued the research by experimentally investigating a membrane-type sample with multiple platelets attached on a rectangular membrane and found that it was able to achieve an average vibration reduction of 24.7dB in 100-1200Hz frequency range [95]. The configuration of the sample is presented in Figure 11. Four of the samples shown in Figure 11 were attached on a steel plate and the vibration control performance of the MemM was compared with a commercial rubber plate designed for vibration damping. The results indicated that the performance of the 4 stacked samples in vibration absorption was better than the commercial plate in relatively lower frequency range.

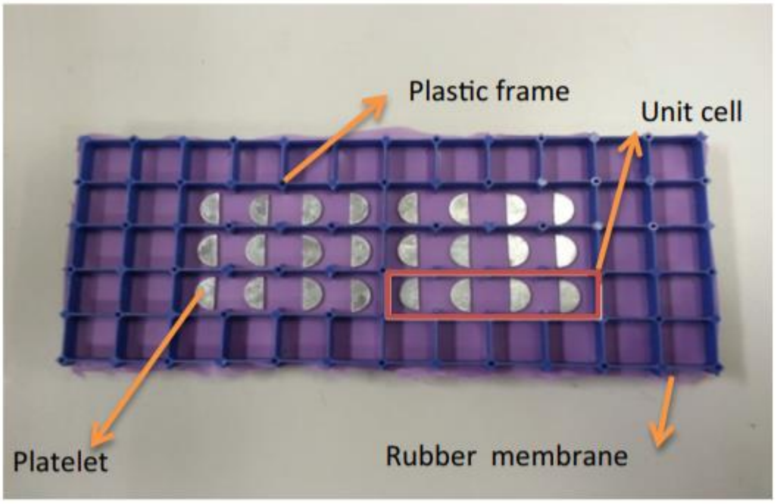

Figure 11. Sample of the MemM. [95]

These research works demonstrate the effectiveness of MemMs in structural vibration control field and thus, further investigation and exploration of MemM is worth conducting.

There were researches mentioned that compared with the Bragg type bandgap, the locally resonant type bandgap is normally narrow. Such phenomenon is also existing in the MemM. As a result, the exploration of possibility to broaden the bandgap of MemM is essential for motivating its actual application.

Pai pointed out that the combination of resonators that have different resonant frequencies can create a relatively broad bandgap [96]. Similar effect can be achieved by stacking MemMs with different bandgap properties. So far, to the best knowledge of the author, there is no research work investigated the structural vibration control capability of MemM with multiple layers. Actually, the stacking of MemMs will not lead to a lot extra demand of space because the relatively thin thickness and multiple layers of membranes can be easily deployed in a certain area. Hence, the multiple layered MemMs have good potential for application.

Ma et al. studied a bilayer plate-type AM and its sound absorption capability [97]. Because of the cavity in-between the two layers of the plates, this AM was able to reveal negative bulk modulus whilst possessing negative effective mass density simultaneously. Also, the asymmetric plate layers were used and the results indicated that the effective parameters will shift to higher frequencies. It was reported that asymmetric platelet can achieve better curvature energy dissipation [98].

Gao el at. proposed a bilayer MemM with magnetic mass and experimentally tested its sound isolation performance [99]. The schematic description of the sample is given in Figure 12. The mass was able to be fixed on the membrane through the magnetic force. However, in this design, the membranes are clinged to each other because of the magnetic force. Therefore these two layers of membrane cannot be considered as two resonator respectively and as a result, only one bandgap is formed by locally resonant, as the dips shown in the sound transmission loss (STL) curve in Figure 12(b) and Figure 12(c). The research found that the sound absorption capability is better than the single layer MemM. Both of the works were closely or directly related with the multiple layered MemM, yet the investigated performance was in acoustic field. Aside from these research works, the bilayer or multiple layered MemMs were rarely explored in the structural vibration field. Therefore, an obvious research gap is found.

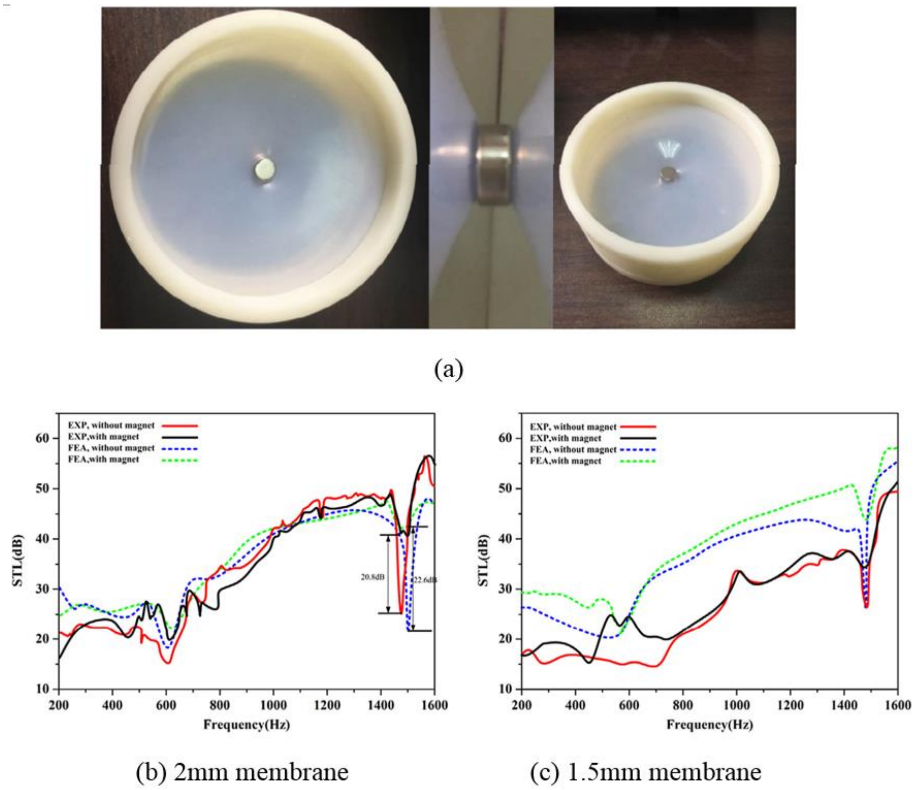

Figure 12. (a) The picture of the configuration of the bilayer MemM with magnetic mass. (b) STLs of sound insulation experiments and simulations results of bilayer MemM with 2mm membrane and (c) 1.5mm membrane. Adapted from [99].

1.4.3.2 Different designs and tuning method of MemM

In actual situation, vibration excitation normally involves waves in different frequencies. Therefore, aside from creating several bandgaps in various frequency ranges, the possessing of tunable bandgap location will also effectively enhance the vibration control performance of a MemM.

There were research works have investigated the possibility tuning different types of AMs' bandgap.

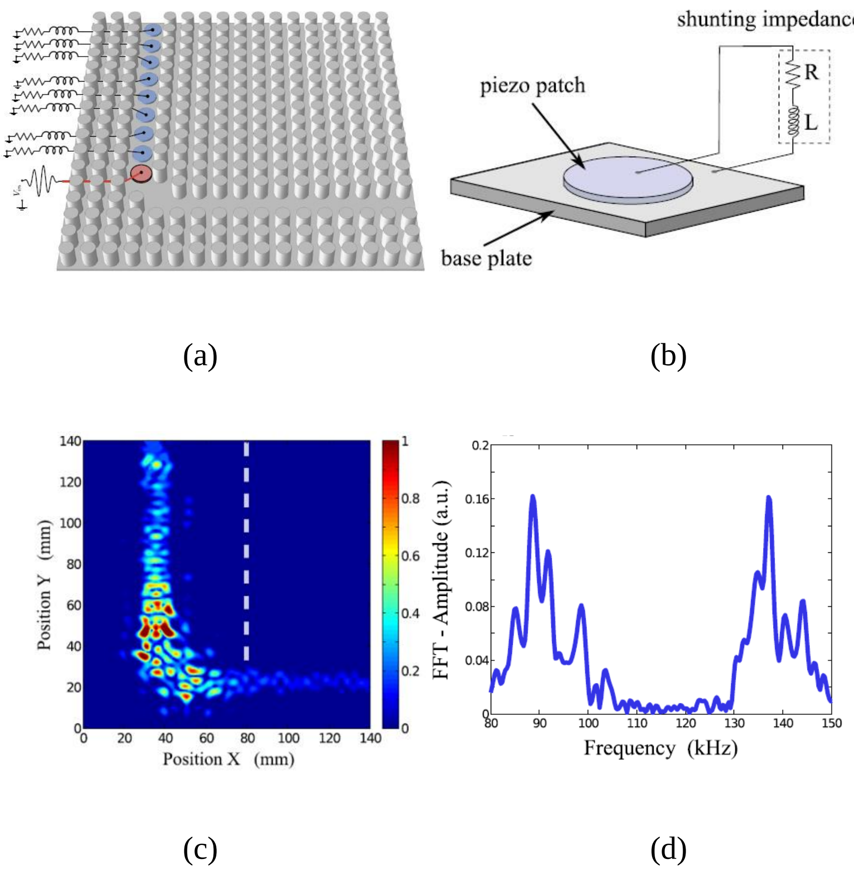

Figure 13. (a) The configuration of the PnC plate with stubs and piezo patches along the waveguide. (b) The model of the piezo patch attached block. (c)Field of wave amplitude when the incident wave is in the Bragg-type bandgap of the PnC at 117 kHz. The piezo patches did not influence the waveguide performance. (d) Frequency response spectrum of the wave filed along the white dashed line in (c). [100]

Casadei et al. reported a tunable acoustic waveguides PnC that contained piezoelectric resonator arrays [100], as shown in Figure 13. Within the deflection of the stub array, a series of shunted piezo-ceramic (PZT) disks were placed. The red patch provided the excitation signal. The shunting of the piezo patches possessed resonant modes and by tuning the inductors the resonant frequencies will shift. Figure 13(c) presents the wave guide effect of the proposed model.

Wang et al. proposed to use harnessing buckling method to achieve bandgap tuning [101]. By applying strain to the metamaterial structure, the supporting beams of the rigid cores will be deformed and turn into buckling status.

Therefore the bandgap location and wave transmission capability is tuned. The configuration of the metamaterial is given in Figure 14.

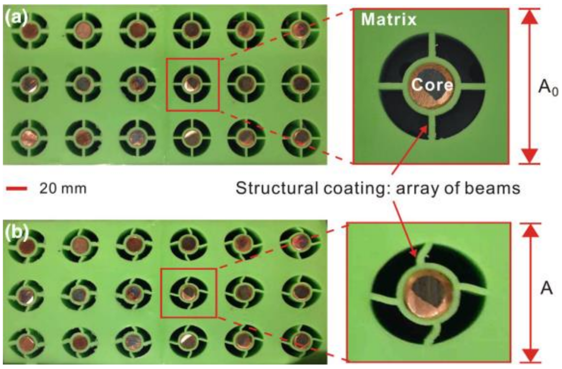

Figure 14. (a) The configuration of the metamaterial consists of metallic mass connected to the matrix through elastic beams. (b) The configuration of the metamaterial under a compressive strain. [101]

From the above mentioned studies, the main tuning method of metamaterial is changing the resonator's effective stiffness. Actually, the changing of mass is very difficult to be realised during the utilization of the metamaterial. Wang et al. proposed [102] a model that use electromagnet as the mass and thus achieve the tuning of bandgap by switching on and off the power supply. The structure is given in Figure 15. The two electromagnets will be attaching when the DC power is switched on and allow the transmission of the incident wave. Therefore, by programming the status of the unit cells, the metamaterial plate can either be a waveguide or stopping the wave propagation. However, this tuning method cannot change the bandgap location and it is not considered as fulfilling the demand of bandgap tuning.

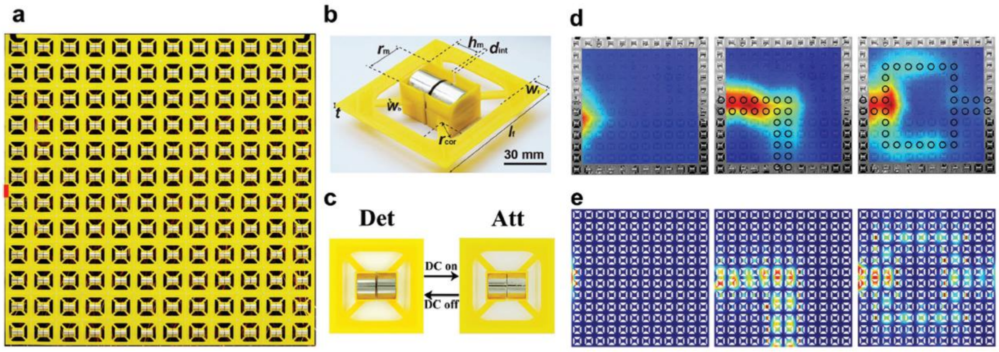

Figure 15. (a) The metamaterial plate with 12×12 unit cells. (b) The configuration of a unit cell that comprises of two electromagnets, supporting beams and a square frame. (c) The detaching and attaching status of the electromagnetics when the power is turned off and on. (d) Experimental and (e) numerical results of wave propagation in the metamaterial with different unit cell setting. The black circles indicate the cells in attaching mode. [102]

The above mentioned methods are tuning the bandgap by physically changing the unit cell in geometrical structure. In addition, the bandgap can also be tuned if there is measure manages to change the material properties. Nimmagadda and Matlack continued their work on the proposed metamaterial structure shown in Figure 7 and tried to use thermal field to realise the tuning of bandgaps [103]. It was pointed out that the modulus of 3D printed polycarbonate material will vary with the temperature. Thus, in the research it was revealed that by setting the metamaterial beam under partitioning thermal field, the various material modulus of the structure will lead to the appearing of various bandgap location and width. Other research works on thermal tuning can also be referred to: [104, 105].

However, there is difficulty when applying partial heating conditions on the structure and leads to extra energy cost in heating and temperature control. Energy consumption is also a common concern in many other control fields, such as the hydraulic system [106]. Therefore the thermal tuning of the metamaterial has lower feasibility, even though it provides an enlightening solution for the active control MemM.

Theoretically, the tuning of a MemM's bandgap can be realised by changing the mass magnitudes, allocation of the mass blocks, and tensile stress on the membrane or the shape of the frames. In reality, the tuning of membrane stress has the highest feasibility since normally the mass is fixed on the membrane and cannot be moved easily.

One of the method that proposed for active tuning a MemM's bandgap is by air inflation [107]. The unit cell is composed of two layers of membranes attached with masses and sealed cavity in-between. Pressurized air is inflated into the cavity and therefore cause obvious deformation of the membrane structure. As shown in Figure 16(c), the sound transmission loss peak shifts to a higher frequency when the air pressure of the cavity is increased and brings a higher stiffness of the membranes.

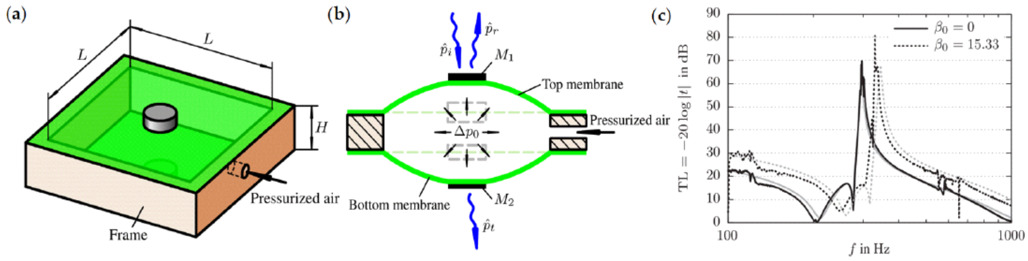

Figure 16. (a) The structure of the inflatable unit cell. (b) The cross-sectional view of the unit cell. (c) Experimental and theoretical normal sound transmission loss (STL) of the MemM at different pressure difference. [107]

However, such method requires extra air inflation equipment, and sealing mechanisms for the unit cells. Hence, the cost for manufacturing and space requirement for deployment will be higher than common MemM.

Another method of tuning MemM is by controlling external electric field. As given in Figure 17, the unit cell contains a membrane-type resonator that attached with a metal electrode platelet, and a fishnet shape cover coated with gold film [108]. By applying DC power to the electrodes, the electrostatic force can be considered as the combination of a constant attractive force that shifts the equilibrium position of the membrane and an anti-restoring force. The transmission peak that attribute to the first eigenmode of the resonator is therefore shifted. With a 900V DC power, the transmission peak can shift from about 160Hz to 125Hz. Otherwise, if applying AC voltage to the electrodes then it is capable of generating the cancelling wave which has the same amplitude and out-of-phase with the incident wave. This model inspired the train of thought that affecting the characteristics of the membrane by applying external electric field, which is easier to be control and generated. However, the required voltage is relatively high and it did not considered the application for structural vibration control.

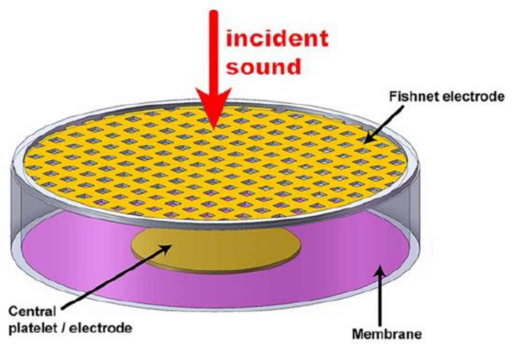

Figure 17. Schematic of the active control MemM. [108]

As shown in Figure 18, Ma et al. reported a type of membrane-type resonator consists of a membrane attached with a magnet, and an electromagnet at the top of the membrane [109]. When the power of the electromagnet is off, the membrane is fixed at the outer range of the membrane, and the boundary condition will change into two fixed edges when turn on the power. The altering boundary condition can effectively make the sound transmission characteristics through this device different, but the bandgap location is not changed in a continuous and linear way, therefore the tuning capacity is not sufficient.

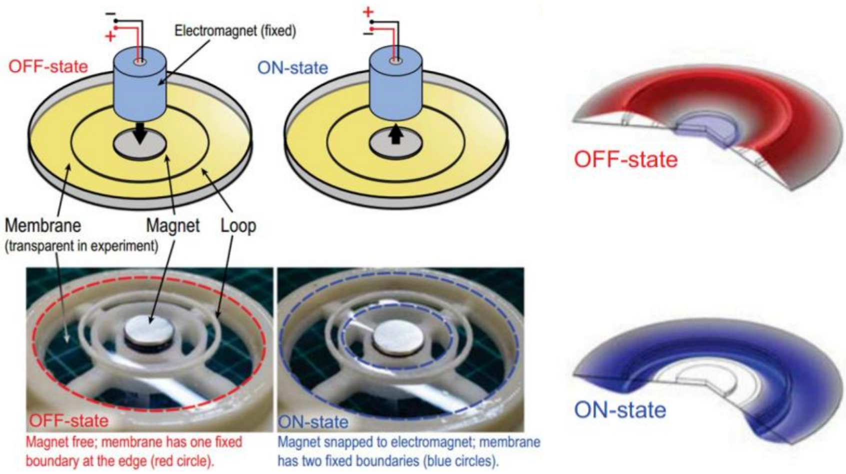

Figure 18. The unit cell design and the status of the membrane when the electromagnet are in off- and on-state. The corresponding mode shapes are shown at the right. [109]

Aside from externally applied electric field, there was also study tried to use magnetic control method. Silicon rubber embedded with ferro ferric oxide particles were adopted for the membrane. The magnetic field gradient in the axial direction on the membrane was increased and the STL peak will move from about 230Hz to 380Hz [110].

The above mentioned methods are focusing the tuning on the status of membranes in the MemMs. Instead of tuning membrane, Zhou et al. used elastic frame for the MemM and by applying strains to the frame, the tensile stress on membrane is elevated and the band structures were tuned [111]. This study demonstrates the feasibility of tuning frame of MemM, but also revealed that the frame tuning method has limit in application. The flexible frame makes the fixation of MemM on the primary structure difficult and easy to generate unexpected deformation of the shape, results in the bandgap shift.

A controllable and predicable bandgap tuning capability is essential if the MemM is deployed for application. Therefore, the utility of smart materials which are fully controllable by the external electric field in membrane fabrication is proposed and developed.

Dielectric elastomer (DE) membrane was studied to be utilized for tunable MemM because of its fast and large deformation when excited by external voltage [112]. The DE membrane consist of a thin elastomer film and two electrodes on both surfaces of the film. As shown in Figure 19, when external high voltage is applied to the electrodes, it will cause an electrostatic pressure between the electrodes and thus squeeze the elastomer in the vertical direction [113]. As a result, the deformation of the elastomer will lead to the change of stress within the membrane and the resonance frequencies.

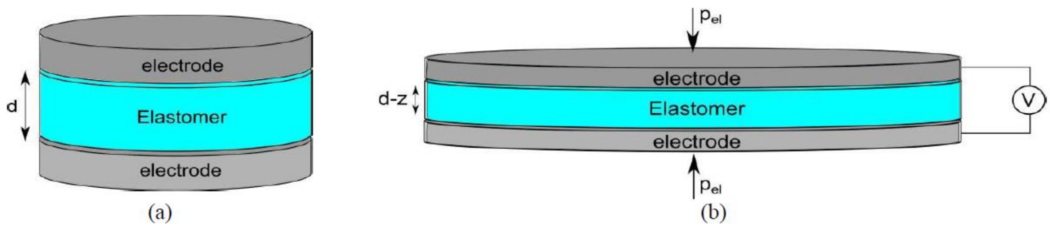

Figure 19. Schematic structure of the DE when in (a) base mode and (b) squeezed by electrodes. [113]

Lu et al. presented a lightweight DE acoustic absorber in their publication and reported that it can achieve effective noise reduction whilst possessing tunable resonance peaks [114]. The device consist of a circular DE membrane that fixed on a rigid frame, and a back cavity. Electrodes are attached at the middle of the membrane. The membrane is pre-stretched, so when applying external voltage, the tensile stress within the membrane will decrease and shift the resonance peaks to lower frequency range. According to their study, when applied with different pre-stretched ratios, it required at least 3 kV voltage to achieve about 20Hz resonance shift. Follow up studies from them can also be referred to: [115, 116, 117].

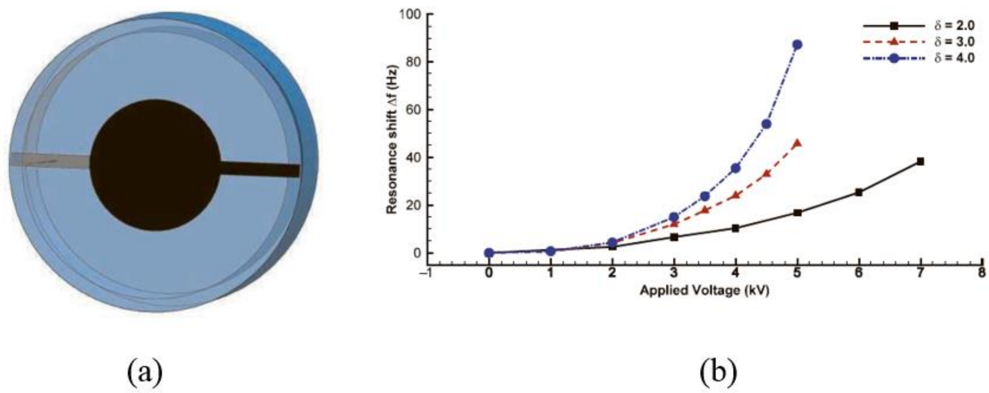

Figure 20. The schematic of the DE acoustic absorber. The black area indicates the electrodes on the DE membrane. [114]

The fast response and relatively low cost grant the DE membrane with advantages in the active controllable MemM. However, it also cannot be neglected that the high voltage required for the tuning of DE membrane.

Another material that was used for the tunable membrane is piezoelectric material. Use shunted piezoelectric patches for the tuning of metamaterial has been studied vastly before [118, 119, 120]. However, using piezoelectric material to form membrane in MemM is rarely investigated. Nouh et al. [21] proposed the MemM plate equipped with PVDF membranes and examined the bandgap tuning characteristics through the analytical mode they developed. The wave propagation surface of the proposed MemM under different external voltage is shown in Figure 21. With a relatively low voltage applied, the bandgap properties are effectively changed. This study demonstrate the effectiveness and feasibility of using PVDF material for the fabrication of membranes in the MemM. However, the relation between the applied voltage and bandgap location is not related directly in the proposed analytical model. An equation that reveals the voltage and bandgap location numerically is essential for the controlling and tuning of bandgap. Therefore, further research work is required in this field.

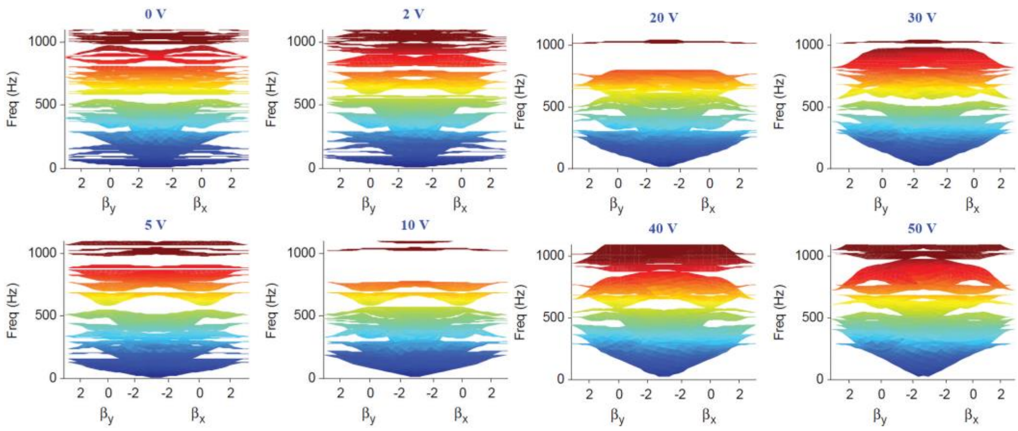

Figure 21. Propagation surfaces of the MemM equipped with PVDF membranes under different external voltages. Adapted and taken from: [21].

1.4.4 Research gaps

As presented in the literature review, many researches about the AM/EM have been conducted. The potential application of AM/EM and PnC involves acoustic wave guide [13, 121], frequency filter [14, 15], sound absorption [122, 123], sound isolation [124], structural vibration control [125] and enhancing energy harvesting [126]. However, despite of these potential applications, to the best of author's knowledge, the actual application of the AM/EM for vibration control are rare. Currently, most of the AMs/EMs are handcrafted in lab, therefore the samples are mostly high-cost and possess low accuracy [94]. Also, calculation is required for the design and optimisation of the metamaterial. Currently the metamaterial related calculation method has a relatively low efficient and facing some difficulty in convergence [127].

For MemM, similar research gaps also exist. In the design of MemM, factors such as the tensile stress level applied and the attached mass magnitude, are essential to control its bandgap properties. The design and optimisation process requires large quantity of calculation, especially for the MemM with multiple layers of membranes. Thus, a theoretical model for fast and convenient bandgap prediction is in demand.

Otherwise, a main barrier of AM/EM application is the relatively narrow bandgap width, especially in the structural vibration control field. In the practical situation, the incident vibration normally consists of various frequencies. Hence the development of an EM that possess tunable and relatively broad bandgap is essential. With multiple layered MemMs, several bandgaps can be formed simultaneously. Such characteristic allow the multiple layered MemMs to possess great potential in actual application. However, the state-of-art development of the MemMs are focusing mainly on the acoustic field and to the best knowledge of the author, only limited number of studies have studied the MemM's structural vibration control performance. Therefore, the study of multiple layered MemM's vibration control capacity will fill the gap and further encourage the MemM towards application.

At last, there were research works also investigating the tuning methods of bandgap. For MemM, the main tuning objects contain the applied tensile stress level, locations and magnitudes of attached mass. By using the piezoelectric material for membranes, the tensile stress of the membrane can be tuned through the adjustment of the applied voltage. However the study of applied piezoelectric materials for membranes is few. As a result, explorations about the feasibility and effectiveness of piezoelectric membrane is desired for the filling of this gap. Also, the applied voltage will result in the tensile stress change on the membrane, therefore to achieve the accurate tuning of bandgap, the sensitivity of stress to voltage should be revealed. In addition, to establish the equation connecting the voltage and tensile stress will provide a theoretical basis for the design of active tuning MemM equipped with piezoelectric material membranes.

In conclusion, the existing research gaps in MemM are explored and the filling of these blanks will effectively motivate the application of MemM.

1.5 Methodology and Pathway

In this work, a technical pathway incorporated with various research methods is designed for achieving the research aims and objectives. The pathway is given in Figure 22. There are 6 stages of the research:

Stage 1

In the first stage, theoretical background research will be conducted, focusing on the vibration theory of relevant structure, such as plate and membrane structure. Also, the bandgap forming mechanism of metamaterial and the calculation methods for bandgaps will be reviewed. The understanding of basic theories will provide instructions to the design of novel EM. In addition, the literatures about using piezoelectric material membrane for MemM and the corresponding performance will be reviewed.

Stage 2

A new EM structure will be designed, for the purpose of providing concept proof of local resonant bandgap formation, and to reveal the EM's structural vibration absorption capability.

We intend to make the proposed EM possess a broad low frequency bandgap for structural vibration. Preliminarily, the bandgap properties of the designed models will be examined by numerical simulation which conducted through the commercial FEA software COMSOL Multiphysics. Numerical simulation will reveal the relation between bandgap formation and resonant modes of the EM. The effect of different parameters on bandgap properties will also be examined. Thus, the bandgap forming mechanism and guidance for EM design can be obtained. We will also conduct numerical simulation and experiments to investigate the vibration absorption performance of the proposed EM.

Through this stage, the local resonant bandgap mechanism and the key design parameters that affect the bandgap properties will be explored. The design principle and design intent of the propose EM are verified.

Stage 3

MemM's analytical model will be developed in this stage.

First of all, PWE model for metamaterial bandgap prediction is modified. Design parameters, such as the tensile stress and attached mass magnitude, is integrated into the PWE model, and thus allow the investigation of relation between parameters and bandgap properties.

Secondly, piezoelectric constitutive equations are integrated with the MemR's analytical model. So the relation between applied electric potential on the piezoelectric membrane and the membrane tensile stress is constructed. Then by incorporating with the modified PWE model, the applied electric field's effect on MemM bandgap properties can be obtained directly.

In addition, the vibration response of thin plate structure with resonator attached is modified to integrate the MemR model. This model can then reveal the vibration response of a thin plate structure attached with MemM.

To the best knowledge of the author, it will be the first time to develop such analytical model for the MemM and allow the incorporation of piezoelectric material.

Stage 4

Numerical simulation of the MemM with normal membrane will be carried out in this stage, for the purpose of verifying the developed analytical model and investigating the vibration control

Finite structures will be constructed in COMSOL Multiphysics. The bandgap structure the vibration absorption performance of the MemM will be numerically simulated, and by comparing the results with the theoretical prediction, the accuracy of the proposed theoretical model can be verified.

Also, through the simulation, the effect of design factors of a MemM, such as the applied tensile stress and mass magnitudes, will be explored. The simulation results provide verification of analytical model accuracy and help confirming the detailed dimension and other information for the experiment design and setup.

Stage 5

The effect of MemM with piezoelectric membranes will be investigated in this stage. By using similar finite models in previous stage, the effect of applied electric field intensity on the bandgap properties of the piezoelectric MemM will be simulated and the results will be compared with the analytical model's prediction. Bandgap tunability and vibration absorption capability of the piezoelectric MemM is examined in this stage. In addition, the analytical model for control algorithm of the piezoelectric metamaterial applied on thin plate structure will be developed based on the thin plate vibration model. The work in this stage provides concept proof for the design and application of semi-active control MemM.

Stage 6

Experimental test of MemM's vibration characteristics and vibration absorption capability are conducted in this stage.

First, membrane stretching mechanisms for MemR assembling will be designed and manufactured. The outer frame of the MemR can be produced by 3D printing technique, and through the stretching mechanism MemR will be manufactured. The prototypes will then be attached to thin aluminium plates for testing.

The vibration absorption performance will be experimentally verified and validated. The bandgap property and vibration absorption performance of the structure when applied to a thin plate will be evaluated.

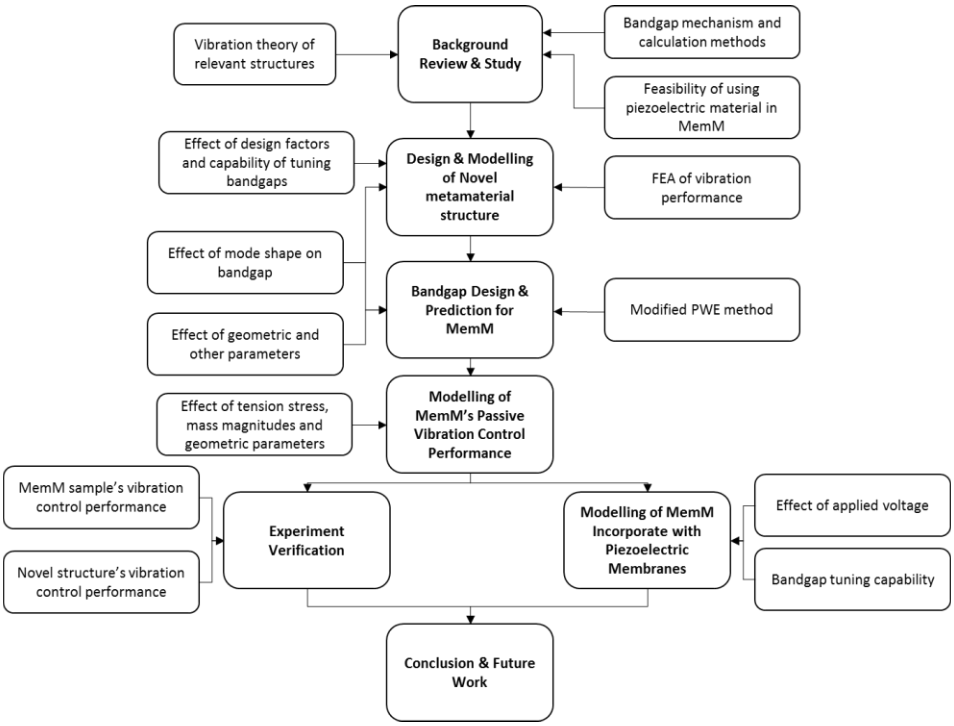

Figure 22. Research pathway of the thesis

1.6 Thesis Content and Structure

This thesis is constructed as follow:

Chapter 2 introduces this study's theoretical background and development of analytical model for the MemM and thin plate structure.

Chapter 3 proposes design of an novel EM and examined its bandgap properties through numerical simulation and experiments.

Chapter 4 presents the numerical simulation and experimental results of MemM with normal material membrane. The accuracy of the modified PWE method was examined by numerical simulation. A prototype of MemM attached on thin plate structure is experimentally tested.

Chapter 5 introduces the constitutive equation of PVDF material and integrate it into the modified PWE model. Also, through numerical simulation, the tuning effect of bandgap by externally applied electric field is investigated.

Chapter 6 presents the derivation of semi-active control algorithm of PVDF MemM.

Chapter 7 is the conclusion of this study and introduced the potential future research work.

Chapter 2

2. THEORETICAL BACKGROUND AND DEVELOPMENT

In this section, the basic vibration theory and characteristics of the plate structure, membrane structure, membrane-mass model and plate with attached resonator model is introduced. The modified PWE method are introduced and derived specifically for the MemM attached to a thin plate structure. In addition, the thin plate – resonator coupling model is also presented as it can be considered as the simplified physical model of MemM on thin plates. [1]

- [1] Part of the content in this Chapter is published as: C. Gao, D. Halim and C. Rudd, "Prediction of bandgaps in membrane-type metamaterial attached to a thin plate," in *INTER-NOISE and NOISE-CON Congress and Conference Proceedings*, Madrid, 2019.

2.1 Vibration Theory of Related Structures

The MemM is mainly applied to plate structure for vibration control purpose. Hence the vibration theory of plate structure and plate with attached resonator are closely relevant. Also, the derivative of membrane-type resonator's resonant frequency depends on the membrane-mass model and the membrane structure vibration theory, therefore, the membrane structure's equation of motion is also presented.

2.1.1 Vibration of membrane structure

For a rectangular membrane, an element and forces that applied on the edges of it can be represented by Figure 23.

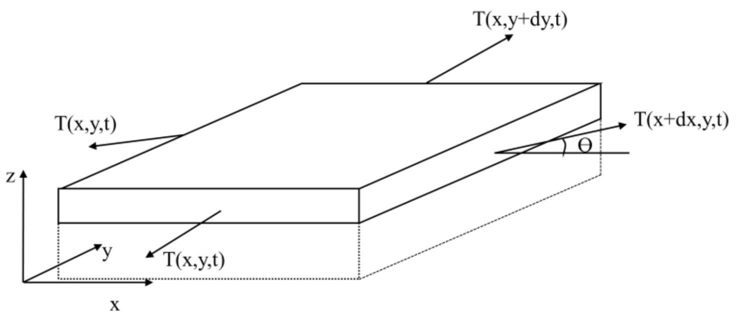

Figure 23: Unit element in a membrane that under tensile stress.

According to Newton's second law, the equilibrium equation of the membrane element is given as:

$$m_s dxdy\frac{\partial^2 w(x,y,t)}{\partial t^2} = \left(Tsin(\theta_1)dy|_{(x+dx,y)} - Tsin(\theta_2)dy|_{(x,y)}\right) + (Tsin(\theta_3)dx|_{(x,y+dy)} - Tsin(\theta_4)dx|_{(x,y)}) \tag{2-1}$$

where $m_s = \rho h$ is the mass per unit area, $w(x,y,t)$ is the transverse displacement, ρ , h , w are the mass density, thickness and transverse displacement of the membrane, T is the tensile force per unit length applied on membrane, θ_n are the angles between the tensile forces and x-y plain. As the angle is very small, $sin(\theta) \approx \tan(\theta) = \frac{\partial w(x,y,t)}{\partial x}$, the equation is transformed into:

$$m_s \frac{\partial^2 w(x,y,t)}{\partial t^2} = Tdy \left[\frac{\partial w(x,y,t)}{\partial x} |_{(x+dx,y)} - \frac{\partial w(x,y,t)}{\partial x} |_{(x,y)} \right] + Tdx [\frac{\partial w(x,y,t)}{\partial y} |_{(x,y+dy)} - \frac{\partial w(x,y,t)}{\partial y} |_{(x,y)}] \tag{2-2}$$

$$\rightarrow \; m_s \frac{\partial^2 w(x,y,t)}{\partial t^2} - T\nabla^2 w(x,y,t) = 0 \tag{2-3}$$

where $\nabla^2 = \frac{\partial^2}{\partial x^2} + \frac{\partial^2}{\partial y^2}$ is the Laplace operator. Equation (2-3) is the free vibration equation of rectangular membrane. If the membrane is under force vibration and excited by pressure that applied on its surface, an extra item $p(x,y,t)$ that represents the external pressure should be added to the equation. In order to solve equation (2-3), assume the displacement in the following form:

$$w(x,y,t) = W(x,y)e^{i\omega t} \tag{2-4}$$

where $W(x,y)$ is the amplitude of transverse displacement $w(x,y,t)$, ω is the natural frequency of the membrane, t is the time and $i^2 = -1$. Substitute equation (2-4) into equation (2-3):

$$-\omega^2 m_s W(x,y) - T\nabla^2 W(x,y) = 0 \tag{2-5}$$

$$\rightarrow \left(\frac{\partial^2 W(x,y)}{\partial x^2} + \frac{\partial^2 W(x,y)}{\partial y^2} \right) + \beta^2 W(x,y) = 0 \tag{2-6}$$

where $\beta^2 = \frac{m_s \omega^2}{T} = \frac{\omega^2}{c^2}$. c is the speed of wave transmission in the membrane.

For convenience of solving equation (2-6), one can further assume the displacement amplitude $W(x,y)$ is composed by two separated functions of variable x and y respectively:

$$W(x,y) = X(x)Y(y) \tag{2-7}$$

Substitute equation (2-7) into equation (2-6):

$$\begin{cases} \dfrac{d^2X}{dx^2} + \alpha^2 X = 0 & \text{(2-8a)} \\ \dfrac{d^2Y}{dy^2} + \gamma^2 Y = 0 & \text{(2-8b)} \end{cases}$$

where $\alpha^2 + \gamma^2 = \beta^2$. Equation (2-8) are two standard PDE that with the form of solutions as:

$$\begin{cases} X(x) = A_1 sin\alpha x + A_2 cos\alpha x & \text{(2-9a)} \\ Y(y) = A_3 sin\gamma y + A_4 cos\gamma y & \text{(2-9b)} \end{cases}$$

Introduce equation (2-9) into equation (2-7):

$$W(x,y) = C_1 sin\alpha x sin\gamma y + C_2 sin\alpha x cos\gamma y + C_3 cos\alpha x sin\gamma y + C_4 cos\alpha x cos\gamma y \tag{2-10}$$

where C are the constants determined by boundary conditions. For the rectangular membrane that all edges are clamped, the mode shapes of the membrane can be assumed as:

$$W(x,y) = C_1 \sin(\alpha x)\sin(\gamma y) \tag{2-11}$$

where C_1 is the amplitude of vibration that determined by the incident excitation. α and γ are the frequency coefficients. When the boundary of the membrane is clamped, the displacement at the edges will always be zero, thus:

$$sin(\alpha a) = 0 \ and \ \sin(\gamma b) = 0 \tag{2-12}$$

So the parameters will be:

$$\alpha_m a = m\pi \ and \ \gamma_n b = n\pi, \qquad m,n = 1,2,3 \ldots \tag{2-13}$$

$$\Rightarrow \alpha_m = \frac{m\pi}{a} \ and \ \gamma_n = \frac{n\pi}{b} \tag{2-14}$$

As $\alpha^2 + \gamma^2 = \beta^2 = \frac{m_s \omega^2}{T}$, one can therefore obtain the natural frequencies of the clamped membrane by:

$$\omega_{mn} = c\pi \sqrt{\left(\frac{m}{a}\right)^2 + \left(\frac{n}{b}\right)^2}, \qquad m, n = 1,2,3 \ldots \tag{2-15}$$

When considering the vibration of a circular membrane with radius a, the equation needs to adopt the polar coordinate system, hence the displacement of membrane will be expressed as $w(r, \theta, t)$, and equation (2-5) will become:

$$T\nabla^2 W(r, \theta, t) = m_s \frac{\partial^2 W(r, \theta, t)}{\partial t^2} \tag{2-16}$$

where $\nabla^2 = \frac{\partial^2}{\partial r^2} + \frac{1}{r}\frac{1}{\partial r} + \frac{1}{r^2}\frac{\partial^2}{\partial y^2}$. To solve equation (2-16), one can assume the displacement in the following form:

$$W(r, \theta, t) = W(r, \theta)\, e^{i\omega t} \tag{2-17}$$

$$W(r, \theta) = R(r)\Theta(\theta) \tag{2-18}$$

Substitute equation (2-17) and (2-18) into equation (2-16):

$$\begin{cases} \dfrac{d^2\Theta}{d\theta^2} + v^2\Theta = 0 & \text{(2-19a)} \\ \dfrac{d^2R}{dr^2} + \dfrac{1}{r}\dfrac{R}{dr} + \left(\beta^2 - \dfrac{v^2}{r^2}\right)R = 0 & \text{(2-19b)} \end{cases}.$$

The solution of equation (2-19a) can be given as a standard form:

$$\Theta_v(\theta) = A_{1v}\sin(v\theta) + A_{2v}\cos(v\theta) \tag{2-20}$$

Equation (2-19b) is a Bessel equation. v is an integer and represents the order of the Bessel function. A are the constant decided by the boundary conditions. So the solution is given by [91]:

$$R_v(r) = A_{3v}J_v(\beta r) + A_{4v}Y_v(\beta r) \tag{2-21}$$

where $J_v(\beta r)$ and $Y_v(\beta r)$ are the first and second kind of Bessel functions of order v.

Assume the boundary conditions of the circular membrane is clamped, substitute equation (2-20) and (2-21) into equation (2-18), equation given as:

$$W_v(r, \theta) = A_{1v}J_v(\beta r)\sin(v\theta) + A_{2v}J_v(\beta r)\cos(v\theta) \tag{2-22}$$

According to boundary condition, the above equation can be transformed as:

$$W_v(a,\theta) = A_{1v}J_v(\beta a)\sin(v\theta) + A_{2v}J_v(\beta a)\cos(v\theta) = 0 \tag{2-23}$$

Therefore, either $J_v(\beta a) = 0$ or $A_{1v}\sin(v\theta) + A_{2v}\cos(v\theta) = 0$. To avoid trivial solution, it requires:

$$J_v(\beta a) = 0 \tag{2-24}$$

It means that to obtain solution for the equation, the independent variable βa should be the zero points for the vth Bessel function of the first kind. As ${\beta_w}^2 = \frac{m_s\omega^2}{T}$, and the number of zero points for each order of Bessel function is infinite, so for each order v, there will be a specific ω_{vw} that corresponds to each of the zeros ($v, w = 1,2,3$ ...). The ω_{vw} is the corresponding natural frequency of the membrane.

2.1.2 Vibration of thin plate structure

For a thin rectangular plate, assume the transverse displacement of plate is much smaller than the plate thickness, then the free vibration equation of motion can be given as [128]:

$$D\nabla^4 w(x,y,t) + m_s\frac{\partial^2 w(x,y,t)}{\partial t^2} = 0 \tag{2-25}$$

where $D = \frac{Eh^3}{12(1-v^2)}$ is the flexural rigidity of the plate, E, h, v are the Young's modulus, thickness and Poisson's ratio of the plate, and $\nabla^4 = \left(\frac{\partial^2}{\partial x^2} + \frac{\partial^2}{\partial y^2}\right)\left(\frac{\partial^2}{\partial x^2} + \frac{\partial^2}{\partial y^2}\right) = \frac{\partial^4}{\partial x^4} + 2\frac{\partial^4}{\partial x^2\partial y^2} + \frac{\partial^4}{\partial y^4}$.

In a membrane structure, the thickness and modulus of the material are relatively small, therefore the flexural rigidity is ignored. Tensile stress is required in membrane structure to avoid winkle. The stiffness of membrane structure is formed because of the stress stiffening effect. Therefore, in equation of motion the tensile stress is involved as a parameter. Compared with the membrane structure's equation of motion (equation (2-3)), one of the obvious difference in the thin plate structure's equation of motion is the involvement of flexural rigidity D.

Similar to the solving procedure of membrane vibration equation, the same assumption of the displacement can be adopted and substitute into equation (2-25):

$$\nabla^4 W(x,y) - \varphi^4 W(x,y) = 0 \tag{2-26}$$

where $\varphi^4 = \frac{m_s\omega^2}{D}$. With the assumption of a simple supported rectangular boundary condition, the solution of the equation can be expressed as [128]:

$$W_{mn}(x,y) = A_{mn}\sin\left(\frac{m\pi x}{a}\right)\sin\left(\frac{n\pi y}{b}\right), \qquad m,n = 1,2,3 \ldots \tag{2-27}$$

where a, b are the dimension of the rectangular plate. The natural frequency of the plate structure is then given as:

$$\omega_{mn}(x,y) = \pi^2\left[\left(\frac{m}{a}\right)^2 + \left(\frac{n}{b}\right)^2\right]\sqrt{\frac{D}{m_s}}, \qquad m,n = 1,2,3 \ldots \tag{2-28}$$

2.2 Vibration of Membrane-Mass Model

The MemR's resonant frequency is essential in predicting bandgap location frequency of the MemM it formed. For a MemR, it can be simplified as a membrane-mass model. In this study, there are two analytical models are investigated for the resonant frequency prediction of membrane-mass model.

2.2.1 Superposition method

A superposition method is proposed for the solution of membrane-mass model's eigenvalue problem by Zhang et al. [93].

Figure 24 presents a membrane-mass model that formed by a rectangular membrane attached with mass blocks on certain location. The equation of free vibration of this rectangular membrane-mass model can be given as [129]:

$$m_s \frac{\partial^2 w(x,y,t)}{\partial t^2} - T\nabla^2 w(x,y,t) + \sum_{i=1}^{I} m_i h(x,y,x_{i,}y_i,l_{xi},l_{yi}) \frac{\partial^2 w(x,y,t)}{\partial t^2} = 0 \tag{2-29}$$

where m_s, T, w are the mass density per unit area, tension stress per unit length and transverse displacement of the membrane, and m_i is the mass density per unit area of the decorated mass. $h(x,y,x_{i,}y_i,l_{xi},l_{yi})$ represents a combination of 4 Heaviside functions that identify the allocation of mass, given as:

$$\begin{aligned} h(x,y,x_{i,}y_i,l_{xi},l_{yi}) &= H(x-x_i,y-y_i) - H(x-x_i-l_x,y-y_i) \\ &-H(x-x_i,y-y_i-l_y) + H(x-x_i-l_x,y-y_i-l_y) \end{aligned} \tag{2-30}$$

where x_i, y_i are the coordination of the left bottom point of the mass area, and l_x, l_y are the side lengths of the area with mass attached.

For a Heaviside function, it has the property of:

$$H(x-x_0,y-y_0) = \begin{cases} 0 & x < x_0 \; or \; y < y_0 \\ 1 & x \geq x_0 \; or \; y \geq y_0 \end{cases}. \tag{2-31}$$

Therefore, the area with mass attached can be marked out in the equation. Otherwise, the transverse displacement of membrane can be defined as:

$$w(x,y,t) = \sum_{n=1}^{N_x}\sum_{m=1}^{N_y} W_{nm}(x,y)q_{nm}(t) \tag{2-32}$$

where $W_{nm}(x,y) = \sin\left(\frac{n\pi}{L_x}x\right)\sin\left(\frac{m\pi}{L_y}y\right)$ is the modal shape function, and $q_{nm}(t) = \tilde{q}_{nm}e^{j\omega t}$ is the generalized coordinates under simple harmonic excitation.

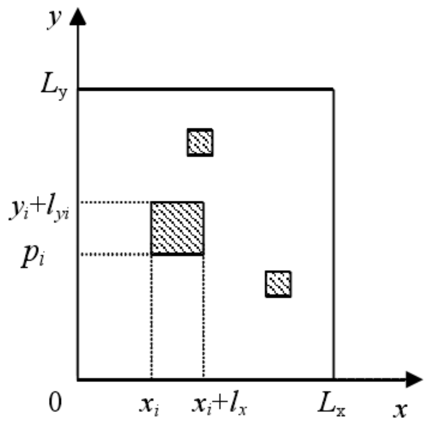

Figure 24: Rectangular membrane with decorated mass [93]

Substitute equation (2-32) into equation (2-29), multiply $W_{rs}(x,y)$ to both side of the equation and conduct integration to both side of the equation, according to the modal orthogonality, equation (2-29) will become:

$$\begin{aligned}
-\omega^2 m_s \int_0^{L_y}\int_0^{L_x}\sum_{n=1}^{N_x}\sum_{m=1}^{N_y} W_{nm}\,W_{rs}\tilde{q}_{nm}dxdy \\
- \omega^2 \sum_{i=1}^{I} m_i \int_{y_i}^{y_i+l_y}\int_{x_i}^{x_i+l_x}\sum_{n=1}^{N_x}\sum_{m=1}^{N_y} W_{nm}W_{rs}\tilde{q}_{nm}dxdy \\
- T\int_0^{L_y}\int_0^{L_x}\nabla^2\sum_{n=1}^{N_x}\sum_{m=1}^{N_y} W_{nm}\,W_{rs}\tilde{q}_{nm}dxdy = 0 \\
\rightarrow -\omega^2 m_s M_{rs}\tilde{q}_{nm} - \omega^2\sum_{i=1}^{I} m_i \sum_{n=1}^{N_x}\sum_{m=1}^{N_y} I_{nm,rs}^{i}\tilde{q}_{nm} + T\,K_{rs}\tilde{q}_{nm} = 0
\end{aligned} \tag{2-33}$$

The $M_{rs}, I^i_{nm.rs}$ and K_{rs} of the above equation are expressed as:

$$M_{rs} = \int_0^{L_x}\int_0^{L_y} W_{rs}\sum_{n=1}^{N_x}\sum_{m=1}^{N_y} W_{nm}\,dxdy = \begin{cases} 0 & r \neq n \; or \; s \neq m \\ \frac{L_x L_y}{4} & r = n \; and \; s = m \end{cases} \tag{2-34}$$

$$K_{rs} = -\int_0^{L_x}\int_0^{L_y} W_{rs}\nabla^2\sum_{n=1}^{N_x}\sum_{m=1}^{N_y} W_{nm}\,dxdy = \begin{cases} 0 & r \neq n \; or \; s \neq m \\ \frac{L_x L_y}{4}\left[(\frac{n\pi}{L_x})^2 + (\frac{m\pi}{L_y})^2\right] & r = n \; and \; s = m \end{cases} \tag{2-35}$$

For $I^i_{nm.rs}$, it is defined as:

$$I^i_{nm.rs} = \int_{y_i}^{y_i+l_y}\int_{x_i}^{x_i+l_x} W_{rs}W_{nm}dxdy \tag{2-36}$$

Substitute the modal shape function of W_{nm} into it:

$$I^i_{nm.rs} = \int_{y_i}^{y_i+l_y}\int_{x_i}^{x_i+l_x} \sin\left(\frac{r\pi}{L_x}x\right)\sin\left(\frac{s\pi}{L_y}y\right)\sin\left(\frac{n\pi}{L_x}x\right)\sin(\frac{m\pi}{L_y}y)dxdy$$

$$= \int_{y_i}^{y_i+l_y} \sin\left(\frac{s\pi}{L_y}y\right)\sin(\frac{m\pi}{L_y}y)\int_{x_i}^{x_i+L_x} \sin\left(\frac{r\pi}{L_x}x\right)\sin\left(\frac{n\pi}{L_x}x\right)dxdy$$

$$= \int_{y_i}^{y_i+l_y} \sin\left(\frac{s\pi}{L_y}y\right)\sin(\frac{m\pi}{L_y}y)dy\int_{x_i}^{x_i+l_x} -\frac{1}{2}\left[\cos\left(\frac{r\pi}{L_x}x + \frac{n\pi}{L_x}x\right) - \cos\left(\frac{r\pi}{L_x}x - \frac{n\pi}{L_x}x\right)\right]dy$$

$$\begin{aligned} &= \frac{1}{4}\int_{y_i}^{y_i+l_y}\left\{\cos\left[\frac{(s+m)\pi}{L_y}y\right] - \cos\left[\frac{(s-m)\pi}{L_y}y\right]\right\}dy \\ &\times \int_{x_i}^{x_i+l_x}\left[\cos\left(\frac{r\pi}{L_x}x + \frac{n\pi}{L_x}x\right) - \cos\left(\frac{r\pi}{L_x}x - \frac{n\pi}{L_x}x\right)\right]dx. \end{aligned} \tag{2-37}$$

For simplification, define the equation (2-37) as the product of two functions:

$$I^i_{nm.rs} = A \times B \tag{2-38}$$

where:

$$\begin{cases} A = \frac{1}{2}\int_{y_i}^{y_i+l_y}\left\{\cos\left[\frac{(s+m)\pi}{L_y}y\right] - \cos\left[\frac{(s-m)\pi}{L_y}y\right]\right\}dy \\ B = \frac{1}{2}\int_{x_i}^{x_i+l_x}\left\{\cos\left[\frac{(r+n)\pi}{L_x}x\right] - \cos\left[\frac{(r-n)\pi}{L_x}x\right]\right\}dx \end{cases}. \tag{2-39}$$

The values of A and B depend on the value of the parameters s, r, n and m.

For A, it can be expressed as:

$$A = \begin{cases} A_1 = \frac{1}{2}\int_{y_i}^{y_i+l_y}\left\{\cos\left[\frac{(s+m)\pi}{L_y}y\right] - \cos\left[\frac{(s-m)\pi}{L_y}y\right]\right\}dy & (s \neq m) \quad \text{(2-40a)} \\ A_2 = \frac{1}{2}\int_{y_i}^{y_i+l_y}\left\{\cos\left[\frac{(2s)\pi}{L_y}y\right] - 1\right\}dy & (s = m) \quad \text{(2-40b)} \end{cases}.$$

Similarly, for B:

$$B = \begin{cases} B_1 = \dfrac{1}{2}\displaystyle\int_{x_i}^{x_i+l_x}\left\{\cos\left[\dfrac{(r+n)\pi}{L_x}x\right] - \cos\left[\dfrac{(r-n)\pi}{L_x}x\right]\right\}dx & (r \neq n) \\ B_2 = \dfrac{1}{2}\displaystyle\int_{x_i}^{x_i+l_x}\left\{\cos\left[\dfrac{(2r)\pi}{L_x}x\right] - 1\right\}dx & (r = n) \end{cases}. \quad \begin{matrix}(2\text{-}41a)\\(2\text{-}41b)\end{matrix}$$

Therefore, $I_{nm.rs}^{i}$ is given as:

$$I_{nm.rs}^{i} = \int_{y_i}^{y_i+l_y}\int_{x_i}^{x_i+l_x} W_{rs}W_{nm}dxdy = \begin{cases} A_1 \times B_1 & (r \neq n \; and \; s \neq m) \\ A_1 \times B_2 & (r = n \; and \; s \neq m) \\ A_2 \times B_2 & (r = n \; and \; s = m) \\ A_2 \times B_1 & (r \neq n \; and \; s = m) \end{cases}. \quad (2\text{-}42)$$

Equation (2-33) can be expressed in a matrix form as:

$$\{\omega^2\{[M] + [Q]\} - [K]\}\{\tilde{q}\} = 0 \quad (2\text{-}43)$$

Then equation (2-43) can be solved as an eigenvalue problem, and the eigenfrequencies of the membrane with mass model can be. The equation (2-43) is composed of infinite series of equations because the superposition of resonant mode shapes of different orders. In actual calculation, a truncation of the resonant order number (N_x and N_y) will be taken and the results' accuracy will not be largely affected when the truncation number is larger than a certain value. According to Zhang et al [130], when modal number is larger than 9, the results will be accurate enough. Also, as in this method, the Young's modulus of membrane and material are ignored and the mass area is allowed to bend, so internal resonant of the area will occur if modal number is too large.

The equation is solved to obtain the eigenfrequencies through Matlab. To examine the accuracy and feasibility of the method, the results are compared with the numerical simulation. The MemR's configuration in the FEA software is shown in Figure 25 and the design parameters are given in table below:

Table 1: Size parameter of membrane-type resonator components

	Membrane		Mass		Frame
l (mm)	80	**a**	10	**L**	90
Thickness **t** (mm)	0.1	**h**	2	**T**	4
Tension stress (Pa)	3.5×10^{5}		-		-

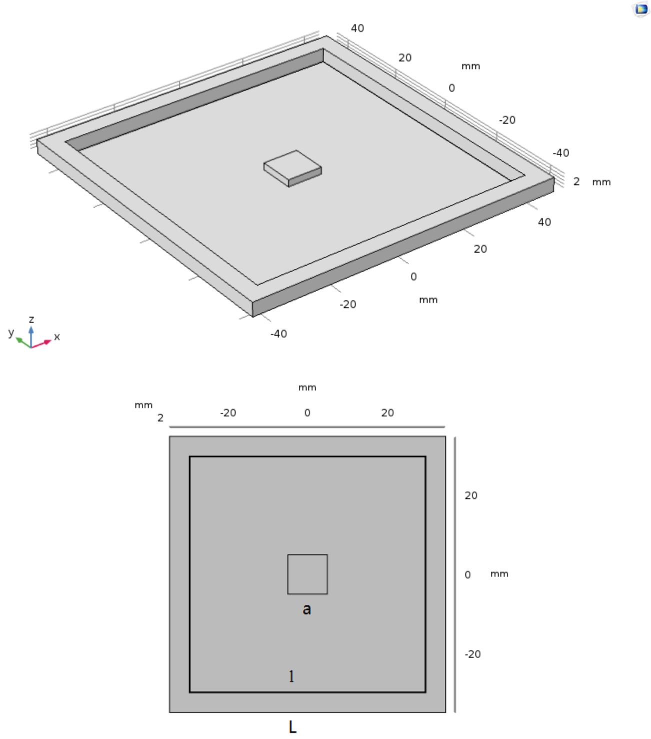

Figure 25: Schematic diagram of membrane-type resonator

By using the same parameters, both analytical and numerical simulation results are compared and given in Table 2.

Table 2: Eigen frequency of the membrane-type resonator by using COMSOL and modal superposition method

Order of frequency	FEA method	Superposition method							
		Truncation in modal number							
		8	9	10	11	12	13	14	20
1	44.69	112.4	56.5	56.3	91.4	91.8	68.3	68.2	67.4
2	152	224.28	246.2	244.6	242.3	245.3	245.6	244.5	247.9
3	233	344.38	281.1	280.9	312.4	314.3	283.9	283.4	293.9
4	269	475.09	491	486.8	473.3	484.5	488.2	484.7	495.7

According to the table, the aforementioned modal superposition method reveals instability when changing the truncation modal number. The difference between this method and the FEA results is large. Also, when running the corresponding Matlab codes of the analytical model, the time consuming is relatively long, because integration is conducted for each modal superposition process.

Also, the inaccuracy of this model is predictable. The reasons are as follows:

1. In this model, the Young's modulus and Poisson's ratio of membrane and mass is not considered. However, in reality, such property is also very important to the vibration property of the membrane.

2. The membrane area on which the mass attached to is not assumed to be rigid and it is able to bend, which is very different from the real situation.

2.2.2 Rayleigh method

Another theoretical method for the prediction of MemR's resonant frequencies is the Rayleigh method. For a MemR shown in Figure 26, assume the mass is a concentrated point mass, the coordinate of the point mass is (q, h).

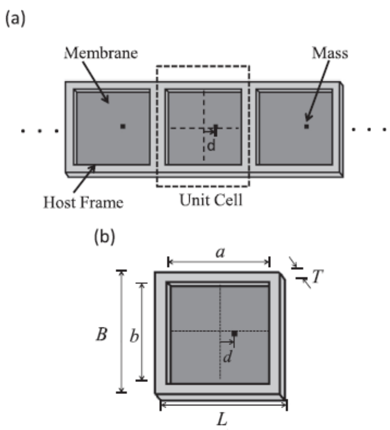

Figure 26: a. metamaterial beam with membrane-type resonator; b. unit cell of the membrane resonator. (Adapted and taken from [131])

By using Rayleigh method, the strain energy and kinetic energy of the MemR can be expressed by [131]:

$$U_{b,max} = \frac{1}{2}\iint D\{(\frac{\partial^2 w}{\partial x^2}+\frac{\partial^2 w}{\partial y^2})^2 - 2(1-v)[\frac{\partial^2 w}{\partial x^2}\frac{\partial^2 w}{\partial y^2} - (\frac{\partial^2 w}{\partial x \partial y})^2]\}dxdy \quad \text{(2-44)}$$
$$+\frac{1}{2}\iint T[(\frac{\partial^2 w}{\partial x^2})^2 + (\frac{\partial^2 w}{\partial y^2})^2]dxdy$$

$$T_{max} = \frac{\omega^2}{2}\{\iint m_s w^2(x,y)dxdy + M(q,h)\, w^2(q,h)\} \quad \text{(2-45)}$$

where $D = \frac{Et^3}{12(1-v^2)}$ is the bending stiffness of the membrane, E, t and v are the Young's modulus, thickness and Poisson's ratio of the membrane respectively. T is the tension stress per unit length on membrane, $M(q,h)$ is the mass located at coordinate (q,h). $w(x,y)$ and $w(q,h)$ are the transverse displacement of the membrane and mass. ω^2 is the natural frequency.

According to equation (2-44) and (2-45), it yields the natural frequency as:

$$\omega^2 = \frac{2U_{b,max}}{\iint m_s w^2(x,y)dxdy + M(q,h)\, w^2(q,h)}. \quad \text{(2-46)}$$

The modal shape function is assumed as:

$$w(x,y) = A_{mn}\sin\left(\frac{\pi x}{a}\right)\sin\left(\frac{m\pi x}{a}\right)\sin\left(\frac{\pi y}{b}\right)\sin\left(\frac{n\pi y}{b}\right). \quad \text{(2-47)}$$

For membrane-type resonator, normally the fundamental resonant frequency is the one generating bandgap. Therefore, the shape function will become:

$$w(x,y) = A_{11}\sin^2\left(\frac{\pi x}{a}\right)\sin^2\left(\frac{\pi y}{b}\right). \quad \text{(2-48)}$$

Substitute equation (2-9) into equation (2-7), the fundamental resonant frequency of the MemR ω_{11} (rad/s) is given as:

$$\omega_{11} = \frac{1}{2\pi}\sqrt{\frac{\frac{\pi^4 D}{4a^3b^3}(3b^4+3a^4+2a^2b^2)+\frac{3(a^2+b^2)T\pi^2}{16ab}}{\frac{9abm_s}{64}+Msin^4(\frac{\pi q}{a})sin^4(\frac{\pi h}{b})}}. \quad \text{(2-49)}$$

As the MemR can be simplified as a spring-mass model, therefore the resonant frequency of the model is given as $\omega_{11} = \sqrt{\frac{k_R}{m_R}}$, where k_R is the equivalent stiffness of the resonator. Hence, the equivalent stiffness of the model can be obtained as:

$$k_R = \frac{m_R}{4\pi^2} \frac{\frac{\pi^4 D}{4a^3b^3}(3b^4+3a^4+2a^2b^2)+\frac{3(a^2+b^2)T\pi^2}{16ab}}{\frac{9abm_S}{64}+Msin^4(\frac{\pi q}{a})sin^4(\frac{\pi h}{b})}. \tag{2-50}$$

The accuracy of the model is examined by numerical simulation as well. With the same example used in section 2.2.1, the obtained resonant frequency by FEA simulation (42Hz) and Rayleigh method (44Hz) are found normally consistent.

Otherwise, the accuracy of the Rayleigh method is further examined by FEA method. The tensile stress applied on the membrane is changed from 0.1MPa to 2.0MPa, and the fundamental resonant frequency obtained through FEA and Rayleigh method is compared and presented in Table 3.

Table 3: The fundamental resonant frequency of a MemR applied with different tension stress

	Tensile stress (MPa)	FEA	Rayleigh's method
1	0.1	27.02	24.68
2	0.2	35.33	33.06
3	0.3	41.84	39.71
4	0.4	47.36	45.39
5	0.5	52.25	50.44
6	0.6	56.68	55.02
7	0.7	60.75	59.26
8	0.8	64.55	63.21
9	0.9	68.12	66.92
10	1.0	71.49	70.44
11	1.1	74.70	73.80
12	1.2	77.77	77.01
13	1.3	80.72	80.08
14	1.4	83.55	83.05
15	1.5	86.29	85.91
16	1.6	88.93	88.68
17	1.7	91.49	91.37
18	1.8	93.98	93.98
19	1.9	96.41	96.52
20	2.0	98.77	98.99

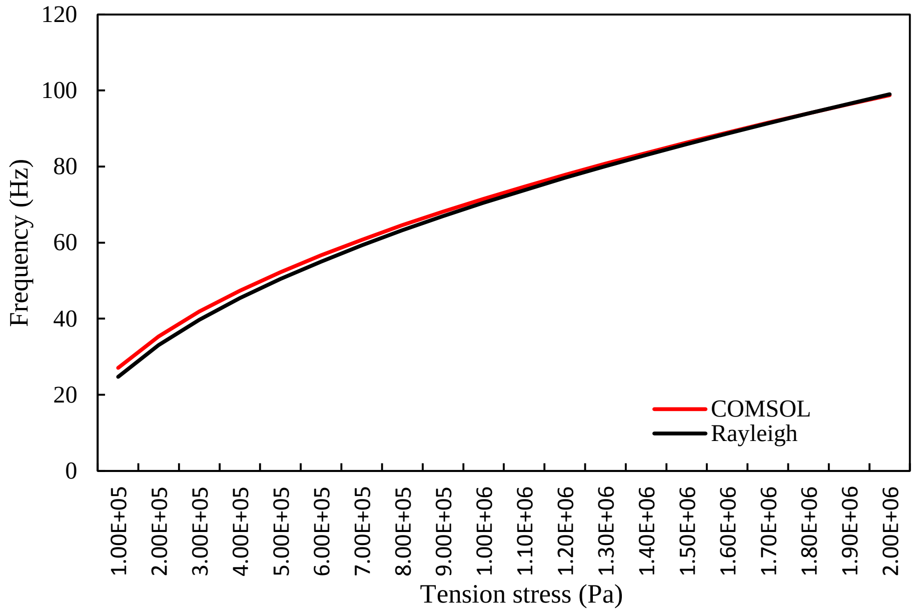

Figure 27: 1st resonance frequency of membrane-type resonator under various tension stress worked out by COMSOL and Rayleigh's method

According to the table, the Rayleigh method is able to predict the resonance frequency of the membrane-type resonator accurately. Small amount of error exist but within an acceptable range.

In the simulation, it is also found that the error caused by the Rayleigh method is related with the size of mass block. In the model, the attached mass is assumed as a concentrated point mass. However, in reality, the mass block has a certain occupied area. Therefore, the existence of the mass block will somehow influence the mode shape of the MemR system. Inaccuracy of the mode shape function is thus occurred and leads to error.

To investigate the influence of mass blocks' size to deviation, the curve of size versus average error is obtained and shown in Figure 28. The size is changed from 6mm to 20mm. For each different size, the tensile stress applied to the membrane is changed from 0.1MPa to 1.0MPa, then the fundamental resonant frequencies of the MemR are obtained by the Rayleigh method (f_R) and compared with the numerical simulation results (f_C) respectively. The differences between f_R and f_C are summed and averaged, then plotted against the dimensionless length ratio of mass radius and membrane side length a/L. The results are shown in Figure 28.

It is found that along with the increase of dimension ratio, the average error is growing. It demonstrates that the increment of mass platelet size will affect the mode shape function accuracy in the assumption and thus amplify the error.

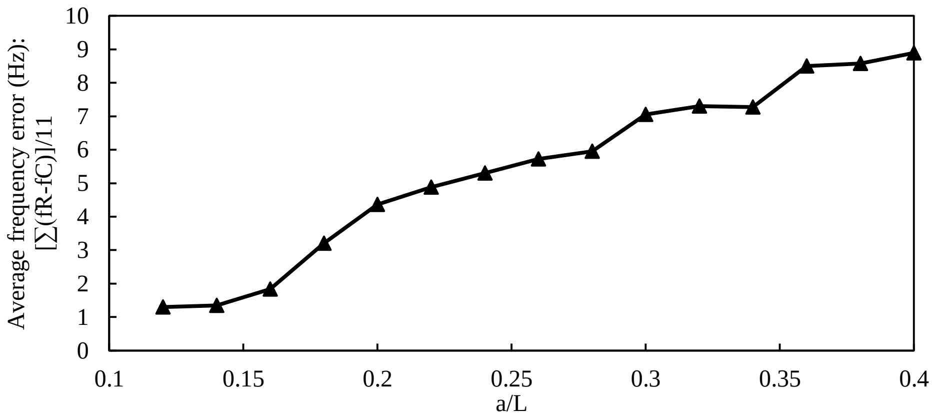

Figure 28. Average of frequency difference between simulation and theoretical model results.

In the Rayleigh's method, the flexural stiffness of the membrane is also considered, which is different from the widely adopted membrane vibration model that ignore the flexural stiffness. The flexural stiffness is defined as a function of materials Young's modulus. Actually, when applied with tensile stress, the membrane will have certain capability in preventing flexural vibration and therefore possess the bending stiffness. However, in the former method, such property is ignored. In order to illustrate the effect of modulus in resonant frequency, numerical simulation is conducted. With the same tensile stress and mass block applied, the Young's modulus of the membrane is adjusted. As shown in Table 4, the increase of modulus will result in the elevating of fundamental resonant frequencies. Hence the Rayleigh method is closer to the actual situation.

Table 4: The fundamental resonant frequency of a MemR with various membrane material Young's modulus

Change membrane's Young's modulus	
Young's modulus (GPa)	Fundamental resonant frequency (Hz)
1.5	107.85
2.0	108.4
2.5	108.89
3.0	109.33
3.5	109.74
4.0	110.12
4.5	110.48
5.0	110.82
5.5	111.14
6.0	111.45

2.3 Plane Wave Expansion (PWE) Method

2.3.1 Band structure of single layer MemM

As the MemM can be simplified as combination of mass-spring resonators. If apply a single layered MemM to a thin plate structure, the system can be simplified as the model shown in Figure 29. To calculate the dispersion relation of this structure, the PWE method is employed and modified accordingly.

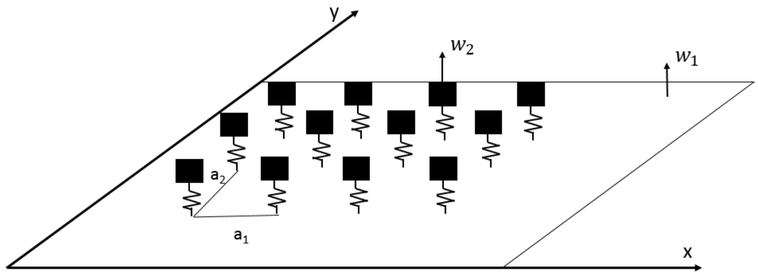

Figure 29: The configuration of plate with periodically allocated spring-mass resonators

For a thin plate with resonators attached, according to equation (2-25), the equation of motion of the system can be given as:

$$\begin{cases} D\left(\frac{\partial^2}{\partial x^2}+\frac{\partial^2}{\partial y^2}\right)^2 w_1(x,y)-\omega^2 m_s w_1(x,y)=\sum_R f_1(X,Y)\delta[(x-X,y-Y)] & \text{(2-51a)} \\ -\omega^2 m_R w_2(X,Y)=f_2(X,Y) & \text{(2-51b)} \end{cases},$$

where (x,y) and (X,Y) are the coordinates of points on the plate and the location of resonators, m_s is the mass density of the plate per unit area and m_R is the mass of the resonator masses. $w_1(x,y)$ and $w_2(X,Y)$ are transverse displacement of plate and resonator at different points, f_1 and f_2 are forces that applied on thin plate and resonator masses, and δ is Dirac function. Change the coordination into vectors of x and y [132]:

$$\begin{cases} r=(x,y) & \text{(2-52a)} \\ R=m\boldsymbol{X}+n\boldsymbol{Y} \quad m,n=1,2,3\ldots' & \text{(2-52b)} \end{cases}$$

where $\boldsymbol{X} = (a_{11}, a_{12}) = (a_1, 0)$ and $\boldsymbol{Y} = (a_{21}, a_{22}) = (0, a_2)$. Therefore equation (2-51) will transform into:

$$\begin{cases} D(\frac{\partial^2}{\partial x^2} + \frac{\partial^2}{\partial y^2})^2 w_1(r) - \omega^2 m_s w_1(r) = \sum_R f_1(R)\delta[(r-R)] & \text{(2-53a)} \\ -\omega^2 m_R w_2(R) = f_2(R) & \text{(2-53b)} \end{cases}.$$

The force f_1 and f_2 are defined as:

$$\begin{cases} f_1(R) = -k_R[w_1(R) - w_2(R)] & \text{(2-54a)} \\ -\omega^2 m_R w_2(R) = f_2(R) & \text{(2-54b)} \end{cases},$$

where k_R is the equivalent stiffness of the resonator.

Furthermore, as the resonators attached are allocated periodically, the thin plate with the resonators can form a periodic structure. According to Bloch theorem, the displacement of the plate can be expressed as:

$$w_1(r) = \sum_G [W_1\,(G)e^{-i(k+G)r}], \tag{2-55}$$

where $k = (k_x, k_y)$ is the Bloch wave vector and G is the reciprocal-lattice vector, $G = m\boldsymbol{b_1} + n\boldsymbol{b_2}$. For the rectangular plate that shown in Figure 7, $\boldsymbol{b_1} = (\frac{2\pi}{a_1}, 0)$ and $\boldsymbol{b_2} = (0, \frac{2\pi}{a_2})$.

Also, because of the periodicity, the displacements of the plate at the resonators attached points can be given as:

$$\begin{cases} w_1(R) = w_1(0)e^{-ikR} & \text{(2-56a)} \\ w_2(R) = w_2(0)e^{-ikR} & \text{(2-56b)} \end{cases}$$

The Dirac function satisfies that [132]:

$$\sum_R e^{-ikR}\,\delta(r-R) = e^{-ikr}\sum_R \delta(r-R). \tag{2-57}$$

Define $g(r) = \sum_R \delta(r-R)$, and because of the periodicity, $g(r)$ can be expanded as:

$$g(r) = \sum_G \tilde{g}(G)\, e^{-iGr}. \tag{2-58}$$

And by definition of inverse Fourier transform:

$$\tilde{g}(G) = \frac{1}{S}\iint_S g(r)e^{iGr}\, dS = \frac{1}{S} \tag{2-59}$$

where S is the area of the unit cell. In this case, $S = a_1a_2$. Substitute (2-54), (2-56), (2-57), (2-58) and (2-59) into (2-53), one can obtain [132]:

$$\begin{cases} D[(k+G)_x^2 + (k+G)_y^2]^2W_1(G) - \omega^2 m_s W_1(G) = (-\frac{k_R}{S})[w_1(0) - w_2(0)] & \text{(2-60a)} \\ -\omega^2 m_R w_2(0) = k_R[\sum_G W_1\,(G) - w_2(0)] & \text{(2-60b)} \end{cases}$$

For equation (2-60a), it can be transformed into:

$$DS\left\{\left[(k+G)_x^2 + (k+G)_y^2\right]^2 - \omega^2 m_s S\right\} W_1(G) + k_R \sum_G W_1\,(G) - w_2(0) = 0 \tag{2-61}$$

Equation (2-60b) can be transformed into:

$$-k_R\left[\sum_G W_1\,(G) + w_2(0)\right] - \omega^2 m_R w_2(0) = 0 \tag{2-62}$$

As equations (2-61) and (2-62) consist of infinite summation, a truncation of plane waves number is needed when conduction calculation. In order to obtain an accurate result, the number of plain waves should not be too small. Assume $m = n = (-M, M)$, then the plain wave number is $N \times N = (2M+1)^2$ [132]. By adopting finite number of plain waves, the equation (2-61) and (2-62) can be expressed in matrix form as:

$$\left(\begin{bmatrix} DS[K] + k_R[U] & -k_R[P] \\ -k_R[P^T] & k_R \end{bmatrix} - \omega^2 \begin{bmatrix} m_s S[I] & \mathbf{0} \\ \mathbf{0} & m_R \end{bmatrix}\right) \times \begin{bmatrix} W_1 \\ w_2(0) \end{bmatrix} = \mathbf{0} \tag{2-63}$$

where:

$$[K] = \begin{bmatrix} [\sum_{j=x,y} (k + G_1)_j^2]^2 & \cdots & 0 \\ \vdots & \ddots & \vdots \\ 0 & \cdots & [\sum_{j=x,y} (k + G_{N\times N})_j^2]^2 \end{bmatrix}$$

$$P = \begin{bmatrix} 1 \\ \vdots \\ \cdot \\ 1 \end{bmatrix} \qquad I = \begin{bmatrix} 1 & 0 & \dots & \dots & 0 \\ 0 & 1 & \dots & \dots & \cdot \\ \cdot & \dots & \dots & \dots & \cdot \\ \cdot & \dots & \dots & 1 & 0 \\ 0 & \dots & \dots & 0 & 1 \end{bmatrix} \qquad [U] = [PP^T]$$

$$W_1 = \begin{bmatrix} W_{1,1} \\ W_{1,2} \\ \cdot \\ \vdots \\ W_{1,N\times N} \end{bmatrix}$$

The dispersion relation can be derived by solving the eigenvalue problem of equation (2-63). This is the commonly used PWE method for the calculation of bandgap property of phononic crystals. For the periodically attached membrane-type metamaterial, the PWE method has not been applied to predict its bandgap before.

In the PWE method, the equivalent stiffness and mass of the MemR are needed. Former researches that used PWE method for the MemM did not mention how to obtain the equivalent stiffness of the MemR, and also in the analytical model, the tensile stress that applied on the membrane is not included as an independent parameter. Therefore, the relation between tensile stress and bandgap location is not established directly.

In this study, by combining the Rayleigh method with the PWE method, an analytical model is developed. The tensile stress applied to the membrane is included in the Rayleigh method, through which the equivalent stiffness of the MemR is obtained. Thus the modified PWE method can reveal the effect of tensile stress on the bandgap property.

2.3.2 Band structure of bilayer layer MemM

Because of the unique structure characteristics of MemM, it can be stacked to each other and form a multi-layer MemM. The modified PWE method can also be used to calculate the bandgap property of the multi-layer MemM. Model modification for bilayer MemM is presented in this section.

The bilayer MemM attached to a thin plate structure can be simplified as the model shown in Figure 30.

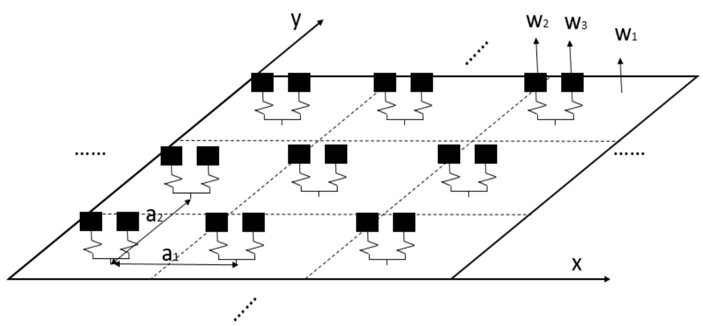

Figure 30. Configuration of thin plate with periodically allocated spring-mass resonators. The two resonators in one unit cell are attached at the same point.

With bilayer MemM, the equation of motion for the above model can be written as:

$$\begin{cases} D\left(\frac{\partial^2}{\partial x^2}+\frac{\partial^2}{\partial y^2}\right)^2 w_1(x,y)-\omega^2 m_s w_1(x,y)=\sum_R f_1(X,Y)\delta[(x-X,y-Y)]+ & \text{(2-64a)} \\ \qquad \sum_R f_2(X',Y')\delta[(x-X',y-Y')] & \\ -\omega^2 m_{R1} w_2(X,Y)=f_{m1}(X,Y) & \text{(2-64b)} \\ -\omega^2 m_{R2} w_3(X',Y')=f_{m2}(X',Y') & \text{(2-64c)} \end{cases}$$

where (x,y), (X,Y) and (X',Y') are the coordinates of points on the plate and the location of resonators, f_1 and f_2 are forces that applied on thin plate by resonators, and f_{m1} and f_{m2} are forces that applied on the resonators.

Similar to the single layer MemM, the equation of motion can be transformed to:

$$
\begin{cases}
D[(k+G)_x^2+(k+G)_y^2]^2 W_1(G)-\omega^2\rho_p h W_1(G)= \\
-\frac{k_{R1}}{S}[\sum_G W_1(G)-W_2(0)]-\frac{k_{R2}}{S}[\sum_G W_1(G)-W_3(0)] & \text{(2-65a)} \\
-\omega^2 m_{R1} w_2(0)=k_{R1}[\sum_G W_1(G)-W_2(0)] & \text{(2-65b)} \\
-\omega^2 m_{R2} w_3(0)=k_{R2}[\sum_G W_1(G)-W_3(0)] & \text{(2-65c)}
\end{cases}
$$

Expressed in matrix form as:

$$
\left(\begin{bmatrix} DS[K]+k_{R1}[U]+k_{R2}[U] & -k_{R1}[P] & -k_{R2}[P] \\ -k_{R1}[P^T] & k_{R1} & 0 \\ -k_{R2}[P^T] & 0 & k_{R2} \end{bmatrix} - \omega^2 \begin{bmatrix} \rho_p hS[I] & \mathbf{0} & \mathbf{0} \\ 0 & m_{R1} & 0 \\ 0 & 0 & m_{R2} \end{bmatrix}\right) \times \begin{bmatrix} W_1 \\ w_2(0) \\ w_3(0) \end{bmatrix} = 0 \qquad \text{(2-66)}
$$

For each given wave vector k, the eigen-frequency $\omega(k)$ can be derived through the solving of the eigen-problem in equation (2-66). Similar to the single layer MemM introduced in 2.3.1, the bandgap property of the bilayer MemM can be obtained through the modified PWE method, and the tensile stress applied on the membranes are included as independent parameters.

2.4 Vibration of Thin Plate Attached With Resonators

An analytical model of a thin plate attached with spring-mass resonators is demonstrated in this section. Through this model the vibration response of the plate can be obtained conveniently.

The configuration of the structure is shown in Figure 31.

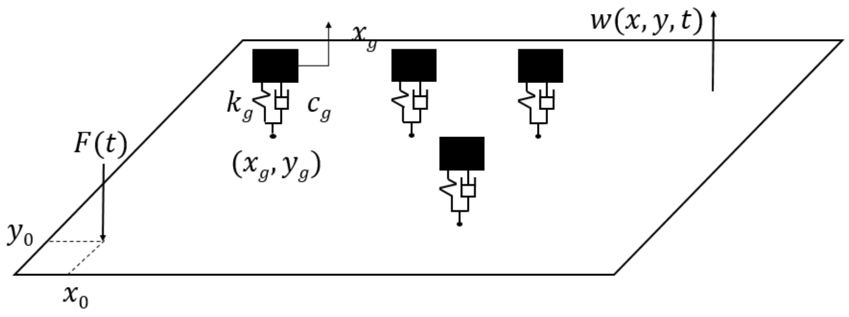

Figure 31. The configuration of a thin plate structure attached with spring-mass resonators randomly.

Similar to the content introduced in section 2.3, equation of motion for the system indicated in Figure 31 are given as:

$$\begin{cases} D\nabla^4 w(x,y,t) + \rho h \dfrac{\partial^2 w(x,y,t)}{\partial t^2} = F(t)\delta(x-x_0, y-y_0) - \displaystyle\sum_g^G m_g \dfrac{\partial^2 x_g(t)}{\partial t^2} & \text{(2-67)} \\ m_g \dfrac{\partial^2 x_g(t)}{\partial t^2} + c_g \dfrac{\partial x_g(t)}{\partial t} + k_g x_g(t) = c_g \dfrac{\partial w(x,y,t)}{\partial t} + k_g w(x,y,t) & \text{(2-68)} \end{cases}$$

where ρ is the mass density of the plate, h is the plate thickness, m_g, c_g and k_g are the mass, damping and stiffness of the spring-mass resonator respectively. Define the displacement and applied force as:

$$\begin{cases} w(x,y,t) = \displaystyle\sum_m^M \sum_n^N W_{nm} e^{i\omega t} \Phi_{nm}(x,y) & \text{(2-69a)} \\ x_g(t) = X_g e^{i\omega t} & \text{(2-69b)} \\ F(t) = F e^{i\omega t} & \text{(2-69c)} \end{cases}$$

Substitute equation (2-69a) and (2-69b) into equation (2-68), one can obtain the expression of resonator displacement:

$$-\omega^2 m_g X_g + i\omega c_g X_g + k_g X_g = i\omega c_g \sum_m^M \sum_n^N W_{nm}\Phi_{nm}(x,y) + k_g \sum_m^M \sum_n^N W_{nm}\Phi_{nm}(x,y)$$

$$\rightarrow \left(-\omega^2 m_g + i\omega c_g + k_g\right) X_g = (i\omega c_g + k_g) \sum_m^M \sum_n^N W_{nm}\Phi_{nm}(x,y)$$

$$\rightarrow X_g = \frac{i\omega c_g + k_g}{-\omega^2 m_g + i\omega c_g + k_g} \sum_m^M \sum_n^N W_{nm}\Phi_{nm}(x,y) \qquad (2\text{-}70)$$

Otherwise, if there is no resonator attached on the plate and it undergoes free vibration, the equation of motion is given as:

$$D\nabla^4 \sum_m^M \sum_n^N W_{nm}\Phi_{nm}(x,y) - \omega_{nm}^2 \rho h \sum_m^M \sum_n^N W_{nm}\Phi_{nm}(x,y) = 0$$

$$\rightarrow D\nabla^4 \sum_m^M \sum_n^N W_{nm}\Phi_{nm}(x,y) = \omega_{nm}^2 \rho h \sum_m^M \sum_n^N W_{nm}\Phi_{nm}(x,y) \qquad (2\text{-}71)$$

where ω_{nm} is the corresponding resonance frequency of each specific mode. Substitute equation (2-69a), (2-69b), (2-70) and (2-71) into equation (2-67):

$$\omega_{nm}^2 \rho h \sum_m^M \sum_n^N W_{nm}\Phi_{nm}(x,y) - \omega^2 \rho h \sum_m^M \sum_n^N W_{nm}\Phi_{nm}(x,y) = F\delta(x - x_0, y - y_0) + \omega^2 \sum_g^G m_g X_g$$

$$\rightarrow \omega_{nm}^2 \rho h \sum_m^M \sum_n^N W_{nm}\Phi_{nm}(x,y) - \omega^2 \rho h \sum_m^M \sum_n^N W_{nm}\Phi_{nm}(x,y)$$

$$= F\delta(x - x_0, y - y_0) + \omega^2 \sum_g^G m_g \left[\frac{i\omega c_g + k_g}{-\omega^2 m_g + i\omega c_g + k_g} \sum_m^M \sum_n^N W_{nm}\Phi_{nm}(x,y)\right] \qquad (2\text{-}72)$$

For the purpose of simplification, define $M = \sum_g^G m_g \frac{i\omega c_g + k_g}{-\omega^2 m_g + i\omega c_g + k_g}$ and substitute into equation (2-72). In the meantime, multiply $\Phi_{rs}(x,y)$ to both sides of above equation and integrate it over the plate surface, according to the orthogonality condition one can obtain:

$$\iint_S \omega_{nm}^2 \rho h \sum_m^M \sum_n^N W_{nm}\Phi_{nm}(x,y)\, \Phi_{rs}(x,y) dS - \iint_S \omega^2 \rho h \sum_m^M \sum_n^N W_{nm}\Phi_{nm}(x,y) \Phi_{rs}(x,y)\, dS$$

$$= \iint_S F\, \delta(x - x_0, y - y_0) \Phi_{rs}(x,y) dS + \iint_S \omega^2 M \sum_m^M \sum_n^N W_{nm}\Phi_{nm}(x,y) \Phi_{rs}(x,y)\, dS$$

$$\Rightarrow W_{nm}[\omega_{nm}^2 \rho h - \omega^2 \rho h - \omega^2 M] \iint_S \Phi_{nm}(x,y)^2 \, dS = F\Phi_{nm}(x_0, y_0) \tag{2-73}$$

Assume the shape function of the structure as $\Phi_{nm}(x,y) = \sin(\frac{n\pi}{L_1}x)\sin(\frac{m\pi}{L_2}y)$, for simplification, define $\mathrm{a} = \frac{n\pi}{L_1}$ and $\mathrm{b} = \frac{m\pi}{L_2}$, then equation (2-73) will be transformed to:

$$W_{nm}[\omega_{nm}^2 \rho h - \omega^2 \rho h - \omega^2 M] \int_0^{L_2} \int_0^{L_1} \sin(ax)^2 \sin(by)^2 \, dxdy = Fsin(ax_0)\sin(by_0)$$

$$\rightarrow \ W_{nm}[\omega_{nm}^2 \rho h - \omega^2 \rho h - \omega^2 M] \frac{L_1 L_2}{4} = Fsin(ax_0)\sin(by_0)$$

$$\rightarrow \ W_{nm} = \frac{4Fsin\left(\frac{n\pi}{L_1}\, x_0\right)\sin(\frac{m\pi}{L_2}y_0)}{[\omega_{nm}^2 \rho h - \omega^2 \rho h - \omega^2 \sum_g^G m_g \frac{i\omega c_g + k_g}{-\omega^2 m_g + i\omega c_g + k_g}] L_1 L_2} \tag{2-74}$$

For a rectangular plate, the natural frequency can be given as:

$$\omega_{nm} = \pi^2[(\frac{n}{L_1})^2 + (\frac{m}{L_2})^2] \sqrt{\frac{D}{\rho h}} \tag{2-75}$$

Substitute equation (2-75) into equation (2-74):

$$W_{mn} = \frac{4Fsin\left(\frac{m\pi}{L_1}\, x_0\right)\sin(\frac{n\pi}{L_2}y_0)}{\left\{\pi^4[(\frac{m}{L_1})^2 + (\frac{n}{L_2})^2]^2 D - \omega^2 \rho h - \omega^2 \sum_g^G m_g \frac{i\omega c_g + k_g}{-\omega^2 m_g + i\omega c_g + k_g}\right\} L_1 L_2} \tag{2-76}$$

Therefore, the vibration response of the plate can be given as:

$$w(x,y,t) = \sum_m^M \sum_n^N W_{mn} e^{i\omega t} \Phi_{mn}(x,y)$$

$$= \sum_m^M \sum_n^N \frac{4Fsin\left(\frac{m\pi}{L_1}\, x_0\right)\sin(\frac{n\pi}{L_2}y_0)}{\left\{\pi^4[(\frac{m}{L_1})^2 + (\frac{n}{L_2})^2]^2 D - \omega^2 \rho h - \omega^2 \sum_g^G m_g \frac{i\omega c_g + k_g}{-\omega^2 m_g + i\omega c_g + k_g}\right\} L_1 L_2} e^{i\omega t} \sin(\frac{m\pi}{L_1}x)\sin(\frac{n\pi}{L_2}y) \tag{2-77}$$

In reality, the above equation is an infinite summation of the resonance modes. However, during the calculation, a truncation of the mode number can be applied and the obtained results will be accurate enough. Normally, the first few modes will contribute to the most of the mode shapes, so the truncation number does not need to be too large. For example, if define the mode number $m = n = 2$, the displacement function can be given as:

$$\begin{aligned}
&\rightarrow w(x,y,t) \\
&= \frac{4Fsin\left(\frac{\pi}{L_1}\,x_0\right)\sin\left(\frac{\pi}{L_2}y_0\right)}{\left\{\pi^4[(\frac{1}{L_1})^2+(\frac{1}{L_2})^2]^2D-\omega^2\rho h-\omega^2\sum_g^G m_g\frac{i\omega c_g+k_g}{-\omega^2 m_g+i\omega c_g+k_g}\right\}L_1L_2}e^{i\omega t}\sin\left(\frac{\pi}{L_1}x\right)\sin\left(\frac{\pi}{L_2}y\right) \\
&+\frac{4Fsin\left(\frac{\pi}{L_1}\,x_0\right)\sin(\frac{2\pi}{L_2}y_0)}{\left\{\pi^4[(\frac{1}{L_1})^2+(\frac{2}{L_2})^2]^2D-\omega^2\rho h-\omega^2\sum_g^G m_g\frac{i\omega c_g+k_g}{-\omega^2 m_g+i\omega c_g+k_g}\right\}L_1L_2}e^{i\omega t}\sin\left(\frac{\pi}{L_1}x\right)\sin\left(\frac{2\pi}{L_2}y\right) \\
&+\frac{4Fsin\left(\frac{2\pi}{L_1}\,x_0\right)\sin(\frac{\pi}{L_2}y_0)}{\left\{\pi^4[(\frac{2}{L_1})^2+(\frac{1}{L_2})^2]^2D-\omega^2\rho h-\omega^2\sum_g^G m_g\frac{i\omega c_g+k_g}{-\omega^2 m_g+i\omega c_g+k_g}\right\}L_1L_2}e^{i\omega t}\sin\left(\frac{2\pi}{L_1}x\right)\sin\left(\frac{\pi}{L_2}y\right) \\
&+\frac{4Fsin\left(\frac{2\pi}{L_1}\,x_0\right)\sin(\frac{2\pi}{L_2}y_0)}{\left\{\pi^4[(\frac{2}{L_1})^2+(\frac{2}{L_2})^2]^2D-\omega^2\rho h-\omega^2\sum_g^G m_g\frac{i\omega c_g+k_g}{-\omega^2 m_g+i\omega c_g+k_g}\right\}L_1L_2}e^{i\omega t}\sin(\frac{2\pi}{L_1}x)\sin(\frac{2\pi}{L_2}y)
\end{aligned} \tag{2-78}$$

Similarly, when change the mode number, equation (2-78) will vary accordingly, and the displacement amplitude of the plate can be obtained. The shape and vibration response of the plate can be revealed by plotting the displacement $w(x, y, t)$ over the coordinate.

2.5 Chapter Summary

The theoretical background of the study is introduced and development of analytical model for the MemM is presented in this chapter.

The vibration theory of the membrane and thin plate structures, which are related with the membrane-type resonator and its target structure for vibration control, are introduced and explained.

Two different analytical methods for the prediction of membrane-type resonator's resonant frequencies were investigated and verified. The Rayleigh method is selected for further study because of the higher accuracy. Since concentrated point mass is assumed in the Rayleigh model, the high density material is recommended to be used in the simulation and experiment for the purpose of enhancing consistency with the analytical prediction.

Otherwise, theoretical model development has been conducted. The PWE model that used for the metamaterial's bandgap prediction was modified to be able to predict the bandgap property of MemM applied on thin plate structures. The modification allows the PWE model to include membrane-type resonator's design parameters, such as material properties, dimension and tensile stress applied on membrane, to be included as independent variables in the model, and reveal directly the design parameters' effect on bandgap properties. In addition, the PWE model is furtherly modified for the purpose of predicting the bandgap properties of multi-layer MemM.

Moreover, the model for the vibration response of a thin plate structure attached with resonators is derived, and this analytical model allows a convenient prediction of vibration response.

Chapter 3

3. DESIGN OF A NOVEL ELASTIC METAMATERIAL WITH BROAD LOW FREQUENCY BANDGAP

In this chapter, the design process of a novel EM is presented and the detailed analysis procedures are introduced. The bandgap property of the proposed structure was investigated and the results indicate that the EM possess a relatively broad bandgap in low frequency region. The purpose of conducting this design and analysis was to make a concept proof for the local resonance bandgap and develop deeper understanding about bandgap forming mechanism and its relationship with resonant mode shapes. Numerical simulation is conducted to assist the design process and parametric analysis. Prototypes are manufacture and experimentally tested.[2]

[2]Part of the content of this chapter has been submitted to: [1] the INTER-NOISE 2020 Congress as a conference paper "Elastic metamaterial with hexagonal prism inclusion for flexural vibration control of a thin plate structure"; [2] the *International Journal of Solids and Structures* as a research article "Bandgap modification of an elastic metamaterial with a broad low-frequency bandgap".

3.1 Structure Design of the Elastic Metamaterial (EM)

The forming of a local resonant type bandgap depends on the resonant frequencies and mode shapes of the unit cells that compose the EM. Therefore, the bandgap performance of the metamaterial can be controlled and adjusted through structural design.

To generate local resonant phenomenon, the EM unit cells normally consist of rigid mass wrapped or supported by elastic material, and matrix frame that holds the inclusions. The unit cell structure can be schematically simplified as mass-spring models: the rigid inclusion and elastic wrapping provide mass and spring stiffness respectively [125]. The utilization of local resonance phenomenon distinguish the EM from PnC, even though the PnC is considered as a special type of AM/EM in many research works. The bandgaps will be formed when the incident wave frequency excites the corresponding resonant modes. Thus the wave energy will be contained within the unit cell and prevent the wave propagation.

Based on this phenomenon, two different EM structures are designed and presented in Figure 32. The designed metamaterial unit cells are composed by three components: a hexagonal prism/cuboid rigid mass, elastic coating of the mass and a supporting frame. The coating material has a hexagon/square cavity for the convenience of rigid mass installation, and six/four supporting beams connecting the inclusion to the frame. With the opening at the top, the hexagonal prism/cuboid mass can be inserted directly and replaced if needed.

For both the designs, the outer side length and height of the unit cell frame are defined as a (59mm), b (66mm) and H (12mm) respectively. The height of the coating material is also 12mm, and the thickness of both the mass are 10mm. Other detailed size parameters are presented in the figure. The material selection for the mass, elastic coating and frame are copper, silicon rubber and epoxy respectively. The material or thickness of the rigid mass can be changed easily for the purpose of adjusting the resonator mass magnitude. The volumes of the hexagonal prism and cuboid are designed to be the same, so to ensure the resonator mass in both types are identical. In the cuboid design, there are four supporting beams connecting the inclusion with the frame, whilst there are six supporting beams in the hexagonal case. The system equivalent stiffness can be effectively tuned if the thickness of the supporting beams are changed. Otherwise, existence of several supporting beams in the unit cell may lead to higher possibility of revealing bending resonant modes and torsional modes in low frequency region.

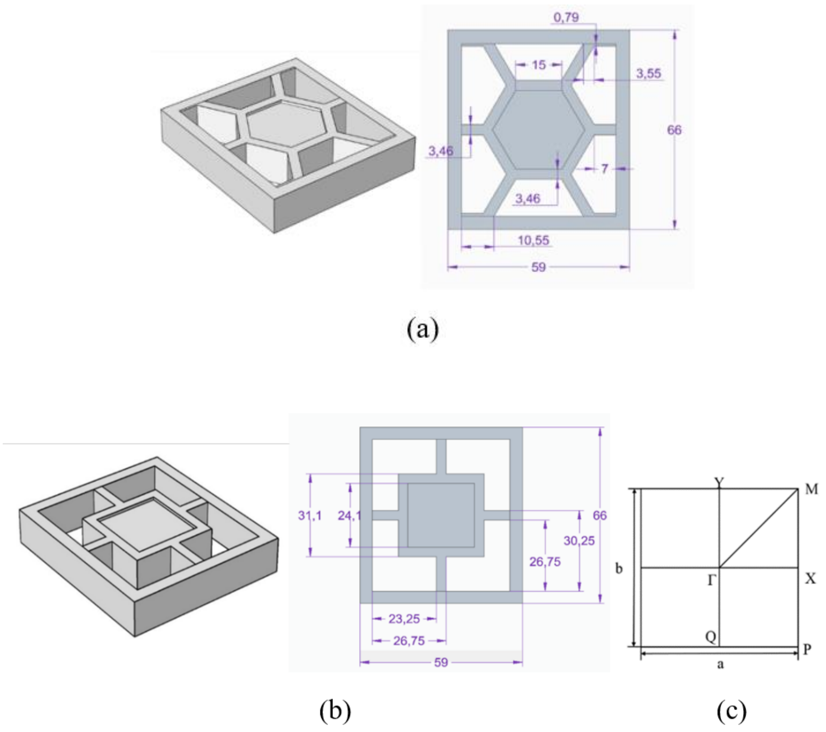

Figure 32. The configuration of the proposed EM unit cells (a) with hexagonal cylinder mass; (b) with cuboid mass. (c) The Brillouin zone of the metamaterial.

Material properties of the metamaterial are determined through Dynamic Mechanical Analysis (DMA) testing. The frame, elastic wrapping and rigid core materials are chosen as 3D printed epoxy, silicon rubber and copper respectively. The obtained material properties are given in Table 5.

Table 5. Material properties of the proposed EM.

	Epoxy	Rubber	Copper
Young's modulus	0.917GPa	3.45MPa	115GPa
Poisson's ratio	0.41	0.49	0.33
Density (kg/m^3)	1100	980	8890

3.2 Proposed EMs' Band Structures and Modal Analysis

The dispersion relation of the proposed structures can reveal the bandgap properties of metamaterials. When simplified as a spring-mass resonator, the governing equation of the unit cell is:

$$(K - M\omega^2)U = 0 \tag{3-1}$$

where K is the stiffness matrix, M is the mass matrix and U is the displacement of the structure. Theoretically, the unit cells should be allocated periodically and form an infinite structure. According to Bloch–Floquet theorem, in infinite periodic structure, all the physical parameter functions should satisfy this condition:

$$f(x_0 + r) = f(x_0)e^{ikr} \tag{3-2}$$

where $r = am + bn$ is a lattice vector representing relative position of the point. a and b as the unit cell sizes and m and n are integers, and k is the wave vector. Therefore, the deformation of the metamaterial structure should also satisfy the Bloch–Floquet condition, and be expressed as:

$$U(x_0 + r) = U(x_0)e^{ikr}. \tag{3-3}$$

Thus, the displacement behaviour of the periodic structure can be derived through the calculation of a primitive unit cell in x_0. By substituting equation (3-3) into equation (3-1), the governing equation can be changed into a function of wave vector k as:

$$[K(k) - M(k)\omega^2]U = 0. \tag{3-4}$$

For each given wave vector k, the solutions of the equation represent the corresponding eigen-frequencies of the metamaterial unit cell.

By scanning the wave vector k along the boundary of irreducible Brillouin zone, the dispersion relation between wave vector and eigen-frequencies can be obtained. This is the widely used $\omega(k)$ method for bandgap prediction [132]. Because the different symmetry properties of the two proposed design, the boundaries of the irreducible Brillouin zones for the cuboid and hexagonal prism designs are Γ-X-M-Γ and M-Γ-X-M-Y-Γ respectively. Due to the complexity of the structure, FEA method is adopted to solve the equation (3-4) and obtain the dispersion relation of the two structures.

3.2.1 Hexagonal prism type EM

The band structure of the metamaterial with hexagonal prism mass is presented in Figure 33. The dispersion relation is obtained through FEA method conducted by software, therefore it includes bending wave bandgap (Z mode) as well as the full bandgap. As a result, the bandgaps are overlapped and cannot be revealed directly. Analysis based on the resonant mode shapes is needed for fully understanding of the bandgap property.

It is mainly the propagation of Lamb waves are concerned about when studying the vibration problem of a plate structure with finite thickness. Normally, the propagating Lamb waves contains three modes: waves in symmetric modes (S mode), in anti-symmetric modes (A mode) and shear-horizontal (SH mode) waves [133]. In addition, infinite overtones of these modes (such as mode A_n, S_n and SH_n, where n is integer) can also propagate through. These wave modes can be identified in the dispersion relation as different band curves originate from point Γ.

For the low frequency waves that possess relatively long wavelength, the metamaterial plate with periodic structure can be considered as homogeneous. So the behavior of the SH_0 wave and S_0 wave are similar and the corresponding curves in band structure are linear. The slopes of these lines originate from point Γ represent the waves' phase velocities [133]. Since the phase velocities of various wave modes are different, the wave modes can be identified through the slopes of the lines. As the flexural wave has the lowest phase speed, the first band is recognized as A_0 mode.

In the meantime, there are also six flat bands found in the band structure. These bands are labelled as A to F in the figure. They represent the local resonances of the metamaterial unit cell. The resonance of a unit cell are decided by the structural configuration but not affected by the external excitation, therefore the band curves are basically maintained flat over all the wave vector directions.

Moreover, the so-called full bandgaps are the frequency regions where no band curve appears at. These regions are also called Lamb wave bandgap [134, 135]. It means any incident waves in these frequencies cannot propagate through the structure. The starting and cut off points of the full bandgaps are labeled as P_1 to P_4 on the band structures. As given in the figure, there are two full bandgaps that exist among the corresponding bands and are marked as shaded area in the figure: (1). 148.1Hz (4^{th} band) – 152.4Hz (5^{th} band); (2). 158.4Hz (5^{th} band) – 176.4Hz (6^{th} band).

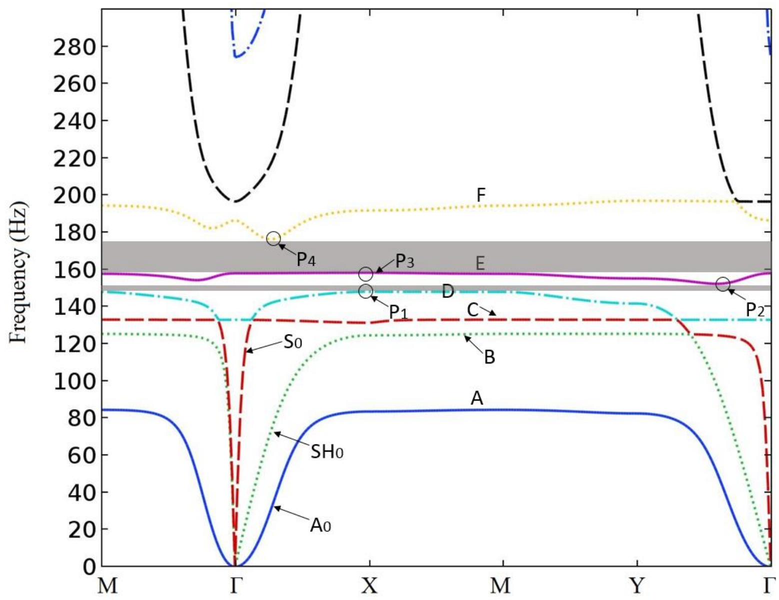

Figure 33. Band structure of EM equipped with hexagonal prism mass and 12mm thick supporting beams.

Aside from the full bandgaps, metamaterial will also be able to form bending wave bandgaps (Z mode) depending on different local resonant modes of the unit cell structure [135]. When the incident wave activate the local resonance of the unit cells, the wave energy will be transformed into the kinetic energy of the inclusion, and therefore prevent the wave energy from affecting the primary structure. Through analysing the mode shapes of local resonance, the bandgap forming mechanism and interaction between the incident wave and resonance can be revealed. Figure 34 presents the mode shapes of the proposed metamaterial unit cell in different bands, and also the corresponding mode shapes of the starting and cut-off points of bandgaps.

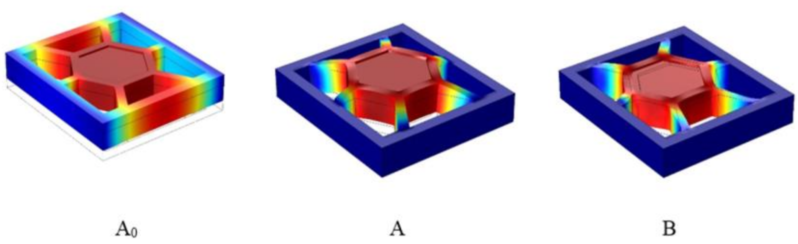

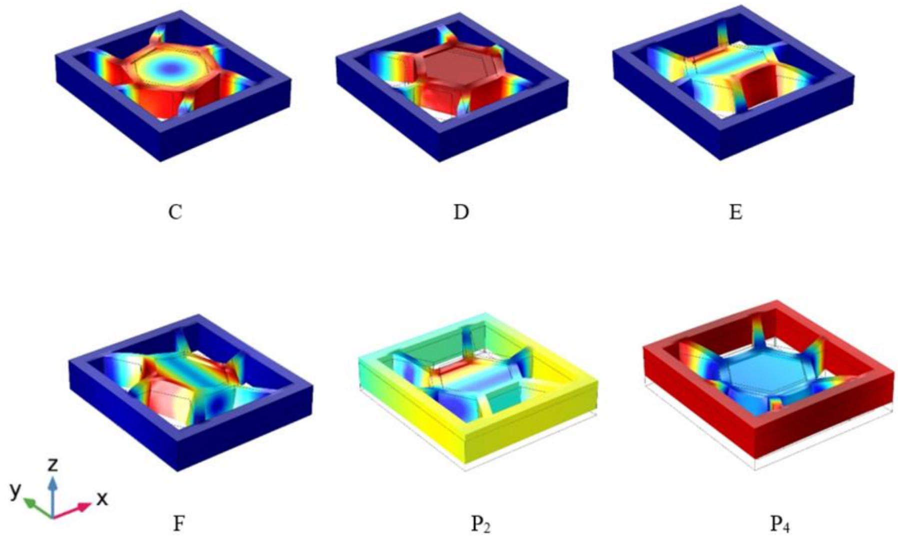

Figure 34. The corresponding mode shapes of the proposed hexagonal prism type EM at different point in the band structure. The inlet presents the coordinate axis.

As shown in the figure, mode A_0 and A are bending mode that polarized in z-direction. Mode B and D are in-plane modes polarized in y- and x- directions respectively. Mode C, E and F are torsional modes of the inclusion, who twists around the z-, x- and y- axis respectively. Otherwise, the corresponding mode shapes at the full bandgaps' starting points P_1 and P_3, are the same as mode D and E respectively. This is because they are the same local resonance modes which are only decided by the unit cell structure. At the cut-off points of the full bandgaps (P_2 and P_4), it is conspicuous that all the corresponding mode shapes have vibrating frames. Hence when the wave frequency approaches the cut-off points, the vibration mode of the metamaterial will shift into modes at P_2 or P_4, so bandgaps will be terminated as the vibration energy is no more contained within the unit cell.

For the bending wave bandgaps, it is worth mentioning that in all the resonance mode shapes, the frame is stabilized and only the inclusion is vibrating, which explains the vibration control capability of the metamaterial beam. However, not all the resonance modes can be activated, so only those who have strong interaction effect with the incident wave can form bandgaps. The width of the bending wave bandgaps are decided by the strength of interaction between the travelling waves and mode shape.

As shown in Figure 34, mode A (at 84.6Hz) is polarized in z- direction so a bending wave with frequency that close to 84.6Hz is able to excite the resonance mode and a bandgap is expected to appear right above 84.6Hz. This bending wave bandgap may be connect with the first full bandgap and thus result in a relatively broad bandgap.

For the full bandgap, as the mode P_1 is an in-plane mode polarized in x- direction, so the first full bandgap will be formed by a transverse incident wave. This bandgap will be cut off when mode shape shift to P_2 (152.4Hz), in which the frame is no longer static and vibration energy starts propagating through the whole structure. Moreover, bending waves can activate mode at P_3 since it is a torsional mode twisting around the x-axis, and the second bandgap will be opened up right above 158.4Hz and stop at P_4 (176.4Hz), due to the same reason that terminate the first full bandgap at P_2. In addition, the counteracting force generated by torsional inclusion is mostly self-balanced and thus the counteracting force for vibration stopping is smaller than mode A. As a result, the bandgap performance in this frequency range (181.4Hz – 221.5Hz) is supposed to be weaker.

It can also be concluded that the bandgap caused by the local resonance with negative mass always starts from the local resonance frequency and the bandgap width is decided by the interaction strength between incident wave and corresponding resonance mode.

3.2.2 Cuboid type EM

Similar to the above section, the band structure of the EM with cuboid mass is presented in Figure 35.

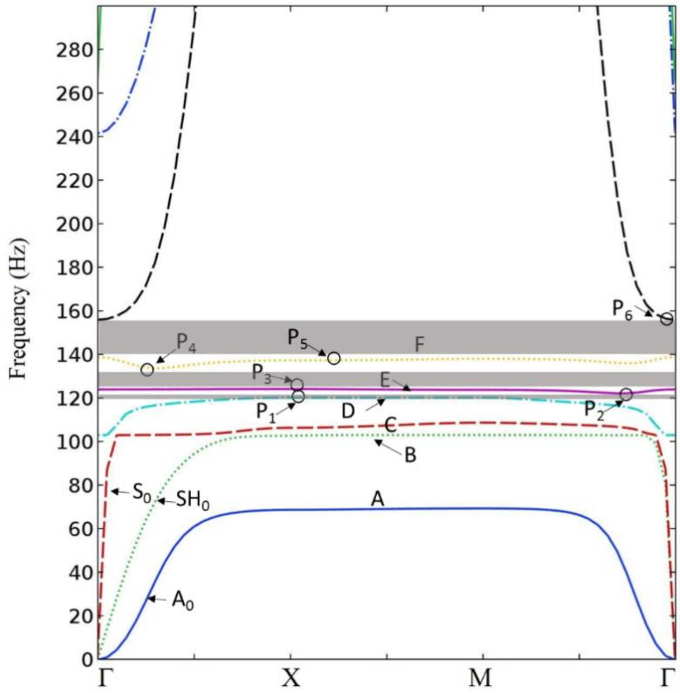

Figure 35. Band structure of cuboid type EM with 12mm thick supporting beams.

According to the figure, there are three full bandgaps appeared at the shaded areas. Different from the hexagonal prism case, a small full bandgap is found between the 4th and 5th bands. The frequency ranges of three full bandgaps are: (1). 120.4Hz – 122.5Hz; (2). 124.4Hz – 133.9Hz; (3) 139.1Hz – 156.1Hz.

The starting and cut-off points of the three bandgaps are labeled as P_1 to P_6 in the figure. Similar to the hexagonal prism case, there are also six flat bands in the band structure figure, labelled as A – F.

The total full bandgap width of this structure is a few hertz larger than the hexagonal prism case, as an extra bandgap is opened up between the 4th and 5th bands. However, the bending mode bandgaps also need to be considered when investigating the bandgap performance of the EM.

The corresponding mode shapes of the structure are presented in Figure 36.

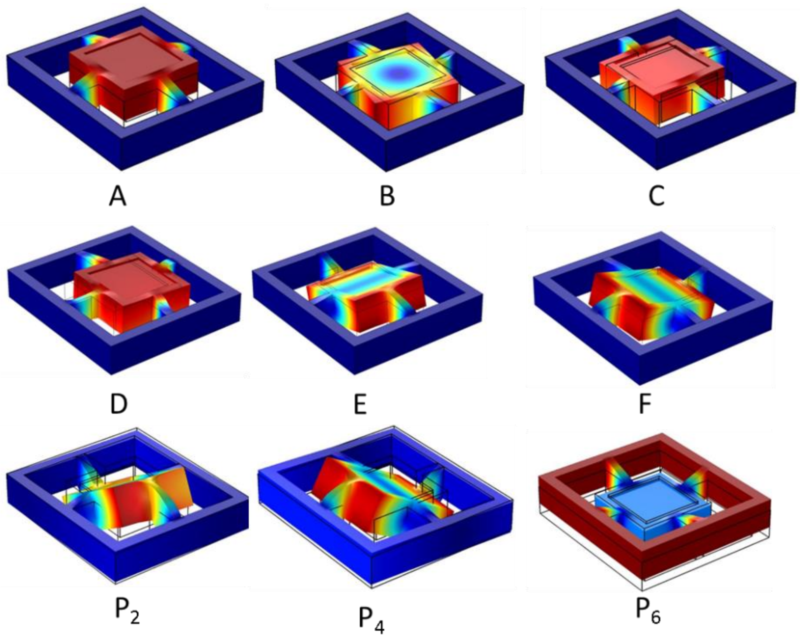

Figure 36. The corresponding mode shapes of the proposed cuboid type EM at different point in the band structure.

The mode shapes at point P_1, P_3 and P_5 are the same as point D, E and F respectively.

According to the figure, the mode at point A is a bending mode which can be excited by the bending wave easily. Mode B is an in-plane torsional type. Mode C and Mode D are polarized in y- and x- direction respectively so they has stronger interaction with the longitudinal and in-plane waves. Modes E and F are torsional modes that twisting around x- and y- axis respectively. These characteristics of the mode shapes are closely related with the bandgap forming mechanism under various excitation.

Otherwise, it is obvious that in all three cut-off points' mode shapes, the frames are not static. The frames are drifted from the original location outlined by the solid black lines, especially the P_6 mode. Therefore, the bandgap may be ended at these modes. Small vibration is revealed in P_2 and P_4 modes. In reality, materials possess damping characteristics. However in the simulation, damping is ignored. Therefore, the small amplitude of vibration in P_2 and P_4 modes may be compromised by the damping and allow the existence of continuous bandgap.

3.2.3 Effect of design parameters on band structure

The supporting beam thickness, geometrical symmetric and material properties of the proposed EMs are adjusted, and the change of band structure brought by these adjustment are investigated in this section. The proposed EMs' feasibility and controllability through design parameter adjustment is revealed.

3.2.3.1 Effect of supporting beam thickness

Different thickness of supporting beams are adopted in the proposed EMs.

Figure 37 presents the bandgap curves of the proposed metamaterials with supporting beams in different thicknesses (10mm, 7mm and 4mm respectively).

The beam thickness is reduced from the bottom side. Since the beams are providing the equivalent stiffness, the thinner thickness shift the resonance frequencies to lower frequency regions accordingly. Also, as given in the figure, the mode shapes will be affected when the structure is adjusted. With the thickness adjusted from 12mm to 10mm, 7mm and 4mm, the first local resonance frequency will shift from 84.6Hz to 74.1Hz, 58.1Hz and 36.3Hz respectively. It demonstrates that the adjustment of the supporting beam thickness can lead to about 50Hz bandgap shifting.

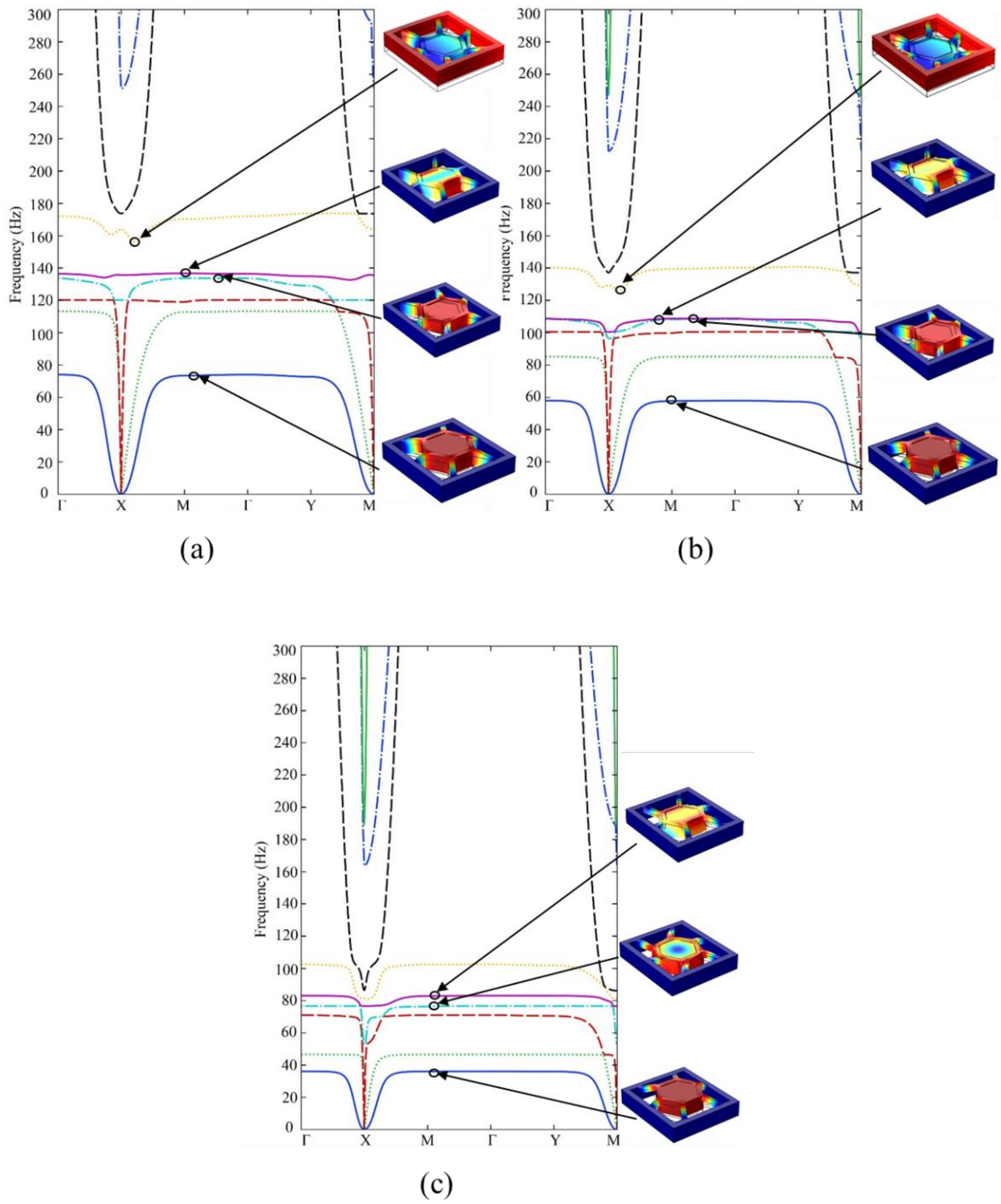

Figure 37. Bandgaps of hexagonal prism type EM with different beam thickness: (a) 10mm; (b) 7mm; (c) 4mm. The corresponding mode shapes at the specific points of the band structure are listed at the right sides.

In addition, when the beam thickness is reduced, the full bandgaps' widths are decreased gradually and both full bandgaps are disappeared if the thickness is reduced to 4mm. This is a side effect caused by reducing supporting beam thickness.

When the beam thickness is reduced to 10mm, as shown in Figure 37(a), the corresponding mode shapes at the 1st, the 4th and the 5th local resonances are not changed. The mode shape of the 2nd bandgap's cut-off point on the 6th band is also the same. However, the first full bandgap disappeared. As an in-plane mode polarized in x-axis direction, the counteracting force of this mode is mainly generated by the compression of supporting beams. Yet the decrease of the thickness reduced the counteracting force and leads to the disappearing of the bandgap. According to Figure 37(b), the second bandgap is further shrunk when the thickness is reduced to 7mm, and the mode shapes are consistent with the 10mm case.

According to Figure 37(c), both full bandgaps are not revealed when the thickness is reduced to 4mm. The 4th local resonance mode shape changes to an in-plane torsional mode instead of the one polarized in x-direction. The torsional mode is difficult to be excited by Lamb wave, so the first full bandgap will not be formed. Moreover, because the smaller size of the beam, the counteracting force from the 5th mode is not enough to form a bandgap after most of the force self-balanced. Nonetheless, bending wave bandgaps are still expected because the first resonance mode is not changed. Numerical simulation is conducted in following subsection and reveal the existence of this bandgap.

Similar investigation is also conducted on the cuboid type EM.

The band structures of the cuboid type EM with different supporting beam thickness are given in Figure 38. According to the figure, the decrease of supporting beam thickness will shift the resonant frequencies to lower frequencies. The mode shapes at the fundamental resonant modes are not changed in all cases. In 12mm case, the 4th mode shape is an in-plane mode polarized in x-axis. However, when the thickness is reduced to 10mm and 7mm, the 4th resonant mode shape contains both in-plane and bending motion. When the thickness is changed to 4mm, the 4th resonant mode shape becomes an in-plane torsional mode. It demonstrates that the adjustment of supporting beam thickness will affect the unit cell's mode shapes, hence the bandgap property will vary accordingly.

The decrease of supporting beam thickness will constantly reduce the number of full bandgaps. At 4mm case, all full bandgaps disappear. The existence of bending wave bandgaps can be revealed through numerical simulation in finite metamaterial structure. The fundamental resonant frequency reduced from 69.5Hz (12mm case) to 31.1Hz (4mm case). Therefore the starting frequency of bending wave bandgap is expected to be decreased accordingly.

The reduction of beam thickness will weaken the counteracting force generated from the unit cell and thus, the bandgap width will shrink as well, especially the bandgap related with twisting modes.

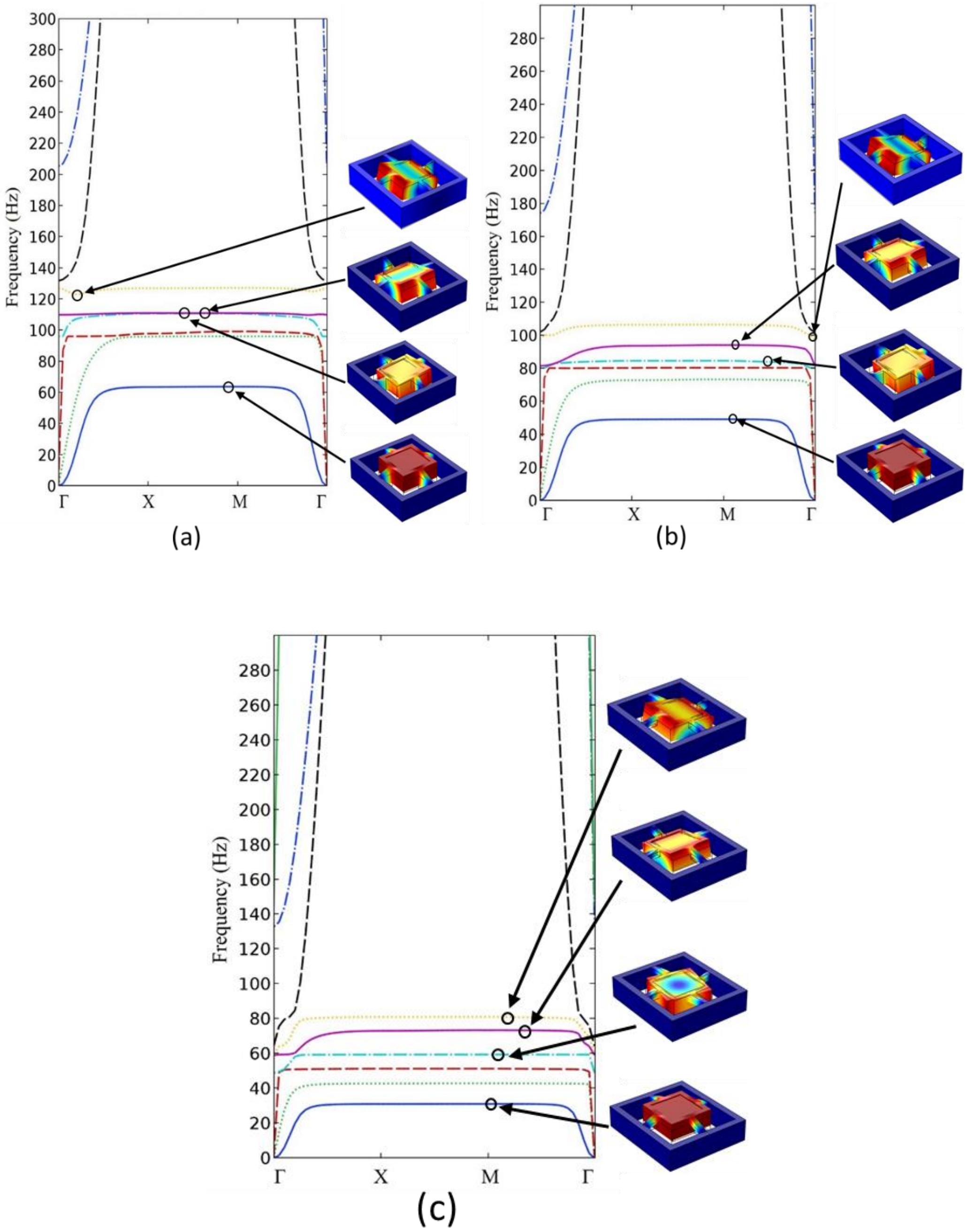

Figure 38. Bandgaps of cuboid type EM with different beam thickness: (a) 10mm; (b) 7mm; (c) 4mm. The corresponding mode shapes at the specific points of the band structure are listed at the right sides.

3.2.3.2 Effect of geometrical symmetric of unit cell

As illustrated earlier, in the hexagonal type EM, the second full bandgap is mainly attributed to the twisting mode, whose force is mostly self-balanced rather than used for counteracting the excitation force. However it is still the widest full bandgap that formed by the hexagonal type EM. Therefore, by tuning the beam thickness to break the asymmetric of the unit cell and maintaining the twisting mode shape, the second full bandgap may be further reinforced and enlarged. Two of the supporting beams in the unit cell is therefore reduced to 7mm whilst maintaining the other four beams' thickness as 12mm. After the adjustment, the structure is only symmetric to y-axis, the irreducible Brillouin zone will thus be enlarged to Y-Q-P-M. However, the scanning results of the former boundary (Γ-X-M-Γ-Y-M) is presented because the identical band structure characteristics.

According to Figure 39, compared with the original unit cell, the 1st local resonance frequency of the asymmetric unit cell decreased from 84.6Hz to 73.1Hz.

The width of the second full bandgap increased from 18.1Hz to 23.3Hz. In addition, a new full bandgap is opened up between the 6th and 7th bands, as shown in the figure. It demonstrates that the adjustment of symmetric will lead to significant change in the bandgap property.

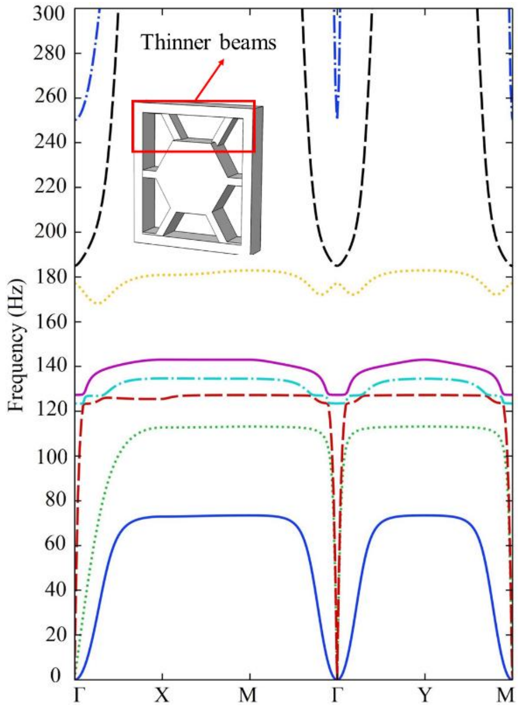

Figure 39. Bandgaps of hexagonal type EM with asymmetric beam design. The inlet presents the backside of the modified unit cell with asymmetric supporting beams.

For the cuboid type EM, the second and third full bandgaps are related with the torsional modes as well. The two modes are twisting around x- and y-axis respectively. Therefore, two supporting beams' thickness are adjusted as 7mm, as shown in Figure 40.

According to the figure, different from the 12mm case, the first full bandgap is not revealed in the asymmetric case. The second and third full bandgaps, which are both formed by the torsional modes, are still existing in the asymmetric structure. The fundamental resonant frequency is about 56.7Hz, which is lower than the original unit cell.

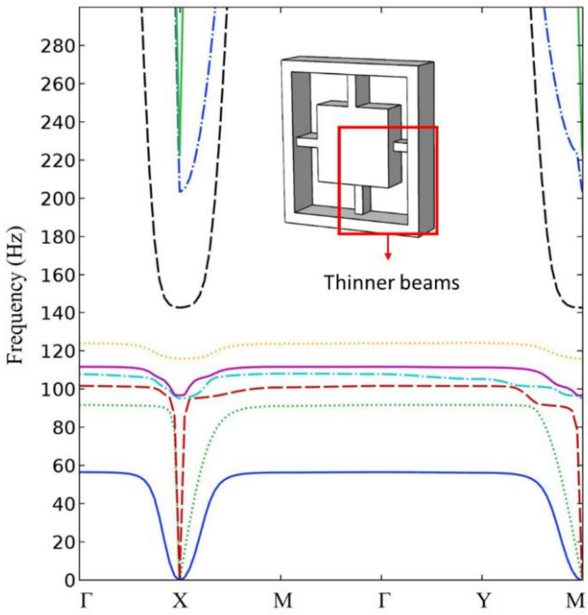

Figure 40. Bandgaps of cuboid type EM with asymmetric beam design. The inlet presents the backside of the modified unit cell with asymmetric supporting beams.

The second full bandgap width is 4.2Hz (111.9Hz – 116.1Hz), and the third full bandgap width is 18.4Hz (124.4Hz – 142.8Hz). The second bandgap width is 5.3Hz smaller than the original symmetric case, but the third bandgap width is 1.4Hz larger.

The above results of both types of proposed EM demonstrate that the symmetric of the unit cell has significant effect on the bandgap property. Through adjustment of the geometrical structure, bandgaps may be opened up or eliminated. However, it is uncertain that the breaking of symmetric will enhance the full bandgap which is related with the torsional modes.

The effect of the symmetric on bending wave bandgap is further examined in the finite structure, presented in later subsection.

3.3 Vibration Response of EM Beams

For the purpose of investigating the vibration absorption performance of the proposed EM, metamaterial beam that composed of 8 unit cells is constructed. Thickness of supporting beams are adjusted in each EM beam, corresponding to the band structure analysis in section 3.2.3.

The configuration of the simulation setting is shown in Figure 41. One end of the beam is fixed. Prescribed displacement boundary condition is applied to the other end of the beam. Excitation with frequency scanning is applied to the structure. The acceleration response of the metamaterial beam is picked up from point A and the input acceleration is detected from the right edge. The frequency response function (FRF) can be obtained by equation: $FRF = 20\log\left(\frac{W_{out}}{W_{in}}\right)$ (dB).

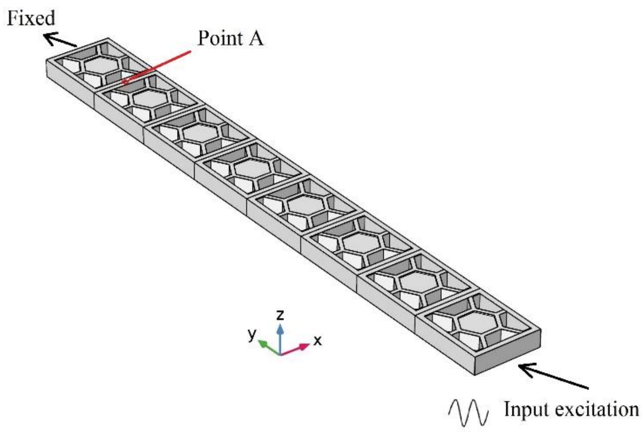

Figure 41. Simulation setup of the finite structure.

3.3.1 EM beams under different incident wave

In order to investigate the relation between bandgap and mode shapes, the finite structure of the proposed EMs with original supporting beam thickness (12mm) are applied with bending, longitudinal and in-plane transverse waves. For the purpose of clarity: the bending wave is vibration in z-axis direction, longitudinal wave is vibration in y-axis direction and the in-plane transverse waves is vibration in x-axis direction, referring to the coordinate in Figure 41.

The vibration response of the hexagonal prism type EM beam under bending wave excitation is shown in Figure 42(a). According to the figure, when the structure is excited by bending wave, two bandgaps are observed. One is from 82.4Hz to 152.8Hz, the other one is from 158.2Hz to 190.4Hz.

The starting and cut-off frequencies of the first bandgap are consistent with the first local resonance and the cut-off point P_2's frequencies respectively. The mode shape of the unit cell in the first bandgap is shown as inlet labelled Z_1. The bending mode shape can be easily excited by the incident bending wave.

The strong interaction between the first local resonance mode shape and the incident bending wave enlarges the bandgap and makes it merge with the full bandgap. As a results, a large continuous bandgap is formed. Along with the increase of incident wave frequency, P_2 mode will be activated and thus terminate the bandgap.

Moreover, the starting frequency of the second bandgap is the same as the frequency of P_3 mode (at 158.4Hz). Therefore it is believed that the P_3 mode leads to the forming of this bandgap. The bandgap width predicted by numerical simulation is larger than the dispersion relation because of the strong interaction between corresponding mode shape and the incident wave. Otherwise, it is obvious that the transmission loss in the second bandgap is weaker, because the twisting mode shape has most force self-balanced, as explained before.

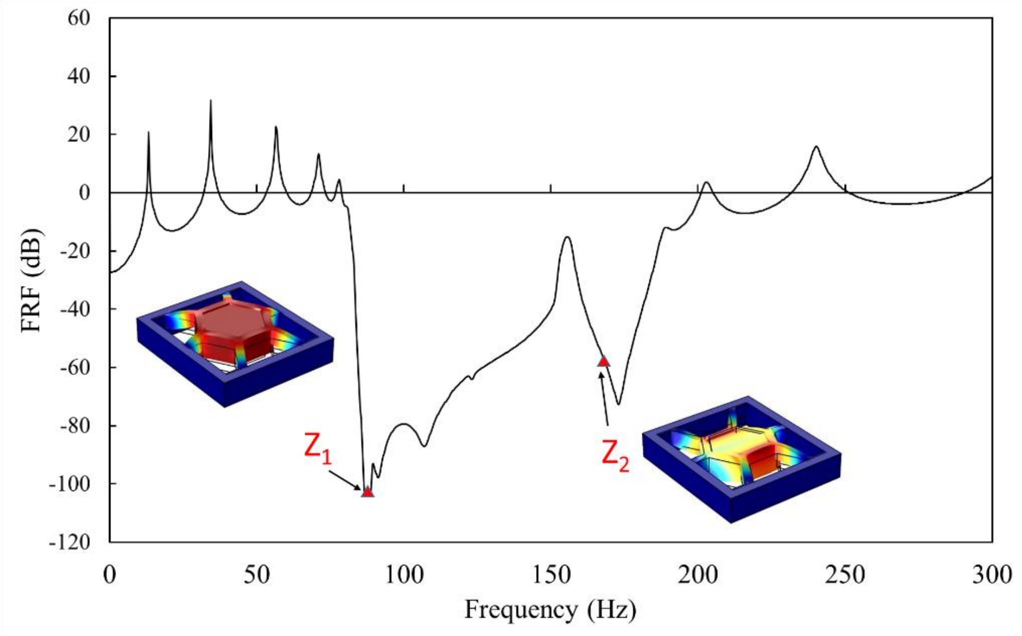

(a)

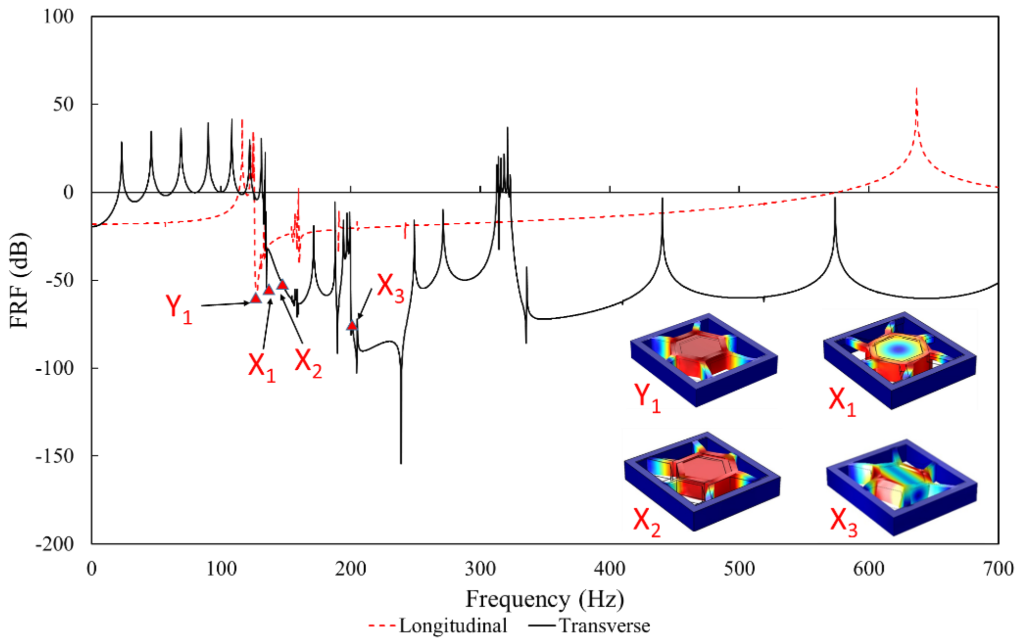

(b)

Figure 42. FRF curve of the hexagonal type EM beam under the excitation of (a) bending wave, (b) longitudinal (red-dashed) and in-plane transverse waves (solid black). The corresponding mode shapes at the points in the bandgap regions are shown in the inlet.

According to Figure 42 (b), when applied with a longitudinal incident wave, the metamaterial beam has one transmission dip at point Y_1 (about 127.2Hz). The corresponding mode shape at this frequency is the mode B, as shown in the inlet. The mode is polarized in y-direction, thus can be excited by the longitudinal wave. However, other types of mode shapes cannot be excited by the longitudinal wave so there is no other obvious bandgap revealed in the FRF curve.

Otherwise, when excited under a transverse wave, the bandgap region starts from point X_1 at 133.1Hz and ends at about 248.6Hz. The first bandgap's corresponding mode shape at labeled at point X_1 is in-plane torsional mode twisting around z-axis. In the following bandgaps, the corresponding mode shape is mode D and F, which are an in-plane mode polarized in x-direction (X_2) and a torsional mode twisting around y-axis (X_3) respectively. Both modes are able to be excited by the transverse wave, however, compared with mode C, mode D and F have stronger interaction effect with the incident waves so a larger bandgap is formed (from 171.6Hz to 248.6Hz).

To reveal the mode shapes' effect in bandgap forming, the deformations of the hexagonal type EM beam at the labelled point in the FRF curves are presented in Figure 43. As shown in the figure, the shapes of the beams are consistent with the mode shapes. It is obvious that in the figure, the vibration energy is contained within the inclusion of the unit cells, so the wave transmission is attenuated and the frame is maintained static.

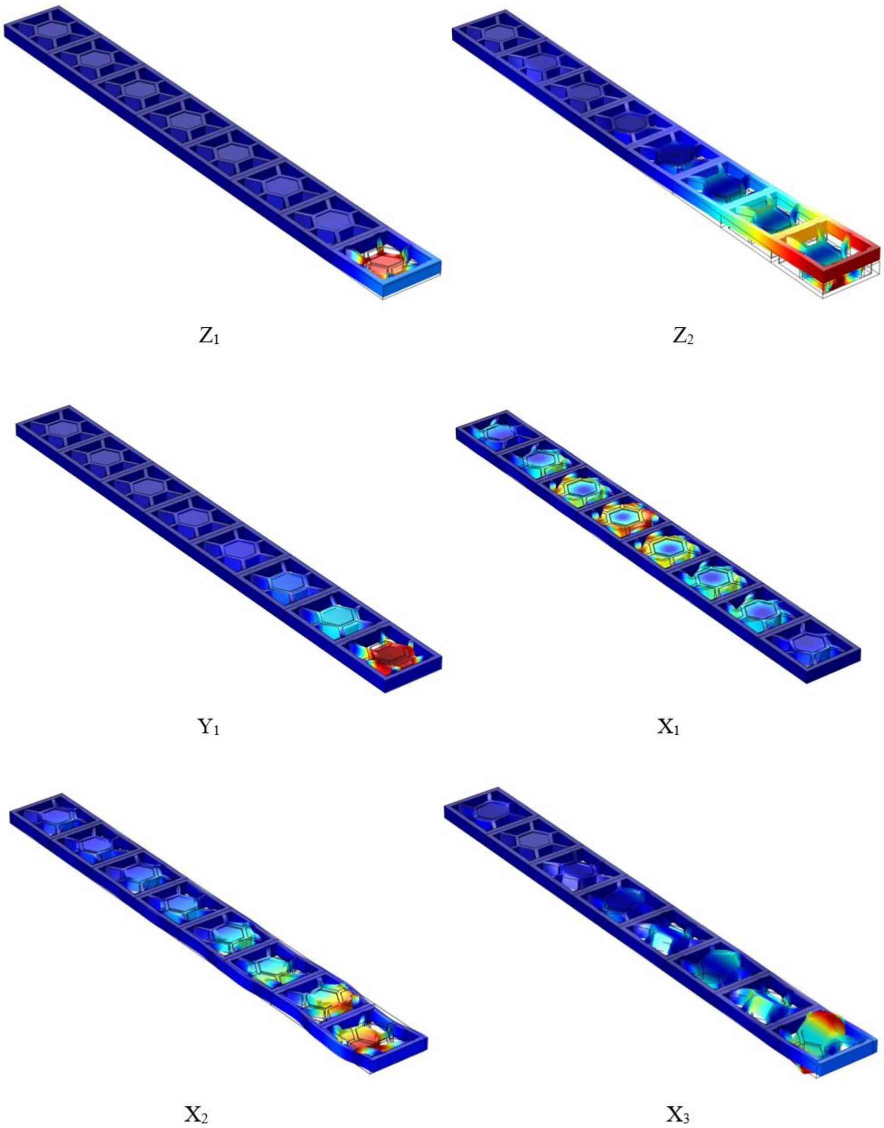

Figure 43. The corresponding shapes of the hexagonal type EM beams at the labelled points in the FRF curves.

The same setup is adopted in the cuboid type EM beam. The FRF curve of the structure is shown in Figure 44.

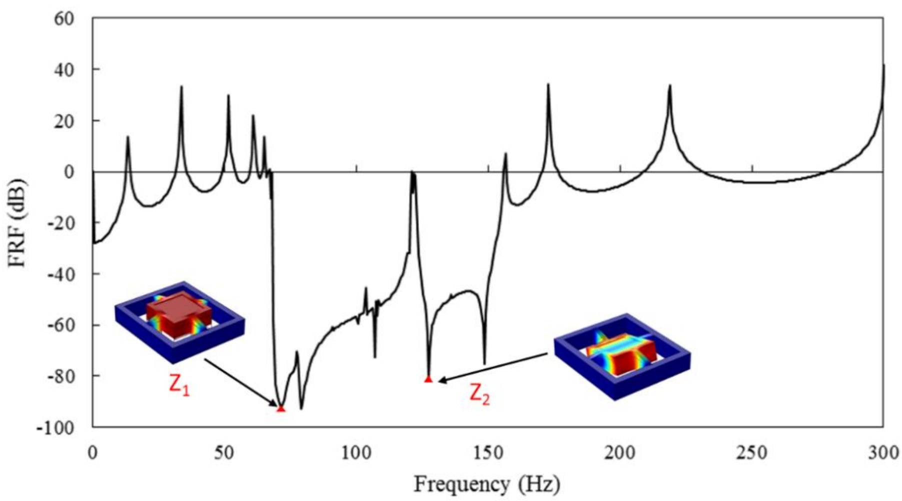

(a)

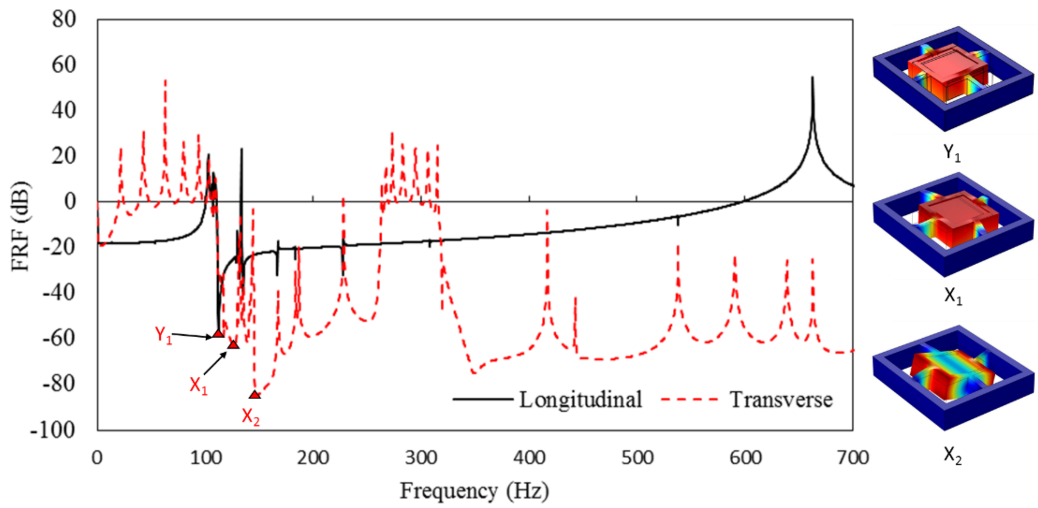

(b)

Figure 44. FRF curve of the cuboid type EM beam under the excitation of (a) bending wave, (b) longitudinal (red-dashed) and in-plane transverse waves (solid black). The corresponding mode shapes at the points in the bandgap regions are shown in the inlet.

According to Figure 44(a), there are two bandgaps formed and adjacent to each other. The frequency ranges of the bandgaps are about: (1) 67.5Hz – 122.5Hz; (2) 124.0Hz – 159.5Hz. The total bending wave bandgap width of the cuboid type is 90.5Hz, whilst the hexagonal type is 102.6Hz.

The starting frequency of the first bandgap is consistent with the fundamental resonant frequency of the structure. Point Z_1 is located within the first bandgap, and its corresponding mode shape is shown in the figure inlet. According to the simulation results, the first bandgap is attribute to mode A as illustrated in Figure 36. The bending wave can easily excite this mode and allows the bandgap to extend to the cut-off point of the first full bandgap. Mode P_2 is a torsional mode twisting around x-axis and can be excited by the bending wave. So the first bandgap stopped.

The mode shape at point Z_2 demonstrates that the second bandgap is formed by mode P_3. It is also a torsional mode that twisting around x-axis. The mode P_4 is a torsional mode twisting around y-axis, so it may not be excited by the incident bending wave. Thus the second bandgap is extended through the second cut-off frequency. The cut-off frequency of the second bandgap is consistent with the frequency of mode P_6 mode. Mode P_6 is a bending mode therefore it can be excited by the incident wave. The second bandgap is thus ended.

Figure 44(b) presents the FRF curves of the cuboid type EM applied with longitudinal and in-plane transverse excitation. When applied with a longitudinal wave, a very narrow dip in the FRF curve is found. This dip is caused by the in-plane mode P_3. There is no other modes that can be easily excited by a longitudinal wave, therefore, no other bandgap is found in the FRF curve.

Otherwise, when applied with in-plane transverse excitation, the EM beam possesses relatively broad bandgaps below 300Hz, and reveals weaker vibration response in the higher frequency region. Similar phenomenon is also found in the hexagonal type EM. The bandgaps are attributed to the transverse mode P_1

and P_5 as shown in the figure, since the modes can be excited by transverse wave. The structural stiffness is higher when dealing with the in-plane transverse vibration because the frames that parallel with x-axis provides extra stiffness.

The deformations of the cuboid type EM beam at the labelled points in the FRF curves are presented in Figure 45. Figure 45

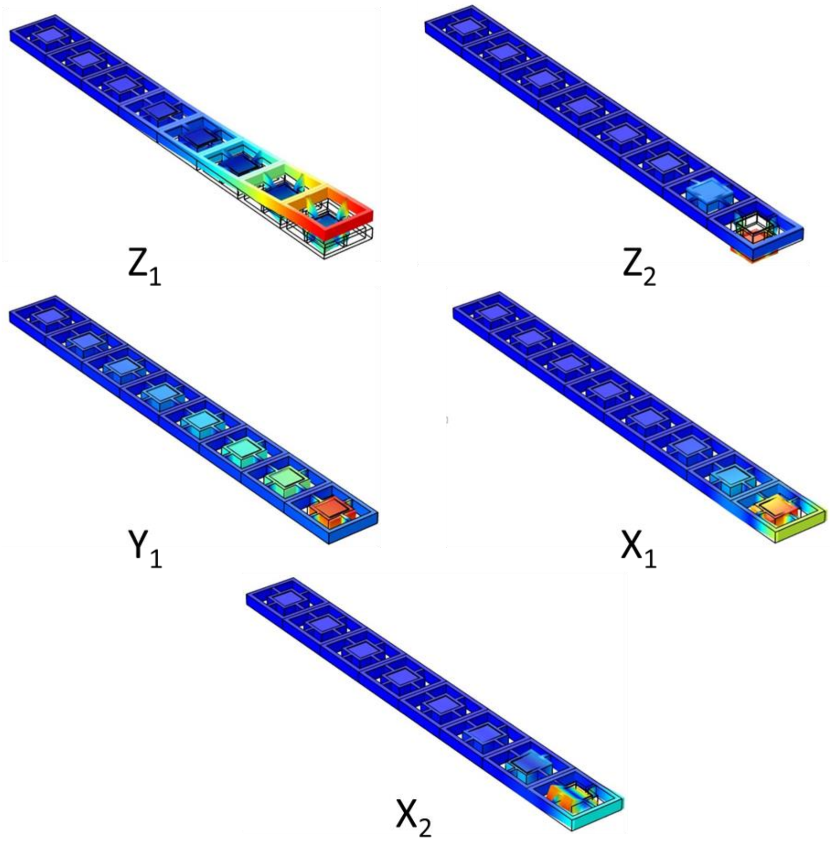

Figure 45. The corresponding shapes of the cuboid type EM beams at the labelled points in the FRF curves.

As shown in the figure, the corresponding mode shape of the unit cells are exactly the same as predicted in the band structure.

The results demonstrates that the bandgap property of the EM is decided by the resonant frequency and mode shape of the unit cell. The formation of bandgaps depend on the excitation of certain mode shapes. With strong interaction between the incident wave and a mode shape, the corresponding bandgap width will be relatively larger.

3.3.2 EM beams with different supporting beam thickness

Similar to the original model with 12mm supporting beams, finite structures with thinner supporting beams are developed. The finite metamaterial structures are presented in Figure 46.

As shown in the figure, the starting frequencies of the bandgaps are 74.4Hz, 59.2Hz and 37.4Hz respectively for the 10mm, 7mm and 4mm samples. The bandgap widths are shrinking along with the decrease of supporting beam thickness. In addition, in the 10mm and 7mm cases, the existence of the second bandgaps can be observed. In both cases, the second bandgap regions revealed in the FRFs are formed by the second full bandgaps that shown in the dispersion relation figure. In the 4mm case, the metamaterial beam did not reveal the second bandgap.

Moreover, the supporting beam thickness has influence on the transmission loss. In 10mm case, the FRF dip reaches -135dB, which means only 0.000018% vibration energy is transmitted through. However, in 4mm case, the dip increased to -107dB.

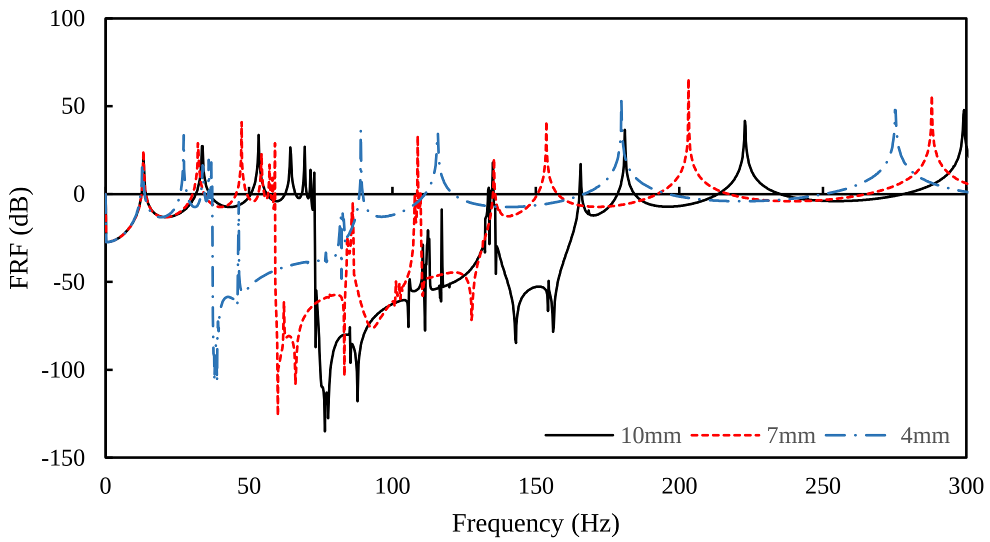

Figure 46. FRF curve of the hexagonal type EM beam with different elastic inclusion supporting beam sizes (4mm, 7mm and 10mm). The frequency resolution is 0.5Hz

Figure 47 shows the FRFs of the cuboid type EM with varying supporting beam thickness. Similarly, the thinning of supporting beam shifts the bandgaps to lower frequency regions. In the 12mm case, the frequency is 67.5Hz. When the supporting beam thickness is adjusted, the starting frequencies of the bandgaps become 65.0Hz (10mm), 51.5Hz (7mm) and 31.1Hz (4mm), respectively. According to the figure, the bandgap widths are reduced when the supporting beams are thinner.

In the 10mm case, two adjacent bandgaps are observed. The ending frequencies of the two bandgaps are consistent with the cut-off frequencies of the two full bandgaps predicted in the band structure. In the 7mm case, there are three separated bandgaps revealed, and the starting frequencies are 51.5Hz, 73.0Hz and 94.3Hz, respectively. These frequencies are corresponding frequencies of the 1st, 2nd and 5th resonant modes, respectively. The mode shapes of the 2nd and 5th ones are both torsional modes, rotating about the x-axis, so they can be easily excited by the bending wave.

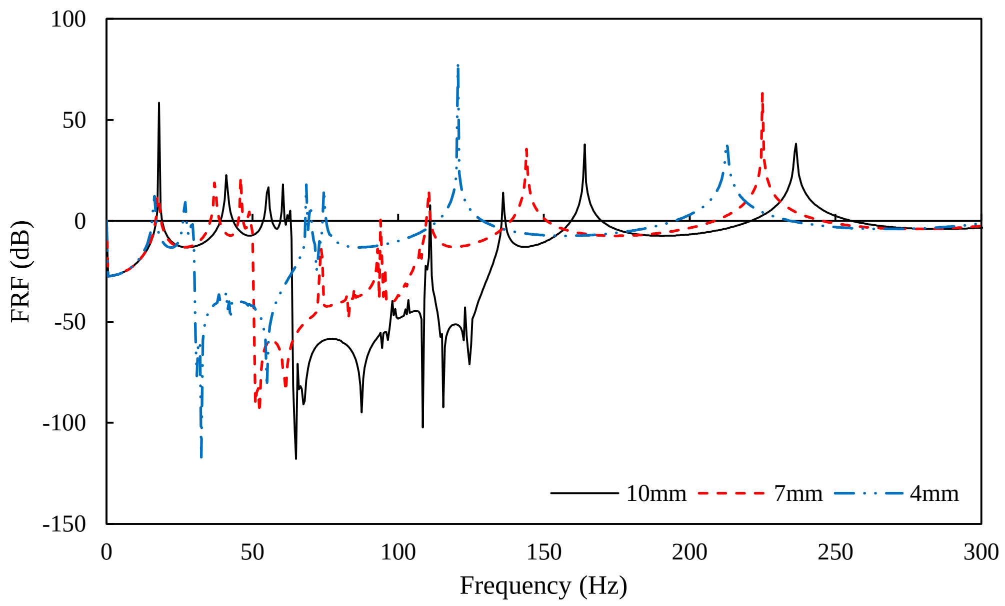

Figure 47. FRF curve of the cuboid type EM beam with different elastic inclusion supporting beam sizes (4mm, 7mm and 10mm). The frequency resolution is 0.5Hz

In 7mm case, three bandgaps that adjacent to each other are formed by the 1st, 2nd and 5th resonant modes, respectively. The corresponding mode shapes of the 2nd and the 5th are both torsional type rotating about the x-axis. In 4mm case, one continuous bandgap is form but within it, two different modes are revealed. The first one appeared at the resonant frequency of the 1st resonant mode, and the second mode shape starts at the second dip at about 55.0Hz.

The above results demonstrate that the adjustment of the supporting beam thickness will lead to the shifting of bandgap location. The geometrical adjustment will affect the mode shapes of the structure and therefore has influence on the bandgap property. Reducing the thickness of supporting beams will shift the bandgap location to different frequency regions. However shifting the bandgap to a lower frequency will have to sacrifice bandwidth and vibration absorption performance in exchange.

3.3.3 EM beams with asymmetric configuration

Figure 48 illustrates the FRF curve of the hexagonal type EM with asymmetric unit cell. The vibration response curve of the sample with 12mm supporting beams is also included for comparison.

According to the figure, when two supporting beams' thickness are decreased, the location of the first local resonance bandgap shifts to a slightly lower frequency because the stiffness of the structure is smaller. The starting frequency of the bandgap (74.8Hz) is basically consistent with the prediction in band structure (73.1Hz), and the corresponding mode is the same as predicted as well.

Most importantly, if compared with the curve of metamaterial with 12mm thick symmetric supporting beams, the second bandgap width of the asymmetric sample is enlarged. Therefore the vibration isolation performance of the asymmetric metamaterial is enhanced. Such performance is consistent with the prediction in modal analysis.

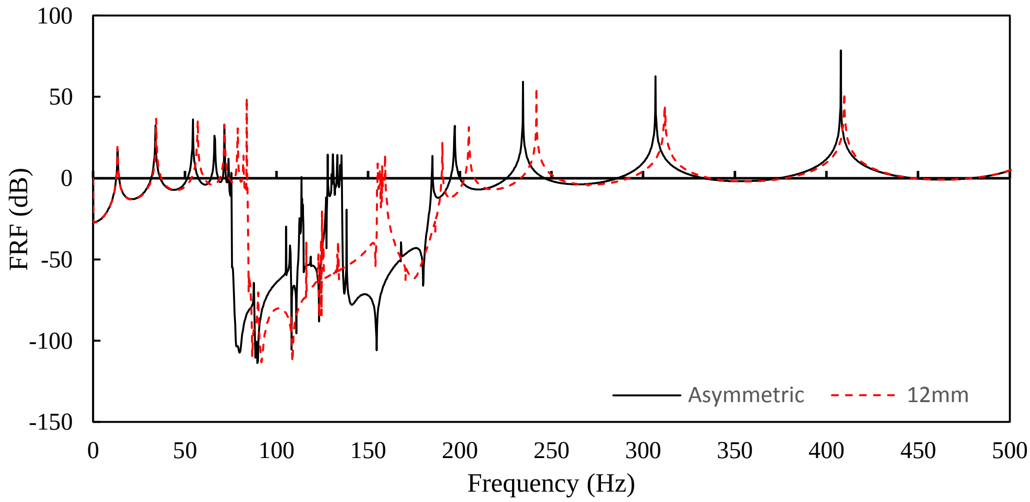

Figure 48. FRF curves of hexagonal type EM with asymmetric beams (black solid line) and 12mm symmetric beams (red dashed line).

Figure 49 shows the vibration response curve of the cuboid type EM with asymmetric supporting beam. The bandgap shifts to lower frequency. However, different from the hexagonal type, the second bandgap is not enhanced. The transmission loss of wave is reduced with the asymmetric structure.

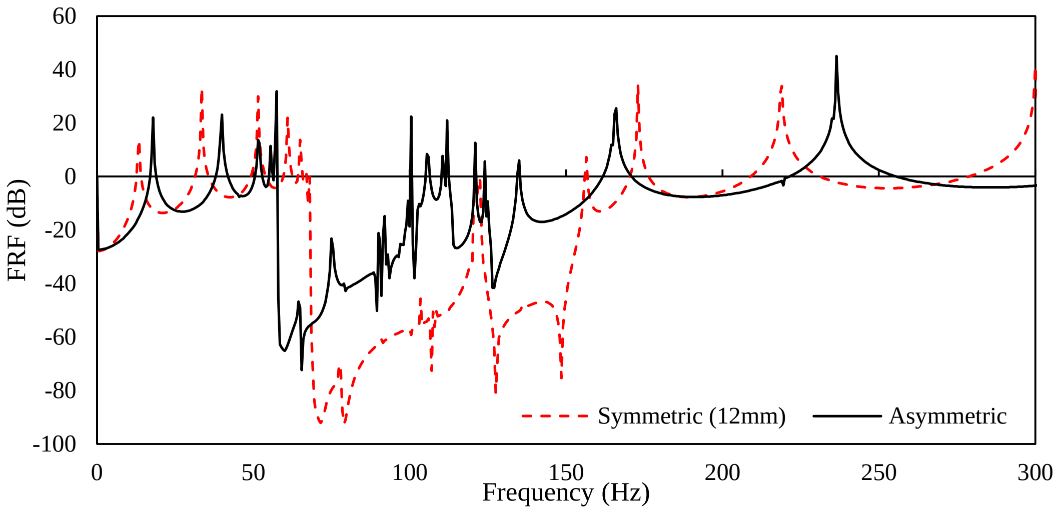

Figure 49. FRF curves of cuboid type EM with asymmetric beams (black solid line) and 12mm symmetric beams (red dashed line).

Therefore, in the hexagonal type EM, breaking the symmetric condition of the unit cell can enhance the second bandgap width. However, the cuboid type EM does not possess such characteristics. The bandgap property tuning through symmetric condition adjustment is not reliable. Further investigation on the asymmetric structure is conducted through experiment.

In addition, the bandgap width of the hexagonal type EM is always larger than the cuboid type EM with the same supporting beam thickness. Thus, the hexagonal type has better vibration absorption property and it is further investigated in the next subsection.

3.4 Vibration Absorption of EM Applied on Thin Plate Structure

In the above subsections, the bandgap property of the hexagonal type EM beam is investigated. In application for vibration control, the EM will be attached to the target structure for vibration absorption. Due to the common use of beam and plate structures in various engineering applications, the vibration absorption of such structures by metamaterial have received much attention [86, 136, 132, 137]. So in this subsection, the performance of the proposed hexagonal type EM applied on a thin plate structure is investigated through simulation.

The hexagonal type EM beam is applied to a thin plate. In engineering applications, the extra weight load on the target structure can affect the performance of functions. Normally, the lighter of the extra weight attached the better. Similarly, for the proposed EM, the vibration absorption performance when 1, 2 and 3 EM beams are attached on the plate structure are investigated. The configurations are shown in Figure 50.

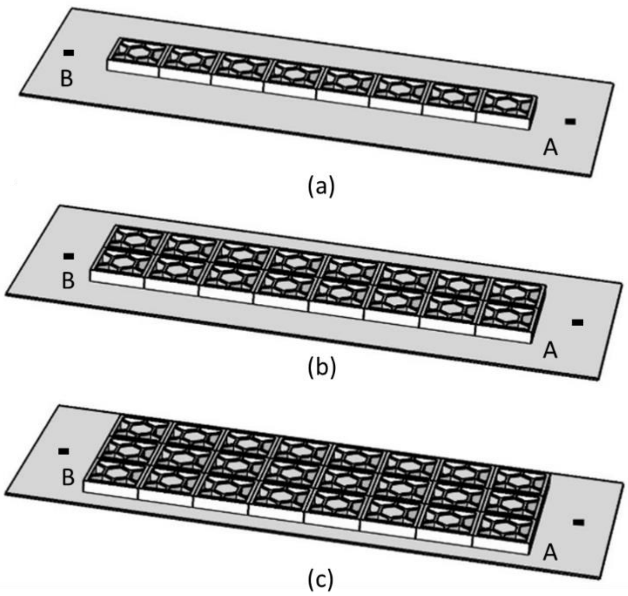

Figure 50. The configurations a thin plate structure attached with (a) one; (b) two and (c) three hexagonal type EM beams. The excitation is applied at point A, and acceleration response is picked up from point B.

Bending wave excitation is applied on the plate at point A, and the acceleration response is picked up from point B. The size of the plate is $240 \times 700\text{mm}$.

The FRFs of these three cases are presented in Figure 51. For the purpose of comparison, the FRF of the 12mm hexagonal type EM beam is also included on the figure, represented by grey dotted line.

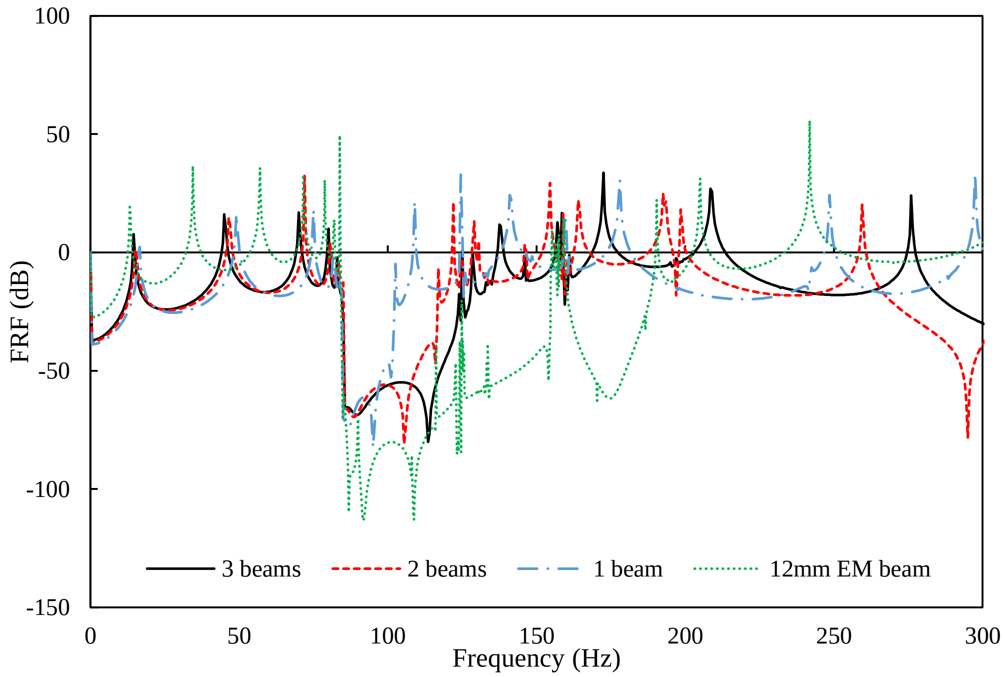

Figure 51.FRF of a thin plate attached with 1, 2, and 3 hexagonal type EM beams.

As shown in the figure, in all three cases, bandgaps are observed and starting from the same frequency. When 3 EM beams are attached, the bandgap width is 41.0Hz, which is smaller than the bandgap revealed by an EM beam itself in Section 3.3.1. The second bandgap of the EM beam is not found when attached on the plate structure. It demonstrates that the torsional mode cannot effectively control the plate vibration. Counteracting force generated from the torsional beam is not sufficient to affect the plate vibration. When the thin plate is attached with 2 EM beams, the bandgap width continues decreasing to about 32.6Hz. According to the aforementioned modal analysis, when the excitation frequency is near the cut-off frequency of bandgap, the frame of the unit cell will start vibrating. The counteracting force from the mass inclusion is thus weakened. As a result, when the number of unit cell is decreased, the total counteracting force generated are smaller and not sufficient to provide effective vibration control, so the bandgap width narrowed. The bandgap width is further decreased to 19.6Hz when only 1 EM beam is attached.

The results demonstrate that the proposed EM can form low frequency bandgaps and effectively control structural vibration. The decrease of unit cells applied for the purpose of avoiding extra weight will not eliminate the bandgap yet certain level of bandgap width will be sacrificed.

3.5 Experimental Study of Hexagonal Type EM

As illustrated in formed subsection, when equipped with the same amount of mass, the hexagonal type EM can generate larger bandgap in low frequency region. Therefore, the hexagonal type EM has better feasibility and vibration absorption performance than the cuboid type. In this section, prototype of hexagonal type EM beams are manufactured for testing. Experiments are conducted on these prototype samples for the examination of vibration control performance and the accuracy of the structure design through FEA method.

3.5.1 Experimental setup

Three types of samples with different supporting beams are produced: 12mm beams, 7mm beams and asymmetric beams. These EM beams are designed to have 8 resonator units aligned in one line. The frame and the rubber inclusion are manufactured through 3D printing, and the metal mass platelet is manufactured by Computer Numerical Control (CNC) technique. Materials of the beam and elastic inclusion are epoxy and silicon rubber respectively. The material properties are tested and obtained through DMA, as illustrated in section 3.1.

The parts are then manually assembled: the copper mass and rubber inclusion are designed with interference fit, so the mass magnets are directly inserted into the cavity, as shown in Figure 52(a). The inclusion are then glued to the frame.

The schematic of experiment is presented in Figure 52(b). Similar to the simulation, the left side is fixed on the steel foundation, and the right side is fixed to a shaker that moves in vertical direction by a pair of clamps. The clamps ensure the metamaterial beam can only move in the vertical direction but not conducting in-plane sliding, exactly the same as the setting within simulation.

In order to pick up output and input signals, two accelerometers are attached to the left and right sides of the beam. The signal generator (Tektronix AFG1022) is connected to the shaker through a power amplifier (YMC LA-200). Signals from the generator and accelerometers are fed into the computer through signal analyser (SignalCal Ace). The experiment setup is shown in Figure 52(c).

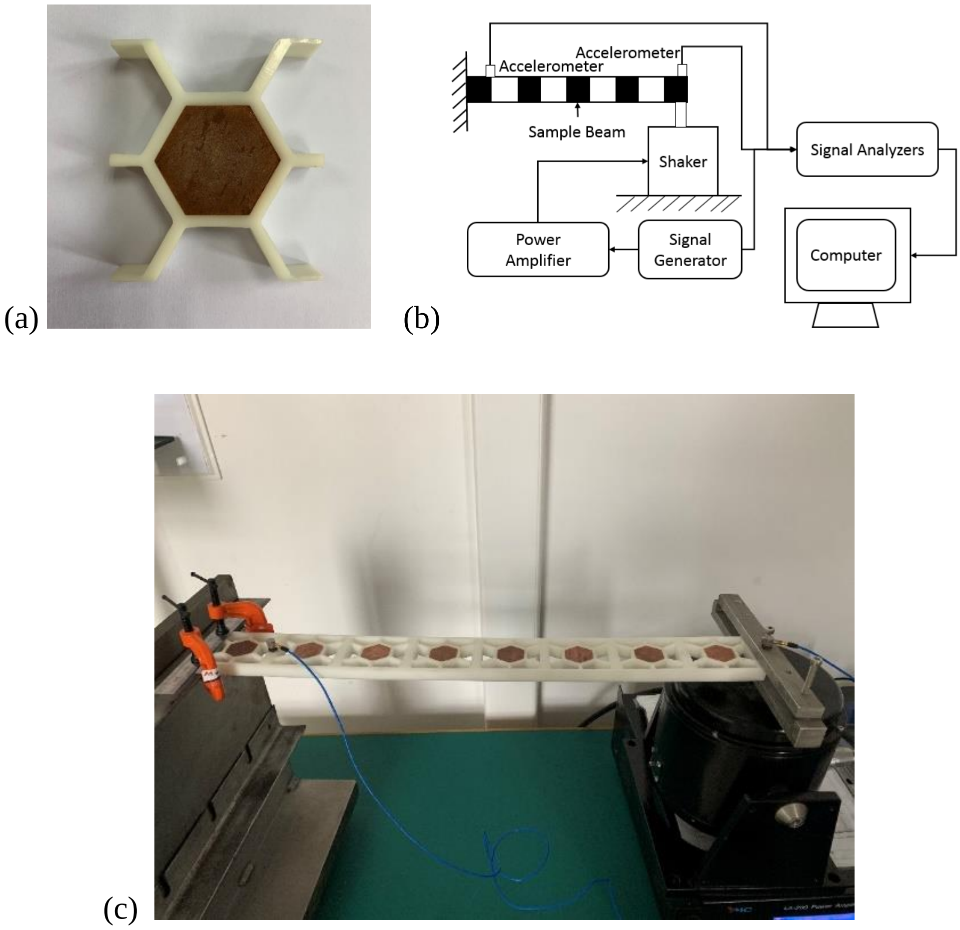

Figure 52. The sample beam and the experiment measurement setup. (a) Assembly of rubber inclusion with 12mm thick supporting beam and a copper mass; (b) schematic arrangement of experiment; (c) photo of sample beam.

To ensure the signals are picked up from the same location on all the samples, the output accelerometer is fixed at the middle point of the frame which is one unit cell away from the left edge. The input accelerometer is put at the clamp of the shaker, right above the middle point of the frame on the right edge. The acceleration signals are obtained and the FRF is calculated.

3.5.2 Results and discussion

Figure 53 presents the FRF curves of the metamaterial beam samples obtained from experimental tests.

The bandgap location shifts to lower frequency when the thickness of the supporting beams are reduced. The bandgap starting frequency of the asymmetric beam sample is higher than the 7mm sample, since in the asymmetric one only two supporting beams are reduced to 7mm and others are kept as 12mm. It is obvious that through adjustment of the supporting beams, the bandgap location of the proposed metamaterial can be tuned effectively.

The bandgap starting frequency of 12mm sample is about 89.4Hz, and the bandgap ends at about 354Hz. When the thickness is adjusted to 7mm, the bandgap range is shifted to about 69.4Hz – 266.2Hz.

On the other hand, the bandgap width of 12mm sample and asymmetric sample are similar because of mild difference. However, different from the estimation in simulation, the vibration absorption performance of the asymmetric sample is not obviously strengthened. Otherwise, compared with 12mm sample, the vibration absorption in 7mm sample is obviously weaker and the bandgap width is also decreased. Such phenomena demonstrate that in reality the forming of bandgap is not attributed to the twisting mode shape. Since the bandgap starting frequencies are close to the first band resonant frequencies in different designs, the vibration attenuation is mainly contributed by the first resonant mode, in which the mass vibrate in out-of-plane mode.

In all three samples' experiment results, continuous large bandgaps are formed instead of two separated bandgaps as predicted in numerical simulation. Also, the bandgap widths of all three samples are much wider than expected. The merging and extension of bandgaps are caused by the damping property of the materials, as also mentioned and occurred in other research works [133, 138].

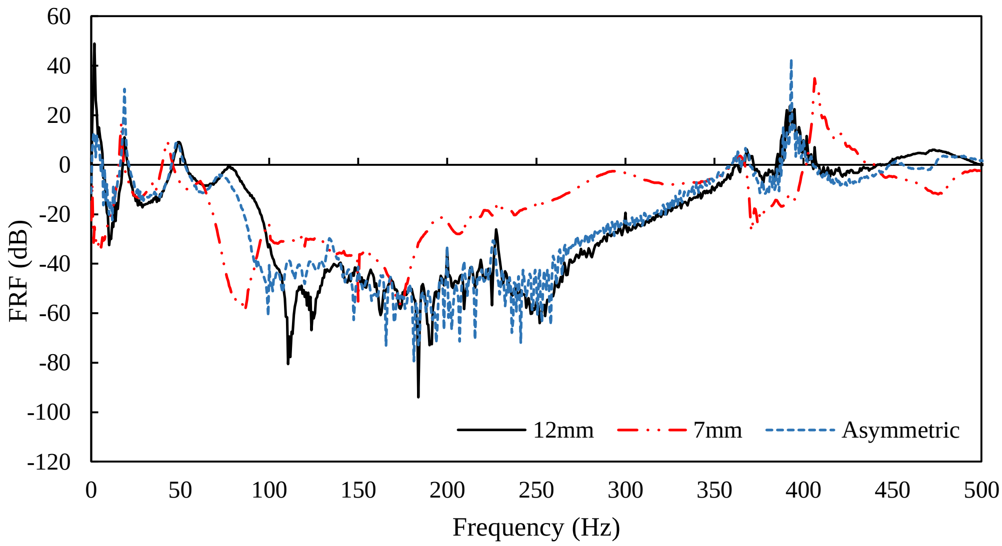

Figure 53. FRF curves of metamaterial beam samples with different supporting beams: 12mm thickness (black solid line), 7mm thickness (red dash double dotted line) and asymmetric beams (blue dotted line).

The manually assembled samples will inevitably possess errors and cause inconsistency with the simulation. According to the experiment result, the bandgap starting frequency and the response peaks in low frequency region are all shifted to higher frequency. This is caused by the extra stiffness provided by boundary condition. In simulation, the fixation are applied at the vertical edges of two sides, yet in practical, part of the lengthwise direction of the structure are clamped as well. Also, the drying and contraction of glue will also increase the stiffness of the rubber.

The experimental results are not totally consistent with the numerical simulation results in the aspect of bandgap locations and widths. However, the variation tendency of samples' bandgap characteristics when tuning geometrical parameters are consistent with the simulation. Hence it is believe that the simulation is able to provide precise design of the proposed metamaterial if supplied with improved manufacturing technique and more accurate material property data.

3.6 Chapter Summary

Designs of two types of EM are introduced and the bandgap tunability is examined in this chapter.

Modal analysis was conducted to reveal the local resonant phenomenon and bandgap forming mechanism of the proposed metamaterial structure. Through numerical simulation and experimental work, the proposed EM was found to be effective in structural vibration control. The bandgap forming mechanism of an EM is closely related with the mode shapes of EM unit cells. Strong interaction between mode shapes and incident wave can generate relatively broad bandgaps. Through adjustment of geometrical parameters of the EM unit cell structures, the bandgap property will be tuned accordingly. Remarkable tuning effect can be achieved with mild adjustment of the structure dimension. Also, aside from the dimension, breaking the symmetricity of the unit cell for the purpose of enhancing certain resonant modes' corresponding local resonant bandgap is also a very useful tuning method for EM. However, compromise between the local resonant bandgap enhancement and total bandgap weakening needs to be seriously considered since the tuning of dimension will result in the system's equivalent stiffness varying.

Experiments are conducted upon the hexagonal type EM since it has revealed better bandgap property than the cuboid type. The results indicate that a broad continuous low frequency bandgap is found in all three types of samples, and it is wider than predicted in the numerical simulation. The findings in this chapter demonstrate the relation between the resonant mode shapes and bandgap forming mechanism of a metamaterial, thus it is considered an significant concept proof for the metamaterial design and optimisation.

Chapter 4

4. PASSIVE VIBRATION CONTROL PERFORMANCE OF MEMBRANE-TYPE METAMATERIAL

In this chapter, a MemM structure is designed and its structural vibration performance for a thin plate structure is investigated. The effect of MemM's design parameters, such as the thickness of the membrane, location and configuration of mass attached on membranes, are studied. Investigation of the bandgap properties of the MemM under various design parameters are essential because the properties can directly reveal the feasibility and controllability of the MemM in application. Otherwise, bilayer MemM is formed by stacking one layer of the designed MemM on another for the purpose of generating two bandgaps. Corresponding modification for the analytical model is conducted for the multiple layer case as well. The passive vibration absorption performance is examined through numerical simulation and experimental work. Numerical simulation and experimental tests are conducted to verify the accuracy of the analytical model. [3]

[3] Part of the content in this Chapter is published as: [1] C. Gao, D. Halim and X. Yi, "Study of bandgap property of a bilayer membrane-type metamaterial applied on a thin plate," *International Journal of Mechanical Sciences*, 2020; [2] C. Gao, D. Halim and C. Rudd, "Vibration absorption performance of membrane-type metamaterial on a thin plate," in *INTER-NOISE and NOISE-CON Congress and Conference Proceedings*, Madrid, 2019; [3] C. Gao, D. Halim and C. Rudd, "Prediction of bandgaps in membrane-type metamaterial attached to a thin plate," in *INTER-NOISE and NOISE-CON Congress and Conference Proceedings*, Madrid, 2019.

4.1 Structure Design of the MemM

Generally, a MemM is composed of unit cells that called membrane-type resonators (MemR). A MemR consists of a prestressed membrane, a mass block attached on the membrane and a supporting frame that the membrane is fixed on. The MemR can be simplified as a spring-mass model when applied for vibration absorption. The equivalent stiffness is provided by the membrane under tensile tress as a results of stress stiffening phenomenon [20]. The MemM has the advantages of light-weight, space saving and low cost. When applied to a target structure for vibration control, it will be attached as an extra layer of MemRs. For the purpose of forming multiple operation frequency regions, multiple layers of MemRs can be stacked and no extra area is needed for the additional layers.

The application of MemM in structural vibration control is not fully investigated as mentioned earlier. Therefore, in this work, the MemM's structural vibration control capability when applied to thin plate structures are investigated.

The designed MemR structure is described in Figure 54. The rectangular membrane is applied with tensile stress and fixed on the supporting frame. A circular mass block is attached at the middle point of the membrane surface. This structure is relatively simple and easy for manufacturing. The material of each component needs to possess different properties for the purpose of generating bandgap effectively. Material for supporting frame should have higher rigidity because it needs to ensure the fixation of the membrane. Elastic material with relatively lower modulus is chosen for the membrane because it is more sensitive to the applied tensile stress, and enabling the generation of low frequency bandgap. For the mass block, the selected material should have high mass density so to achieve the same weight with smaller volume if compared with other materials. As mentioned in Section 2.2.2, the error between analytical model and numerical simulation will be larger if the dimension of the mass block is increased. Therefore, metal material is normally chosen for mass block.

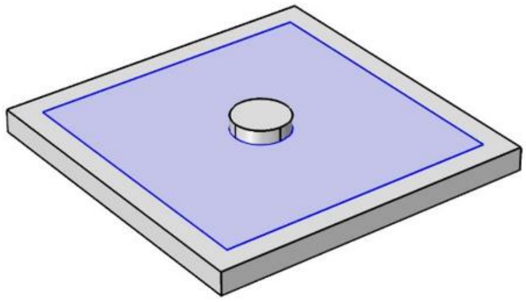

Figure 54. The configuration of designed MemR.

Samples of the MemR is manually assembled for experimental tests. The supporting frame is made by 3D printing and the epoxy is selected as the frame material. Silicone rubber membrane is prestressed and glued on the frame, and copper mass block is glued at the middle of the membrane. Dynamic Mechanical Analysis (DMA) testing was conducted to confirm the material properties of the 3D printed epoxy and silicone rubber. The material properties are given in Table 6. For the purpose of accuracy, these property data are also used in numerical simulation.

Table 6.Material properties of materials.

	Epoxy	Rubber	Copper
Young's modulus	0.917GPa	3.41MPa	115GPa
Poisson's ratio	0.41	0.49	0.33
Density (kg/m^3)	1100	980	8890

The dimension of the MemR is given in Table 7. The width of the frame is 5mm, this is designed for ensuring the strength of the frame in accordance with the manufacturing requirement of the 3D printing supplier. In the following subsections, the thickness and side lengths will be adjusted to reveal the effect of these parameters on the bandgap property.

Table 7. Dimension of the proposed MemR

	Side length L(mm)	Radius R (mm)	Thickness/Height t (mm)
Frame	60	-	5
Membrane	50	-	1
Mass	-	6	2

4.2 Band Structure of the MemM and Influence of Design Parameters

The bandgap property of a MemM can be predicted through the band structure figure. When MemRs are applied and form a periodic structure, the dispersion relation can be obtained through calculation of a primitive unit cell according to the Floquet-Block theory. As mentioned in García and Fernández-Álvarez's paper [139], Floquet's theory was first developed to solve the 1D partial differential equations with periodic coefficients, referring to [140]. Bloch broadened Floquet's results to 3D periodic structures and "obtained the description of the wave function associated with an electron travelling across a periodic crystal lattice" [139].

In the situation that considering the wave propagation in periodic mechanical systems, the theory is adopted to simplify the calculation. For an infinite structure, it can be considered forming by periodic unit cells that adjacent to each other. According to Floquet-Bloch theory, one of the periodic structure unit cell's physical field values, such as displacements and velocities, can be equal to the corresponding physical field values of the adjacent unit cell multiplied by an evolution factor, described as:

$$f(x_n + L) = f(x_{n-1})e^{ikL} \tag{4-1}$$

where $f(x)$ is the physical field function, L is the periodic of the structure, k is the wavenumber that related with the structure dimension. The evolution factor e^{ikL} is also known as Floquet multiplier.

Therefore, the physical field value outside a periodic can be expressed by the value inside a periodic with the multiplier. Thus, to reveal the physical field of the infinite structure, computing over a primitive unit cell is sufficient. The function can be expressed as:

$$f(x_n + nL) = f(x_0)e^{iknL} \tag{4-2}$$

where x_0 is the coordinate of points within the primitive unit cell, and nL is the vector representing the location of the unit cell that outside the periodic. By substitute this equation into the equation of motion of the system, then it will become an equation series of wavenumber k.

Therefore, to calculate the dispersion relation of the metamaterial by FEA method, only one unit cell applied with Floquet boundary condition is needed. Such characteristics allows the calculation to be effectively simplified.

In the case of MemM, the dispersion relation of the structure formed only by MemRs can be obtained by the FEA software. Otherwise, as mentioned in Section 2.3, when applied to a thin plate structure, PWE method can be adopted for the dispersion relation. The main difference between these two pathways is: for the infinite structure formed by MemRs, the calculation reveals the MemM's dispersion relation whilst the PWE method reveals the effect of MemM applied to a thin plate structure.

According to the findings in Chapter 3, although the band structure of the metamaterial can represent the bandgap property, the band structure will still be different when the metamaterial structure is applied to a thin plate. Therefore, in the design process, the investigation of band structure of MemM is still necessary, however the band structure after it is applied for utilization also needs exploration.

In this section, the band structure of the MemR under different design parameters are investigated. In different application conditions, design of the MemM configuration may be adjusted accordingly to satisfy the demand, especially the operation frequency for vibration absorption. The design parameters of a MemM have influence on the bandgap property and it is essential to clarify their effect for the purpose of MemM design and application.

4.2.1 Effect of membrane tensile stress on bandgap properties

Normally, bandgap of a membrane-type resonator is formed by the fundamental resonant mode [86]. Hence by tuning the resonant frequency the bandgap location of the MemM can be changed. As a MemR can be considered as a spring-mass model, the resonant frequency is related with the mass magnitude and stiffness level. The tensile stress is the main cause of membrane flexural stiffness because of the stress stiffening effect. According to equation (2-49), the increase of tensile stress will shift the resonant frequency to higher frequency region.

By using the FEA software, the effect of tuning tensile stress on bandgap location is examined. As shown in Figure 55, the MemM is assumed to be applied in an infinite surface and extending in two dimensions. Hence, the irreducible Brillouin zone is given as the inset. The band structure of the MemM is obtained through scanning the wave vector around the boundary.

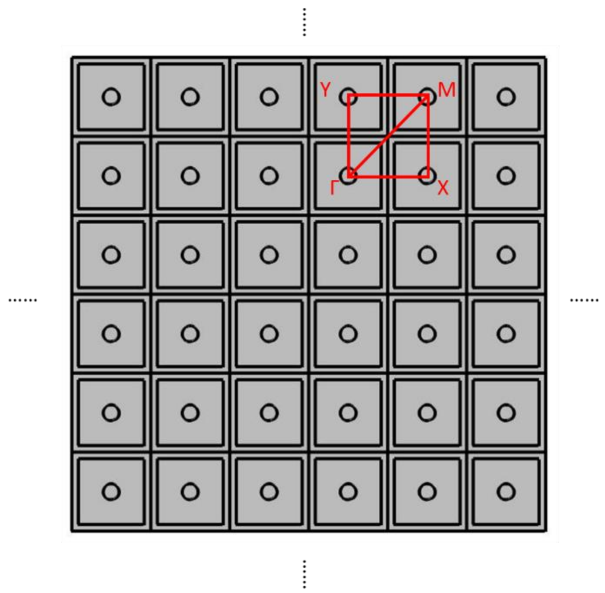

Figure 55. 2D MemM structure and the corresponding Brillouin zone.

The tensile stress of the membrane is changed from 0.10MPa to 2.00MPa. In the original design, the cross-sectional size of the membrane part is $50mm \times 1mm$, so the area $S = 5 \times 10^{-5} m^2$. Thus the range of the required force F for stretching the membrane is from 5N to 100N. Since the membrane is silicon rubber which has relatively lower strength, the stretching force should not be too large in case the membrane breaks during the assembly.

Figure 56 presents the band structures of the proposed MemM when applied with different tensile stress. Since the study mainly focus on the low frequency region and the low order resonant modes, the first 10 frequency bands are presented in the figure. As indicated earlier, the bandgap of a MemM is mainly formed by the fundamental resonant mode, and the fundamental resonant frequency is the starting frequency of the corresponding bandgap. It is observed that the increase of tensile stress will shift the bandgap to higher frequency region, which is the same as predicted in the theoretical model.

When the tensile stress is 0.10MPa, the fundamental resonant frequency is 78.2Hz and the corresponding resonant mode shape is a bending mode in which the polarized direction of the unit cell is in z-direction. According to the figure, when a bending wave is travelling along the structure and excite the fundamental resonant mode, the mass block will conduct out-of-plane vibration and stretch the elastic membrane, so the wave energy is stored in the unit cell as kinetic or potential energy. In addition, it can also generate counteracting force through this mode shape when the MemR is applied to a target structure for vibration control. The frequency bands increased gradually along with the rising of tensile stress. The fundamental resonant frequency increased to 299.7Hz when the tensile stress is adjusted to 2.00MPa. This is an effective change if compared with the 0.10MPa case.

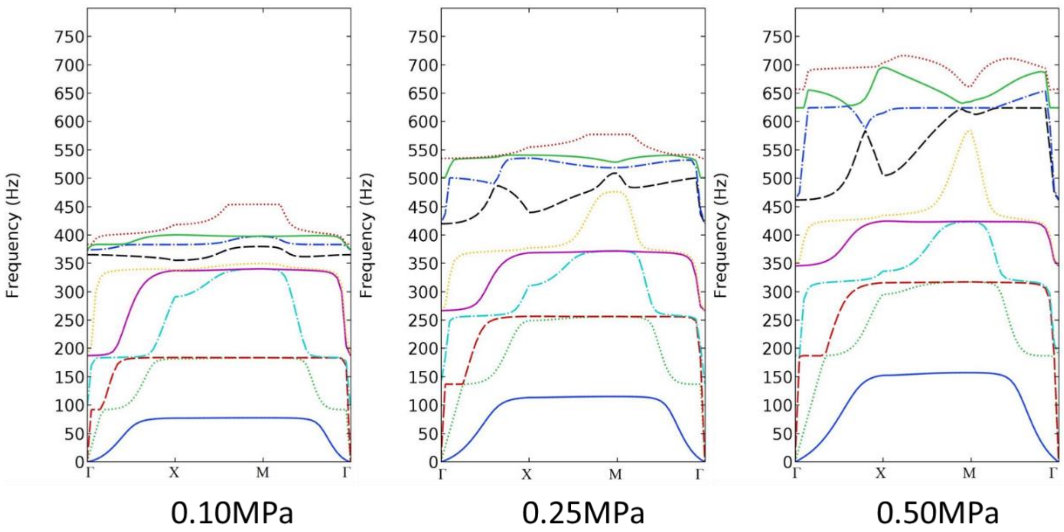

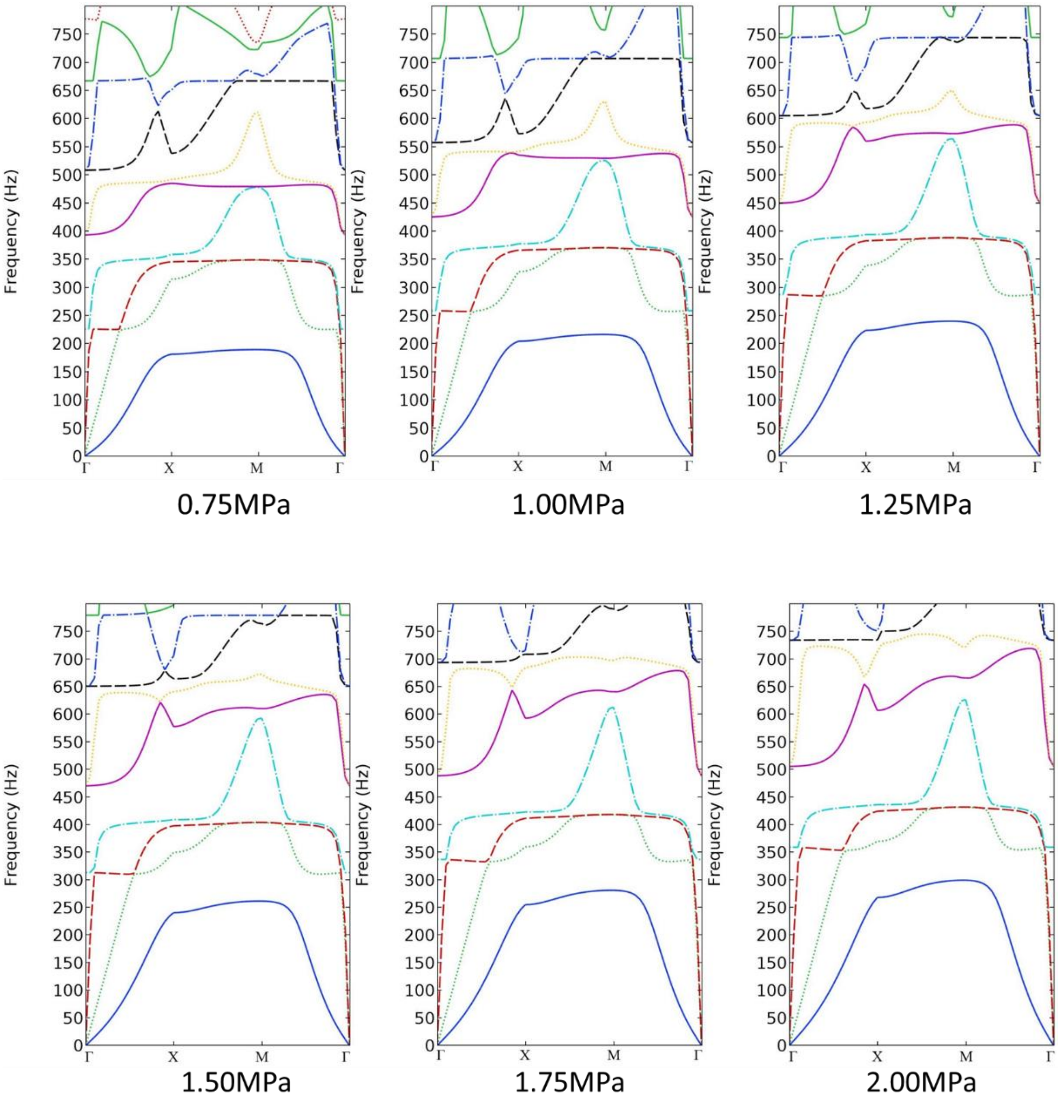

Figure 56. Band structure of the proposed MemM applied with different tensile stress.

To investigate the bandgap forming mechanism, the mode shapes of the MemR are revealed in Figure 57 as well. Since the bandgap is related with the fundamental resonant mode, considering of the first 6 resonant modes are sufficient. The first 5 resonant mode shapes are not changed along with the adjustment of tensile stress. However, the 6th resonant mode shape is changed when the tensile stress increased. When the tensile stress is 0.10MPa and 0.25MPa, the 6th resonant mode is also possessing a bending mode shape in which the mass block is kept static whilst the membrane is conducting out-of-plane vibration. The bending modes have stronger interaction between the incident bending wave and the modes can be excited easily. However, bandgap is not supposed to be formed by this mode shape because compared with the fundamental mode, the kinetic energy of membrane is much less than the vibration of mass block. Also, the potential energy change caused by the membrane is smaller than the mass block as well. Hence, even though with bending mode, the 6^{th} mode cannot form a bandgap. The existence of bandgap will be verified by the finite structure in the later section.

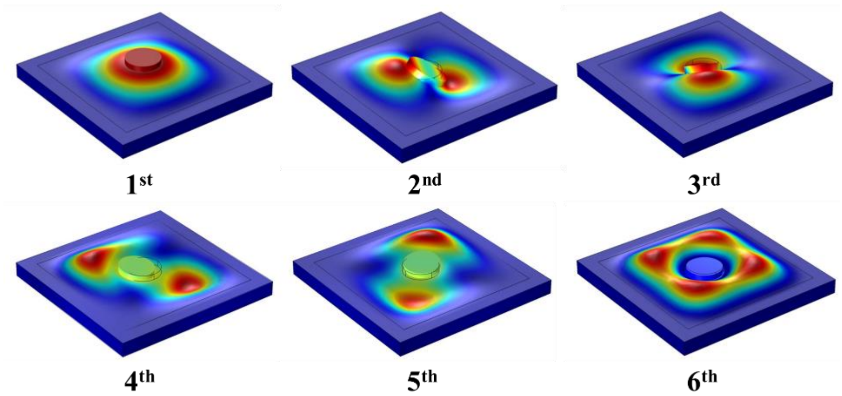

(a)

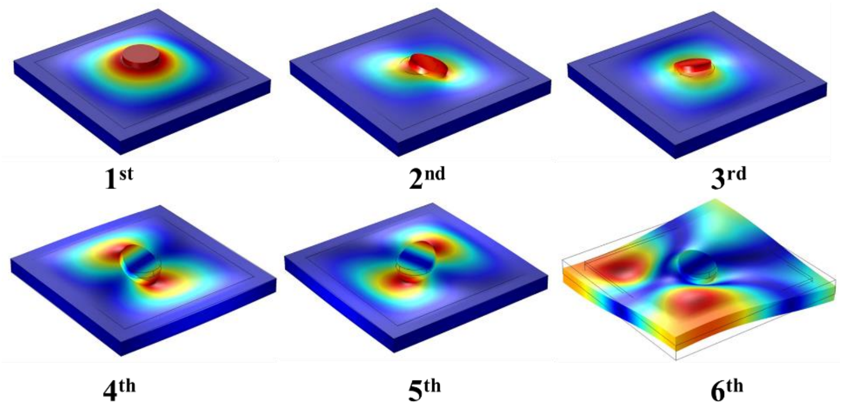

(b)

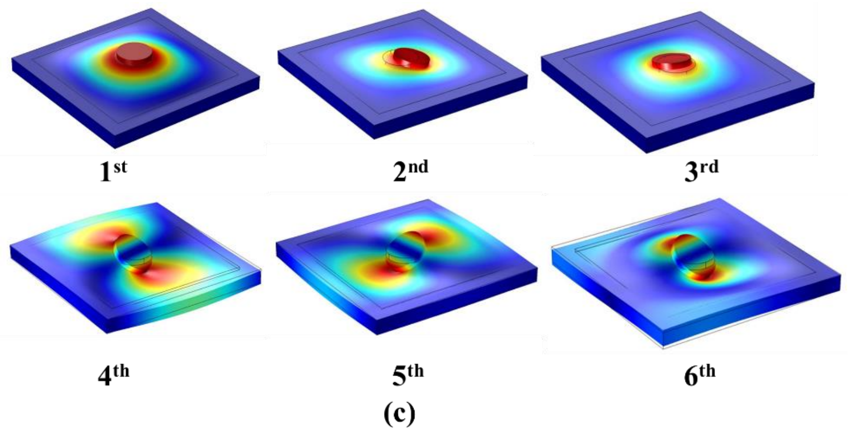

Figure 57. The first 6 resonant modes of the MemR when the applied tensile stress is (a) 0.10MPa, 0.25MPa; (b) 0.50MPa, 0.75MPa, 1.00MPa, 1.25MPa and (c) 1.50MPa, 1.75MPa and 2.00MPa.

Similar to the proposed EM introduced in **Chapter 3**, in the band structure analysis of the MemM, the full bandgap is not revealed yet local resonant bandgap is expected. The fundamental resonant mode shape is a bending mode which can be easily excited by the bending wave and there will be strong interaction between each other. Therefore, a local resonant bandgap will be found right above the fundamental frequency. However, the width of this bandgap cannot be revealed in the band structure. Finite MemM structure is needed for the purpose of investigating the bandgap widths and the bandgap widths' changes when tensile stress is adjusted.

4.2.2 Effect of mass magnitude on bandgap properties

Mass magnitude can directly affect the resonant frequency, so its adjustment has essential effect on the bandgap property. In this section, the mass magnitude is changed from 1.0g to 5.0g. The tensile stress is maintained constant as 0.50MPa. The band structure of the MemM with various mass magnitude are given in Figure 58.

With 1.0g mass attached on the membrane, the fundamental resonant frequency is 201.0Hz. When the mass magnitude increases to 1.5g, the frequency bands slightly shift to lower frequency region, yet the shapes of the bands are not changing obviously. The fundamental resonant frequency becomes 173.4Hz. Along with the increasing of mass magnitude, the frequency bands gradually shift to lower frequency region whilst the shapes of the curves are constant. When the mass magnitude is increased to 5.0g, the fundamental resonant frequency decreased to 105.8Hz. Thus, by amplifying the mass magnitude fivefold, the MemM achieves operation frequency tuning of 95.2Hz. The fundamental resonant modes are identical in all cases, so the bandgap mechanism is not changed by the mass magnitude adjustment.

The mass adjustment directly affect the equivalent mass of the MemR, so the resonant frequency is changed accordingly and the bandgap width should be enlarged when the mass magnitude increased. Such characteristic can be revealed in the finite structure study. Otherwise, the adjustment of mass magnitude can only be implemented during the manufacturing process and once applied in utilization, it is not changeable. Moreover, in application, designers will avoid extra mass load to the primary system if possible, thus the feasibility of tuning through mass magnitude is low. According to the author's literature review so far, the bandgap tuning through mass magnitude was not studied before.

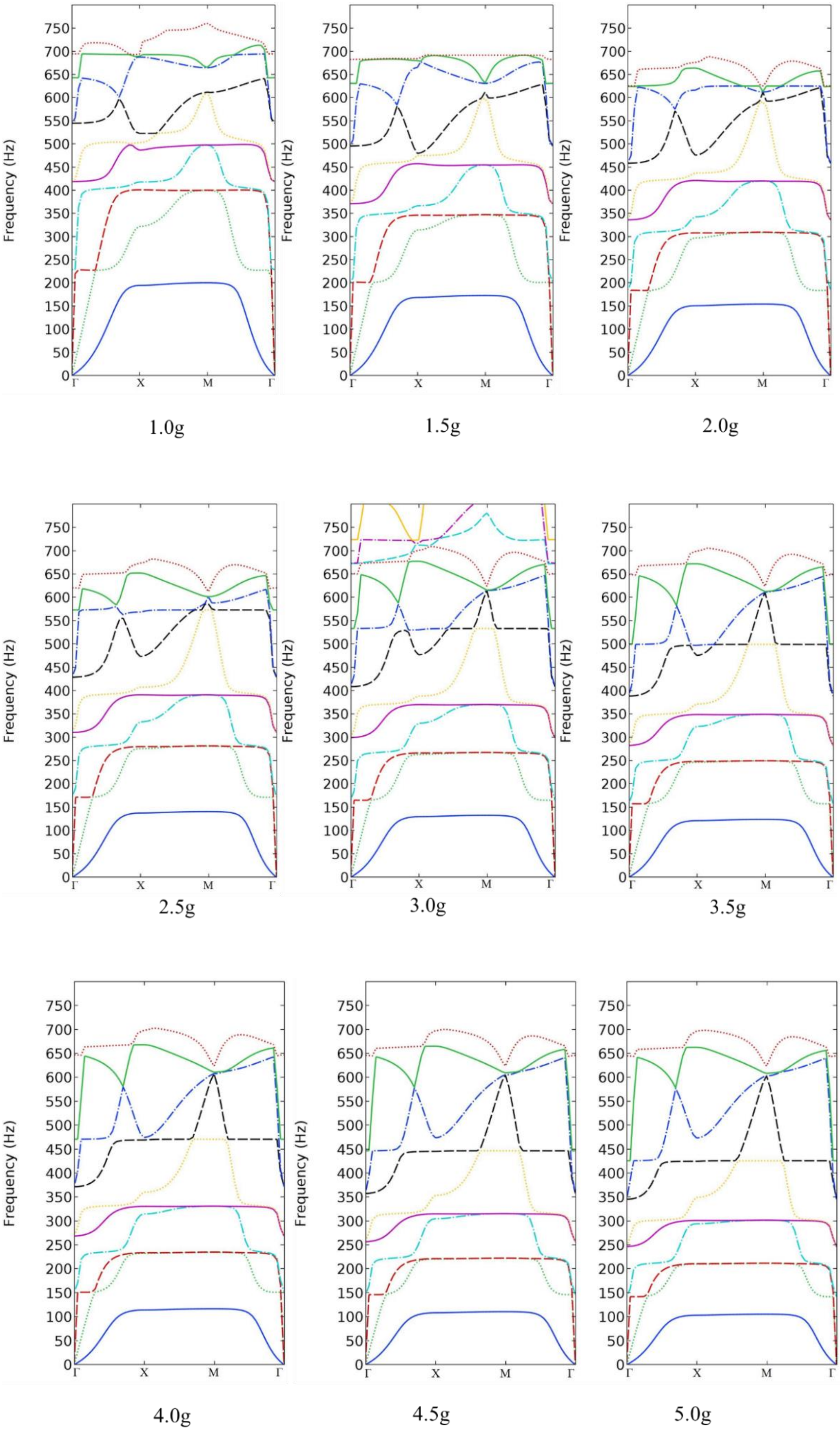

Figure 58. Band structure of the MemM applied with different mass magnitude.

4.2.3 Effect of membrane thickness on bandgap properties

Membrane thickness is another design parameter that may affect the bandgap property of the proposed MemM, because the flexural stiffness of the membrane is closely related with the thickness. To reveal the effect of membrane thickness on bandgap property, the tensile stress applied is kept as a constant: 0.50MPa.

The band structure of MemR with different membrane thickness are presented in Figure 59. The thickening of membrane will significantly increase the flexural stiffness of the membrane and the frequency bands are shifted to higher frequency region. When the dimension ratio of membrane thickness t and membrane side length L is increased from 0.004 to 0.04, the fundamental resonant frequency rose from 75.5Hz to 212.2Hz, and the fundamental mode shape does not change along with the tuning of thickness.

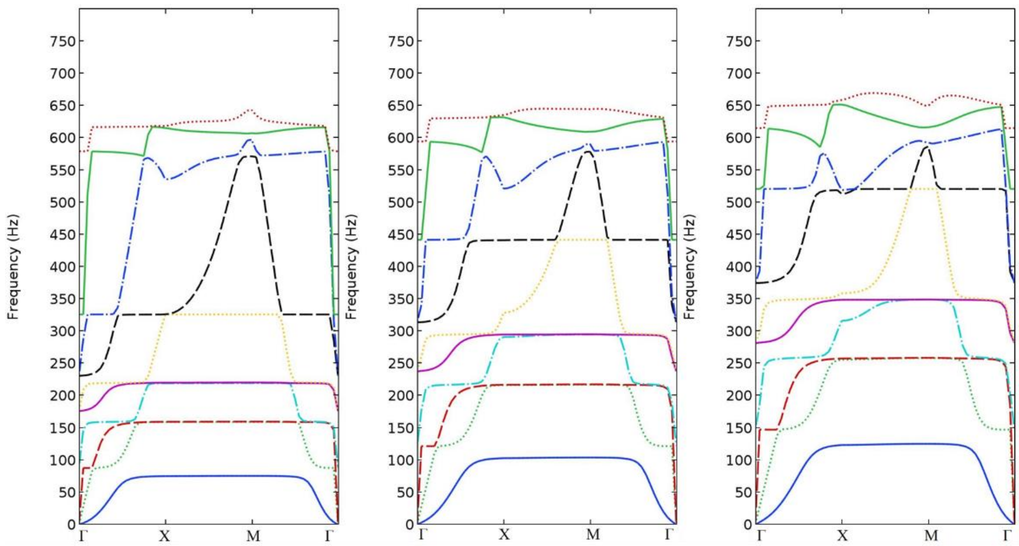

0.004 0.008 0.012

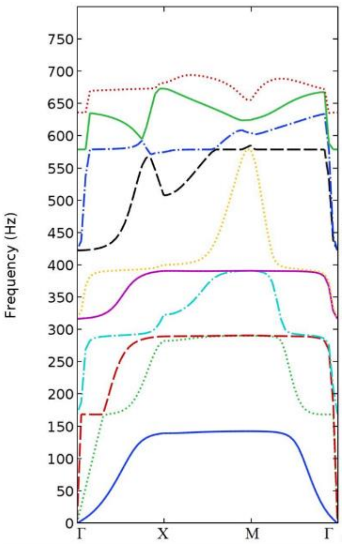

0.016

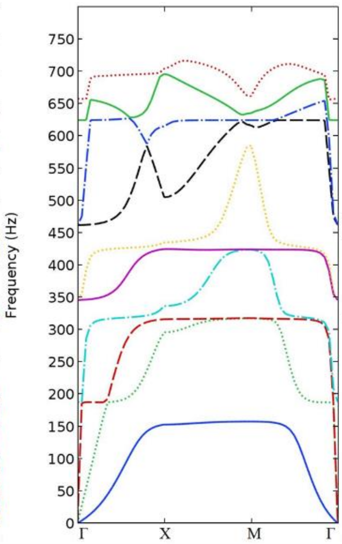

0.02

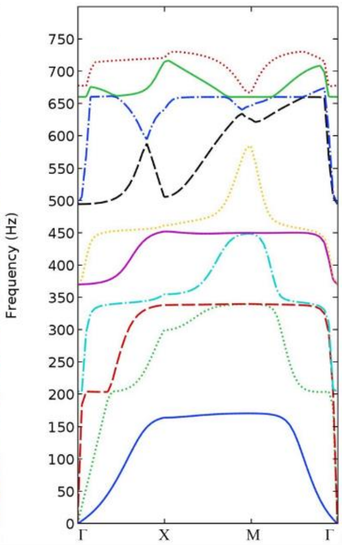

0.024

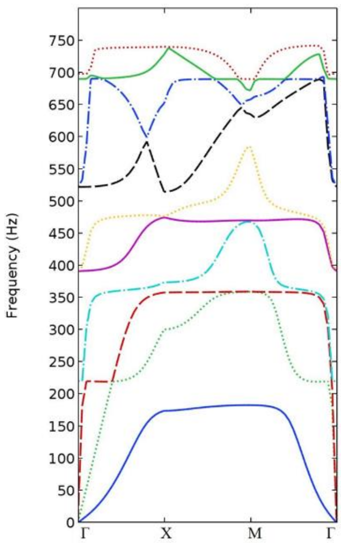

0.028

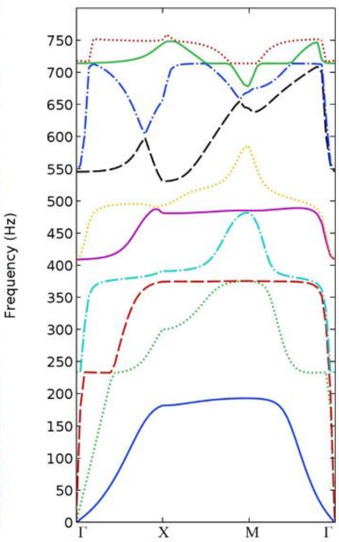

0.032

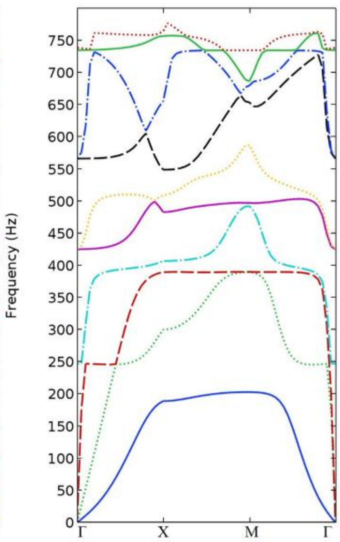

0.036

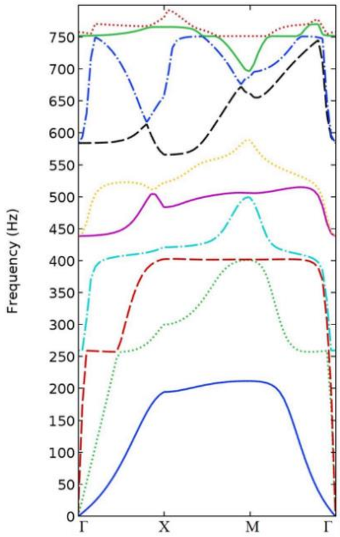

0.04

Figure 59. Band structure of the proposed MemM equipped with membranes in different thickness.

The fundamental resonant frequency of the MemM with different membrane thickness are listed in Table 8. According to the theoretical model mentioned in **Section 2.2.2**, the resonant frequency is linear with the square root of the dimension ratio. The frequency is plot against the square root of dimension ratio as shown in Figure 60, and the equation of trend line is displayed as well. Thus, according to the trend line equation, when the dimension ratio is increased 0.004, the resonant frequency will shift about 63.2Hz. So the fundamental resonant frequency is very sensitive to the membrane thickness adjustment.

Table 8. Fundamental resonant frequencies of MemM with different membrane thickness.

Dimension ratio	Frequency (Hz)	Dimension ratio	Frequency (Hz)
0.004	75.5	0.024	171.1
0.008	103.9	0.028	182.8
0.012	125.3	0.032	193.5
0.016	142.8	0.036	203.2
0.02	157.8	0.04	212.2

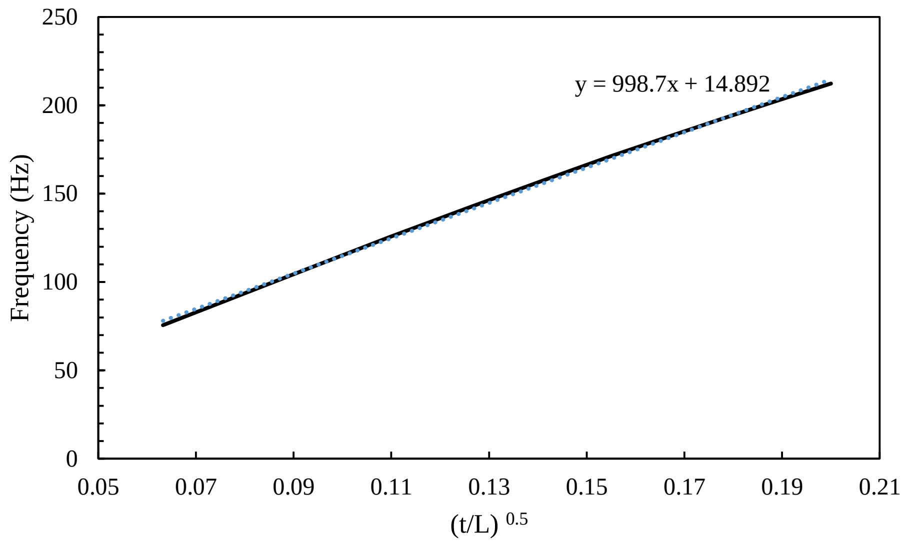

Figure 60. The relation of fundamental resonant frequency of a MemR (black-solid line) when the membrane thickness is adjusted. The trend line is presented in blue-dashed line.

In addition, the fundamental mode shape of the MemR is the same as those in Section 4.2.1. This characteristic ensure the MemR can form a local resonant bandgap when equipped with membranes in different thickness.

The adjustment of membrane thickness is difficult to be implemented when the MemM is in utilization, though it has good effect on resonant frequency. Through using membrane made of smart material, such as DE material, the thickness of membrane can be tuned through the externally applied voltage [114]. However, because of the thickness change is relatively small in a single layer of DE membrane, stacking of membranes are required. Otherwise, high voltage is in demand to generate effect deformation of membrane [141]. Such requirements limit the utilization of DE material in MemM and the tuning of MemM through thickness adjustment.

4.2.4 Effect of mass configuration on bandgap properties

The mass configuration or locations of the MemR will also change the bandgap property because the resonant mode shape and the resonant frequencies will be changed as well.

In this section, three different types of mass configurations are proposed and studied.

In the first type, the circular mass block is separated into two semicircle mass blocks for the purpose of maintaining the total mass of the MemR. The configuration of the MemR is shown in Figure 61.

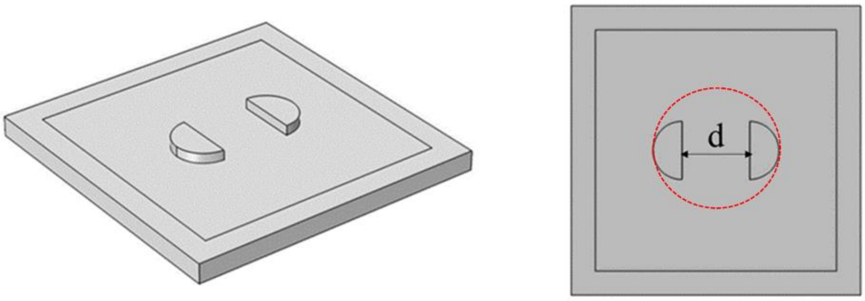

Figure 61. The configuration of the MemR with two semicircle mass attached. The distance between the semicircle mass blocks are defined as d.

The masses are located in symmetry with respect to the middle axis of the membrane. The distance d between the two masses is considered as the design for the location of masses.

The corresponding band structures of the MemM with two semicircle mass blocks are given in Figure 62. In accordance to the symmetric characteristics of the structure, the irreducible Brillouin zone is different from the MemR mentioned in above subsections, and the wave vector is scanned along M-Γ-X-M-Y-Γ, which is the same as **Chapter 3, Section 3.2.2**.

As shown in the figure, when the distance between the two mass blocks is increased, the resonant frequency bands are moving to higher frequency regions, while the shapes of band structure are barely changed. There are no obvious full bandgap revealed according to the band structure. However, the elastic wave travelling within the structure is still possible having interaction with the resonant. Therefore, similar to the other MemRs mentioned in above subsections in this chapter, local resonant bandgap may be revealed. Mode shape analysis is conducted for prediction of bandgap prediction.

To explain the increase of resonant frequencies when the distance between the two mass blocks become further, one can consider the average mass density within the area highlighted by the red dashed circle in Figure 61. The circle contains the two mass blocks exactly and its radius is increased accordingly with the distance d. Therefore, when d increased, the area of the circle is rising and the average mass density is reduced. According to the analytical model mentioned in **Section 2.2.1**, the decrease of average mass density attached on membrane surface will therefore results in the increase of resonant frequency. Thus, in such configuration, the resonant frequency of the structure can be adjusted through the changing of mass block distance.

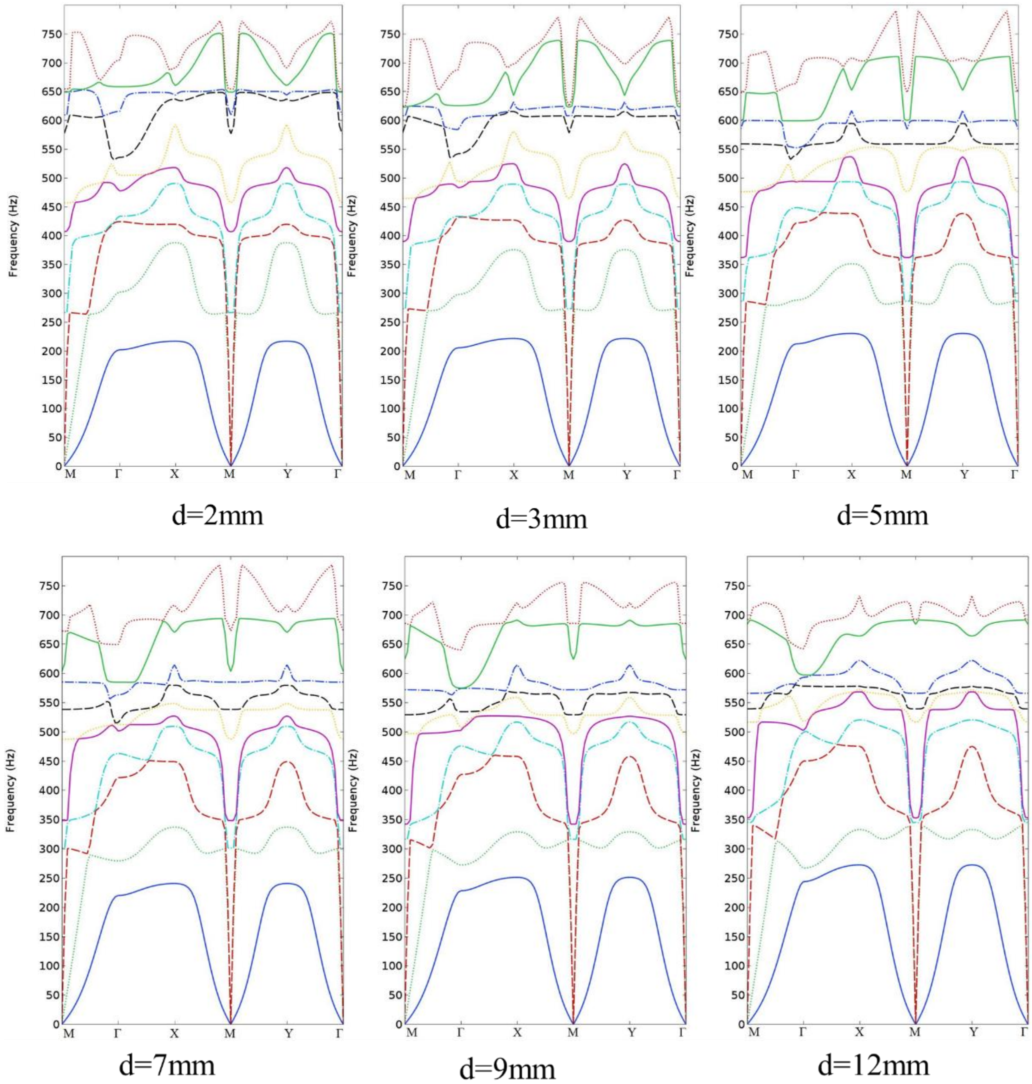

Figure 62. Band structures of the MemM with two semicircle mass blocks attached. The distance between the mass blocks are adjusted.

When $d = 2$ mm, 3mm, 5mm, 7mm, 9mm and 12mm, the first 6 mode shapes of the resonator are depicted in Figure 63. According to the figure, the first resonant modes of the resonator in all distances are bending modes with the two mass blocks conducting out-of-plane vibration. It indicates that the resonator with two masses also has the potential to generate a local resonant bandgap by the fundamental resonant mode.

However, when the distance is increased, the two mass blocks are more apart from each other and the mass allocation is not as concentrated as the short distance case. The deviation of mass blocks from the centre of the membrane will lead to the decrease of vibration amplitude in the fundamental resonant mode. Otherwise, as shown in Figure 63, in the fundamental resonant mode, when the distance increased gradually, the two mass blocks will have small deflection angles between the plane of the membrane. So part of the stretching force in the membrane generated by the mass blocks will be in opposite direction of each other and cancelled out. Consequently, the MemR with larger mass blocks distance will generate smaller counteracting force to control vibration, therefore the local resonant bandgap may disappear when the distance is larger than a certain value.

In addition, the higher order resonant modes are also changed when distance is adjusted. For example, when the distance d is 2 mm, in the 6^{th} resonant mode, the two mass blocks are flipping symmetrically. However, when the distance is increased to 3 mm, the mass blocks are twisting in an asymmetric mode in the 6^{th} resonant mode. These resonant modes are not related with the local resonant bandgap formed by the fundamental mode and they are not supposed to be able to form local resonant bandgap because they are antisymmetric modes where the counteracting force generated from the MemR is mostly self-balanced because of the twisting, similar to the findings of the EM in **Chapter 3**. The existence of the bandgap will be further investigated in section 4.3.4.

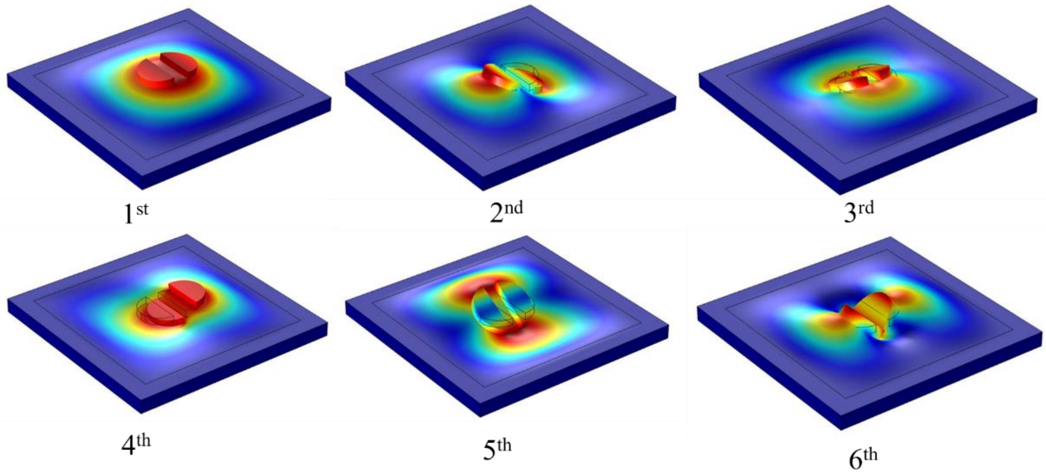
1st
2nd
3rd
4th
5th
6th

d=2
(a)

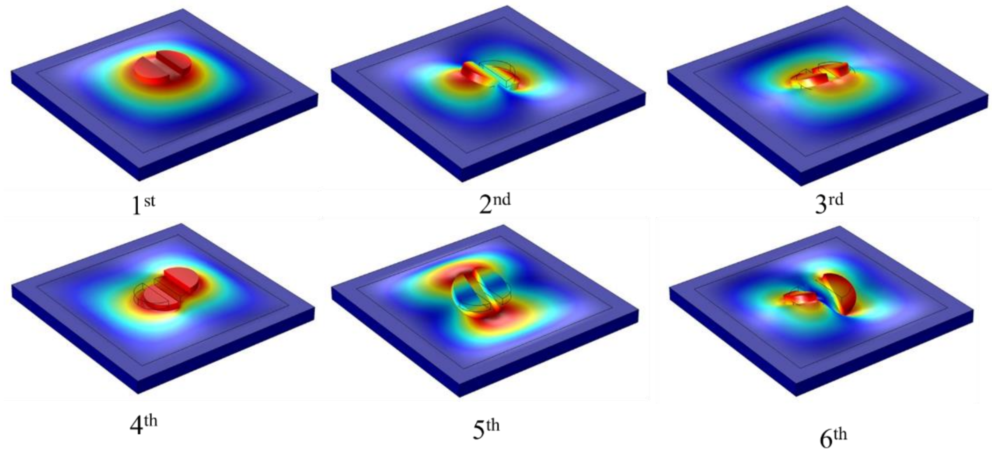
1st
2nd
3rd
4th
5th
6th

d=3
(b)

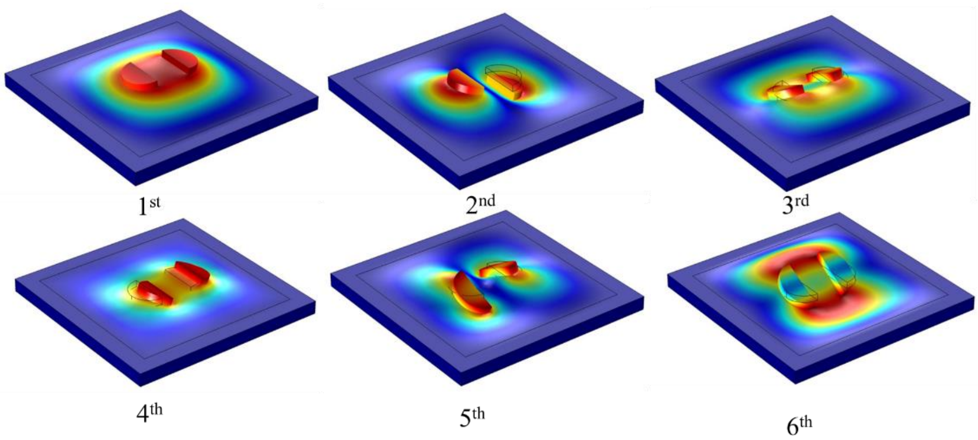
1st
2nd
3rd
4th
5th
6th

d=5
(c)

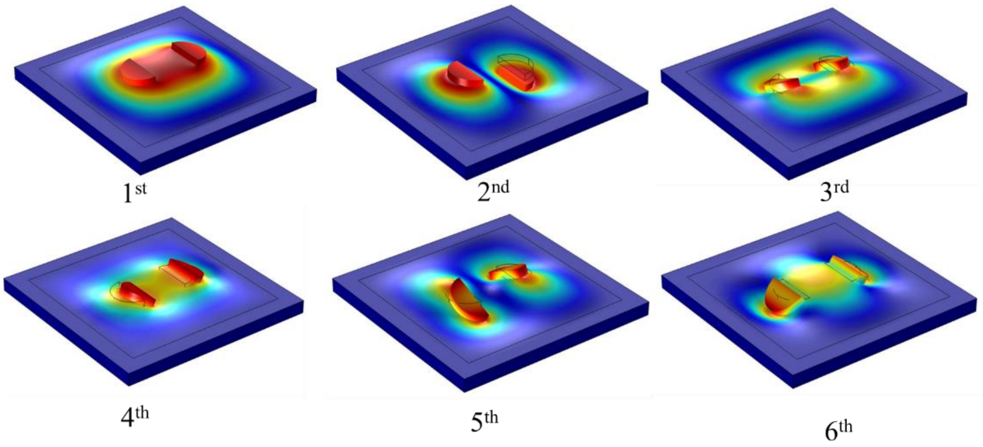

d=7
(d)

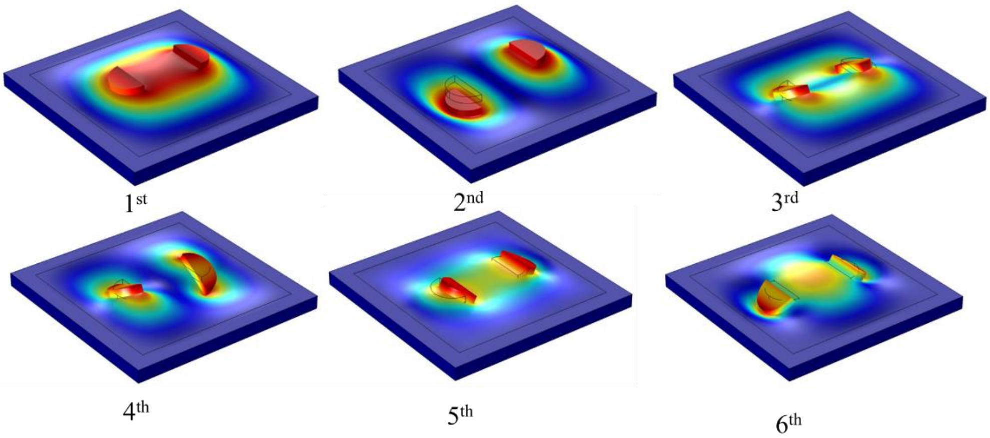

d=9
(e)

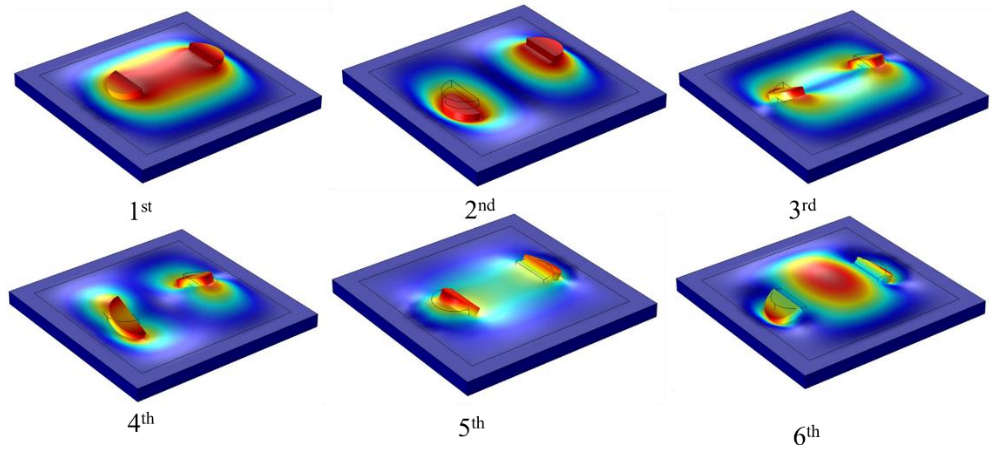

d=12
(f)

Figure 63. First 6 resonant modes of the MemR with two semicircle mass blocks when the distance between the two blocks d are (a) 2mm; (b) 3mm; (c) 5mm; (d) 7mm; (e) 9mm and (f) 12mm.

In the second type, three circular mass blocks are attached on the membrane.

The third type of configuration is a nested mass combination. The configuration is shown in Figure 64. A circular mass block with radius r_{m1} is located at the middle point of a ring mass. For the convenience of conducting parametric analysis, the width of the ring mass w_0 is fixed as 3mm, and the outer radius of the ring mass is defined as r_{m2}. Since the ring mass block requires more space for installation, the side length of the membrane L_m is increased to 70mm. The outer side length of the frame L_o= 80mm.

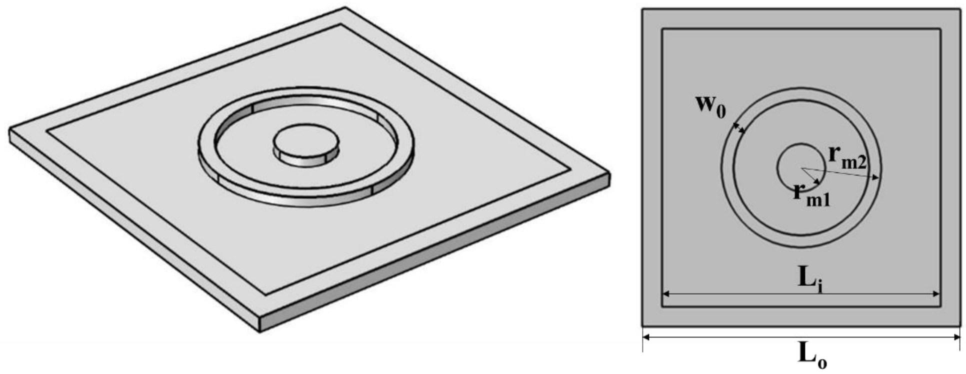

Figure 64.The configuration of the MemM with nested mass blocks.

The detailed dimension of the configuration are given in Table 9. The radius of the circular mass block is fixed as 5mm and the radius of the ring mass is adjusted from 10mm to 20mm. The ratio of the two mass block radius $R = \frac{r_{m2}}{r_{m1}}$ is adopted as the design parameter.

Table 9. Dimension data of the nested mass configuration.

r_{m1}(mm)	5	Membrane thickness (mm)	0.1
r_{m2} (mm)	10-20	L_m (mm)	70
w_0 (mm)	3	L_o (mm)	80
Frame thickness (mm)	5	Tensile stress (MPa)	0.5

As discussed in above subsections, the formation of local resonant bandgap is decided by the resonant mode shape. By designing the structure that possess multiple bending resonant mode shapes, it may lead to the existence of several bandgaps with only one layer of membrane. In the nested mass configuration, two mass blocks are used and both of their geometrical centres are overlapped and at the middle point of the membrane. For illustration, the first 9 resonant mode shapes of the MemR when $R = 4$ are presented in Figure 65. Through the analysis, it is found that there are two resonant modes (the 1st and the 7th) in which the two mass blocks are vibrating in bending mode. Therefore, it is likely that there are two bending mode local resonance bandgaps being formed by this type of MemM.

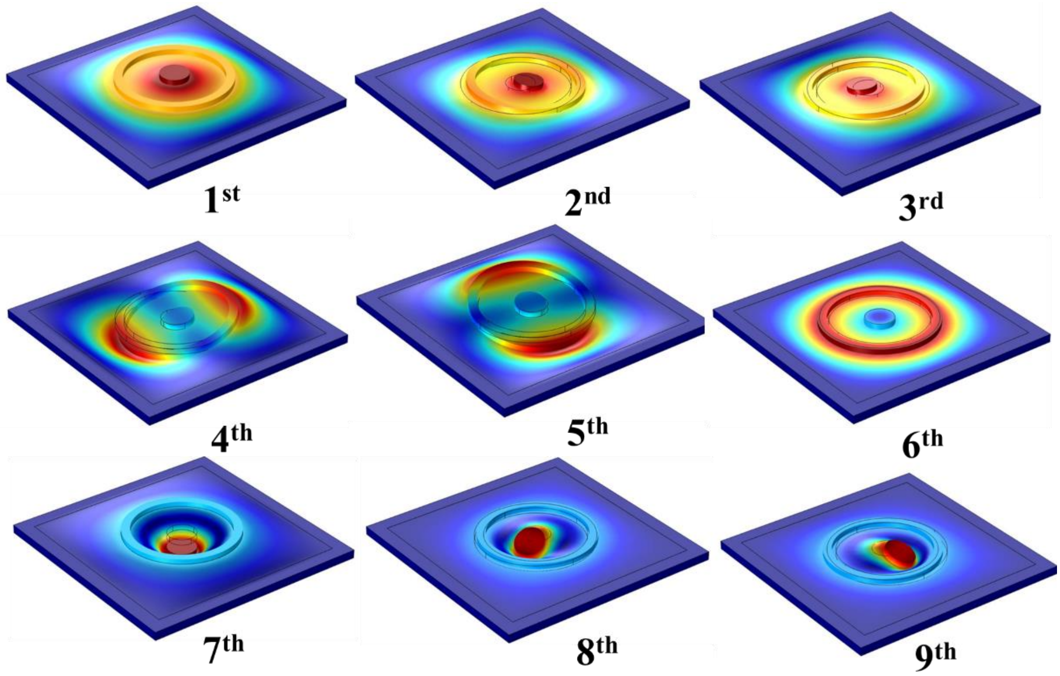

Figure 65. The first 9 resonant mode shapes of the nested mass MemR when radius ratio R=4.

However, when the ratio radius is reduced, which means the distance between the ring mass's inner circle is closer to the circular mass, the mass system is more compact. Therefore, the resonant mode shape of the two mass vibrating in opposite direction (as the 7^{th} resonant mode that mentioned in the R=4 case) will not appear.

Since the band structure cannot effectively reveal the local resonant bandgaps, the bandgap property of this type of MemM are further analysed by FEA and presented in **Section 4.3.4**.

4.3 Wave Transmission in Finite Structure of MemM

To investigate the wave transmission characteristics in a finite structure that formed by the proposed MemM, numerical simulation is conducted. The designed parameters' adjustment is supposed to be affecting the bandgap property of the MemM, therefore the wave transmission within the structure with different parameters will be changed in accordance to the analysis of the band structure.

In this subsection, finite structures of MemM plate are constructed for numerical simulation. The MemM plate consist of 8×8 MemRs, as shown in Figure 66

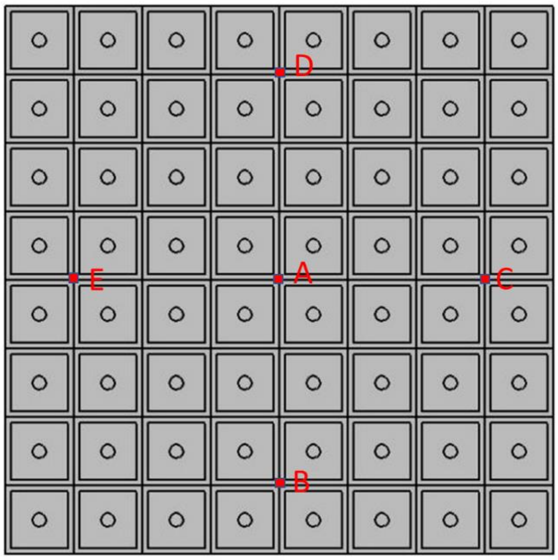

Figure 66. The configuration of the MemM plate.

Point excitation is applied at the middle point A of the plate by prescribed displacement. Frequency scanning is applied and the frequency response signals of the plate are picked up from the points labelled as B to E. The FRF is calculated by: $FRF = 20\log\left(\frac{a_{out}}{a_{in}}\right)\ dB$, where a_{out} and a_{in} are the output and input acceleration signal, respectively.

4.3.1 MemM applied with different tensile stress

In section 4.2.1, the band structures of the MemM applied with different tensile stress are investigated and the results demonstrate that the increase of tensile stress will shift the bandgap to higher frequency regions. In this section, the existence of bandgap and widths are explored by the wave scanning conducted on the finite structure.

The FRFs are obtained through the detected acceleration signals. Through comparison, the FRFs from points *B* to *E* are similar because the symmetric of the structure. Therefore, only the responses of the MemM with different tensile stress at point *B* are presented in Figure 67.

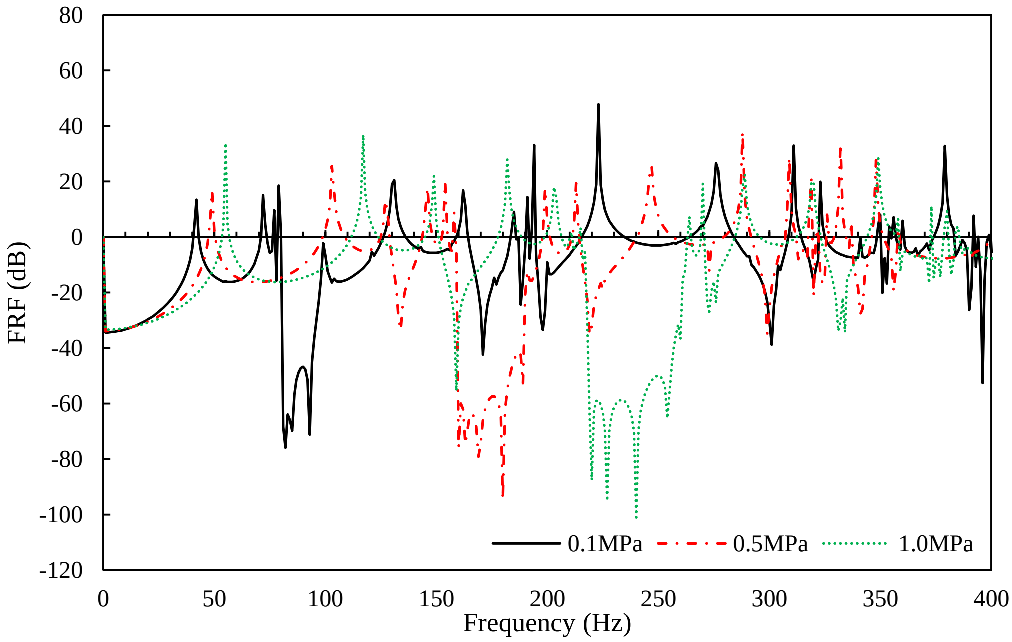

(a)

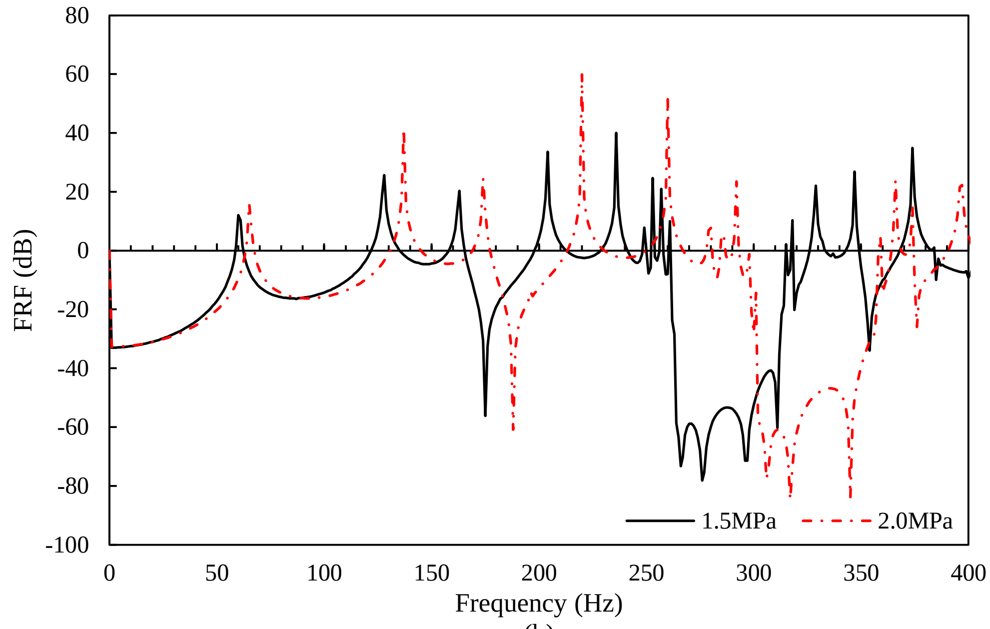

(b)

Figure 67. FRF of the proposed MemM plates applied with different tensile stress (a) 0.1MPa, 0.5MPa and 1MPa; (b) 1.5MPa and 2.0MPa.

According to the figure, the bandgaps' lower edges under these 5 different tensile stress are: 81.0Hz, 160.0Hz, 219.0Hz, 262.0Hz and 299Hz. In section 4.2.1, the corresponding bandgaps' lower edges are predicted as: 78.2Hz, 157.8Hz, 216.8Hz, 261.9Hz and 299.7Hz. Bandgap location shifted 270% when the tensile stress is increased from 0.1MPa to 2MPa. It is a significant change for the operation frequency tuning in vibration control application.

Through the finite structure study, the bandgap existence is revealed and the bandgap width is relatively broad, even though compared with the EM proposed in **Chapter 3** it is still narrower.

It is noted that the bandgap starting frequencies revealed in the finite structure are slightly higher than the band structures' prediction. Different boundary conditions contribute to the occurrence of error. In FEA, the band structure is calculated through a unit cell applied with periodic boundary conditions. However, in the finite structure, fixed boundary conditions are applied. Thus, extra stiffness is supplied to the system and the resonant frequencies will be increased.

In Figure 68, the bandgaps' lower edge obtained by FEA and the finite structure, bandgaps' cut-off frequencies and the bandgap widths are presented. It reveals that when the starting frequencies and bandgap widths increase along with the increase of tensile stress. Such characteristic allows the MemM to broaden the bandgap width without increasing mass load.

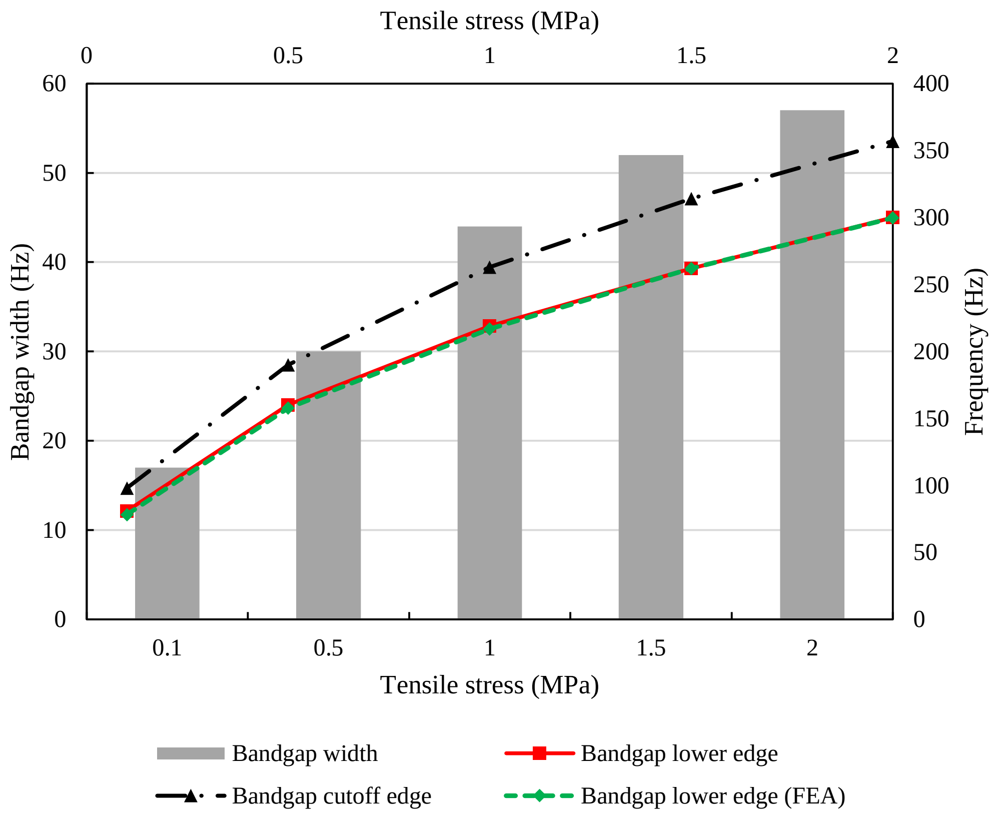

Figure 68. Bandgap widths, lower edge and cut-off frequencies of the proposed MemM applied with different tensile stress.

As shown in Figure 69, when the excitation frequency is inside the bandgap region, the fundamental resonant mode of the MemR is activated and the resonator starts vibrating. Therefore the wave energy is used to support the vibration of the resonator mass and as a result, the vibration cannot transmitted through the finite structure. When the excitation frequency is outside the bandgap region, the local resonant of the MemRs cannot be excited so the bending wave can transmitted through the whole structure and leads to the vibration of the whole structure.

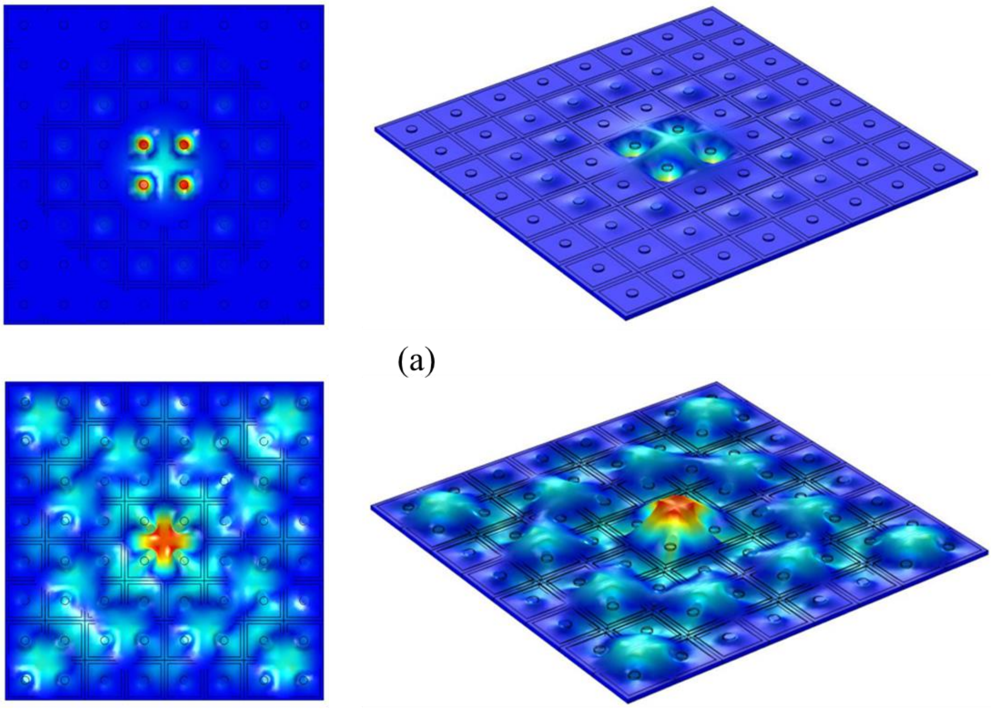

Figure 69.Deformation of the MemM plate when the excitation frequency is (a) inside bandgap frequency region and (b) outside bandgap frequency region.

Aside from the deformation under certain frequency, the transient status of the finite structure excited under different frequencies are also studied. The frequency response of the finite structure in different time spots when excited under different frequencies are presented in Figure 70. The excitation frequencies are chosen as 170.0Hz (insider bandgap) and 380.0Hz (outside bandgap), respectively. The time spots are expressed in the form of the excitation signal's period *T*.

As shown in Figure 70 (a), when the time is *T*, the MemRs around the excitation point is activated and vibrating in the unit cells around the excitation points. At 5*T* and 8*T*, the vibration is still contained within the unit cells that around the excitation points, and the bending wave cannot transmitted through the plate structure.

When the excitation frequency is outside the bandgap region, as shown in Figure 70 (b), the wave is transmitted through the unit cells around the excitation point already at *T*. The vibration transmits through the whole structure later on and leads to the vibration of the whole finite structure. Because the similarity and symmetric characteristics of the finite structure, the wave also transmits symmetrically. The deformation in the transient status is consistent with the one revealed in Figure 69.

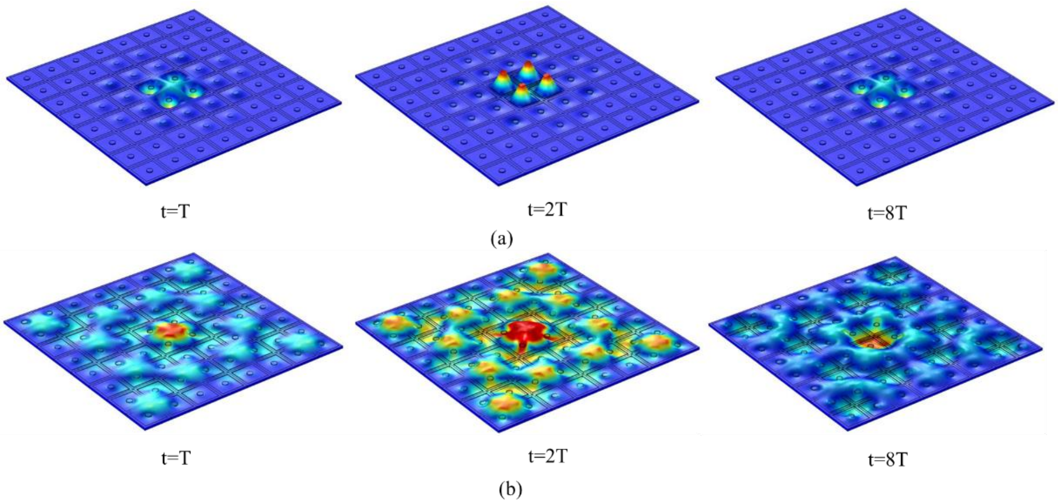

Figure 70. Finite MemM structure's vibration response at different time spots when excited under the frequencies: (a) 170Hz and (b) 380Hz.

4.3.2 MemM with different mass magnitude

The FRFs of the finite MemM structures applied with different mass magnitudes are investigated and presented in Figure 71. The tensile stress is maintained at 0.5MPa while the mass magnitudes are adjusted as 1.0g, 1.5g, 2.0g, 3.0g, 4.0g and 5.0g, respectively. When the mass magnitude is 1g, the starting frequency of the bandgap is 206.0Hz, and the bandgap width is 29.0Hz. As the mass magnitude increases, the bandgap starting location shifts to lower frequency regions accordingly. It is the same tendency predicted by the band structure analysis in section 4.2.2. The increase of mass magnitude makes the MemR system obtain larger equivalent mass and therefore the resonant frequencies decreased. Otherwise, in order to reveal the influence of mass magnitude, the starting and cut-off frequencies of the finite structure and bandgap widths are presented in Figure 72.

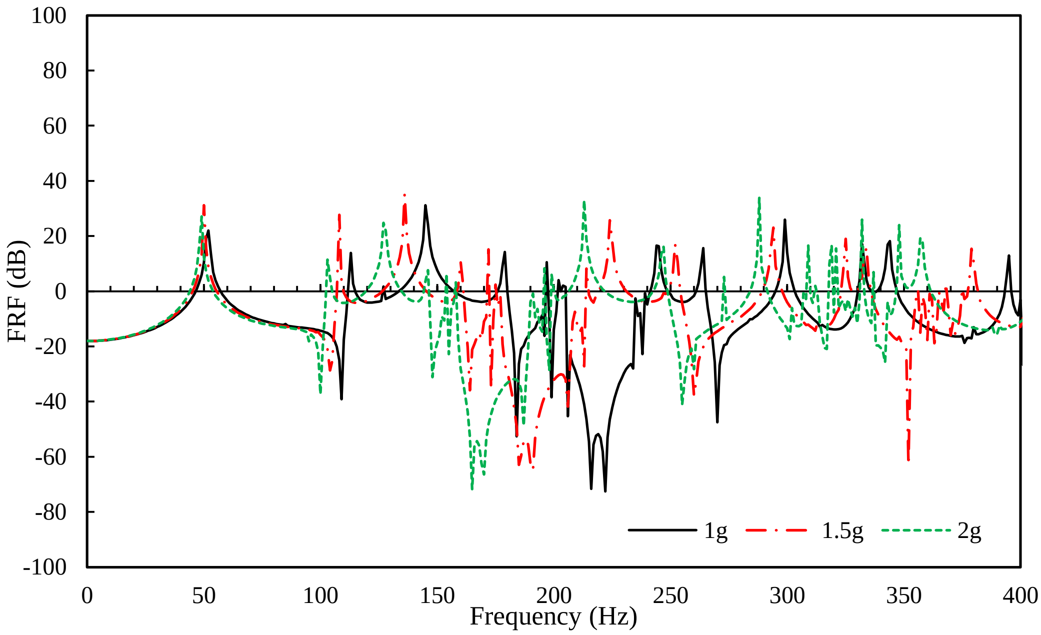

(a)

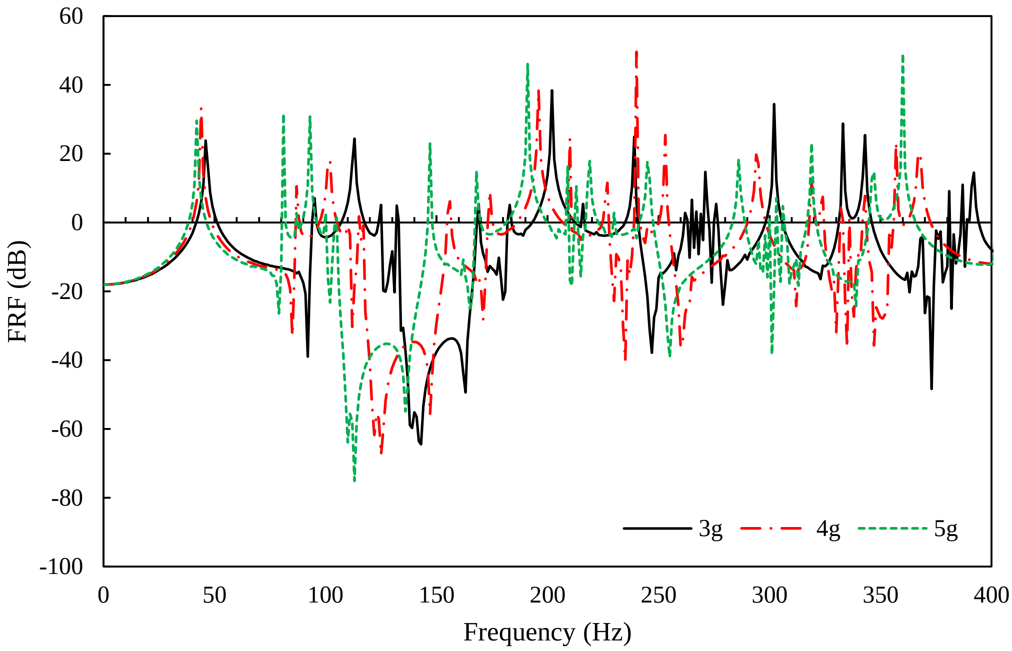

(b)

Figure 71. FRF of the proposed MemM plates applied with different mass magnitudes: (a) 1.0g, 1.5g, 2.0g and (b) 3.0g, 4.0g, 5.0g.

According to Figure 72, the bandgap width with 1.0g mass attached is 29.0Hz. When the mass magnitude increased the bandgap width grows as well. The width decrease from 38.0Hz to 36.0Hz when the mass magnitude increased from 3.0g to 4.0g, yet comprehensively, the bandgap width increased gradually when the mass magnitude is increased. The slop of the bandgap location change trend line becomes subtle gradually when the mass magnitude is increased. The finding reveals similar effect as the adjustment of tensile stress. However, if the bandgap width is broadened by this way, the total attached mass will be increased and it may lead to the compromise of primary system's functioning performance in application.

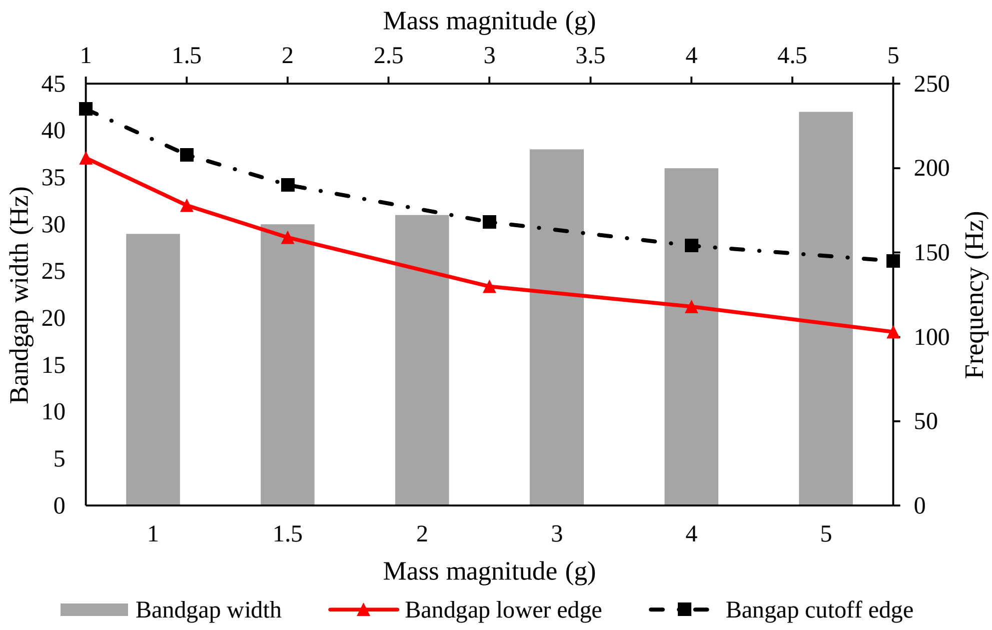

Figure 72. Bandgap widths, lower edge and cut-off frequencies of the proposed MemM applied with different mass magnitudes.

4.3.3 MemM with different membrane thickness

To investigate the bandgap property of the MemM with different membrane thickness and side length ratio, the finite structure's FRFs are obtained and presented in Figure 73. The ratios are selected as 0.008, 0.02, 0.032 and 0.04, respectively.

The increase of size ratio can make the bandgap location to higher frequency regions. The bandgap starting frequencies are 105.0Hz, 160.0Hz, 196.0Hz and

216.0Hz, respectively. Growing membrane thickness increase the stiffness of the membrane and therefore the resonant frequency becomes higher.

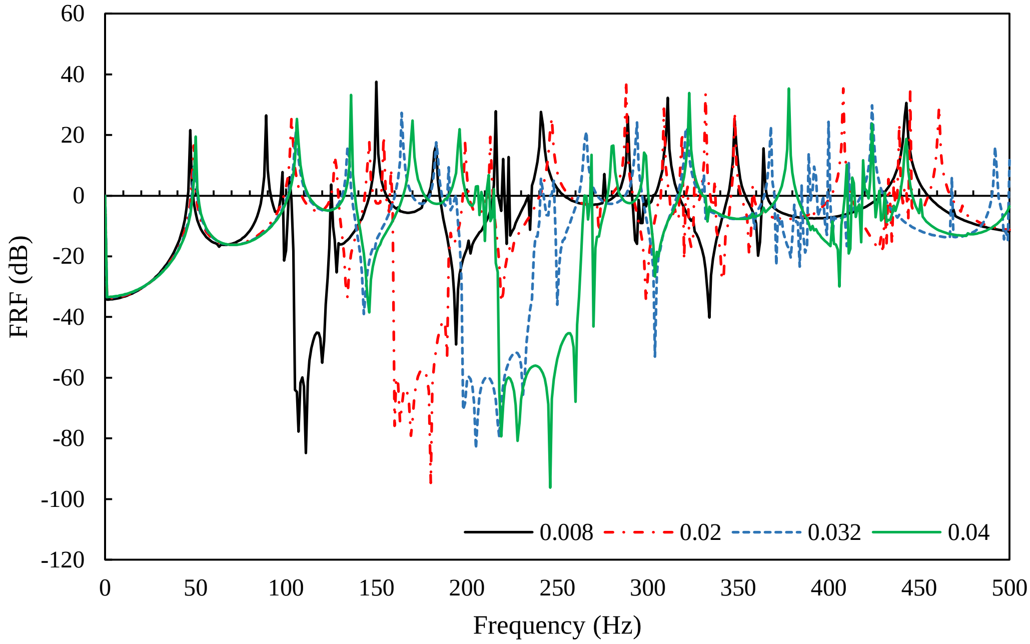

Figure 73. FRFs of MemM with different membrane thickness and side length size ratio.

The existence of local resonant bandgap is not affected by the adjustment of thickness because the fundamental resonant mode is not changed. According to Figure 74, the bandgap widths are also increased along with the rising of the size ratio. As mentioned in Section 4.3.1, the rising stiffness will lead to the increase of bandgap width. Similarly, the increase of membrane thickness achieved the same effect.

The results reveal that the tuning of membrane thickness can also affect the bandgap property of the MemM. However, similar to the mass magnitude, the tuning of membrane thickness can only be realised in the manufacturing process.

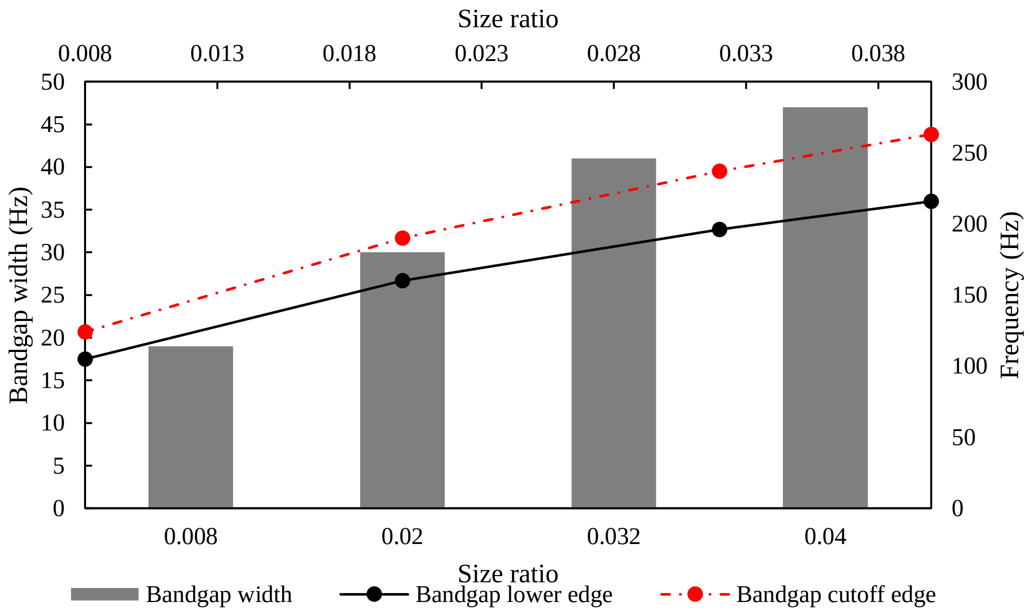

Figure 74. Bandgap widths, lower edge and cut-off frequencies of the proposed MemM applied with different mass magnitudes.

4.3.4 MemM with different mass configurations and locations

Semicircle mass

Similar to the above mentioned subsections, finite metamaterial structures that composed of 8×8 unit cells are constructed. With a point excitation in the middle of the structure, the vibration response of the structure is detected.

The FRFs of the finite structure with different distances are presented in Figure 75. A local resonant bandgap of flexural wave is formed in the finite structure of the MemM formed by this type of MemRs. The location of the full bandgaps are consistent with the location of fundamental resonant frequencies mentioned in **Section 4.2.4**.

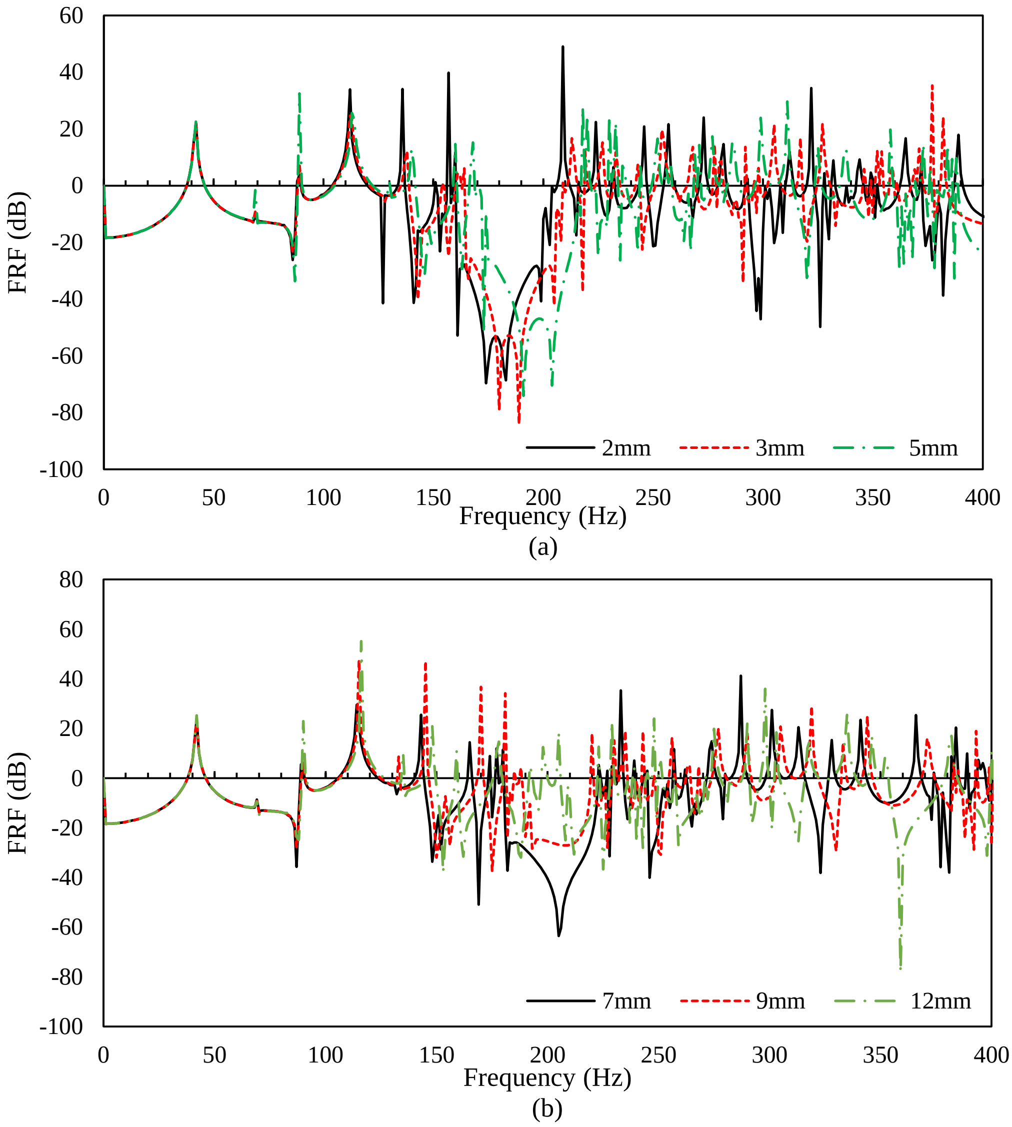

Figure 75. FRFs of MemM with two semicircle mass blocks. The distance between the mass blocks: (a) 2mm, 3mm, 5mm and (b) 7mm, 9mm, 12mm.

According to Figure 75, when the distance between the two mass blocks is increased from 2mm to 7mm, the existence of the local resonant bandgap is obvious, and the locations of the bandgap are shifting gradually. However, as shown in Figure 75 (b), when the distance is 9mm, the wave attenuation in around the fundamental resonant frequency region is not obvious anymore and the existence of bandgap disappeared when the distance is continuously increased to 12mm. Such phenomenon can be explained by the analysis indicated in **Section 4.2.4** that the distance increment results in the decrease of force generated by the MemR and therefore the suppression of the vibration is weakened.

The result demonstrates that the MemR with two mass blocks can be tuned by the adjustment of distance between the mass blocks: the location of bandgap will shift to higher frequency regions when the distance is increased. However, the disadvantage of such configuration is also very obvious as well: the bandgap will disappear when the distance is larger than a certain value . It is therefore not an ideal configuration for application.

Nested mass

For the nested mass configuration, the bandgap property of the MemM and the effect of the configuration dimension on the bandgap are investigated through the finite structure. The setting parameters of the resonators are consistent with those introduced in Table 9.

By defining the dimension ratio $R = \frac{r_{m2}}{r_{m1}}$ (where r_{m2} and r_{m1} are the radius of the ring mass and circular mass respectively), the change of bandgap location is studied. The finite structure of the MemM is also an 8×8 MemR plate. R is changed by tuning the value of r_{m2} from 20mm to 10mm. The FRFs of the finite structure is given in Figure 76.

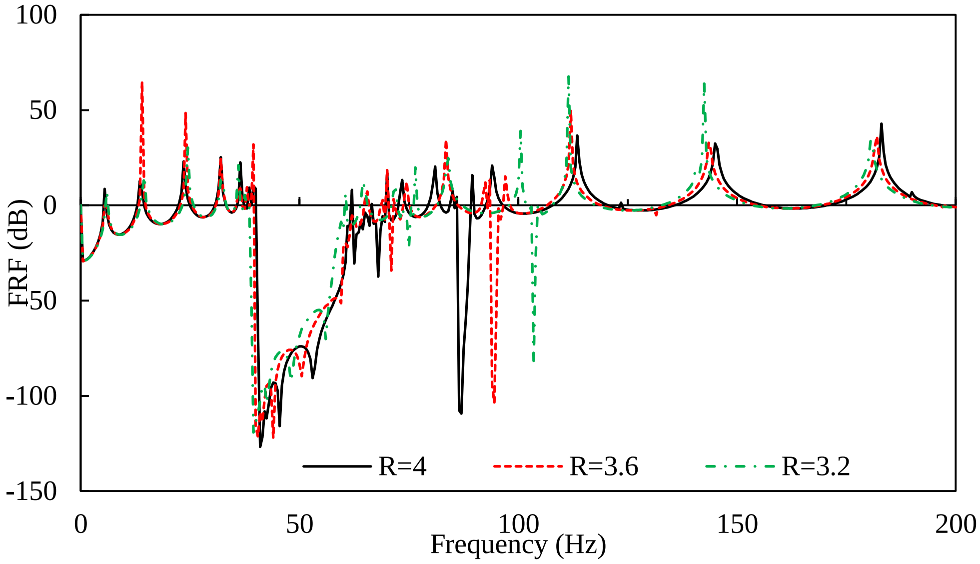
100
50
0
-50
-100
-150
FRF (dB)
0
50
100
150
200
Frequency (Hz)
R=4
R=3.6
R=3.2

(a)

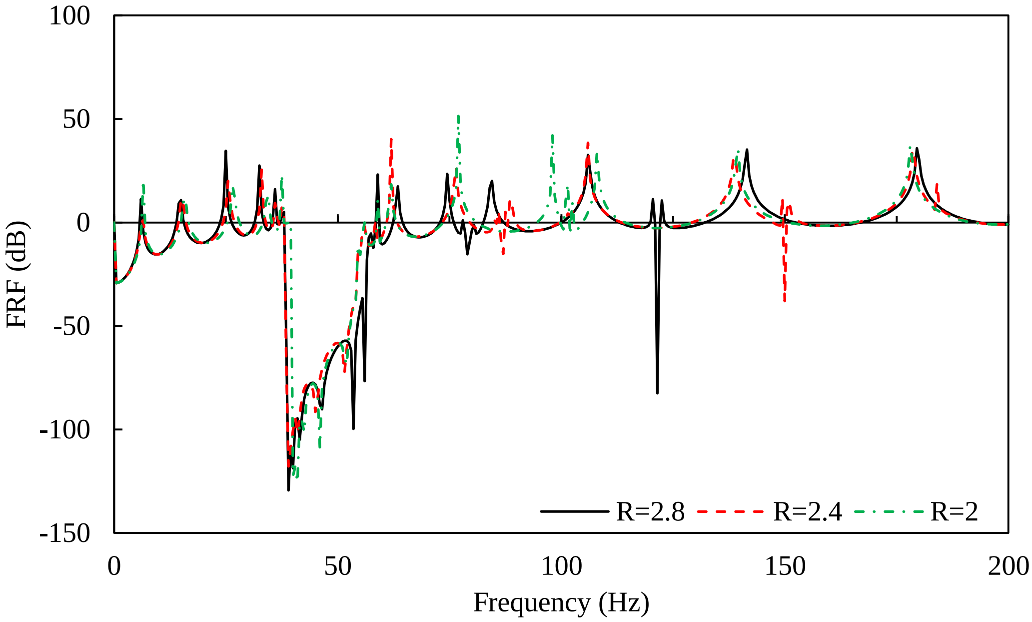
100
50
0
-50
-100
-150
FRF (dB)
0
50
100
150
200
Frequency (Hz)
R=2.8
R=2.4
R=2

(b)

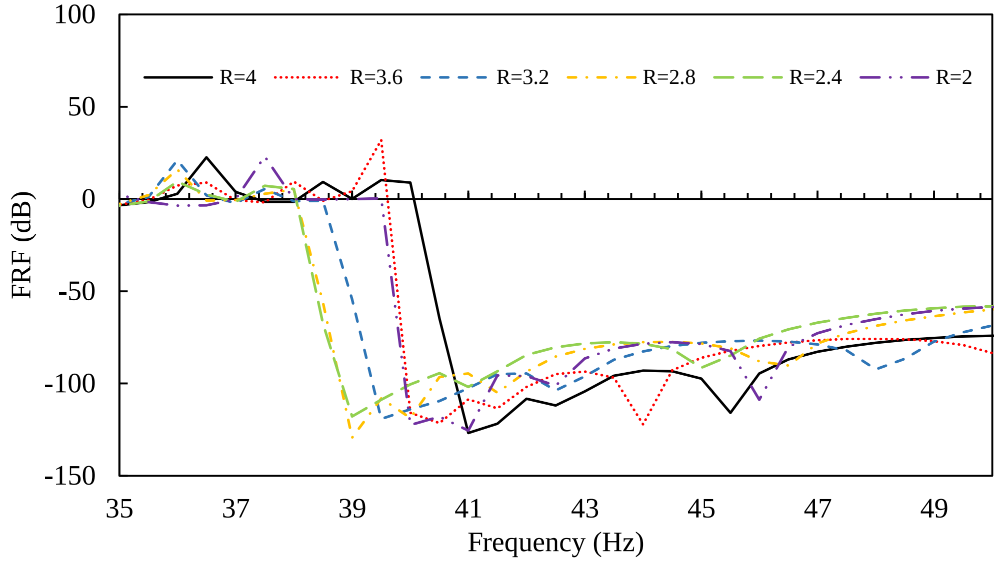

(c)

Figure 76. FRFs of finite structure of MemM with nested mass configuration when mass radius ratio is (a) 4.0, 3.6, 3.2 and (b) 2.8, 2.4 and 2.0; (c) FRFs around the first bandgap starting frequency region.

According to the figure, when the radius ratio is properly designed, two flexural bandgaps will be formed. The first bandgaps are broader than the second ones. The first bandgap widths are about 20.0 – 23.0Hz. The increase of the radius ratio has limited effect on the location of the first bandgap.

When the dimension ratio is decreased, the location of the first bandgap is moving to lower frequency region slightly and the second bandgap changed evidently. When *R* changed from 4.0 to 2.8, as shown in Figure 76, the location of the first bandgap shifts from 40.5Hz to 38.5Hz, and the location will fluctuate slightly when *R* continue decreasing. However the second bandgap increased from 86.5Hz to 122.0Hz. When R changed from Otherwise, as the radius of the ring mass block is reduced and the inner radius approaching the radius of the circular mass block, the second bandgap will gradually disappear because the two mass blocks are getting closer. The second bandgap disappeared when the ratio *R* decreased to 2. The relatively small radius will make the two mass blocks close to each other, and the membrane between the two mass is thus small. During vibration, the stretching of the membrane leads to the generate of force for suppressing the structural vibration. When the membrane area are too small, the force generated by the stretching membrane is small and not sufficient to suppress the vibration.

In order to illustrate the forming mechanism of bandgaps, Figure 77 presents the corresponding deformation of the finite structure when excitation signal's frequency is inside or outside of the bandgap regions.

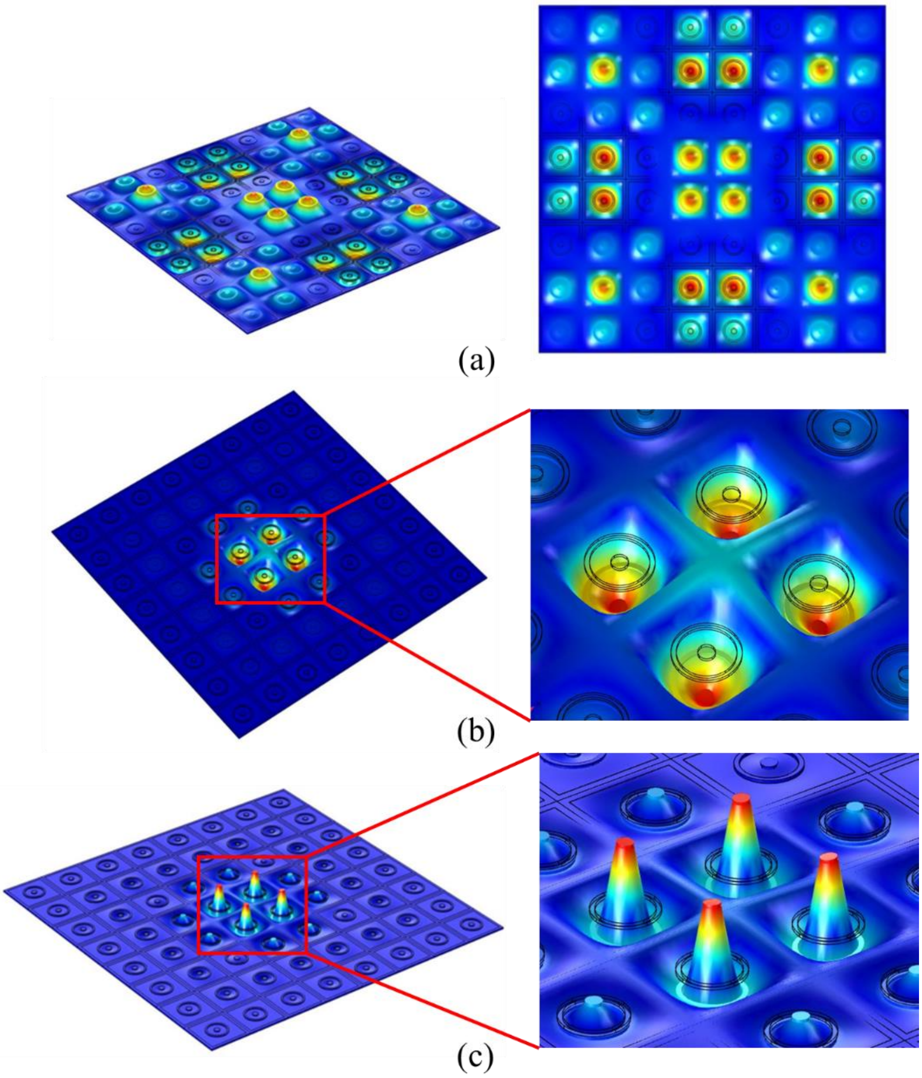

Figure 77. Deformation of the finite structure of MemM with nested mass configuration when the excitation signal's frequency is at the (a) outside of bandgap region (38.0Hz), (b) inside of the 1st bandgap region (45.0Hz) and (c) inside of the 2nd bandgap region (87.0Hz). The dimension ratio of the MemR is R=4.

Figure 77 (a) shows the deformation of the finite MemM structure when the excitation signal is in 38Hz, which is outside the bandgap region, and it is found that the wave is not contained within the MemRs and transmitted through the whole structure. If the excitation frequency is within the first bandgap region, the vibration is constrained at the MemRs that adjacent to the input point, and the elastic wave is not transmitted through. The MemRs are vibrating in the 1st resonant mode as indicated in Figure 65. In addition, when the excitation frequency is within the second bandgap region, the resonator will conduct vibration in the 7th resonant mode. So the two mass blocks are experiencing vibration in opposite direction. Such vibration characteristics results in the smaller second bandgap width because the two mass blocks are moving in opposite, and the stretching of membrane will generate forces in opposite directions. As a result, the output force from the MemR used for suppressing vibration is reduced and thus, the width of the second bandgap is much smaller than the first one.

4.4 Bilayer MemM Attached to A Thin Plate Structure

The existence of bandgap of the proposed MemM are verified in the previous section. However, similar to the EM introduced in **Chapter 3**, the band structure and vibration absorption performance of the MemM when applied to a thin plate structure may be different.

As introduced in **Chapter 2**, PWE method is modified and applied to obtain the band structure of MemM attached to a thin plate. In previous research works, the PWE method was not adopted for the bandgap property study of a MemM, thus the PWE method did not include the membrane tensile stress as an independent variable. In this study, modification of the PWE method is conducted and it is able to predict the bandgap property of a MemM attached on a thin plate for the purpose of structural vibration control. Compared with using the FEA software in Section 4.2, calculation of band structures through the PWE method is more convenient and time-saving.

In this section, the band structure and vibration control performance of the bilayer MemM applied on a thin plate is investigated. The band structures of the bilayer MemM under different design parameters are obtained through the modified PWE method, and finite structure of bilayer MemM are constructed for FEA to examine the accuracy of the analytical method.

4.4.1 Band structure of bilayer MemM

Stacking of the single layer MemM can allow the existence of multiple bandgaps simultaneously while the occupied area of the MemM does not increased. In this section, the band structure of the bilayer MemM formed by stacking one layer of MemM to another one is investigated through the proposed model introduced in **Chapter 2**.

As mentioned in section 2.3.2, the modified PWE method can also be used to study the band structure of the bilayer MemM. Consider bilayer membrane-type resonators that are attached to a thin plate, forming periodic unit cells. The bilayer membrane-type resonators are considered as two separate spring-mass resonators. The attached masses are denoted as m_{R1} and m_{R2}, whilst the effective stiffness are denoted as k_{R1} and k_{R2}, respectively. k is the stiffness of the plate. The section of a primary plate structure that the membrane-type resonator attached to is considered as the target mass m_1. Assuming the plate is under excitation of a harmonic force with amplitude F and frequency ω, the governing equation of motion of the system can be described as:

$$\begin{bmatrix} m_1 & 0 & 0 \\ 0 & m_{R1} & 0 \\ 0 & 0 & m_{R2} \end{bmatrix} \begin{Bmatrix} \ddot{w}_1 \\ \ddot{w}_2 \\ \ddot{w}_3 \end{Bmatrix} + \begin{bmatrix} k + k_{R1} + k_{R2} & -k_{R1} & -k_{R2} \\ -k_{R1} & k_{R1} & 0 \\ -k_{R2} & 0 & k_{R2} \end{bmatrix} \begin{Bmatrix} w_1 \\ w_2 \\ w_3 \end{Bmatrix} = \begin{Bmatrix} F \\ 0 \\ 0 \end{Bmatrix} \qquad (4\text{-}3)$$

where m_1 is the mass of the plate's section; w_1, w_2 and w_3 are the transverse displacements of the plate and resonators, respectively; and $\ddot{w}_1$, $\ddot{w}_2$ and $\ddot{w}_3$ are the respective accelerations of the plate and resonator.

To demonstrate the relationship between the resonant frequency and bandgap location, a particular case study is undertaken. Define the masses attached to both membranes as $m_{R1} = m_{R2} = 2g$, and the stresses applied to the upper and lower membrane layer as $0.6MPa$ and $0.8MPa$, respectively. For $a = 60mm$ and plate thickness of $h = 2mm$, the mass of the bottom aluminium plate area is $m_1 = 19.4g$. The respective effective stiffness of the two resonators can be obtained as $k_{R1} = 217.4N/m$ and $k_{R2} = 290.6N/m$.

Assume the resonant frequencies of the two resonators m_{R1} and m_{R2} are ω_{n1} and ω_{n2} ($\omega_{n1} < \omega_{n2}$), respectively. According to equation (4-3), the displacements of resonators can be described as:

$$\begin{cases} w_2 = \dfrac{1}{1-\left(\dfrac{\omega}{\omega_{n1}}\right)^2} w_1 \\ w_3 = \dfrac{1}{1-\left(\dfrac{\omega}{\omega_{n2}}\right)^2} w_1 \end{cases} \tag{4-4}$$

As given in equation (4-4), the ratio of excitation frequency and resonant frequency determines the relative displacement of resonators. When the excitation frequency ω is smaller than ω_{n1}, both displacements are positive so both resonator masses are mainly moving in-phase or the phase angle difference is smaller than 90° with m_1. Therefore, in this frequency region, the resonators tend to increase vibration of the primary mass rather than suppressing it.

When incident frequency ω is in the region of $[\omega_{n1}, \omega_{n2})$, resonator attached with m_{R1} will experience out-of-phase vibration with m_1 or the phase angle difference with m_1 is larger than 90°. However, m_{R2} is experiencing in-phase vibration with m_1 or the phase angle difference is smaller than 90°, thus the vibration reduction effect of m_{R1} is weakened. When $\omega_{n2} < \omega$, both resonators are vibrating in opposite direction to m_1 and when damping is applied, the phase angle difference will be larger than 90° for both resonators, so the vibration absorption performance of m_{R2} will be reinforced by m_{R1}. Such enhancement leads to extension of m_{R2}'s corresponding bandgap width.

Based on the developed model, an investigation on the bandgap property of an infinite membrane-type metamaterial structure is conducted. The parameters used in the example are similar to those used in the effective mass calculation. Figure 78 shows that there are two clear full bandgaps at: (1) 52.5 – 54.3Hz; (2) 60.7 – 64.5Hz. The location of these bandgaps are the same as the frequency region of negative effective mass. These two bandgaps are contributed by the fundamental resonant of the two membrane resonators. When the incident wave's frequency lies within one of the bandgaps, the corresponding resonance of the resonator will be excited, leading to the attenuation of the propagated wave [98].

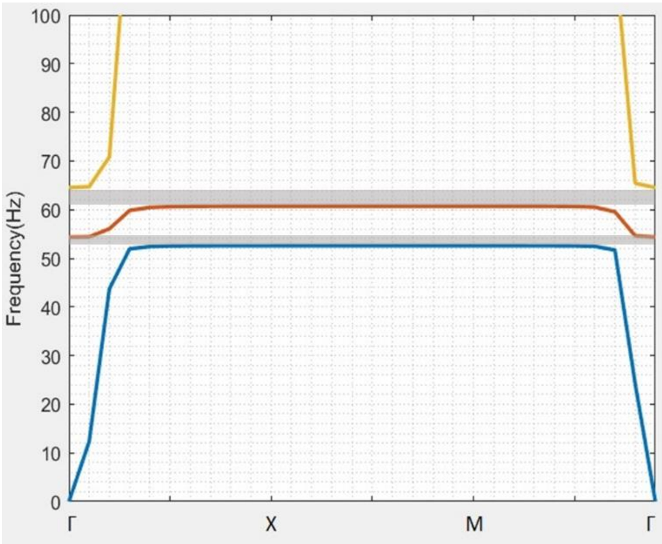

Figure 78. The bandgap structure of a bilayer membrane-type metamaterial with membranes' tensile stresses of 0.6MPa and 0.8MPa, respectively. Two full bandgaps (shaded areas) exist at 52.5 – 54.3Hz and 60.7 – 64.5Hz.

As shown in the figure, the red curve separates the two full bandgaps, which is associated with the resonant frequency of the resonator with the higher membrane tensile stress at 0.8MPa. By applying different membrane tensile stress in the two resonators, a bilayer membrane-type metamaterial can thus be utilized to control structural vibration in two separated frequency ranges, albeit in relatively narrow operation frequency regions.

4.4.1.1 Effect of mass magnitude on bilayer MemM

Figure 79(a) presents the change in the bandgap width and location for a bilayer metamaterial when the magnitudes of both masses m_{R1} and m_{R2} are simultaneously varied from 2.0g to 60.0g.

Figure 79 (b) shows the bandgap as the magnitudes of the attached masses are varied. As the bilayer membrane-type resonators are composed by two single-layer resonators, the bandgap structures of the single layer metamaterials are also depicted in Figure 79 (c) and Figure 79(d) for comparison.

For clarity, the layer of membrane applied with lower tensile stress is denoted as the resonator m_{R1} and the other is denoted as the resonator m_{R2}.

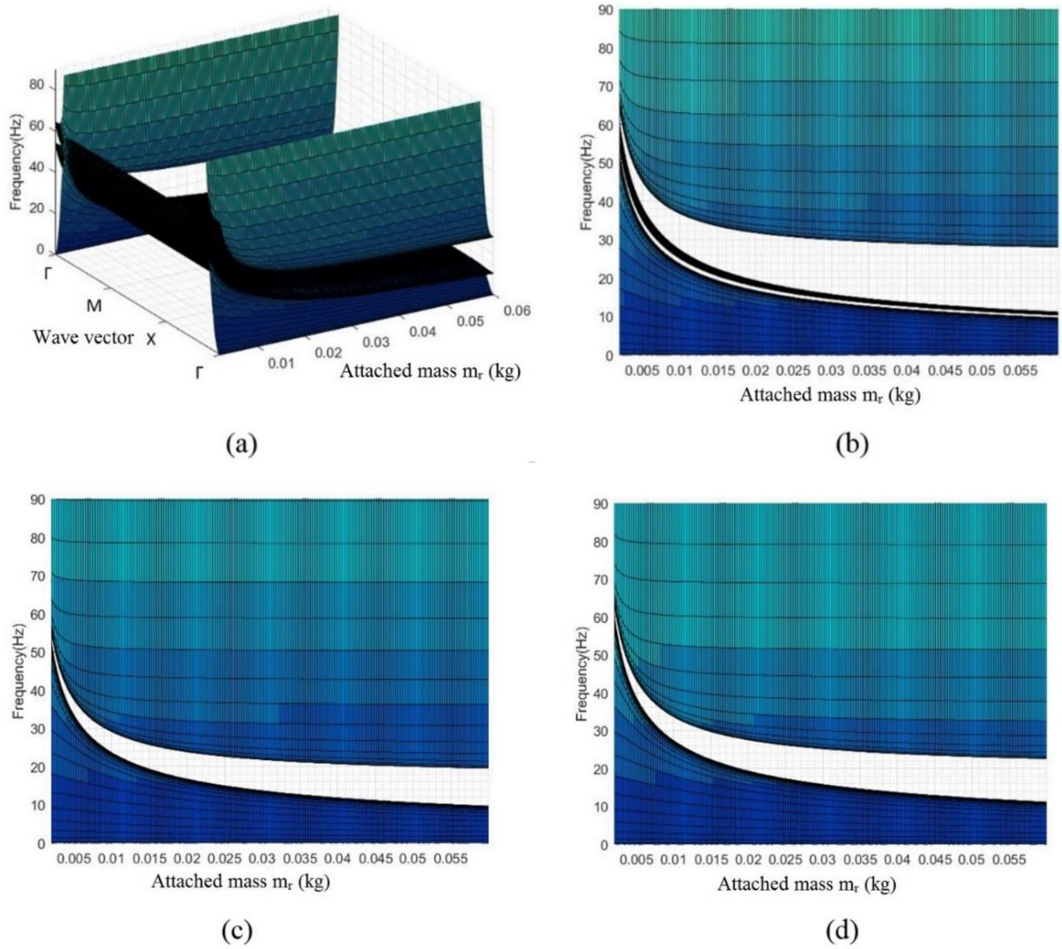

Figure 79. (a) The band structures of the bilayer metamaterial attached with different mass platelets and (b) the band structures of different mass magnitudes; (c) change of bandgap width of single-layer metamaterial applied with 0.6MPa and (d) 0.8MPa.

According to the figure, when the mass magnitude is increased from 2.0g to 60.0g, the bandgap width of m_{R1} is enlarged from 2.6Hz to 9.8Hz, whilst the bandgap of m_{R2} is also enlarged from 3.1Hz to 11.4Hz.

For the bilayer resonator, the first bandgap's lower edge shifts from 52.6Hz to 9.7Hz, and the second bandgap location shifts from 60.7Hz to 11.2Hz. The width of the first bandgap, which is associated to m_{R1}, decreased from 1.7Hz to 0.65Hz. When the mass is increased to 60g, the first bandgap width of bilayer resonator is 93.4% smaller than the corresponding bandgap width of single layer resonator with the same mass. Meanwhile, the width of the second bandgap increased from 3.8Hz to 16.8Hz, which is about 47.4% larger than the single layer resonator.

Therefore, the bandgap behaviour of bilayer membrane-type resonator is not a simple combination of two independent single layer resonators. In a single layer resonator, the increase of attached mass magnitude will effectively amplify the bandgap width. In a bilayer resonator, however, for fixed membrane stress, the increase of mass magnitude will cause reduction of the first bandgap width and the increase of the second bandgap width.

As elucidated in section 2.2, if the excitation frequency is within m_{R1}'s bandgap range, the counteracting force is partially eliminated by resonator m_{R2}. Thus, m_{R1}'s vibration absorption performance is weakened, leading to the narrowing of the first bandgap. On the other hand, if the excitation frequency is within the second bandgap, the absorption capability of resonator m_{R2} will be reinforced by the resonator m_{R1} and the second bandgap is therefore broadened. Naify et al. [142] demonstrated that the increase of mass loaded on membrane can broaden the frequency bandwidth for sound isolation applications. A similar effect is also found in structural vibration applications as discussed in this work.

4.4.1.2 Effect of tensile stress on bilayer MemM

Figure 80 exhibits the change of bandgaps caused by the tuning of the tensile stress applied to the membranes. Here, 2.0g and 4.0g mass platelets are attached to the upper and lower layer of membranes respectively. The tuning range of the applied stress on membranes is from 0.4MPa to 12MPa, with the results shown in Figure 80. As the magnitudes of attached masses are kept constant, the increased tensile stress will lead to higher equivalent stiffness and therefore the bandgap location will shift to higher frequency. In the bilayer resonator, the first bandgap's starting edge changes from 30.5Hz to 166.7Hz, while the second bandgap's starting edge increases from 42.9Hz to 234.7Hz.

In a bilayer resonator, the first bandgap is produced by the membrane layer with heavier mass (4g). According to the figure, it can be observed that the increase of tensile stress can enlarge the bandgaps. As shown in Figure 80(c) and (d), when the stress is increased to 12MPa, the bandgap width of the single layer resonator attached with 2g mass rises from 2.2Hz to 12.1Hz. In addition, the other single layer resonator's bandgap width rises from 3.0Hz to 16.6Hz. Meanwhile, in the bilayer case, the first bandgap width increases from 2.6Hz to 14.3Hz and the second changes from 2.4Hz to 13.5Hz, respectively. Similar to the results in Section 2.4.1, when the tensile stress is 12MPa, the first bandgap is 18.7% smaller than the corresponding single layer resonator's bandgap width. In contrast, when the tensile stress is 12MPa, the second bandgap is 18.2% larger than the 0.4MPa case. The results indicate that the design parameters can be optimised to avoid weakening of the first bandgap.

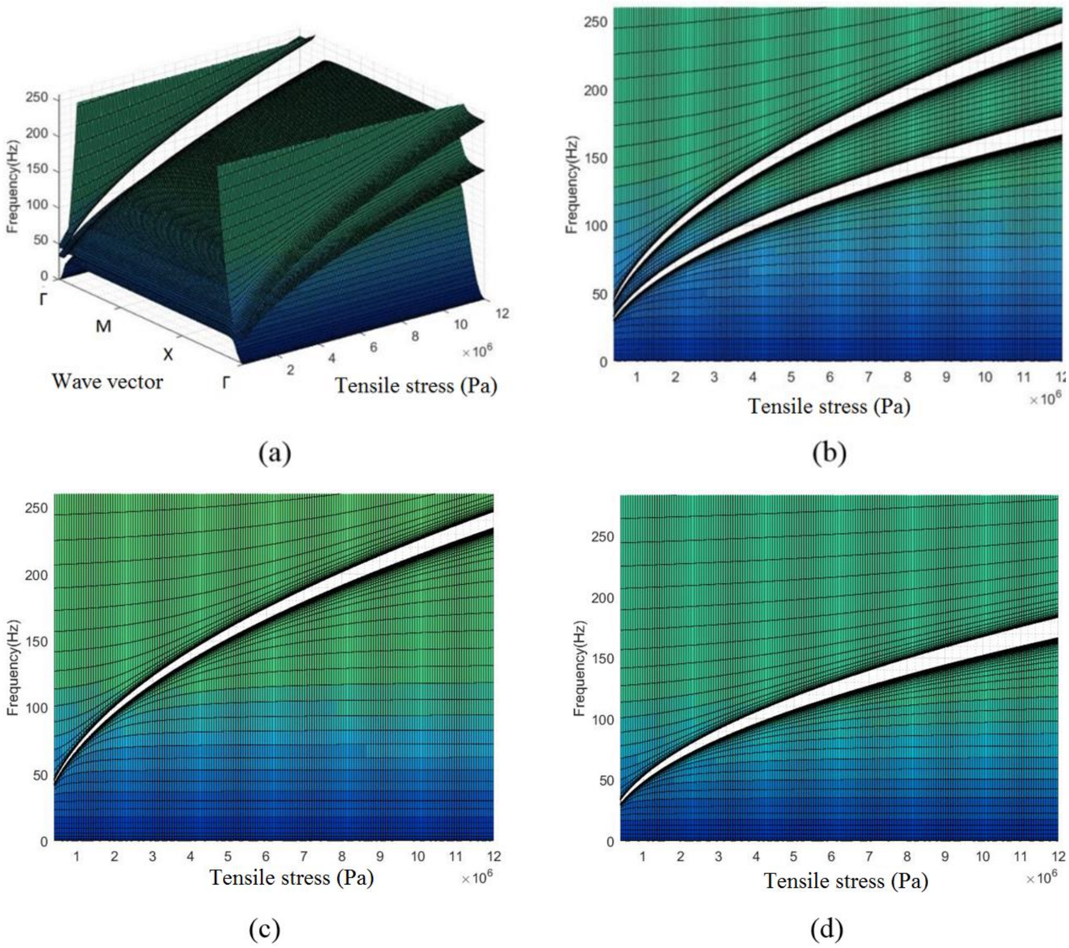

Figure 80. (a) The band structures of the bilayer metamaterial attached with 2.0g and 4.0g mass; (b) bilayer metamaterial's bandgaps vary with tensile stress applied to membrane; bandgap of single layer metamaterial attached with (c) 2.0g mass and (d) 4.0g mass with varying tensile stress.

4.4.1.3 Effect of periodicity of bilayer MemM

The periodicity of membrane-type metamaterial is defined as the distance between the adjacent membrane-type resonators attached to the plate. The periodicity may be different in accordance to the application requirement. To control a relatively strong vibration, the number of resonators on the plate area is required. On the other hand, in situations that have strict limitation on extra weight, the number of resonators should be as small as possible. In this section, the effect of periodicity of bilayer membrane-type metamaterial is investigated. The range of resonator's periodicity is varied from 0.05m to 0.195m, with a 0.05m resolution. The tensile stresses of the two membrane-type resonators are respectively defined as 2MPa and 4MPa, whilst the attached mass are 10g and 5g respectively.

As shown in Figure 81, the starting frequency of bandgap is maintained because the periodicity adjustment is not affected by the resonator's resonant frequency. Otherwise, the increase of the metamaterial's periodicity will significantly decrease the bandgap width. When the periodicity is increased, the bandgap width will decrease because the number of resonators is smaller, leading to a lower vibration absorption capacity. Theoretically, when the lattice constant is approaching infinity, it describes an infinite size plate with only one resonator attached so the bandgap will finally disappear.

In practice, the bandgap will disappear when the lattice constant increases to a certain value. Figure 81(b) presents the bandgap change of the same bilayer resonator when the periodicity is adjusted from 0.05m to 0.4m. It is observed that the second bandgap, which is associated with a resonator with smaller mass, disappears when the periodicity is larger than 0.21m. In addition, the first bandgap disappears at about 0.34m.

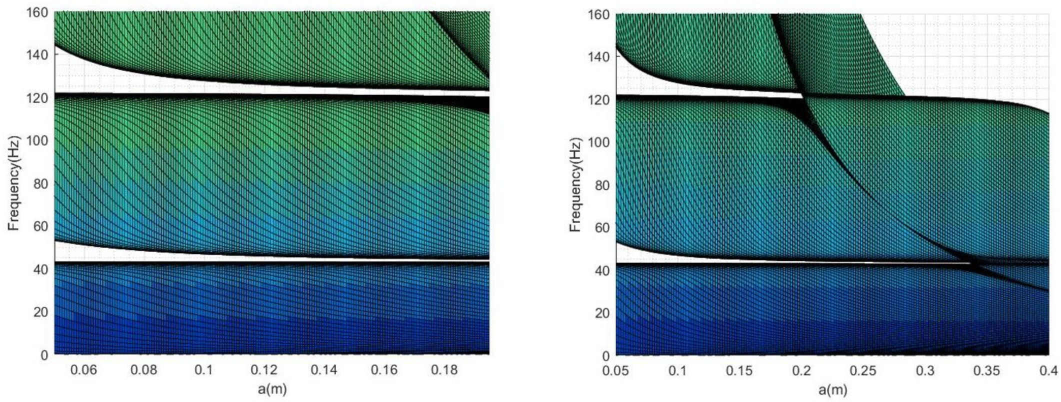

(a) (b)

Figure 81. The change of bandgap when the periodicity of attached resonators, a, is tuned from 0.05m to (a) 0.195m; (b) 0.4m.

On the other hand, the magnitudes of attached masses are also closely related to the vibration absorption performance. To demonstrate the effect of attached mass and periodicity on bandgap property, three configurations are taken for comparison. In these cases, the periodicities are set as 60mm, 120mm and 240mm, respectively. In addition, the masses on both membranes are adjusted as 2.0g, 8.0g and 32.0g correspondingly to ensure the total attached mass is the same in three cases. In the meantime, the stress is accordingly adjusted as well to maintain similar resonant frequencies.

Figure 82 presents the bandgap location and widths of these cases. According to the results, both the first and second bandgaps' widths are broadened when the periodicity, attached mass and the applied stress are simultaneously increased. In a unit area, the total attached mass of the resonator is the same, yet the one with larger mass and higher tensile stress will reveal larger bandgap if compared with the counterparts. It demonstrates that for the purpose of forming a broader bandgap, the membrane-type resonator's tensile stress and mass should be designed as high as possible. However, it is also worth noticed that the high periodicity will cause high concentration of mass on the primary structure. Such characteristic may lead to shifting of system's centre of gravity or stability. Therefore, periodicity should be chosen carefully in accordance to the application conditions.

Detailed data of bandgap locations and widths are given in Table 10.

Based on this characteristics of the bilayer MemM, a good compromise is needed to solve the contradiction between resonator number and vibration performance.

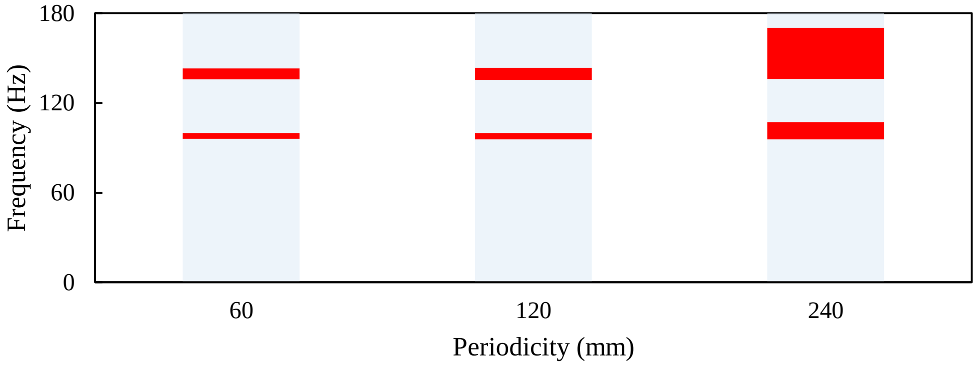

Figure 82. The bandgap location and width for 3 different periodicities. The red areas indicate the bandgap region.

Table 10. Data of bandgap location and width for 3 different periodicities.

	Periodicity		
Frequency (Hz)	60mm	120mm	240mm
Lower edge 1	95.97	95.56	95.56
Upper edge 1	99.95	99.87	107.05
Band width 1	3.98	4.31	11.49
Lower edge 2	135.69	135.36	135.97
Upper edge 2	143.16	143.58	170.21
Band width 2	7.47	8.22	34.24

4.4.2 Parametric analysis for bandgap property and optimisation

The bilayer membrane-type resonator can be optimised by tuning the combination of design parameters. In this section, the total bandgap widths of the bilayer resonator with different mass and tensile stress settings are studied in comparison to those of single layer resonators' bandgap widths.

The mass and tensile stress of the lower layer membrane are respectively defined as: m_{R1}=4.0g and T_1=1MPa. The mass of the upper layer is changed from 0.8g to 8g and tensile stress is changed from 2MPa to 12.5MPa. Figure 83(a) presents the first bandgap width difference when the mass ratio and tensile stress ratio are adjusted. The differences of bandgap width between bilayer and single layer resonators are calculated and plotted against the mass ratio (m_{R2}/m_{R1}) and the tensile stress ratio (T_2/T_1). A negative value of the bandgap width difference indicates the bilayer bandgap width that is smaller than the corresponding single layer resonator's bandgap width.

As previously mentioned, the first bandgap width is suppressed in a bilayer membrane-type resonator. According to Figure 83(b), the increase of mass ratio will further suppress the first bandgap width. When the tensile stress ratio is relatively small, the increase of mass ratio will lead to rapid decrease of the first bandgap width although the effect is weakened if the tensile stress ratio is higher.

Otherwise, according to Figure 83(c), when the mass ratio is small, the change of tensile stress ratio has no significant effect on the bandgap width. On the contrary, when the mass ratio is relatively large and the tensile stress ratio is increased, the bandgap width difference will first decrease rapidly before stabilizing. Thus if the mass ratio is large, higher tensile stress ratio is recommended in order to reduce the bandgap difference of the first bandgap.

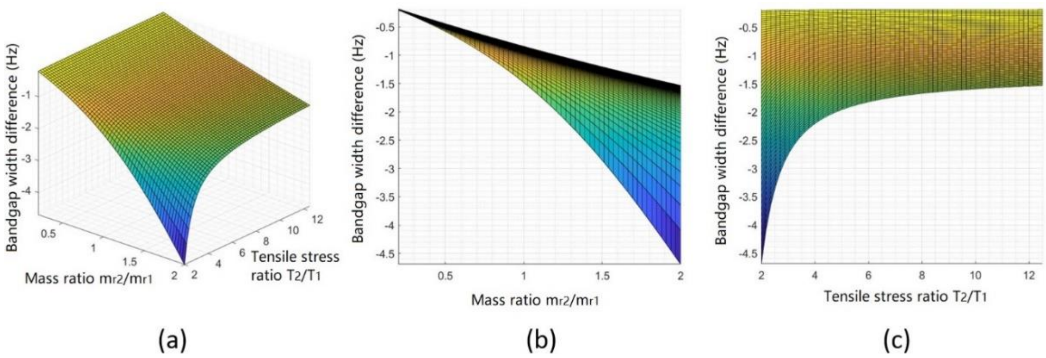

Figure 83. (a) The lower bound bandgap width difference between bilayer and corresponding single layer resonators; (b) bandgap width difference vs. mass ratio; (c) bandgap width difference vs. tensile stress ratio.

Figure 84 presents the change of the second bandgap width. As shown in Figure 84(b), in contrast to the first bandgap, the increase of mass ratio will enlarge the second bandgap width of the bilayer resonator, whose effect is stronger particularly when the tensile stress ratio is lower. In addition, according to Figure 84(c), when the mass ratio is relatively low, the change of tensile stress ratio has no effect on the bandgap width difference. However, when the mass ratio is relatively high, the increase of tensile stress ratio will weaken the second bandgap. Therefore, for the purpose of widening the higher bandgap, the mass ratio should be adjusted to higher value whilst the tensile stress ratio being kept as low as possible.

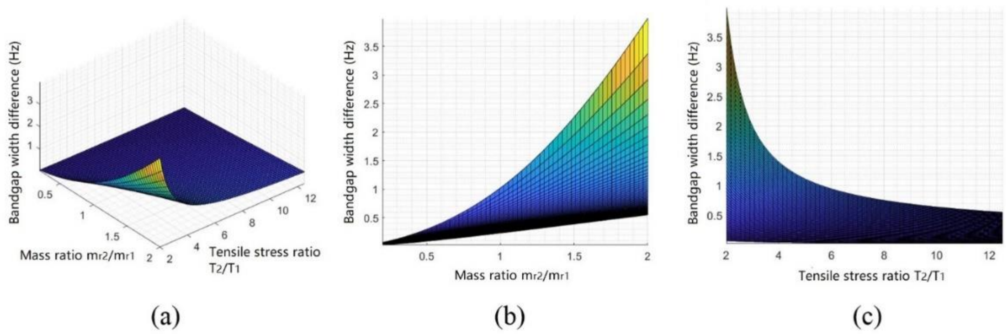

Figure 84. (a) The upper bound bandgap's width difference between bilayer and corresponding single layer resonators; (b) bandgap width difference vs. mass ratio; (c) bandgap width difference vs. tensile stress ratio.

Figure 85 reveals that the total bandgap width of the bilayer resonator is slightly smaller than the sum of bandgap widths of two single layer resonators. Figure 85(b) illustrates that the increase of mass ratio will enlarge the bandgap width difference. In addition, when the tensile stress ratio is higher, level of the reduction of the bilayer resonator's total bandgap width will be larger under the same amount of mass ratio increase.

Otherwise, in accordance to Figure 85(c), the bandgap width will only change with tensile stress ratio when the mass ratio is relatively large. The higher tensile stress ratio will make the total bandgap width of bilayer resonator even smaller.

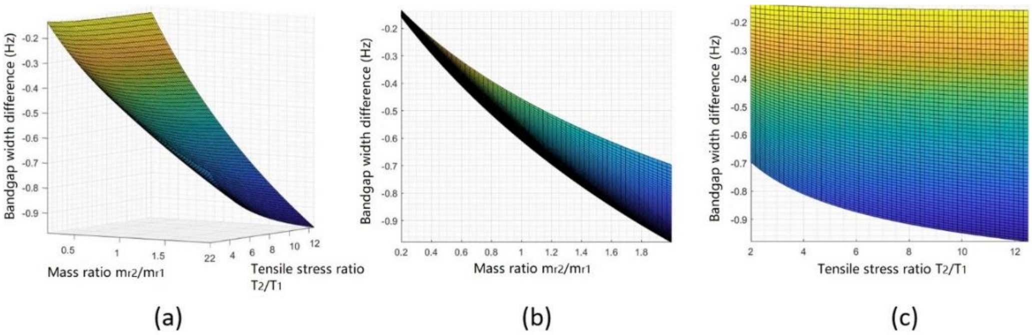

Figure 85. (a) The total bandgap width difference between bilayer and corresponding single layer resonators; (b) bandgap width difference vs. mass ratio; (c) bandgap width difference vs. tensile stress ratio.

The results provide important design guidelines for the bilayer membrane-type metamaterial. The total bandgap width of bilayer resonator is only slightly smaller (less than 1Hz) than the sum of two single layer resonators. To maintain the first bandgap width of the bilayer membrane-type metamaterial, a small mass ratio should be used, and the location of bandgap can be tuned by adjusting the tensile stress ratio. By adopting this design parameter combination, the bilayer membrane-type metamaterial's total bandgap width is only slightly suppressed.

However, the second bandgap can be widened by adopting a large mass ratio and a low tensile stress ratio. Such characteristics allow the bilayer resonator possesses more agile bandgap tuning capability whilst still keeping the same total bandgap width. Moreover, compromise is needed when choosing different design parameters. The utilisation of bilayer resonators also only requires smaller area than the combined utilisation of two single membrane-type resonators. As a result, the bilayer one can have better application potential and more agile tuning capability.

4.4.3 Vibration absorption performance of bilayer MemM

To examine the bandgap property of bilayer MemM attached to a thin plate, a 240×600mm aluminium plate with attached bilayer MemM is constructed and shown in Figure 86. Otherwise, in order to simulate the real condition, 10% damping is incorporated to the imaginary part of modulus. The left edge of the plate is applied with fixed boundary condition, while the excitation input is applied at the right edge of the structure and pre-stress conditions are applied to the membranes.

The thin plate's vibration response is detected as the acceleration signal, and it is measured at point A, while the input acceleration signal is measured from the edge at which the excitation input is applied. The upper layer membrane is applied with 0.6 MPa stress, whilst the lower level membrane is applied with 0.8 MPa stress. Each of membrane has a rigid mass block of 2.0g at its centre.

Figure 87 shows the thin plate's FRF when the incident excitation frequency is scanned from 30Hz to 90Hz.

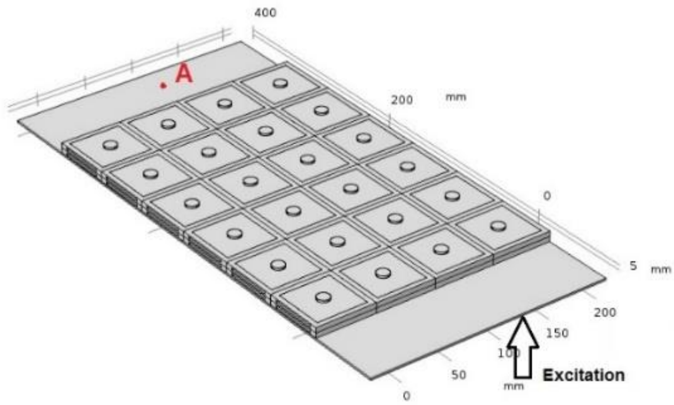

Figure 86. The finite structure of a 4×6 units of bilayer membrane-type resonators attached to an aluminium plate.

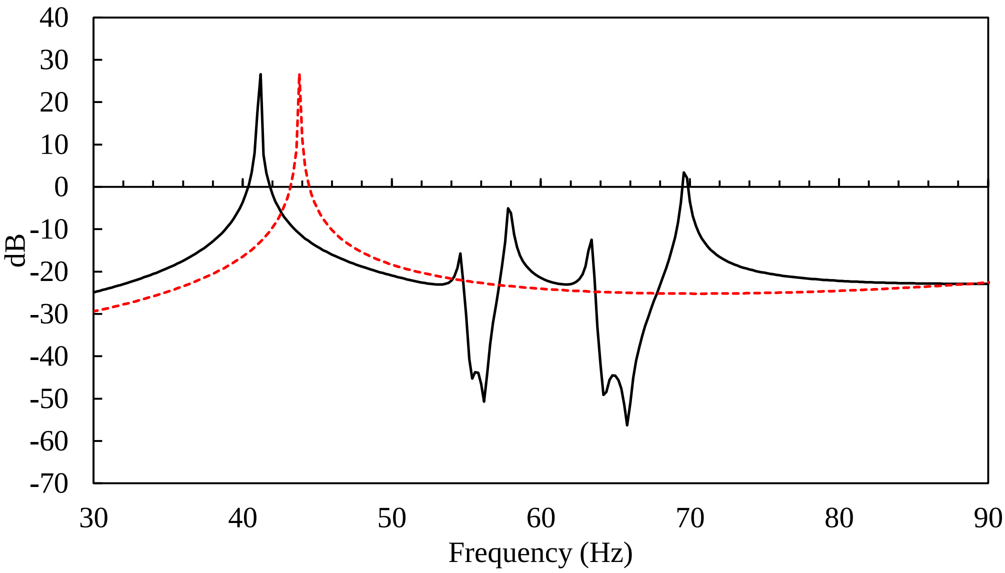

Figure 87. Frequency responses of the bare plate (dashed black) and the plate attached with the bilayer membrane-type metamaterial (solid red).

The results show that the plate's fundamental resonance has been shifted to a lower frequency when bilayer membrane-type metamaterial is attached, because the additional mass that metamaterial contributed to the plate. In addition, there are two bandgaps that appear at frequency ranges of 54.4Hz – 57.2Hz and 63.2Hz – 67.6Hz. For the analytical model, the obtained bandgaps are located at: 52.5-54.3Hz and 60.7-64.5Hz. So the analytical model indicates slightly lower bandgap locations than the FEA results. Differences in boundary condition settings contribute to differences in the results. In the PWE model, the infinite periodic boundary conditions are used, in contrast to fixed boundary condition used for the finite structure model, contributing to higher structural stiffness for the finite structure. However, despite the small differences in bandgap prediction, the bandgap location and width estimation provided from the modified PWE model is consistent with the numerical simulation results, demonstrating the effectiveness of the model.

It should be noted the frequency response in bandgap region has an asymmetrical shape. This is due to Fano interference effect that is generated by the periodically allocated resonators [143]. The travelling waves and scattering of the resonant modes of the periodic unit cells will cause the asymmetric dispersion curve. Otherwise, the resonant frequencies of the bare plate are higher than the one attached with membrane-type resonators, because the attached metamaterial increased the system mass.

The deformation of the plate at different frequencies are shown in Figure 88. When the incident wave frequency is within the first bandgap range, the first resonant mode of unit cell will be excited and significant amount of wave energy will be absorbed and stored within the unit cells. In contrast, when the incident wave frequency is outside the bandgap range, the resonators movement will be mainly in phase with the plate, allowing the wave to propagate through the plate. Figure 88(c) presents the two vibration modes that generate bandgaps of the bilayer resonator.

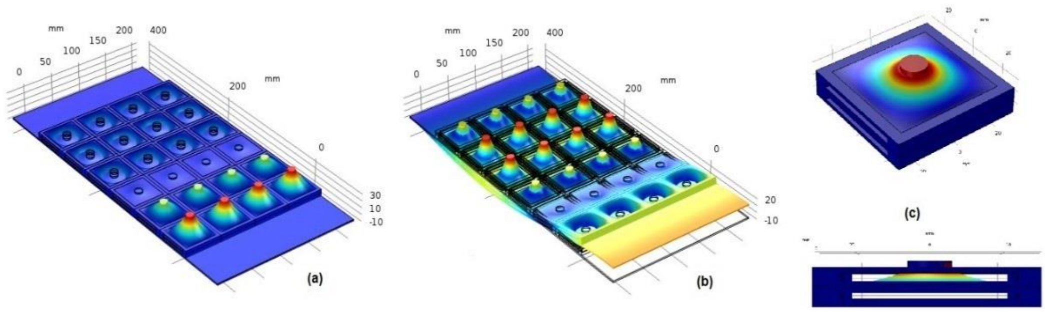

Figure 88. The deformation of the structure when incident wave frequency is: (a) within bandgap and (b) outside bandgap; (c) the first and second vibration mode shapes of the bilayer membrane-type resonators. The attached mass magnitude is 2g.

To further verify the accuracy of the proposed theoretical model, two other cases are used. Case 1 defines $T_1 = T_2 = 2$MPa and attached mass $m_{R1} = 2.0$g and $m_{R2} = 5.0$g, respectively. Case 2 defines $T_1 = 2$MPa and $m_{R1} = 2.0$g, whilst $T_2 = 4$MPa and $m_{R2} = 5.0$g.The setting and the corresponding bandgaps obtained through the proposed method and simulation are both presented in Table 11, while the frequency responses are shown in Figure 89.

It is observed that the locations of bandgaps estimated by the proposed method are slightly different with the simulation results but the deviation is within a reasonable range as discussed earlier. In both examples, the second bandgaps, which start from 96.0Hz, are associated by the resonator with mass m_{R1}. As shown by the results, the second bandgap width will extend when the tensile stress ratio is increased and such results are consistent with the prediction described in section 4.4.2.

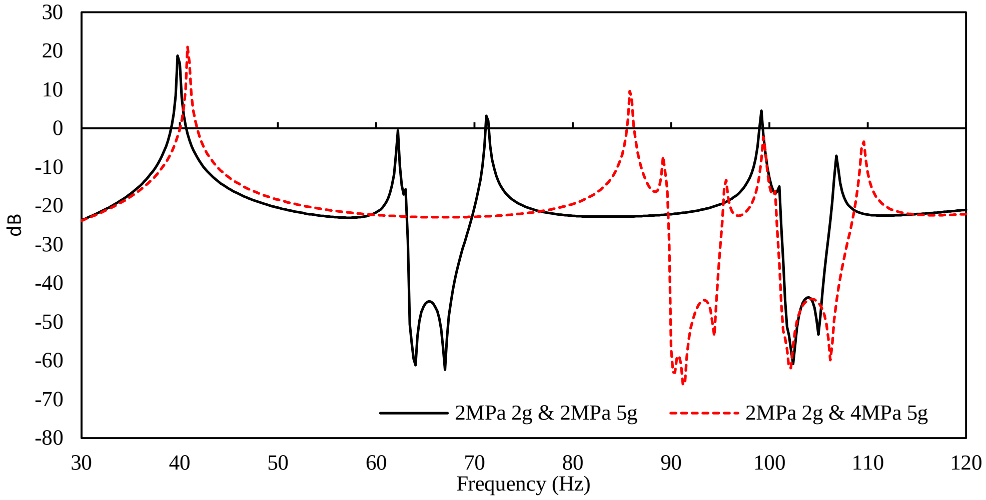

Figure 89. The frequency responses of the plate attached with bilayer membrane-type resonators with different stress and mass magnitudes.

Table 11: The bandgap property of bilayer membrane-type metamaterial predicted by the modified PWE method and simulation.

		Membrane 1	**Membrane 2**	**Membrane 1**	**Membrane 2**
Setting	Stress (MPa)	2.0	2.0	2.0	4.0
	Mass (g)	2.0	5.0	2.0	5.0
		Modified PWE	**Simulation**	**Modified PWE**	**Simulation**
Bandgap 1	Lower edge (Hz)	61.0	62.0	86.3	89.2
	Upper edge (Hz)	67.2	68.0	91.4	94.0
	Width (Hz)	**6.2**	**6.0**	**5.1**	**4.8**
Bandgap 2	Lower edge (Hz)	96.0	101.0	96.0	99.8
	Upper edge (Hz)	101.6	104.0	105.7	106.8
	Width (Hz)	**5.6**	**3.0**	**9.7**	**7.0**

4.5 Experiment on MemM

4.5.1 Experiment setup, equipment and sample assembly

In order to manually produce the MemR samples, a membrane stretching mechanism is designed and manufactured in advance. The structure of the mechanism is shown in Figure 90.

The stretching mechanism is designed with an octagonal shape outer frame. A clamp connected by a screw rod is mounted on each side of the frame. The clamps can be tightened by the screws and thus fixed the membrane within the frame. A force sensor is connected with one of the screw rods to detect the force applied on the membrane. The sensor is connected with a display screen to show the current force value. Screw nuts are used to fix the screw rods on the frame, and the location of the clamps can be adjusted through rotating of the screw nuts, consequently, the tensile force applied to the membrane can be tuned accurately.

When assembling a relatively small MemR, one can use only 4 clamps to simplify the process and for a larger MemR, all clamps can be used to ensure the stretching force is applied evenly.

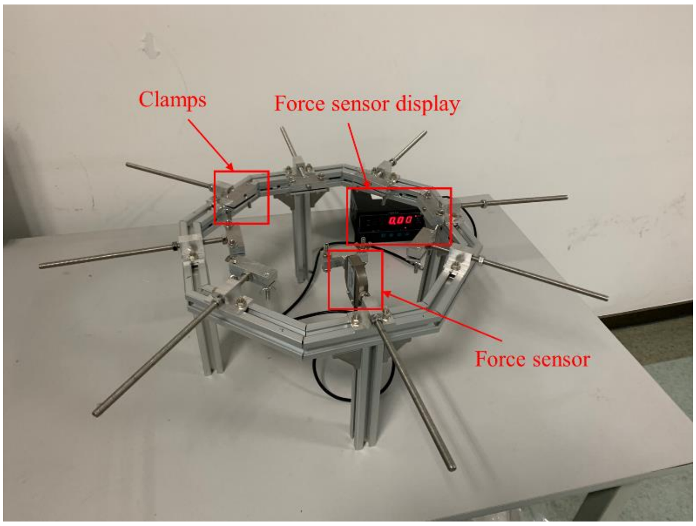

Figure 90. A photo image of the membrane stretching mechanism.

The frames of the MemRs are manufactured through 3D printing. The frame is exactly the same as the one used in the numerical simulation, including the material properties. The membrane is silicone rubber sheet purchased from supplier. The material properties are measure through DMA testing as mentioned before.

The assembling process of a MemR is presented in Figure 91. The membrane is first tailored into required shape and dimension and fixed on the stretching mechanism. Through tuning the screw nuts, the tensile force applied on the membrane can be adjusted to the desired level. After the force on the membrane is stable, the frame can be glued onto the membrane. In this step, it is important to keep the pressure on the frame until the glue is dried for the purpose of maintaining the tensile stress within the membrane. The membrane can then be taken out from the stretching mechanism, and cut off the extra parts of the membrane.

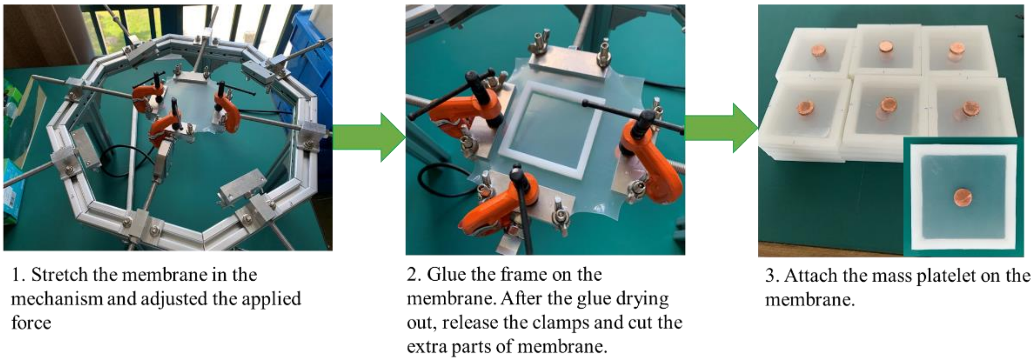

Figure 91. Assembling process of a membrane-type resonator by using the designed stretching mechanism.

After fixing the membrane on the frame, the copper mass platelet can then be glued at the middle of the membrane. The location of the membrane's middle point should be marked beforehand to ensure the accuracy of assembly. Since the MemR is manually manufactured, the error of the mass location and membrane tensile stress will lead to the shifting of MemRs' resonant frequencies. The manufactured MemRs are then glued on a thin aluminium plate for experimental testing.

The experimental setup is shown in Figure 92. The test rig is put on an optical isolation platform to avoid the external vibration disturbance. The metamaterial structure is clamped on the right side, and the left side is fixed by a clamp that connected with a shaker. The incident excitation signal is detected by the accelerometer attached on the shaker clamp, and the vibration response signal of the plate structure is detected by the accelerometer attached on the other side. Sinusoidal excitation signal is generated from the signal generator and sent to an amplifier that connected with the shaker. Data analyser is connected with the signal generator and the two accelerometers. The equipment are the same as those used in **Chapter 3**.

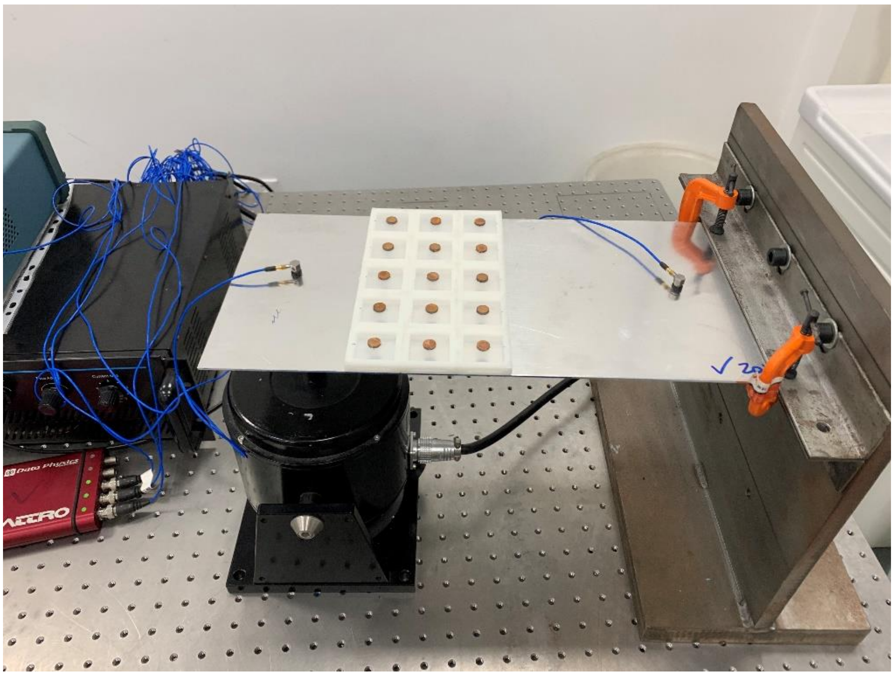

Figure 92. A photo image of the experimental setup for MemM.

4.5.2 Results and discussion

To reveal the effect of attached MemM, the vibration response of an aluminium thin plate ($200 \times 450 \times 2$mm) is tested first. Similar to the numerical simulation setting, one short edge of the plate is clamped and the other side is fixed onto the shaker, as shown in Figure 92. Sinusoidal excitation is used and the excitation frequency is scanned from 0Hz to 600Hz. The vibration transmissibility curve of the bare plate is obtained and presented in Figure 93.

As shown in the figure, there is a resonant peak in 104Hz in the bare plate. The resonant frequency of the MemR is therefore designed as 104Hz, and then attached to the thin plate to examine whether the resonant peak is eliminated.

The dimension of the MemR is $50 \times 50 \times 5$mm, and attached mass is 2.0g. According to the analytical model introduced earlier, to make the resonant frequency as 104Hz, the tensile stress applied to the membrane should be 0.27MPa. Therefore in the stretching mechanism, the stretching force should be tuned to 13.5N. The MemRs are manually produced and then attached to the thin plate. The plate attached with the MemM is then tested with the same setting.

The vibration transmissibility of the MemM is obtained and compared with the bare plate results in Figure 93. As revealed in the figure, the vibration transmissibility at 104Hz is reduced obviously as the resonant peak disappeared. However, the transmissibility decreasing is not as obvious as the ones shown in numerical simulation results. This is mainly because the resonant frequencies of the manually produced MemRs are not exactly the same. Error of resonant frequencies in each individual resonator is inevitable because the manual assembling. So not all the resonators are contributing to the vibration absorption at 104Hz, and the frequency range in which the vibration transmissibility decreased is larger (97.5Hz – 113Hz). However, in numerical simulation, all the MemRs are exact the same and therefore the vibration absorption performance is much obvious than the experiment.

In addition, the vibration transmissibility in the frequency regions of 243Hz – 364Hz and 446Hz – 526Hz are also decreased when compared with bare plate. Instead of causing by bandgap, it is actually because the application of MemRs changed the vibration characteristics of the thin plate.

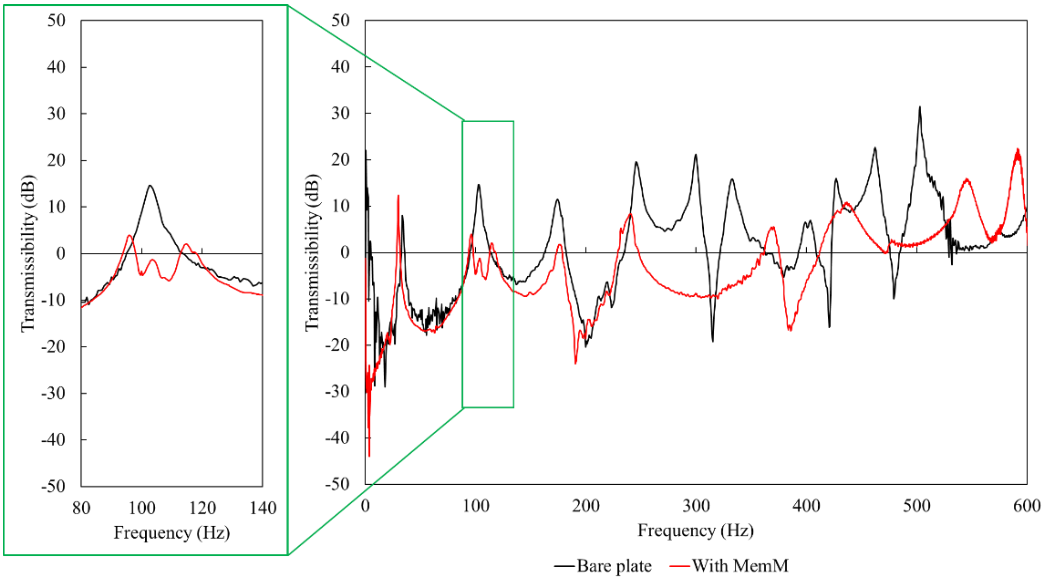

Figure 93. Vibration transmissibility of the bare thin aluminium plate and plate attached with MemRs.

In conclusion, the employment of MemM can achieve vibration suppression for a thin plate structure. However, the inaccuracy of the MemR assembling process weakens the bandgap performance in experiment. A more accurate manufacturing process of MemR should be developed in the future work.

4.6 Chapter Summary

In this chapter, the bandgap properties of MemM is investigated through the developed PWE model, and the vibration absorption capability of the MemM is examined through numerical simulation and experiment.

The design parameters' effect on the bandgap properties is explored through the analytical model. It is found that the tensile stress applied on the membrane can affect the stiffness of the MemR directly and therefore change the bandgap locations. Increase of tensile will shift the bandgap to higher frequency region, vice versa. The bandgap width will be affected by the attached mass magnitude and tensile stress. To achieve a wider bandgap width, larger mass magnitude and tensile stress level should be employed. The PWE model is modified to enable the bandgap prediction for bilayer MemM and interaction between the two membrane layers are confirmed. Through parametric analysis, the optimisation and design guidelines of the design parameters of the bilayer MemM is obtained.

Otherwise, MemMs with different configuration of mass blocks attached on membrane are investigated. The results demonstrate that the bandgap location of the two semicircle mass can be tuned by the adjustment of distance between the mass blocks. Meanwhile, MemM with a nested mass configuration can generate two bandgaps simultaneously and the bandgap property can be changed by the adjustment of the mass dimension.

Numerical simulation and experiments are conducted to verify the vibration suppression performance of the MemM applied to a thin plate structure. The numerical simulation results are consistent with the PWE model prediction. Since the MemM prototype is manually manufactured, error is inevitable in each

MemR. Therefore the bandgap performance is not as perfect as in simulation. However, the results can still reveal the existence of bandgap and the vibration suppression effect caused by the attached MemM.

Chapter 5

5. VIBRATION CONTROL PERFORMANCE OF TUNABLE MEMBRANE-TYPE METAMATERIAL

In previous research works, the tuning method of MemM's bandgap property were mainly focused on the adjustment of tensile stress and the main tuning target is the bandgap location. Actually, from the theoretical aspect, the realisation of bandgap tuning relies on the changing of tensile stress or mass. The adjustment of tensile stress can be realised through the change of mass block, frame and membrane. Mass block or frame that possess capacity of deformation can lead to the tensile stress variation accordingly. However, in application, the realisation of tunable mass block and frame are difficult. As a result, there are barely any studies have focused on tuning tensile stress through the mass and frame components.

In this chapter, the tuning of membrane tensile stress through the application of piezoelectric material membrane in MemM is investigated. The PWE analytical model will be modified to allow external voltage input as a design parameter. The constitutive equation of piezoelectric material is included to connect the voltage with the stress applied in the piezoelectric membrane. Semi-active control of the piezoelectric membrane can thus be implemented with the equation connecting voltage and resonant frequency of the resonator.

The passive vibration absorption performance of the piezoelectric membrane resonator is investigated since the material property is different from silicon rubber. Otherwise, the operational bandgap location of the piezoelectric membrane resonator is explored and numerically verified through simulation. [4]

[4] Part of the content of this chapter has been submitted to the INTER-NOISE 2020 Congress as a conference paper "The modified Plane Wave Expansion method for membrane-type metamaterial equipped with piezoelectric material membrane".

5.1 Constitutive Equation

When some dielectric materials are loaded with external force and deformed, polarization phenomenon will occur internally and electric charge will be accumulated at the surfaces of the materials. Such phenomenon is called the direct piezoelectric effect [144]. Meanwhile, when the material is applied with certain electric field in the poling direction, deformation will appear correspondingly and it is called the inverse piezoelectric effect [144].

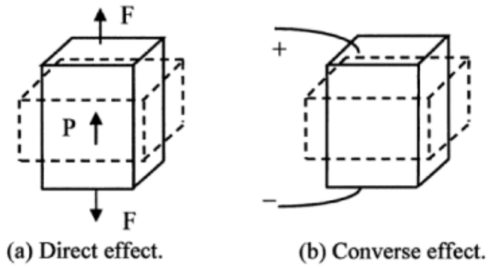

Figure 94. (a)Deformation and poling direction P of dielectric material when applied with external force F. (b) Deformation of dielectric material when applied with external electric field. (Taken and adapted from [144])

The piezoelectricity is a relation of the electromechanical couplings. According to IEEE Standard on Piezoelectricity [145], the polarized direction of the piezoelectric material z-axis is normally denoted as 3-axis, and the plane formed by the x- and y-axis is denoted as 12-plane [146]. The variables that normally used in describing piezoelectric material include: stress (T), strain (S), electric field intensity (E), and electric displacement (D). Constitutive equations are employed to describe the relation between the electric and mechanic physical quantity. Strain-charge form constitutive equation can be expressed as:

$$\begin{gathered} S = s_E T + dE \\ D = dT + \varepsilon_i E. \end{gathered} \tag{5-1}$$

where s_E is the compliance parameter, d is the strain constant, and ε_i is the permittivity. The boundary conditions that influence the material properties include both electrical and mechanical. For a piezoelectric material, there are totally four different types of boundary conditions and in each situation, the independent and dependent variables are different. The detail information is presented in Table 12.

Table 12. Boundary conditions and parameters of the piezoelectric material

Type	Boundary Condition	Independent Variable	Dependent Variable
1	Mechanical free, electrical short circuit	T and E	S and D
2	Mechanical clamped, electrical short circuit	S and E	T and D
3	Mechanical free, electrical open circuit	T and D	S and E
4	Mechanical clamped, electrical open circuit	S and D	T and E

The explanation of the electric boundary conditions is as follow:

Short circuit: the electric charge generated cannot accumulate on the electrode surface so the internal electric field intensity is not affected, E is constant or zero.

Open circuit: the electric charge generated will accumulate on the electrode, so the internal electric field is changing and the electric displacement D is constant or zero.

Since the piezoelectric membrane is fixed on the supporting frame of the membrane-type resonator, it is clamped on the boundaries, the strain S is constant or zero, and the external voltage is applied to the membrane by a power source, therefore the electric filed in constant. So in a membrane-type resonator, the piezoelectric material's boundary condition is the second type, the corresponding constitutive equation is:

$$\begin{aligned} T_i &= c_{ik}^E S_k - e_{ij}^E E_j \\ D_i &= e_{ik}^E S_k + \varepsilon_{ij} E_j. \end{aligned} \tag{5-2}$$

where c_{ik}^E is the coefficient of elastic stiffness, e_{ij}^E is the stress constant and ε_{ij} is the permittivity constant. The strain S_k and the electric field intensity E_j are the independent variables under such boundary conditions, whilst the tensile stress T_i and electric displacement D_i are depend variables.

With the given prestressed level of the membrane and the applied electric field intensity, the tensile stress on the membrane can be derived by the constitutive equations.

5.2 Modified PWE Model

The PWE model is further revised to include the voltage applied to the PVDF membrane as an independent variable. The modified model can construct the connection between applied voltage and the bandgap properties of the PVDF MemM.

For a prestressed PVDF membrane, assume the elastic constant c_{ik}^{E} is an isotropic constant and equals to the Young's modulus of the material, which is 3.8GPa for PVDF.

The equation (5-2) can be expressed as:

$$\begin{Bmatrix} T_x \\ T_y \\ T_z \end{Bmatrix} = \begin{Bmatrix} T_{x0} \\ T_{y0} \\ T_{z0} \end{Bmatrix} - \begin{Bmatrix} 0 & 0 & e_{xx} \\ 0 & 0 & e_{yy} \\ 0 & 0 & e_{zz} \end{Bmatrix} \begin{Bmatrix} E_x \\ E_y \\ E_z \end{Bmatrix} \tag{5-3}$$

where T_{i0} is the initial tensile stress applied on the membrane in different directions, e_{ij} is the stress constants and in this paper, the constants are assumed to be isotropic in the xy-plane, so $e_{xx} = e_{yy} = 0.024\ N/mV$. E_j is the electric field intensity in x, y and z directions respectively. Normally the voltage is applied at the polarized direction only, therefore $E_x = E_y = 0$, and $E_z = \frac{V}{t}$, where V and t are the applied voltage and thickness of the membrane, respectively.

In the Rayleigh model, the tensile stress applied to the membrane T is used. When the tensile stress within the membrane T_x and T_y are not equal, the stress will be self-adjusted and achieve uniform distribution over the membrane. In order to simplify, the stress constant of the tensile stress is assumed to be isotropic, so the tensile stress within membrane will be equal to the stress in x- and y-direction.

Substitute $T = T_0 - e\frac{V}{t}$ into equation (2-50), the stiffness will then be expressed as a function that is related with the external applied voltage:

$$k_R = \frac{m_R}{4\pi^2}\frac{\frac{\pi^4 D}{4a^3b^3}(3b^4+3a^4+2a^2b^2)+\frac{3(a^2+b^2)(T_0-e\frac{V}{t})\pi^2}{16ab}}{\frac{9abm_s}{64}+Msin^4(\frac{\pi q}{a})sin^4(\frac{\pi h}{b})}. \tag{5-4}$$

Then by substituting the above equation into equation (2-63), the voltage can be integrated to the PWE model. Therefore, the relation between the external applied voltage and bandgap properties of the PVDF MemM attached on a thin plate structure can be obtained.

5.3 Tuning of PVDF MemM's Bandgap Properties

According to the equation (5-4), aside from the geometry design parameters and attached mass magnitude, the effective stiffness of the PVDF MemR is also influenced by the voltage and membrane thickness. Therefore, through the modified PWE method, parametric study is conducted to reveal the tunability of the PVDF MemM's bandgap properties.

To explain the mechanism of tensile stress tuning, a piezoelectric material pillar model is constructed, as shown in Figure 95. The top surface of the pillar is defined as fixed referencing surface, electric potential is applied to the surfaces of the pillar to reveal the deformation of the piezoelectric material whose polarization direction is assumed to be in positive z-axis. According to the figure, when positive electric potential is applied at the top surface, the piezoelectric material will be extended in z-direction and shrink in the xy-plane, thus increase the tensile stress. On the contrary, when the electric potential is applied at the bottom, the piezoelectric material will be compressed in the z-direction and leads to the extension in xy-plane, thus the in-plane tensile stress will decrease. Similar phenomenon will also appear in a piezoelectric membrane and results in the changing of resonant frequencies of the MemR.

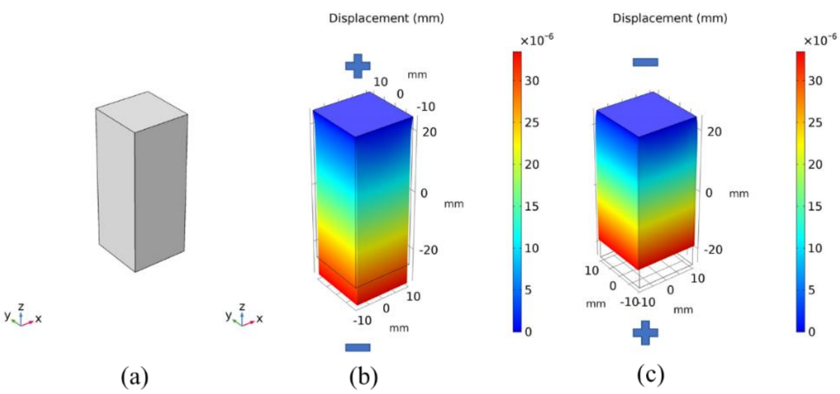

Figure 95. (a) The model of a piezoelectric material pillar; deformation of the piezoelectric pillar when voltage is applied at (b) the top surface and (c) the bottom surface.

The bandgap property of a thin plate attached with PVDF MemM under different voltage is investigated through parametric study.

The PVDF membrane thickness is an essential parameter because the smaller the thickness, the higher the electric field intensity, thus the change of membrane stress will be larger as well. PVDF material requires high voltage polarization procedure before forming piezoelectric properties, and such procedure cannot be implemented in the vibration lab. Hence, suppliers are contacted to obtain the specific data and dimension of the PVDF membrane. The PVDF membrane product from TE connectivity is then selected and 6 different thicknesses are provided according to the product catalogue: 0.028mm, 0.04mm, 0.052mm, 0.064mm, 0.11mm and 0.122mm.

When the applied electric potential across the membrane is tuned from -1000V to 1000V, the tensile stress difference caused by the electric potential in PVDF membranes are given in Table 13. The stress constant of the PVDF material is assumed to be isotropic (e_{31}=e_{32}=0.075N/Vm) in the xy-plane to avoid the error caused by imbalance of stress in x- and y-direction. With the same magnitude of voltage applied, the tensile stress variation in the thinner membrane is larger. When the thinnest membrane is employed, applying 1000V voltage will result in ±2.679MPa tensile stress differences, which are able to cause bigger resonant frequency shifting in a MemR. As a result, the thinnest membrane thickness (0.028mm) is employed in the following study.

Table 13. Data of tensile stress change when different voltage is applied to membranes with various thickness.

Thickness (mm)	0.122	0.11	0.064	0.052	0.04	0.028
Voltage (V)	Tensile stress variation (MPa)	Tensile stress variation (MPa)	Tensile stress variation (MPa)	Tensile stress variation (MPa)	Tensile stress variation (MPa)	Tensile stress variation (MPa)
-1000	-0.615	-0.682	-1.172	-1.442	-1.875	-2.679
-900	-0.553	-0.614	-1.055	-1.298	-1.688	-2.411
-800	-0.492	-0.545	-0.938	-1.154	-1.500	-2.143
-700	-0.430	-0.477	-0.820	-1.010	-1.313	-1.875
-600	-0.369	-0.409	-0.703	-0.865	-1.125	-1.607
-500	-0.307	-0.341	-0.586	-0.721	-0.938	-1.339
-400	-0.246	-0.273	-0.469	-0.577	-0.750	-1.071
-300	-0.184	-0.205	-0.352	-0.433	-0.563	-0.804
-200	-0.123	-0.136	-0.234	-0.288	-0.375	-0.536
-100	-0.061	-0.068	-0.117	-0.144	-0.188	-0.268
0	0.000	0.000	0.000	0.000	0.000	0.000
100	0.061	0.068	0.117	0.144	0.188	0.268
200	0.123	0.136	0.234	0.288	0.375	0.536
300	0.184	0.205	0.352	0.433	0.563	0.804
400	0.246	0.273	0.469	0.577	0.750	1.071
500	0.307	0.341	0.586	0.721	0.938	1.339
600	0.369	0.409	0.703	0.865	1.125	1.607
700	0.430	0.477	0.820	1.010	1.313	1.875
800	0.492	0.545	0.938	1.154	1.500	2.143
900	0.553	0.614	1.055	1.298	1.688	2.411
1000	0.615	0.682	1.172	1.442	1.875	2.679

The vibration control performance of the PVDF MemR when attached to a thin plate will be investigated. The configuration of the PVDF MemR is shown in Figure 96. The dimensions of the PVDF MemR and material properties are given in Table 14. Compared with the rubber membrane used in **Chapter 4**, the PVDF MemR is 10mm bigger. This is due to the consideration of difficulty of PVDF membrane's extra wiring assembly. Wiring and electrodes layer are applied to the membrane surfaces because the need of electric potential control.

Table 14. Dimension and material properties of PVDF MemR

	PVDF membrane	Frame	Mass
Side length/radius (mm)	60	70	6
Thickness/height (mm)	0.028	5	2
Young's modulus (GPa)	3.8	0.917	115
Poisson's ratio	0.25	0.41	0.33

Density (kg/m^3)	1780	1100	8890
Stress constant (N/Vm)	0.075	-	-

According to the PVDF product catalogue, the electrode layers are very thin, the mechanics effect of the electrodes are therefore ignored in the analytical model and numerical simulation.

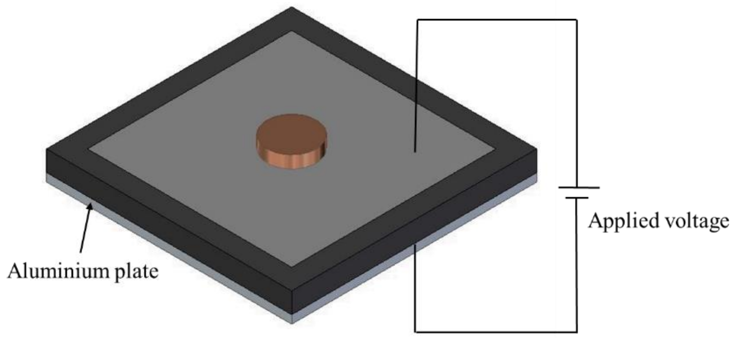

Figure 96. Configuration of the PVDF MemR.

In accordance with the modified PWE model, the MemR and the part of thin plate that the resonator attached on are considered as the unit cell. Dispersion relation of the structure when different electric potential applied is obtained and presented in Figure 97. The thickness of the plate attached under the resonator is 2mm, the mass attached on the membrane is 2.0g, and the initial tensile stress applied on membrane is 3.0MPa. Especially, it is essential to ensure the initial stress applied on the membrane is larger than the stress tuning range of voltage, or the membrane resonator will lose efficacy when the total tensile stress turns negative and become wrinkle.

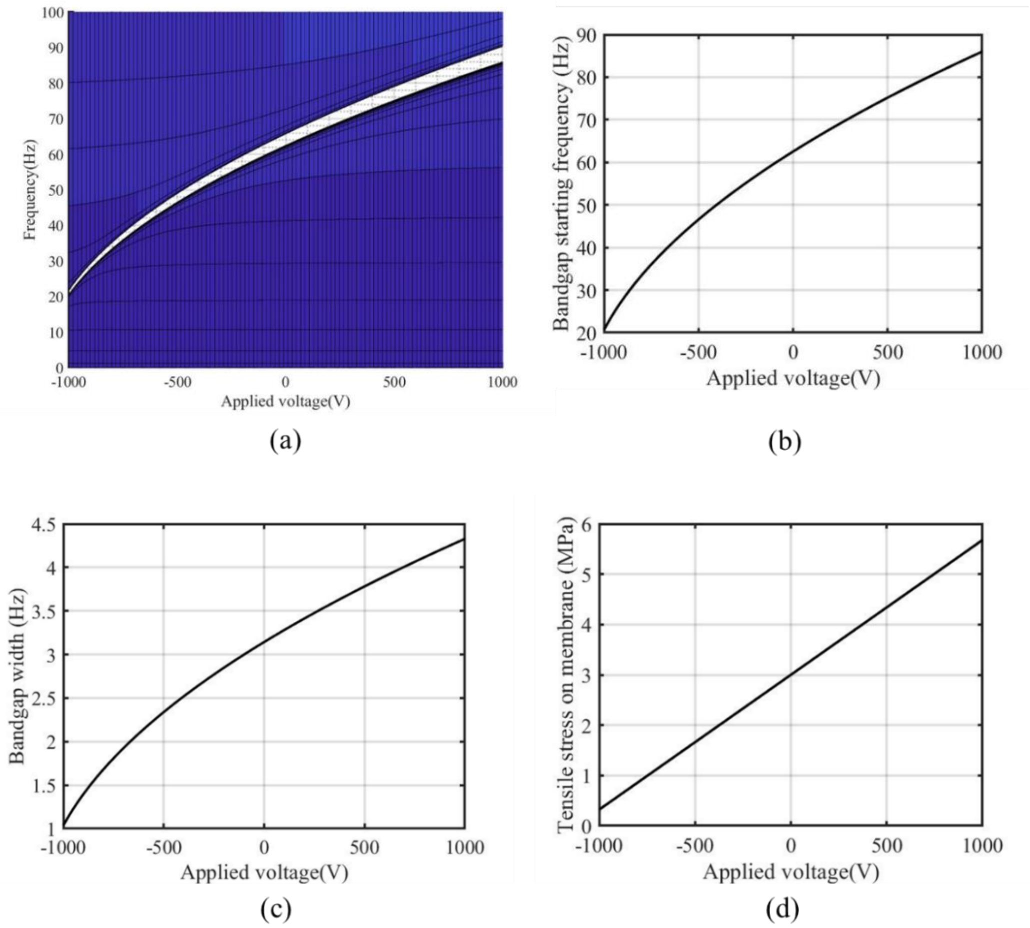

Figure 97. (a) The band structure of the PVDF MemM applied on a thin plate when applied electric potential is tuned from -1000V to 1000V; (b) bandgap starting frequency vs. electric potential; (c) bandgap width vs. electric potential and (d) tensile stress on membrane vs. electric potential.

As shown in the figure, when positive electric potential is applied at the top surface of the membrane, the tensile stress will be increased and thus leads to the rising of bandgap starting frequency. The tensile stress is changed from the initial 3.0MPa to 5.679MPa according to the modified PWE model. On the contrary, when the applied electric potential at the top surface is negative, the tensile stress will be decreased and will drop to 0.321MPa.

The bandgap width become smaller when the tensile stress decreased, as also mentioned earlier in **Chapter 4**. The smallest bandgap width is only 1.1Hz and the largest one is 4.3Hz when tensile stress is varied from 0.321MPa to 5.679MPa.

In the case shown in Figure 97, a 65.4Hz bandgap shifting (from 20.6Hz to 86.0Hz) is achieved when the electric potential is changed from -1000V to 1000V. Different from the MemM with normal material membrane that only possess fixed narrow bandgap, the PVDF MemM can be adjusted swiftly in accordance with the incident wave frequency and achieve a relatively broad range of vibration control.

In addition, to investigate the effect of attached mass magnitude on the tunability of PVDF MemM, the bandgap location of attached mass increased to 4.0g, 8.0g and 12.0g are obtained as well. The change of bandgap location are presented in Figure 98.

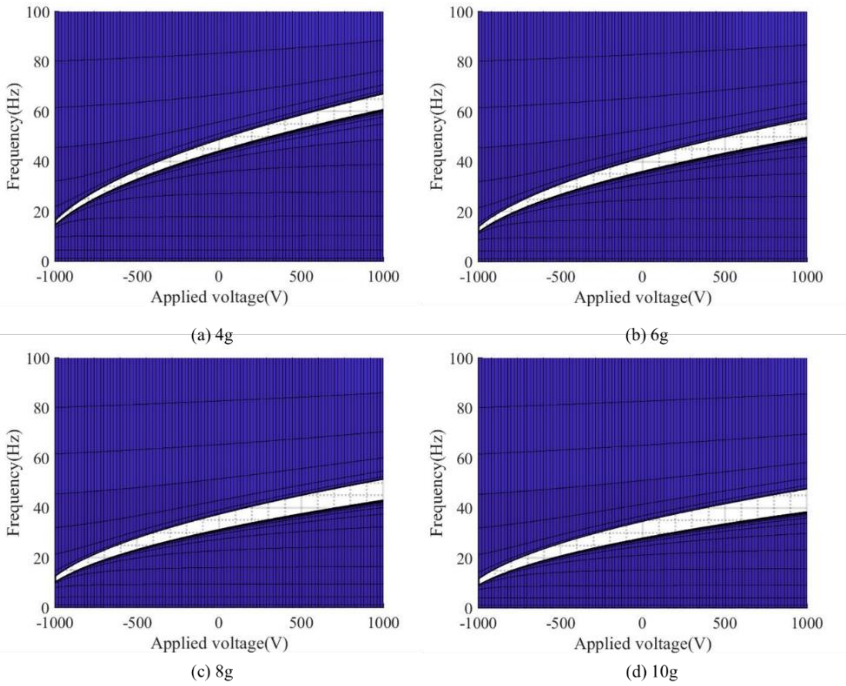

Figure 98. The band structures of the PVDF MemM applied on a thin plate with the attached mass magnitude as: (a) 4.0g; (b) 6.0g; (c) 8.0g and (d) 10.0g.

According to the figure, when the mass magnitudes are increased, the changing trend of the bandgap location and width are the same as the 2.0g case. However, the bandgap location shifts to lower frequency region because of the larger mass, and also similar to the findings in **Chapter 4**, the bandgap width also increased. To clearly describe the effect of mass magnitude on the bandgap property, the detailed data and location of bandgaps when the applied electric potential is 1000V, which leads to the maximum tensile stress in membrane, are presented in Table 15 and Figure 99.

Table 15. Data of bandgap shifting range and largest bandgap width of the PVDF MemM with different mass magnitude utilized when the externally applied voltage is tuned from -1000V to 1000V.

Attached mass (g)	2.0	4.0	6.0	8.0	10.0
Bandgap shifting range (Hz)	65.4	46.3	37.9	32.8	29.3
Largest bandgap width (Hz)	4.3	6.0	7.2	8.1	8.9

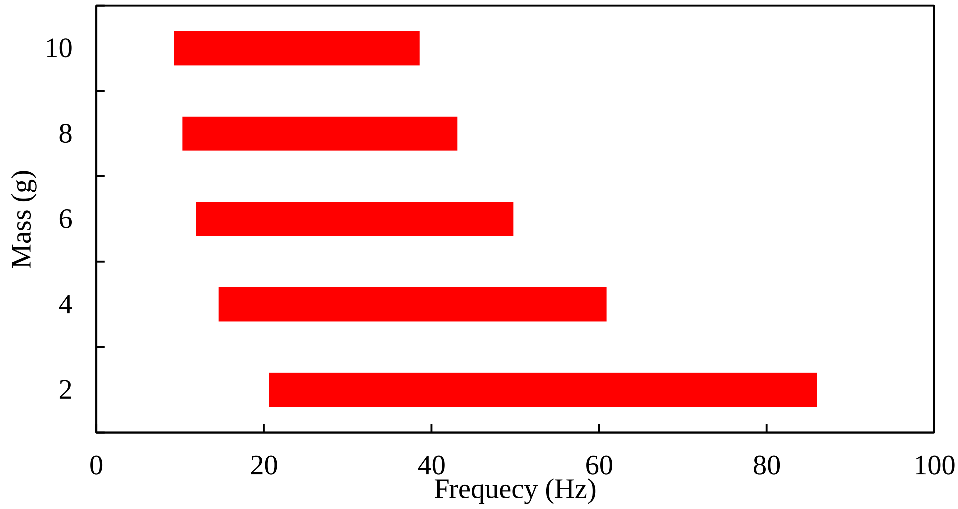

Figure 99. Frequency regions of PVDF MemM's bandgap starting frequencies when the externally applied electric potential is tuned from -1000V to 1000V.

It is clearly stated in the table that the bandgap shifting range will be broader when smaller mass magnitude is used but the corresponding bandgap width under each electric potential value will be narrower as well. However, with a broader tuning range, the 2.0g case can cover a wider frequency region.

The finding demonstrates a design guideline for the PVDF MemM that thinner membrane thickness and smaller mass magnitude is preferred for the purpose of increasing the tunable bandgap range. However, compromise also needs to be considered since smaller mass magnitude may lead to the weakening of vibration suppression efficiency. Hence, finite structure is set up in FEA software and conduct vibration response analysis upon.

5.4 Vibration Control Performance of the PVDF MemM

Firstly, the accuracy of the numerical simulation in PVDF membrane tensile stress calculation is examined. As shown in Figure 100, when the voltage is tuned from -1000V to 1000V, the change of tensile stress obtained by the analytical model and numerical simulation are mostly consistent with each other.

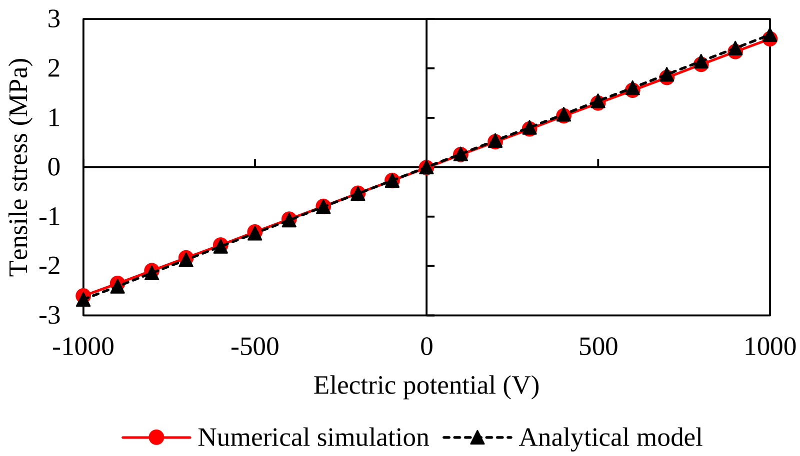

Figure 100. Change of tensile stress in PVDF membrane when applied electric potential is adjusted.

Similar to the MemM with silicone rubber membrane, the resonators are attached periodically on a thin plate. The configuration of the structure is presented in Figure 101. As described earlier, the voltage is applied at the upper surface of the membrane. The vibration response signal detection line is labelled with red solid line in the figure. The average acceleration on the line is used as the vibration response of the plate so to avoid influence of nodal points of the structure. The vibration transmissibility when voltage is defined as -1000V, -500V, -300V, 0V, 300V, 500V and 1000V are shown in Figure 102.

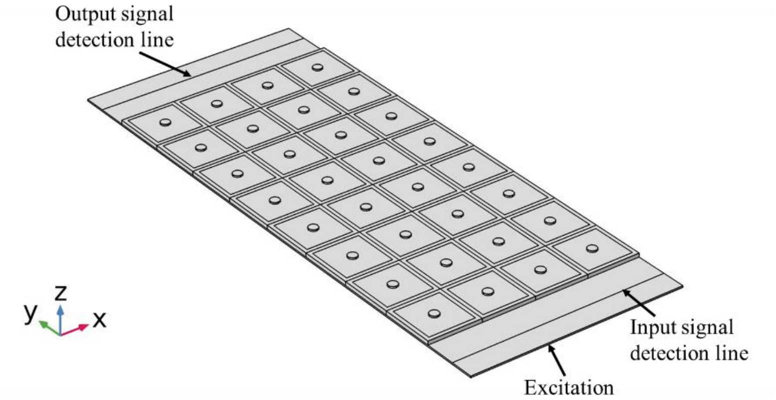

Figure 101. Configuration of the finites structure of thin plate attached with PVDF MemM.

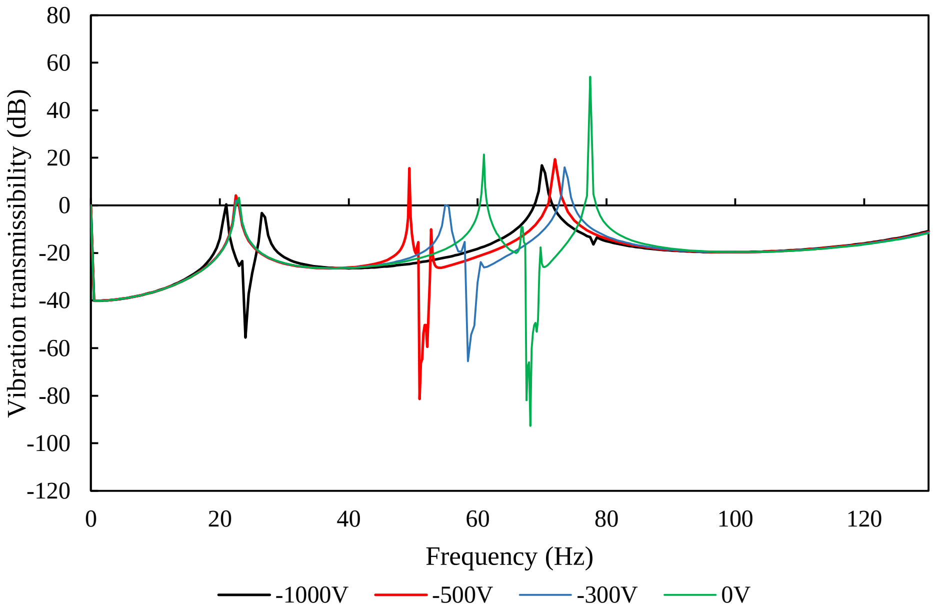

(a)

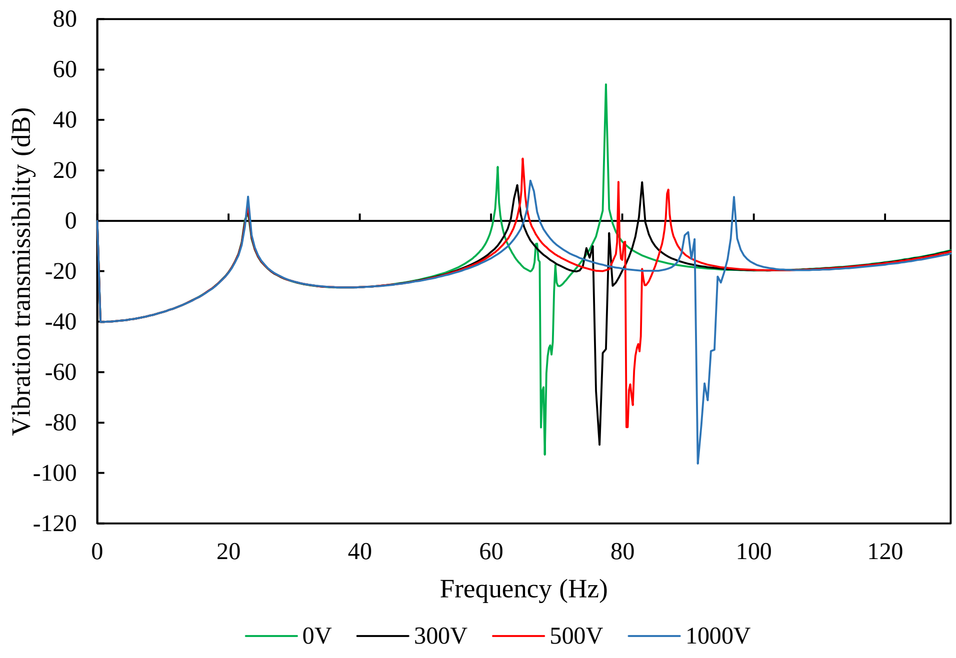

(b)

Figure 102. (a) The vibration transmissibility of the PVDF MemM when the electric potential applied across the membrane is (a) -1000V, -500V, -300V and 0V; and (b) 0V, 300V, 500V and 1000V.

According to the figure, bandgaps are formed by the attached PVDF MemM when the applied electric potential is tuned. From -1000V to 1000V, the bandgap location is shifted from 25.0Hz to 91.5Hz. The finite structure has a resonant peak revealed at 22.5Hz, and with -1000V electric potential applied, the resonant peak is eliminated effectively. The bandgap widths are relatively narrow in all cases, but the 1000V case has the largest bandgap width, which is consistent with the prediction by the modified PWE model.

The starting frequencies of the bandgaps when different electric potential values are applied are obtained. The tensile stress under different electric potential values are previously calculated, and the corresponding resonant frequency of the MemR can be worked out through the modified Rayleigh method. The bandgap starting frequencies obtained from the transmissibility curves and the analytical model are presented and compared in Figure 103. According to the figure, all the bandgap starting frequencies in the FEA analysis are about 5.0 – 6.0Hz higher than the analytical results. The cause of the error is the same as the one mentioned in **Chapter 4**. The error is in an acceptable range so the modified model can still be used for the prediction of PVDF MemM bandgap properties.

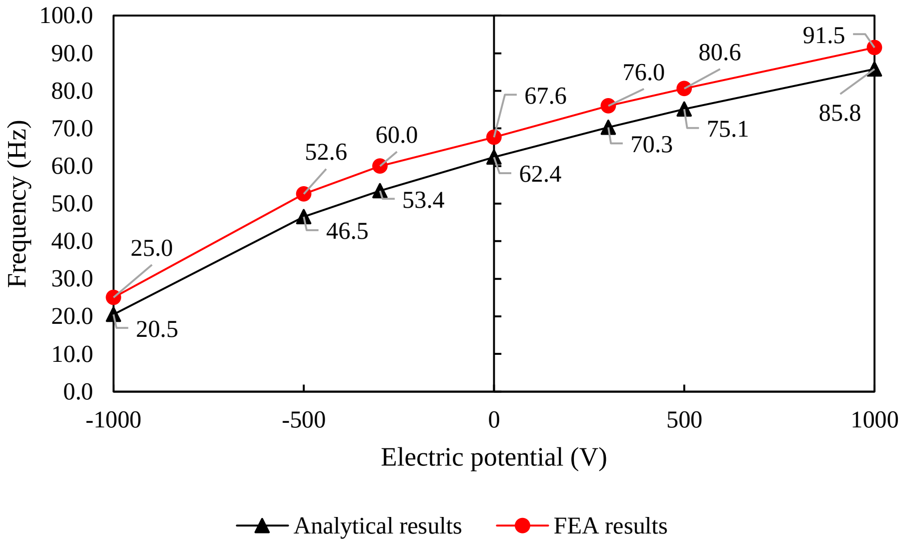

Figure 103. Bandgap starting frequency of the PVDF MemM obtained by analytical model and FEA analysis.

5.5 Chapter Summary

The bandgap tunability and the vibration suppression performance of MemM equipped with PVDF membrane is investigated in this chapter. The constitutive equation of piezoelectric material is incorporated with the PWE model, thus the applied electric potential across the PVDF membrane is integrated in the modified PWE model. The influence of membrane thickness on the membrane tensile stress is revealed by the analytical model and it is found that for the purpose of increasing bandgap tunability, membrane with smaller thickness should be utilised. In addition, through the modified PWE model, the bandgap tunability of the PVDF MemM is predicted. When the electric potential is adjusted from -1000V to 1000V, the bandgap location of PVDF MemM with 3MPa prestressed level can be tuned from 20.6Hz to 86.0Hz. Also, the increase of attached mass magnitude can increase the individual bandgap width of the MemM under certain electric potential. However, the heavier of the attached mass, the smaller of the bandgap tuning range when the same electric potential tuning range is employed.

Through FEA of a finite metamaterial structure applied on a thin plate, the accuracy of the modified PWE model in predicting PVDF MemM's bandgap performance is verified. The FEA and PWE model results are basically consistent with each other, despite the existence of some error that is in acceptable range.

The bandgap range is increased significantly when PVDF membrane is employed in the MemM. The normal MemM normally has narrow bandgap width, and multiple layers of MemM can be applied for the purpose of forming multiple bandgaps and increase the bandgap width. However, in the PVDF

MemM, because the operation frequency can be tuned rapidly in accordance with the incident wave’s frequency, the bandgap width will be largely enhanced.

The findings in this chapter demonstrates the feasibility of conducting semi-active control in MemM through the application of piezoelectric membrane material.

Chapter 6

6. DEVELOPMENT OF SEMI-ACTIVE CONTROL ALGORITHM

In previous chapters, the vibration characteristics of a thin plate attached with or without MemM are investigated. The MemM is demonstrated to be effective in thin plate structure's vibration suppression. The modified PWE model can accurately predict the bandgap location of the MemM when applied on a thin plate, and through numerical simulation, the frequency response is obtained. Results are consistent with the prediction in PWE model. However, FEA process is time-consuming and inconvenient, especially when conducting for parametric study that requires repeating calculation. Meanwhile, the PWE model can only predict the vibration suppression of periodically distributed MemM, and cannot allow the bandgap prediction for nonperiodic attached MemM, so it cannot conduct optimisation for the distribution of attached mass and the location of resonators on the structure. In addition, as mentioned in **Chapter 5**, the employment of PVDF membrane in MemR enables the tuning of MemR's operational frequencies. If equipped with independent control circuit, each of the PVDF MemM's unit cell can possess various resonant frequencies. Therefore, the operational frequencies of each resonator can be controlled precisely to achieve the optimum vibration suppression performance.

Based on the above mentioned disadvantages of PWE model and actual need in PVDF MemM, a semi-active control algorithm for the PVDF MemM is developed. The algorithm is based on the thin plate – resonator coupling model, and the effect of tuning electric potential applied to the PVDF is incorporated with this model by taking advantage of the modified PWE model.

6.1 Thin Plate – Resonator Coupling Model

6.1.1 Model development

Firstly, the analytical model of the thin – plate coupled with resonators is developed. The configuration of the structure is the same as the one shown in Figure 29. Based on the previous of Cheng Yang's thesis [147], the equation of motion of the system can be written as:

$$\begin{cases} D\nabla^4 w(x,y,t) + \rho h \dfrac{\partial^2 w(x,y,t)}{\partial t^2} = F(t)\delta(x-x_0, y-y_0) \\ \qquad - \sum_g^G m_g \dfrac{\partial^2 x_g(t)}{\partial t^2} \delta(x-x_g, y-y_g) & \text{(6-1)} \\ m_g \dfrac{\partial^2 x_g(t)}{\partial t^2} + c_g \dfrac{\partial x_g(t)}{\partial t} + k_g x_g(t) = c_g \dfrac{\partial w(x_g, y_g, t)}{\partial t} + k_g w(x_g, y_g, t) & \text{(6-2)} \end{cases}$$

where $D = \frac{Eh^3}{12(1-v^2)}$, ρ is the mass density of the plate, h is the plate thickness, m_g, c_g and k_g are the mass, damping and stiffness of the resonator respectively. $F(t)$ is the external force applied to the plate. Assume:

$$\begin{cases} w(x,y,t) = \sum_m^M \sum_n^N W_{mn} e^{i\omega t} \Phi_{mn}(x,y) & \text{(6-3a)} \\ x_g(t) = X_g e^{i\omega t} & \text{(6-3b)} \\ F(t) = F e^{i\omega t} & \text{(6-3c)} \end{cases}$$

Substitute equation (6-3a) and (6-3b) into equation (6-2):

$$-\omega^2 m_g X_g + i\omega c_g X_g + k_g X_g =$$

$$i\omega c_g \sum_m^M \sum_n^N W_{mn} \Phi_{mn}(x,y) + k_g \sum_m^M \sum_n^N W_{mn} \Phi_{mn}(x,y)$$

$$\rightarrow \left(-\omega^2 m_g + i\omega c_g + k_g\right) X_g = (i\omega c_g + k_g) \sum_m^M \sum_n^N W_{mn} \Phi_{mn}(x,y)$$

$$\rightarrow X_g = \frac{i\omega c_g + k_g}{-\omega^2 m_g + i\omega c_g + k_g} \sum_m^M \sum_n^N W_{mn} \Phi_{mn}(x_g, y_g) \qquad \text{(6-4)}$$

Otherwise, when the plate without resonators attached undergoes free vibration, the equation of motion can be given as:

$$\begin{gathered}D\nabla^4\sum_m^M\sum_n^N W_{mn}\Phi_{mn}(x,y)-\beta_{mn}^2\rho h\sum_m^M\sum_n^N W_{mn}\Phi_{mn}(x,y)=0\\ \rightarrow D\nabla^4\sum_m^M\sum_n^N W_{mn}\Phi_{mn}(x,y)=\beta_{mn}^2\rho h\sum_m^M\sum_n^N W_{mn}\Phi_{mn}(x,y)\end{gathered}\tag{6-5}$$

where β_{mn} is the corresponding resonance frequency to each specific resonant mode of the bare plate.

Substitute equation (6-3a) (6-3b) and (6-5) into equation (6-1):

$$\begin{aligned}\rho h\sum_m^M\sum_n^N \beta_{mn}^2 W_{mn}\Phi_{mn}(x,y)-\omega^2\rho h\sum_m^M\sum_n^N W_{mn}\Phi_{mn}(x,y)\\ =F\delta(x-x_0,y-y_0)+\omega^2\sum_g^G m_g X_g\delta(x-x_g,y-y_g)\end{aligned}$$

Multiply $\Phi_{rs}(x,y)$ to both sides of above equation and integrate over the surface of the plate:

$$\begin{aligned}\rho h\sum_m^M\sum_n^N \beta_{mn}^2 W_{mn}\Phi_{mn}(x,y)\,\Phi_{rs}(x,y)-\omega^2\rho h\sum_m^M\sum_n^N W_{mn}\Phi_{mn}(x,y)\Phi_{rs}(x,y)\\ =F\delta(x-x_0,y-y_0)\Phi_{rs}(x,y)\\ +\omega^2\sum_g^G m_g X_g\Phi_{rs}(x,y)\delta(x-x_g,y-y_g)\end{aligned}\tag{6-6}$$

Integrate the above equation over the surface of the plate:

$$\begin{aligned}\frac{\rho h}{S}\beta_{mn}^2 W_{mn}\iint_S[\Phi_{mn}(x,y)^2]dxdy-\frac{\rho h}{S}\omega^2 W_{mn}\iint_S[\Phi_{mn}(x,y)^2]dxdy\\ =F\Phi_{mn}(x_0,y_0)+\omega^2\sum_g^G m_g X_g\Phi_{mn}(x_g,y_g)\end{aligned}\tag{6-7}$$

Define $\mathrm{M}_{mn}=\frac{\rho h}{S}\iint_S[\Phi_{mn}(x,y)^2]dxdy$, divide the above equation by M_{mn}:

$$\beta_{mn}^2 W_{mn}-\omega^2 W_{mn}=F\frac{\Phi_{mn}(x_0,y_0)}{M_{mn}}+\omega^2\sum_g^G\frac{m_g X_g\Phi_{mn}(x_g,y_g)}{M_{mn}}\tag{6-8}$$

In addition, the damping term can be introduced to the equation directly as:

$$\beta_{mn}^2 W_{mn} - \omega^2 W_{mn} + 2i\omega\xi_{mn}\beta_{mn}W_{mn} = F\frac{\Phi_{mn}(x_0,y_0)}{M_{mn}} + \omega^2\sum_g^G m_g \frac{\Phi_{mn}(x_g,y_g)}{M_{mn}}X_g \tag{6-9}$$

Substitute equation (6-4) into equation (6-9), the equation will be:

$$(\beta_{mn}^2 - \omega^2 + 2i\omega\xi_{mn}\beta_{mn})W_{mn} = F\frac{\Phi_{mn}(x_0,y_0)}{M_{mn}} + \omega^2\sum_g^G m_g \frac{\Phi_{mn}(x_g,y_g)}{M_{mn}} \frac{i\omega c_g + k_g}{-\omega^2 m_g + i\omega c_g + k_g}\sum_r^M\sum_s^N W_{rs}\Phi_{rs}(x_g,y_g) \tag{6-10}$$

The subscript of the X_g's expression are changed to r, s because in X_g, all the corresponding displacement amplitude W and Φ are needed to form the summation, yet after the integration, the W and Φ in other parts of the equation are designated to be a certain mode that can identified by m and n. Therefore, subscript is changed to indicate the difference.

The equation can then be transformed into this form depends on the value of r and s:

$$[(\beta_{mn}^2 - \omega^2 + 2i\omega\xi_{mn}\beta_{mn}) - \omega^2\sum_g^G m_g \frac{i\omega c_g + k_g}{-\omega^2 m_g + i\omega c_g + k_g}\frac{\Phi_{mn}(x_g,y_g)^2}{M_{mn}}]W_{mn} = F\frac{\Phi_{mn}(x_0,y_0)}{M_{mn}} + \omega^2\sum_g^G m_g \frac{i\omega c_g + k_g}{-\omega^2 m_g + i\omega c_g + k_g}\frac{\Phi_{mn}(x_g,y_g)}{M_{mn}}\sum_{r\neq m}^M\sum_{s\neq n}^N W_{rs}\Phi_{rs}(x_g,y_g) \tag{6-11}$$

Define:

$$\begin{cases} A_{mn} = \beta_{mn}^2 - \omega^2 + 2i\omega\xi_{mn}\beta_{mn} \\ B_g = m_g \dfrac{i\omega c_g + k_g}{-\omega^2 m_g + i\omega c_g + k_g} \end{cases} \tag{6-12}$$

Substitute equation (6-12) into equation (6-11):

$$\left[A_{mn} - \omega^2\sum_g^G B_g \frac{\Phi_{mn}(x_g,y_g)^2}{M_{mn}}\right]W_{mn} = F\frac{\Phi_{mn}(x_0,y_0)}{M_{mn}} + \omega^2\sum_g^G B_g \frac{\Phi_{mn}(x_g,y_g)}{M_{mn}}\sum_{r\neq m}^M\sum_{s\neq n}^N W_{rs}\Phi_{rs}(x_g,y_g). \tag{6-13}$$

The equation can be further simplified by defining $P_{mn} = A_{mn} - \omega^2\sum_g^G B_g \frac{\Phi_{mn}(x_g,y_g)^2}{M_{mn}}$. Thus equation (6-13) is transferred to:

$$P_{mn}W_{mn} = F\frac{\Phi_{mn}(x_0, y_0)}{M_{mn}} + \omega^2 \sum_{g}^{G} B_g \frac{\Phi_{mn}(x_g, y_g)}{M_{mn}} \sum_{r\neq m}^{M} \sum_{s\neq n}^{N} W_{rs}\Phi_{rs}(x_g, y_g) \qquad \text{(6-14)}$$

For each specific combination of m and n, an equation that includes other combinations of displacement W will be formed. Therefore, the above equation can be expressed in the matrix form as:

$$[K][W_{mn}] = F[\Phi] \qquad \text{(6-15)}$$

where:

$$[K] = \begin{pmatrix} P_{11} & -\omega^2 \sum_g^G B_g \frac{\Phi_{11}(x_g, y_g)\Phi_{12}(x_g, y_g)}{M_{11}} & \cdots & -\omega^2 \sum_g^G B_g \frac{\Phi_{11}(x_g, y_g)\Phi_{m(n-1)}(x_g, y_g)}{M_{11}} & -\omega^2 \sum_g^G B_g \frac{\Phi_{11}(x_g, y_g)\Phi_{mn}(x_g, y_g)}{M_{11}} \\ -\omega^2 \sum_g^G B_g \frac{\Phi_{12}(x_g, y_g)\Phi_{11}(x_g, y_g)}{M_{12}} & P_{12} & & -\omega^2 \sum_g^G B_g \frac{\Phi_{12}(x_g, y_g)\Phi_{m(n-1)}(x_g, y_g)}{M_{12}} & -\omega^2 \sum_g^G B_g \frac{\Phi_{12}(x_g, y_g)\Phi_{mn}(x_g, y_g)}{M_{12}} \\ \vdots & & \ddots & & \vdots \\ -\omega^2 \sum_g^G B_g \frac{\Phi_{m(n-1)}(x_g, y_g)\Phi_{11}(x_g, y_g)}{M_{m(n-1)}} & -\omega^2 \sum_g^G B_g \frac{\Phi_{m(n-1)}(x_g, y_g)\Phi_{12}(x_g, y_g)}{M_{m(n-1)}} & & P_{m(n-1)} & -\omega^2 \sum_g^G B_g \frac{\Phi_{m(n-1)}(x_g, y_g)\Phi_{mn}(x_g, y_g)}{M_{m(n-1)}} \\ -\omega^2 \sum_g^G B_g \frac{\Phi_{mn}(x_g, y_g)\Phi_{11}(x_g, y_g)}{M_{mn}} & -\omega^2 \sum_g^G B_g \frac{\Phi_{mn}(x_g, y_g)\Phi_{12}(x_g, y_g)}{M_{mn}} & \cdots & -\omega^2 \sum_g^G B_g \frac{\Phi_{12}(x_g, y_g)\Phi_{m(n-1)}(x_g, y_g)}{M_{mn}} & P_{mn} \end{pmatrix}$$

$$[W_{mn}] = \begin{bmatrix} W_{11} \\ W_{12} \\ \vdots \\ W_{m(n-1)} \\ W_{mn} \end{bmatrix}$$

$$[\Phi] = \begin{bmatrix} \frac{\Phi_{11}(x_0, y_0)}{M_{11}} \\ \frac{\Phi_{12}(x_0, y_0)}{M_{12}} \\ \vdots \\ \frac{\Phi_{m(n-1)}(x_0, y_0)}{M_{m(n-1)}} \\ \frac{\Phi_{mn}(x_0, y_0)}{M_{mn}} \end{bmatrix}$$

Theoretically, the vibration response of the structure is formed by infinite resonant mode shapes. However, in order to calculate the vibration amplitude of the structure $[W_{mn}]$, a truncation in the resonant modes can be made by defining a finite number to m and n, and the mode shape function can be assumed as: $\Phi_{mn}(x, y) = \sin(\frac{m\pi}{L_1}x)\sin(\frac{n\pi}{L_2}y)$. Thus, by substituting the function into the above matrix function, the vibration response of the structure can be calculated.

For a thin plate structure with MemRs attached, the MemRs can be simplified as the spring-mass resonator model. As illustrated in former chapters, the effect of the design parameters of the MemR, such as tensile stress or applied electric potential across the piezoelectric material membrane, can be integrated into the model through the equivalent stiffness k_g.

Thus, different from the original model, the MemR is integrated into the thin plate – resonator coupling model and it can then be utilised for the examination and investigation of the effect of MemR's design parameters on the thin plate structure vibration suppression.

6.1.2 Optimisation of resonator distribution through the developed analytical model

First of all, the vibration transmissibility of a bare aluminium plate is calculated by the developed analytical model and compared the results with the FEA for the purpose of verifying accuracy.

As shown in Figure 104(a), the plate is defined as 0.55×0.4×0.002m, and simply supported on all the boundaries. In order to calculate the vibration response of the bare plate, the resonator mass is tuned to be zero and incident force with 1N amplitude is applied. The vibration transmission of the plate is compared with the FEA results. The curves are presented in Figure 104(b). According to the figure, the first 6 resonant peaks are highly consistent in both FEA and analytical model, and small deviation starts to appear in the higher frequency ranges yet still in an acceptable range. Thus, it is believed that the analytical model is accurate for the thin plate structure.

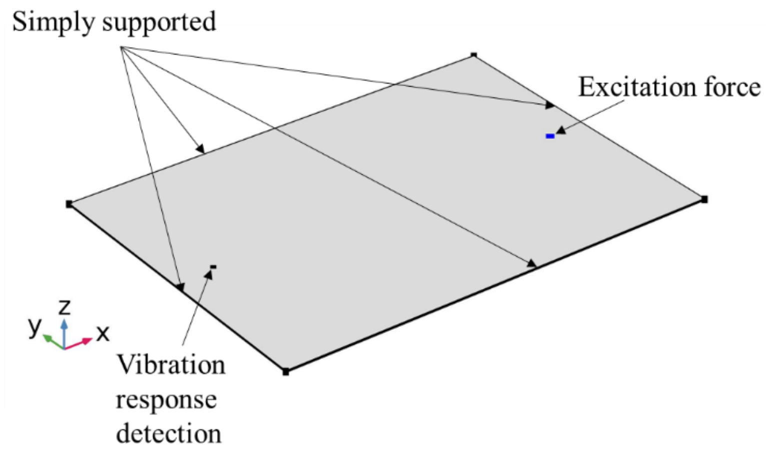

(a)

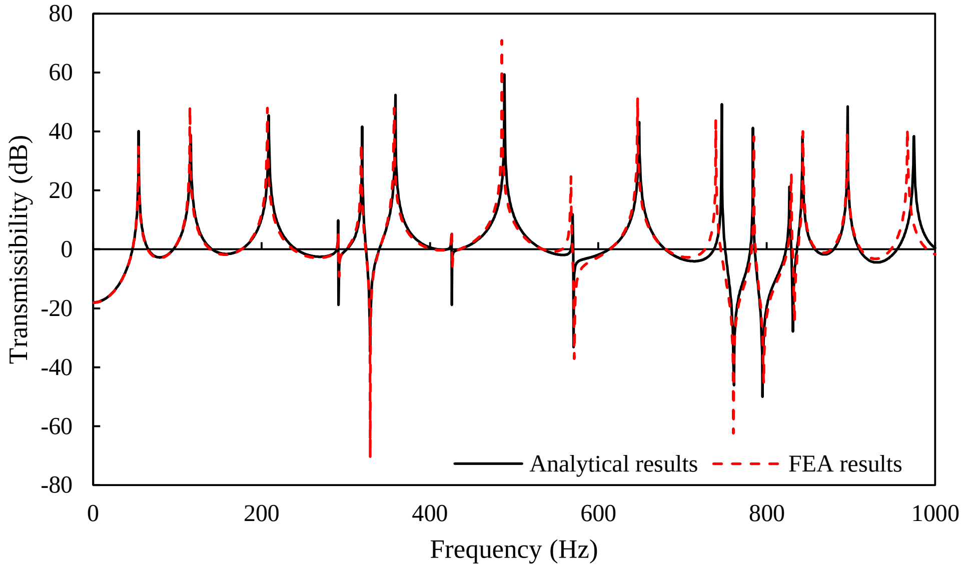

(b)

Figure 104. (a) Configuration of the thin plate; (b) Vibration transmissibility of a 0.55×0.4×0.002m aluminium plate obtained by analytical model and FEA calculation.

Secondly, several case studies are conducted to find out the optimum distribution of MemR on a thin plate structure.

The extra mass load caused by the vibration suppression mechanism is always a concern in the vibration control design process. For a tuned mass damper, to ensure the vibration suppression effect, the mass of resonators should be about 10% of the target structure's mass [148]. In this coupling model, the allocation of resonators can be designed and adjusted easily, with the attached mass varying. Therefore, investigation can be conducted to find out the optimum distribution, number of resonator and total attached mass for a certain type of thin plate.

In this section, a 0.55×0.4×0.002m thin aluminium plate is used as an example. To reveal the different vibration suppression effect, the total attached resonator mass is defined and the number of the resonators is adjusted, and the corresponding vibration suppression performance is obtained for analysis.

The mass of the bare plate is 1.188kg, and the total attached mass is defined as 0.2kg, which is 16.8% of the plate’s mass and it should be sufficient to achieve vibration control for the plate. Similar to the bare plate, the amplitude of incident force is still 1N, and applied at the point that located at the right side of the plate and signal detected from the left side. According to Figure 104(b), there are totally 14 resonant peaks revealed in the 0 – 1000Hz frequency region.

Through FEA, the corresponding shape of the first 10 peaks are presented in Figure 105. Under forced vibration, the deformation shape of the plate will be different from the resonant modes. For the purpose of comparing the deformation extents of the plate under different frequencies, the same deformation ratio, which is 1000 times, is adopted. In low order of resonant peaks, the vibration deformation is larger and more concentrated, whilst the deformations in the higher frequency resonant peaks are smaller and distributed all over the plate.

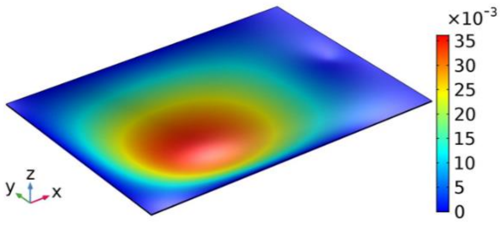

54.0Hz

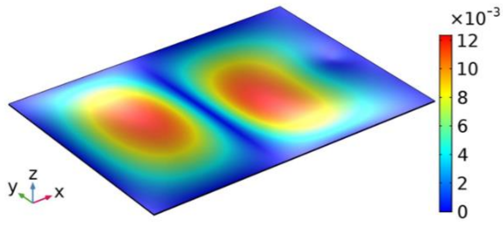

115.0Hz

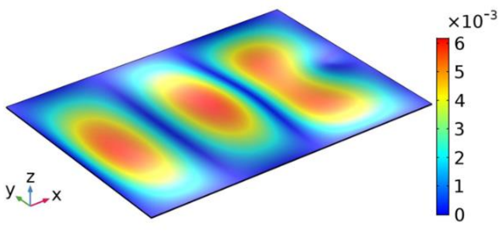

207.0Hz

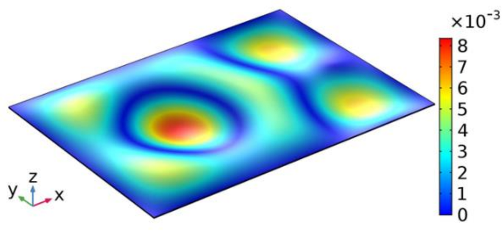

318.5Hz

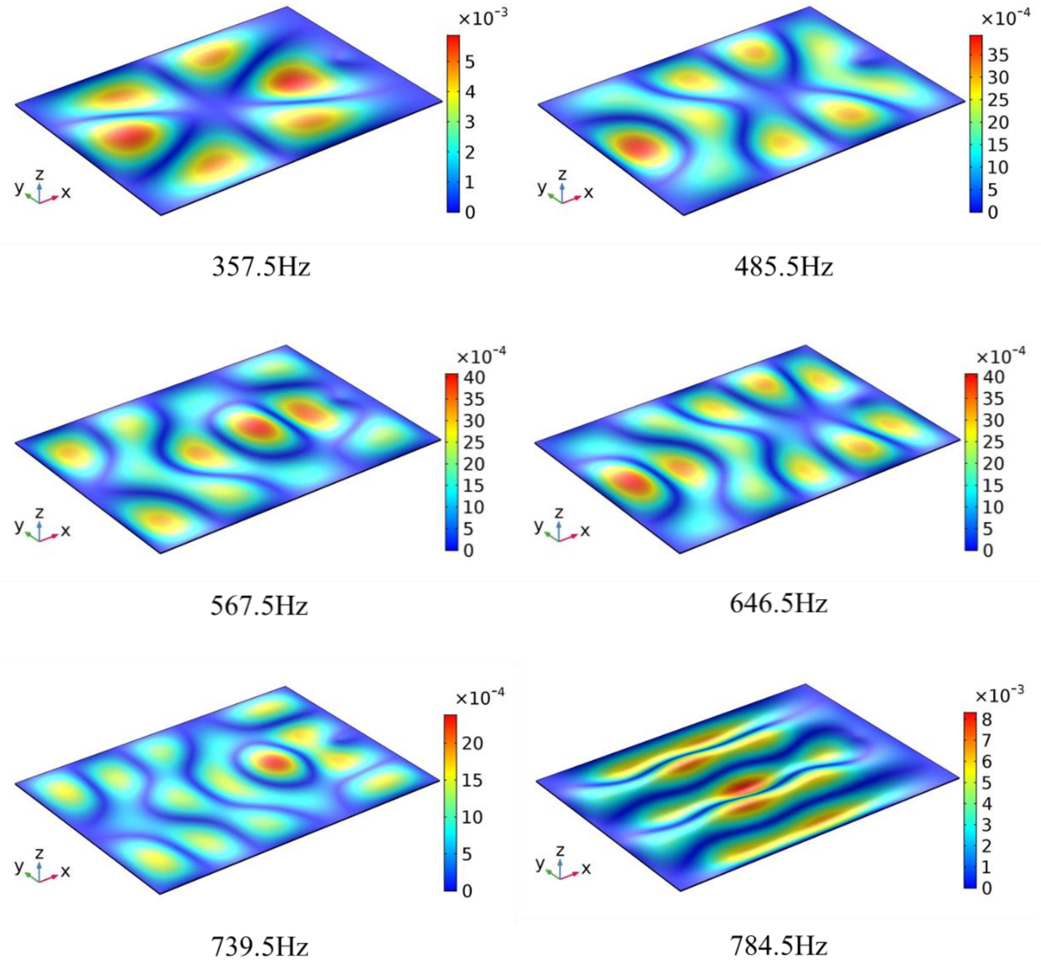

Figure 105. Shape of the bare plate at the resonant peak frequencies. The unit of the legend on the right is mm.

To maximise the vibration suppression effect of a resonator, it should be allocated at the point that has the largest displacement during vibration since the vibration energy density will be the highest at that point. Hence, when the total attached mass is the same, the number of resonator should be smaller and allocated as a cluster. Otherwise, for the higher order of resonant frequencies, the resonator should be distributed averagely and widely over the whole surface of the plate.

In order to examine the actual influence of resonator distribution, comparison are made and analysed. When aiming for eliminating the 1st resonant peak in the transmissibility curve, use 1 or 20 resonators respectively and the total resonator mass is defined as 0.2kg. The resonator mass for the 1 and 20 resonators cases are 0.2kg and 0.01kg respectively, and to ensure the resonant frequencies are the same in the two cases, the tensile stress of the MemR in the model will be adjusted accordingly.

When only 1 resonator with 0.2kg mass is employed, according to the deformation shape shown in Figure 105, it should be attached at the middle point of the plate since it is the largest displacement point. In addition, in the 20 resonators case, the resonators are distributed over the surface of the plate averagely. The vibration transmissibility of both cases are obtained and presented in Figure 106.

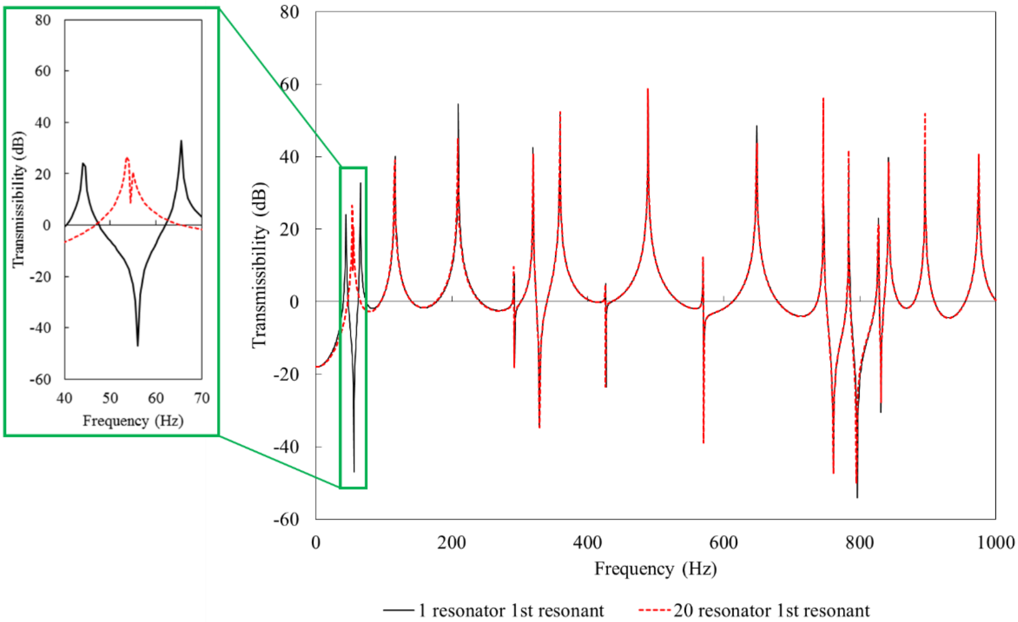

Figure 106. The vibration transmissibility curves of the 0.55×0.4×0.002m aluminium plate when 1 resonator (black-solid) or 20 resonators (red-dashed) are attached respectively. The resonant frequency of the resonators are set the same as the 1st order resonant frequency. Total resonator mass is 0.2kg.

As shown in the figure, when multiple resonators are attached, the vibration suppression in the 1st resonant peak is not obvious. On contrary, the resonant peak is effectively suppressed when only 1 resonator is applied and two anti-resonant peaks are revealed.

When tuned the operational frequency of the resonator to the 7th resonant peak (488.5Hz) of the plate, the vibration suppression of the plate with 1 and 20 resonators attached are also obtained and presented in Figure 107. The results indicate that for a higher resonant mode, the averagely distributed resonators can achieve better vibration suppression performance than the single resonator. The vibration energy in higher order resonant is distributed all over the plate rather than concentrating on one point.

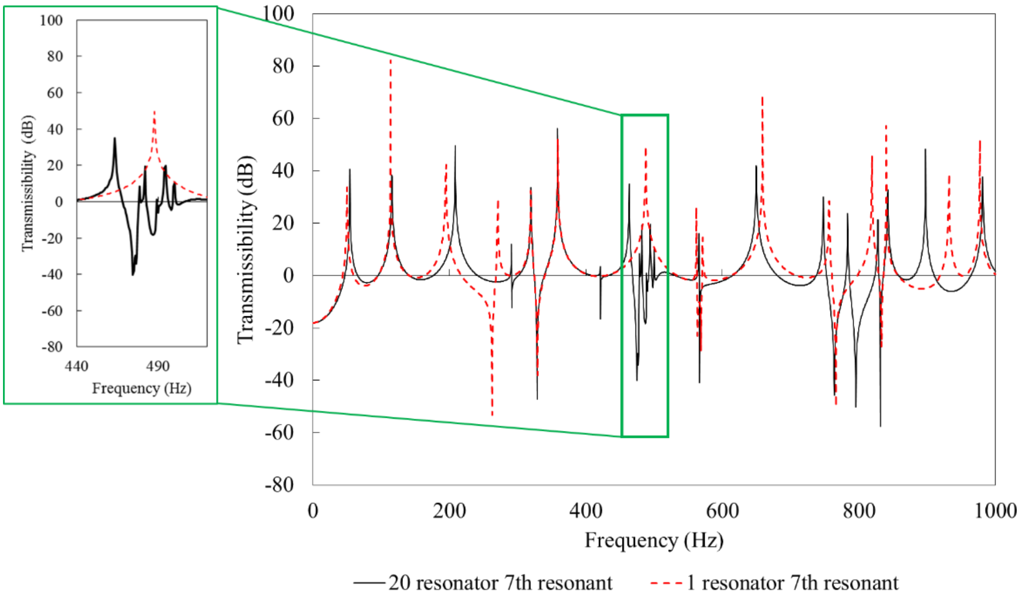

Figure 107. The vibration transmissibility curves of the 0.55×0.4×0.002m aluminium plate when 1 resonator (black-solid) or 20 resonators (red-dashed) are attached respectively. The resonant frequency of the resonators are set the same as the 7th order resonant frequency. Total resonator mass is 0.2kg.

Therefore, the proposed thin plate – resonator model can be utilized for the optimisation of membrane-type resonator allocation and design on the thin plate structure.

Also, since in this model, each of the resonator's property can be defined individually, the non-periodic allocation of MemRs can also be utilised and the vibration suppression performance be revealed.

Such function can be used for optimisation of the resonator location and resonant frequency tuning. It will be a promising direction in the future research. With different given incident frequencies, the model can analyse which resonators will experience the largest displacement. It means the vibration in that exact area is much fiercer than in the other parts. Therefore, the resonator's resonant frequency can be adjusted to become the same as the incident frequency which makes the resonator experience the maximum displacement. Such setting will achieve the optimum vibration suppression performance. Also, in a semi-active control system, this algorithm will allow the system to rapidly decide the optimal voltage distribution to different resonators to achieve best vibration control performance.

6.2 PVDF MemM Control System's Transfer Function and Algorithm

To conduct semi-active control of the PVDF MemM, the control system model of should be constructed. If define the displacement of the resonator attached point on plate W as the output signal, and forces applied to the plate by the MemRs as input signal, a feedback control system can be constructed and the block diagram of the system is given in Figure 108.

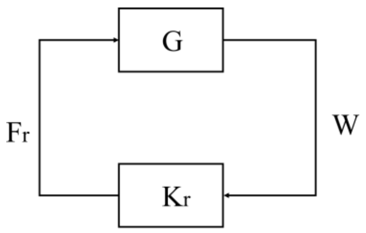

Figure 108. Block diagram of the PVDF MemM's feedback control system.

The derivation of the control system is stated as following:

For the membrane-type resonators attached on a thin plate structure, if the number of resonators is R, the system's equation of motion can be given as:

$$\begin{cases} D\nabla^4 W(r,t) + \rho h W(r,t)'' = \sum_{r}^{R} F_r(t)\delta(r - R_r) & \text{(6-16a)} \\ m_r \dfrac{\partial^2 X_r(t)}{\partial t^2} = k_r[W(R_r,t) - X_r(t)] & \text{(6-16b)} \end{cases}$$

where D is the flexural stiffness of the plate, $W(r,t)$ and $W(R_r,t)$ are the transverse displacements of the plate at point $r = (x,y)$ and at the point where resonator r is attached; ρ is the mass density of the plate material; h is the plate thickness; m_r is the mass of the resonator r; k_r is the equivalent stiffness of the resonator; X_r is the resonator's transverse displacement; $F_r(t)$ is the force applied to the plate by the resonator r and it can be expressed as:

$$F_r(t) = -k_r[W(R_r,t) - X_r(t)] \tag{6-17}$$

If assume the displacement as a series expansion:

$$W(r,t) = \sum_{j}^{J} \phi_j(r) q_j(t) \tag{6-18}$$

Substitute equation (6-18) into equation (6-17) and conduct Laplacian transform:

$$F_r(s) = -k_r \left[\sum_{j}^{J} \phi_j(R_r) q_j(s) - X_r(s) \right] \tag{6-19}$$

Substitute equation (6-18) into equation (6-16b) and conduct Laplacian transform:

$$m_r X_r(s) s^2 = k_r \left[\sum_{j}^{J} \phi_j(R_r) q_j(s) - X_r(s) \right]$$

$$\rightarrow X_r(s) = \frac{k_r}{k_r + m_r s^2} \sum_{j}^{J} \phi_j(R_r) q_j(s) \tag{6-20}$$

Substitute equation (6-20) into equation (6-19):

$$F_r(s) = -k_r \left[\sum_{j}^{J} \phi_j(R_r) q_j(s) - \frac{k_r}{k_r + m_r s^2} \sum_{j}^{J} \phi_j(R_r) q_j(s) \right]$$

$$\rightarrow F_r(s) = -\frac{k_r m_r s^2}{k_r + m_r s^2} \sum_{j}^{J} \phi_j(R_r) q_j(s) \tag{6-21}$$

The above equation can be changed into matrix form as:

$$[F_r(s)] = [K_r][W]$$

where:

$$[F_r(s)] = [F_1(s), F_2(s), F_3(s), \dots \dots, F_R(s)]^T$$

$$[K_r] = \begin{bmatrix} \frac{-k_1 m_1 s^2}{k_1 + m_1 s^2} & 0 & 0 \\ 0 & \ddots & 0 \\ 0 & 0 & \frac{-k_R m_R s^2}{k_R + m_R s^2} \end{bmatrix}$$

$$[W] = [W(R_1, s), W(R_2, s), W(R_3, s), \dots \dots, W(R_R, s)]^T.$$

Therefore the $[K_r]$ matrix is obtained. Then for the transfer function $[G]$, equation (6-16a) can be transformed into:

$$D \sum_j^J \phi_j(r)'''' q_j(t) + \rho h \sum_j^J \phi_j(r) q_j(t)'' = \sum_r^R F_r(t) \delta(r - R_r). \tag{6-22}$$

Apply the orthogonally condition and integrate over the plate surface S, and conduct Laplacian transform, the above equation in changed into:

$$D\int_S \sum_j^J \phi_j(r)''''q_j(t)\phi_i(r)\,dS + \rho h\int_S \sum_j^J \phi_j(r)q_j(t)''\,\phi_i(r)dS$$
$$= \int_S \sum_r^R F_r(t)\phi_i(r)\delta(r-R_r)dr$$
$$\to \left(\omega_j^2 + s^2\right)q_j(s) = \sum_r^R F_r(s)\phi_j(R_r)$$
$$\to q_j(s) = \sum_r^R \frac{\phi_j(R_r)}{\omega_j^2 + s^2}F_r(s) \tag{6-23}$$

The displacement of the plate at the points where resonators are attached can be expanded as:

$$W(R_r, s) = \sum_j^J \phi_j(R_r)q_j(s) \tag{6-24}$$

Substitute equation (6-23) into equation (6-24):

$$W(R_r, s) = \sum_j^J \phi_j(R_r)\left[\sum_r^R \frac{\phi_j(R_r)}{\omega_j^2 + s^2}F_r(s)\right]$$

$$= \phi_1(R_r)\left[\frac{\phi_1(R_1)}{\omega_1^2+s^2}F_1(s) + \frac{\phi_1(R_2)}{\omega_1^2+s^2}F_2(s) + \frac{\phi_1(R_3)}{\omega_1^2+s^2}F_3(s) + \cdots + \frac{\phi_1(R_R)}{\omega_1^2+s^2}F_R(s)\right]$$

$$+ \phi_2(R_r)\left[\frac{\phi_2(R_1)}{\omega_2^2+s^2}F_1(s) + \frac{\phi_2(R_2)}{\omega_2^2+s^2}F_2(s) + \frac{\phi_2(R_3)}{\omega_2^2+s^2}F_3(s) + \cdots + \frac{\phi_2(R_R)}{\omega_2^2+s^2}F_R(s)\right]$$

$$+ \cdots$$

$$+ \phi_J(R_r)\left[\frac{\phi_J(R_1)}{\omega_J^2+s^2}F_1(s) + \frac{\phi_J(R_2)}{\omega_J^2+s^2}F_2(s) + \frac{\phi_J(R_3)}{\omega_J^2+s^2}F_3(s) + \cdots + \frac{\phi_J(R_R)}{\omega_J^2+s^2}F_R(s)\right] \tag{6-25}$$

According to the above equation, the force terms can be extracted and thus transform the equation into:

$$W(R_r,s)=F_1(s)\left[\frac{\phi_1(R_r)\phi_1(R_1)}{\omega_1^2+s^2}+\frac{\phi_2(R_r)\phi_2(R_1)}{\omega_2^2+s^2}+\cdots+\frac{\phi_J(R_r)\phi_J(R_1)}{\omega_J^2+s^2}\right]$$

$$+F_2(s)\left[\frac{\phi_1(R_r)\phi_1(R_2)}{\omega_1^2+s^2}+\frac{\phi_2(R_r)\phi_2(R_2)}{\omega_2^2+s^2}+\cdots+\frac{\phi_J(R_r)\phi_J(R_2)}{\omega_J^2+s^2}\right]$$

$$+\cdots$$

$$+F_R(s)\left[\frac{\phi_1(R_r)\phi_1(R_R)}{\omega_1^2+s^2}+\frac{\phi_2(R_r)\phi_2(R_R)}{\omega_2^2+s^2}+\cdots+\frac{\phi_J(R_r)\phi_J(R_R)}{\omega_J^2+s^2}\right] \quad \text{(6-26)}$$

The above equation can be changed into matrix form:

$$[W]_{R\times 1}=[G]_{R\times R}[F_r(s)]_{R\times 1}$$

where:

$$[G]=\begin{bmatrix} \frac{\phi_1(R_1)\phi_1(R_1)}{\omega_1^2+s^2}+\frac{\phi_2(R_1)\phi_2(R_1)}{\omega_2^2+s^2}+\cdots+\frac{\phi_J(R_1)\phi_J(R_1)}{\omega_J^2+s^2}, & \ldots, & \frac{\phi_1(R_1)\phi_1(R_R)}{\omega_1^2+s^2}+\frac{\phi_2(R_1)\phi_2(R_R)}{\omega_2^2+s^2}+\cdots+\frac{\phi_J(R_1)\phi_J(R_R)}{\omega_J^2+s^2} \\ \frac{\phi_1(R_2)\phi_1(R_1)}{\omega_1^2+s^2}+\frac{\phi_2(R_2)\phi_2(R_1)}{\omega_2^2+s^2}+\cdots+\frac{\phi_J(R_2)\phi_J(R_1)}{\omega_J^2+s^2}, & \ldots, & \frac{\phi_1(R_2)\phi_1(R_R)}{\omega_1^2+s^2}+\frac{\phi_2(R_2)\phi_2(R_R)}{\omega_2^2+s^2}+\cdots+\frac{\phi_J(R_2)\phi_J(R_R)}{\omega_J^2+s^2} \\ \vdots & & \vdots \\ \frac{\phi_1(R_R)\phi_1(R_1)}{\omega_1^2+s^2}+\frac{\phi_2(R_R)\phi_2(R_1)}{\omega_2^2+s^2}+\cdots+\frac{\phi_J(R_R)\phi_J(R_1)}{\omega_J^2+s^2}, & \ldots, & \frac{\phi_1(R_R)\phi_1(R_R)}{\omega_1^2+s^2}+\frac{\phi_2(R_R)\phi_2(R_R)}{\omega_2^2+s^2}+\cdots+\frac{\phi_J(R_R)\phi_J(R_R)}{\omega_J^2+s^2} \end{bmatrix}_{R\times R}$$

$$\rightarrow [G]=\sum_j^J \frac{P_j^T P_j}{s^2+2\xi_j\omega_j s+\omega_j^2}F_r(s) \quad \text{(6-27)}$$

where $P_j=\left[\phi_j(R_1),\right]$

If define $[Q(t)]=[q_1(t),q_2(t),\ldots,q_J(t),\dot{q}_1(t),\dot{q}_2(t),\ldots,\dot{q}_J(t)]^T$, then the state-space form of the transfer function can be written as:

$$\begin{cases}[\dot{Q}(t)]=\begin{bmatrix}\mathbf{0} & \boldsymbol{I}\\ \boldsymbol{H} & \boldsymbol{\Theta}\end{bmatrix}[Q(t)]+\begin{bmatrix}\mathbf{0}\\ \overline{\boldsymbol{P}}\end{bmatrix}[F(t)]^T & \text{(6-28a)}\\ [W(R_r,t)]=[\boldsymbol{U}\ \mathbf{0}][Q(t)] & \text{(6-28b)}\end{cases}$$

where:

$$\boldsymbol{I}=\begin{bmatrix}1 & \cdots & 0\\ \vdots & \ddots & \vdots\\ 0 & \cdots & 1\end{bmatrix}_{J\times J},\ \overline{\boldsymbol{P}}=\begin{bmatrix}P_1\\ \vdots\\ P_J\end{bmatrix}_{J\times R}$$

$$\boldsymbol{\Theta}=diag\left(-2\xi_1\omega_1,-2\xi_2\omega_2,\ldots,-2\xi_J\omega_J\right)_{J\times J},$$

$$\boldsymbol{H}=diag(-\omega_1^2,-\omega_2^2,\ldots,-\omega_J^2)_{J\times J},$$

$$[W(R_r, t)] = [W(R_1, t), \dots, W(R_R, t)]_{1\times R}^T,$$

$$\boldsymbol{U} = \begin{bmatrix} \phi_1(R_1) & \cdots & \phi_J(R_1) \\ \vdots & \ddots & \vdots \\ \phi_1(R_R) & \cdots & \phi_J(R_R) \end{bmatrix}_{R\times J},$$

$$[F(t)] = [F_1(t), \dots, F_R(t)]_{1\times R}^T.$$

The equation can be transferred into Matlab programme and be used to conduct fast frequency response analysis of the structure, which is useful in the optimisation of the allocation of MemM and design. Also, it provides the analytical foundation for the semi-active control algorithm, which can be further developed in future work.

Chapter 7

7. CONCLUSIONS AND FUTURE WORK

In this research, bandgap properties, key design parameters, structural vibration absorption capability and the corresponding analytical models of proposed metamaterial is investigated and developed. Conclusions can be drawn as below:

1. The proposed EM can suppressed the structural vibration of a thin plate structure effectively. The bandgap performance of the EM is consistent with the prediction based on the local resonant phenomenon and dispersion relation. The bandgap properties can be tuned effectively through geometrical structure adjustment. Broad low frequency bandgap is revealed in numerical simulation and the experimental results demonstrates even better vibration absorption performance. The results confirm the effectiveness of the local resonant phenomenon in bandgap formation.
2. PWE model is modified to contain the MemR's analytical model and can be used for the prediction of MemM's bandgap property. Through further modification of the model, bandgap property of the multi-layer metamaterial can also be estimated, which is also a novelty in the MemM research field. The accuracy of the model is then verified by numerical simulation.
3. Effect of MemM's design parameters on bandgap properties is systematically studied by the modified PWE model. It is found that increase of MemR's equivalent stiffness and attached mass magnitudes can increase the bandgap width. In bilayer MemM, interaction between

the two membrane layers will affect the bandgap width. In order to achieve maximum bandgap width or bandgap tunability, design guidelines for the bilayer MemM is concluded.

4. Analytical model of PVDF MemM applied on thin plate is developed. The model constructs the relation between applied electric field intensity and PVDF MemM bandgap properties. The model reveals that the application of ±1000V electric potential across the PVDF membrane can cause a 65.4Hz bandgap location shift. In addition, the analytical model results are consistent with the numerical simulation. Therefore, the PVDF MemM possess a significant bandgap tunability, and demonstrates the feasibility of conducting semi-active control for the purpose of broadening bandgap width.
5. Numerical simulation and experiment testing verify the effectiveness of MemM in thin plate vibration absorption. Vibration suppression of an aluminium thin plate is achieved obviously when attached with MemM.
6. Analytical model of semi-active control system for PVDF MemM applied on a thin plate is developed. Based on the thin plate – resonator coupling model, the design parameters, such as tensile stress, mass magnitude, electric filed intensity and membrane thickness, can be adjusted freely and reveal their effect on bandgap performance.

Several potential future work directions are recommended as below:

1. Design and optimisation of MemR's producing and assembling process and technique. In this research, the MemRs were mainly manually assembled. Hence, error occurred inevitably and leads to an unideal experiment results. The accurate and reliable manufacturing process can

ensure the effective of future research of MemM and encourage the actual application.

2. Based on the derived semi-active control algorithm of the PVDF MemM, complete the derivation and construction of control system. Build up numerical simulation model for the algorithm and control model in Simulink to verify its controllability and robustness. Also, through the model, further study the vibration suppression performance of the PVDF MemM. T
3. Study the multi-layer PVDF MemM's bandgap property and vibration absorption performance based on the research outcome of this study. Since the utilization of PVDF MemM can achieve a considerable bandgap tuning range, the combination of multiple PVDF MemM can significantly increase the bandgap width. The corresponding control system and analytical model should also be developed and verified.
4. Conduct experimental study on the PVDF MemM's vibration absorption performance. Experimental testing is a compulsory step for the verification and application of PVDF MemM.
5. Based on the analytical model proposed in Chapter 6, optimise the distribution, attached mass magnitude and total number of MemM. Current results have suggested that for different incident frequencies, there will be various optimal resonator allocations. As a result, optimisation guidelines should be concluded for the purpose of achieving the best vibration suppression performance whilst causing the smallest influence to the target structure.

-Total word count: 37,564-

Excluding topic, titles, footnotes, captions and tables.

REFERENCES

[1] M. Acar and C. Yilmaz, “Design of an adaptive-passive dynamic vibration absorber composed of a sring-mass system equipped with negative stiffness tension adjusting mechanism,” *Journal of Sound and Vibration,* vol. 332, pp. 231-245, 2013.

[2] B. Fu, H. Jiang and T. Wu, “Comparative studies of vibration control effects between structures with particle dampers and tuned liquid dampers using substructure shake table testing methods,” *Soil Dynamics and Earthquake Engineering,* vol. 121, pp. 421-435, 2019.

[3] E. Nobrega, F. Gautier, A. Pelat and J. Dos Santos, “Vibration band gaps for elastic metamaterial rods using wave finite element method,” *Mechanical Systems and Signal Processing,* vol. 79, pp. 192-202, 2016.

[4] A. Kumar, S. Panda, A. Kumar and V. Narsaria, “Performance of a graphite wafer-reinforced viscoelastic composite layer for active-passive damping of plate vibration,” *Composite Structures,* vol. 186, pp. 303-314, 2018.

[5] F. Cotes and M. Elejabarrieta, “Structural vibration of flexural beams with thick unconstrained layer damping,” *International Journal of Solids and Structures,* vol. 45, pp. 5805-5813, 2008.

[6] J. Hartog, Mechanical Vibration, 4 ed., New York: McGraw-Hill, 1956.

[7] M. Maslanka, “Optimised semi-active tuned mass damper with acceleration and relative motion feedbacks,” *Mechanical Systems and Signal Processing,* vol. 130, pp. 707-731, 2019.

[8] T. Igusa and K. Xu, “Vibration control using multiple tuned mass dampers,” *Journal of Sound and Vibration,* vol. 175, no. 4, pp. 491-503, 1994.

[9] M. Kushwaha, P. Halevi, L. Dobrzynski and B. Djafari-Rouhani, “Acoustic band structure of periodic elastic composites,” *Physical Review Letters,* vol. 71, no. 13, p. 2022, 1993.

[10] S. John, “Strong localization of photons in certain disordered dielectric superlattices,” *Physical review letters,* vol. 58, no. 23, p. 2486, 1987.

[11] E. Yablonovitch, “Inhibited spontaneous emission in solid-state physics and electronics,” *Physical Review Letters,* vol. 58, no. 20, p. 2059, 1987.

[12] M. Sigalas and E. Economou, “Band structure of elastic waves in two dimensional systems,” *Solid State Commun.,* vol. 86, pp. 141-143, 1993.

[13] R. Olsson and I. El-Kady, “Microfabricated phononic crystal devices and applications,” *Measurement Science and Technology* , vol. 20, p. 012002, 2009.

[14] G. Piazza, P. Stephanou and A. Pisano, “Single-chip multiple frequency AIN MEMS filters based on contour-mode piezoelectric resonators,” *Microelectromechanical systems,* vol. 16, pp. 319-328, 2007.

[15] Y. Pennec, B. Djafari-Rouhani, J. Vasseur, A. Khelif and P. Deymier, “Tunable filtering and demultiplexing in phononic crystals with hollow cylinders,” *Physical Review E,* vol. 69, no. 4, p. 046608, 2004.

[16] J. Wu, F. Ma, S. Zhang and L. Shen, “Application of acoustic metamaterials in low-frequency vibration and noise reduction,” *Journal of Mechanical Engineering,* vol. 52, no. 13, pp. 68-78, 2016.

[17] Z. Liu, X. Zhang, Y. Mao, Y. Zhu, Z. Yang, C. Chan and P. Sheng, “Locally resonant sonic materials,” *Science,* vol. 289, no. 5485, pp. 1734-1736, 2000.

[18] U. Pranav, S. Sudheesh, P. Stanly, S. Sankar, R. Devika and A. Pradeep, “Metamaterial based energy harvester,” *Procedia Computer Science,* pp. 74-80, 2016.

[19] C. Shuang, Y. Fan, Q. Fu, H. Wu, Y. Jin, J. Zheng and F. Zhang, “A Review of Tunable Acoustic Metamaterials,” *Applied Sciences,* vol. 8, no. 9, p. 1480, 2018.

[20] F. Langfeldt and W. Gleine, “Membrane- and plate-type acoustic metamaterials with elastic unit cell edges,” *Journal of Sound and Vibration,* vol. 453, pp. 65-86, 2019.

[21] M. Nouh, J. A. Osama and A. Baz, “Periodic metamaterial plates with smart tunable local resonators,” *Journal of Intelligent Material Systems and Structures,* vol. 27, no. 13, pp. 1829-1845, 2016.

[22] L. Brillouin, Wave propagation in periodic structures electric filters and crystal lattices, New York: Dover Publications, Inc., 1946.

[23] M. Hussein, M. Leamy and M. Ruzzene, “Dynamics of phononic materials and structures: Historical origins, recent progress, and future outlook,” *Applied Mechanics Reviews,* vol. 66, p. 040802, 2014.

[24] C. Sun, J. Achenbach and G. Herrmann, “Continuum Theory for a Laminated Medium,” *Journal of Applied Mechanics,* vol. 35, no. 3, pp. 467-475, 1968.

[25] S. Nemat-Nasser, “General variational methods for waves in elastic composites,” *Journal of Elasticity,* vol. 2, pp. 73-90, 1972.

[26] A. Fahmy and E. Adler, “Propagation of acoustic waves in multilayers: a matrix description,” *Applied Physics Letter,* vol. 20, pp. 495-497, 1973.

[27] H. Murakami and A. Akiyama, “A mixture theory for wave propagation in angle-ply laminates, Part 2: application,” *ASME Journal of Applied Mechanics,* vol. 52, p. 338, 1985.

[28] V. Veselago, “The electrodynamics of substances with simultaneously negative values of ε and μ,” *Soviet Physics Uspekhi,* pp. 509-514, 1968.

[29] B. Djafari-Rouhani, J. Vasseur, A. Hladky-Hennion, P. Deymier, F. Duval, B. Dubus and Y. Pennec, “Absolute band gaps and waveguiding in free standing and supported phononic crystal slabs,” *Photonics and Nanostructures: Fundamentals and Applications,* vol. 6, pp. 32-37, 2008.

[30] R. Mártinez-Sala , J. Sancho, J. Sánchez , V. Gomez and J. Llinares, “Sound attenuation by sculpture,” *Nature,* vol. 378, p. 241, 1995.

[31] A. Khelif and A. Adibi, Eds., Phononic Crystals: Fundamentals and Applications, 1 ed., London: Springer, 2016.

[32] F. de Espinosa, E. Jimenez and M. Torres, “Ultrasonic band gap in a periodic two-dimensional composite,” *Physical Review Letters,* vol. 6, p. 1208, 1998.

[33] G. Ma and P. Sheng, “Acoustic metamaterials: From local resonances to broad horizons,” *Science advances,* vol. 2, no. 2, p. e1501595, 2016.

[34] L. Fok, M. Ambati and X. Zhang, “Acoustic Metamaterials,” *MRS Bulletin,* vol. 33, pp. 931-934, 2008.

[35] Z. Chen, B. Guo, Y. Yang and C. Cheng, “Metamaterials-based enhanced energy harvesting: A review,” *Physica B,* pp. 1-8, 2014.

[36] R. Harne, Y. Song and Q. Dai, “Trapping and attenuating broadband vibroacoustic energy with hyperdamping metamaterials,” *Extreme Mechanics Letters,* vol. 12, pp. 41-47, 2017.

[37] A. Dubey and T. Shami, “Metamaterials in Electromagnetic Wave Absorbers,” *Defence Science Journal,* vol. 62, no. 4, pp. 261-268, 2012.

[38] S. Shoukat, S. Ahmed, M. Aqueel Ashraf, A. Syed and Q. Naqvi, “Scattering of electromagnetic plane wave from a chiral cylinder placed in chiral metamaterials,” *Journal of Electromagnetic Waves and Applications,* vol. 27, no. 9, pp. 1127-1135, 2013.

[39] H. Liu, J. Wu, S. Zhang and S. Li, “The research progress of acoustic metamaterials,” *Open Journal of Acoustic and Vibration,* pp. 7-13, 2013.

[40] J. Mei, G. Ma, M. Yang, J. Yang and P. Sheng, Acoustic Metamaterials and Phononic Crystals, New York: Springer, 2013.

[41] K. Ho, C. Cheng, Z. Yang, Zhang, X.X. and P. Sheng, “Broadband Locally Resonant Sonic Shields,” *Applied Physics Letter,* vol. 83, pp. 5566-5568, 2003.

[42] N. Fang, D. Xi, J. Xu, M. Ambati, W. Srituravanich, C. Sun and X. Zhang, “Ultrasonic metamaterials with negative modulus,” *Nature Materials,* vol. 5, pp. 452-456, 2006.

[43] J. Li and C. Chan, “Double-negative acoustic metamaterial,” *Physical Review E,* vol. 70, p. 055602, 2004.

[44] X. Zhou and G. Hu, “Analytic model of elastic metamaterials with local resonances,” *Physical Review B,* vol. 79, no. 19, p. 195109, 2009.

[45] Y. Ding, Z. Liu, C. Qiu and J. Shi, “Metamaterial with simultaneously negative bulk modulus and mass density,” *Physical Review Letters,* vol. 99, no. 9, p. 093904, 2007.

[46] X. Liu, G. Hu, G. Huang and C. Sun, “An elastic metamaterial with simultaneously negative mass density and bulk modulus,” *Applied Physics Letters,* vol. 98, p. 251907, 2011.

[47] Y. Lai, Y. Wu, P. Sheng and Z.-Q. Zhang, “Hybrid elastic solids,” *Nature Materials,* vol. 10, pp. 620-624, 2011.

[48] H. Huang and C. Sun, “Wave attenuation mechanism in an acoustic metamaterial with negative effective mass density,” *New Journal of Physics,* vol. 11, p. 013003, 2009.

[49] D. Chronopoulos, I. Antoniadis and T. Ampatzidis, “Enhanced acoustic insulation properties of composite metamaterials having embedded negative stiffness inclusions,” *Extreme Mechanics Letters,* vol. 12, pp. 48-54, 2017.

[50] D. DePauw, H. Al Ba'ba'a and M. Nouh, “Metadamping and energy dissipation enhancement via hybrid phononic resonators,” *Extreme Mechanics Letters,* vol. 18, pp. 36-44, 2018.

[51] J. Mei, Z. Liu, W. Wen and P. Sheng, “Effective dynamic mass density of composites,” *Physic Review B,* vol. 76, p. 134205, 2007.

[52] V. Garcia-Chocano, R. Gracia-Salgado, D. Torrent, F. Cervera and J. Sanchez-Dehesa, “Quasi-two-dimensional acoustic metamaterial with negative bulk modulus,” *Physical Review B,* vol. 85, p. 184102, 2012.

[53] S. Estéve and M. Johnson, “ Reduction of sound transmission into a circular cylindrical shell using distributed vibration absorbers and

Helmholtz resonators," *The Journal of the Acoustical Society of America,* vol. 112, no. 6, pp. 2840-2848, 2002.

[54] Q. Mao and S. Pietrzko, "Experimental study for control of sound transmission through double glazed window using optimally tuned Helmholtz resonators," *Applied Acoustics,* vol. 71, no. 1, pp. 32-38, 2010.

[55] A. Selamet and I. Lee, "Helmholtz resonator with extended neck," *The Journal of the Acoustical Society of America,* vol. 113, no. 4, pp. 1975-1985, 2003.

[56] R. Chanaud, "Effects of geometry on the resonance frequency of Helmholtz resonators," *Journal of Sound and Vibration,* vol. 3, pp. 337-348, 1994.

[57] S. Chen, Y. Fan, Q. Fu, Q. Wu, H. Wu, Y. Jin, J. Zheng and F. Zhang, "A review of tunable acoustic metamaterials," *Appliced Sciences,* vol. 8, p. 1480, 2018.

[58] A. Liu, W. Zhu, D. Tsai and N. Zheludev, "Micromachined tunable metamaterials: a review," *Journal of Optics,* vol. 14, p. 114009, 2012.

[59] M. Hirsekorn, P. Delsanto, N. Batra and P. Matic, "Modelling and simulation of acoustic wave propagation in locally resonant sonic materials," *Ultrasonics,* vol. 42, no. 1, pp. 231-235, 2004.

[60] M. Hirsekorn, P. Delsanto, A. Leung and P. Matic, "Elastic wave propagation in locally resonant sonic material: Comparison between local interaction simulation approach and modal analysis," *Journal of Applied Physics,* vol. 99, no. 12, p. 124912, 2006.

[61] P. Qi, J. Du, J. Jiang, Y. Dong and J. Zhang, "Study on the phononic crystals bandgap properties of double local resonance mechanism," *Materials Review B,* vol. 30, no. 5, pp. 144-147, 2016.

[62] A. Nateghi, L. Van Belle, C. Claeys, E. Deckers, B. Pluymers and W. Desmet, "Stopband behavior in infinite metamaterial pipes," in *PROCEEDINGS OF ISMA2016 INTERNATIONAL CONFERENCE ON NOISE AND VIBRATION ENGINEERING AND USD2016 INTERNATIONAL CONFERENCE ON UNCERTAINTY IN STRUCTURAL DYNAMICS,* Leuven, Belgium, 2016.

[63] J. He and H. Huang, "Complete vibrational bandgap in thin elastic metamaterial plates with periodically slot-embedded local resonators," *Archive of Applied Mechanics,* vol. 8, pp. 1263-1274, 2018.

[64] Y. Huang, J. Li, W. Chen and R. Bao, "Tunable bandgaps in soft phononic plates with spring-mass-like resonators," *International Journal of Mechanical Sciences,* vol. 151, pp. 300-313, 2019.

[65] K. H. Matlack, A. Bauhofer, S. Krodel, A. Palermo and C. Daraio, "Composite 3D-printed metastructures for low-frequency and broadband vibration absorption," *PNAS,* vol. 113, no. 30, pp. 8386-8390, 2016.

[66] X. Ren, J. Shen, P. Tran, T. Ngo and Y. Xie, "Design and characterisation of a tuneable 3D buckling-induced auxetic metamaterial," *Materials & Design,* vol. 139, pp. 336-342, 2018.

[67] Y. Wang, "Bandgap properties and design of phononic crystals with resonant units," Beijing Jiaotong University, Beijing, 2015.

[68] M. Lu, L. Feng and Y. Chen, "Phononic crystals and acoustic metamaterials," *Materials Today,* vol. 12, no. 12, pp. 34-42, 2009.

[69] M. Sigalas and E. Economou, "Elastic and acoustic wave band structure," *Journal of Sound and Vibration,* vol. 158, no. 2, pp. 377-382, 1992.

[70] J. Vasseur, B. Djafari-Rouhani, L. Dobrzynski, M. Kushwaha and P. Halevi, "Complete acoustic band gaps in periodic fibre reinforced composite materials: the carbon/epoxy composite and some metallic systems," *Journal of Physics: Condensed Matter,* vol. 42, no. 6, p. 8759, 1994.

[71] R. Camley, B. Djafari-Rouhani and L. Dobrzynski, "Transverse elastic waves in periodically layered infinite and semi-infinite media," *Physic Review B,* vol. 27, no. 12, pp. 7318-7329, 1983.

[72] R. Esquivel-Sirvent and G. Cocoletzi, "Band structure for the propagation of elastic waves in superlattices," *The Journal of the Acoustical Society of America,* vol. 95, no. 1, pp. 86-90, 1994.

[73] M. Kafesaki and E. Economou, "Multiple-scattering theory for three-dimensional periodic acoustic composites," *Physical Review B,* vol. 60, no. 17, p. 11993, 1999.

[74] I. Psarobas, N. Stefanou and A. Modinos, "Scattering of elastic waves by periodic arrays of spherical bodies," *Physical Review B,* vol. 62, no. 1, p. 278, 2000.

[75] Z. Liu, C. Chan, P. Sheng, A. Goertzen and J. Page, "Elastic wave scattering by periodic structures of spherical objects: Theory and experiment," *Physical Review B,* vol. 62, no. 4, p. 2446, 2000.

[76] D. Garcia-Pablos, M. Sigalas, F. Montero de Espinosa, M. Torres, M. Kafesaki and N. Garcia, "Theory and experiments on elastic band gaps," *Physical Review Letters,* vol. 84, no. 19, p. 4349, 2000.

[77] Y. Tanaka, Y. Tomoyasu and S. Tamura, "Band structure of acoustic waves in phononic lattices: Two-dimensional composites with larger

acoustic mismatch," *Physical Review B,* vol. 62, no. 11, pp. 7387-7392, 2000.

[78] J. Wen, "Vibration attenuation and band gap characteristics of phononic crystals," University of Defense Technology, Changsha, China, 2005.

[79] M. Wilm, S. Ballandras, v. Laude and T. Pastureaud, "A full 3D plane-wave-expansion model for 1-3 piezoelectric composite structures," *The Journal of the Acoustical Society of America,* vol. 112, no. 3, pp. 943-952, 2002.

[80] C. Goffaux and J. Sánchez-Dehesa, "Two-dimensional phononic crystals studied using a variational method: Application to lattices of locally resonant materials," *Physical review B,* vol. 67, no. 14, p. 144301, 2003.

[81] Y. Cao, Z. Hou and Y. Liu, "Convergence problem of plane-wave expansion method for phononic crystals," *Physics Letters A,* vol. 327, no. 2-3, pp. 247-253, 2004.

[82] J. Hsu and T. Wu, "Efficient formulation for band-structure calculations of two-dimensional phononic-crystal plates," *Physical Review B,* vol. 74, no. 14, p. 144303, 2006.

[83] T.-T. Wu, Z.-G. Huang and S. Lin, "Surface and bulk acoustic waves in two-dimensional phononic crystal consisting of materials with general anisotropy," *Physical Review B,* vol. 69, p. 094301, 2004.

[84] Y. Tanaka and S. Tamura, "Surface acoustic waves in two-dimensional periodic elastic structures," *Physical Review B,* vol. 58, no. 12, p. 7958, 1998.

[85] Z. Yang, J. Mei, M. Yang, N. Chan and P. Sheng, "Membrane-type acoustic metamaterial with negative dynamic mass," *Physical review letters,* vol. 101, no. 20, p. 204301, 2008.

[86] J.-S. Chen, Y.-J. Huang and I.-T. Chien, "Flexural wave propagation in metamaterial beams containing membrane-mass structures," *International Journal of Mechanical Sciences,* Vols. 131-132, pp. 500-506, 2017.

[87] Q. Zhu, H. Bai, C. Lu, K. Huang, T. Li and C. Yang, "Analysis on the equivalent properties of metamaterial membranes," *Journal of Vibration and Shock,* vol. 36, no. 18, pp. 91-97, 2017.

[88] M. Nouh, O. Aldraihem and A. Baz, "Metamaterial Structures with Periodic Local Resonances," in *Health Monitoring of Structural and Biological Systems 2014,* San Diego, 2014.

[89] L. Dong, M. Grissom and F. T. Fisher, “Resonant frequency of mass-loaded membranes for vibration energy harvesting applications,” *AIMS Energy,* vol. 3, no. 3, pp. 344-359, 2015.

[90] H. Zhang, Y. Xiao, J. Wen, D. Yu and X. Wen, “Flexural wave band gaps in metamaterials beams with membrane-type resonators: theory and experiment,” *Journal of Physics D: Applied Physics,* vol. 48, p. 435305, 2015.

[91] K. Nagaya and K. Poltorak, “Method for solving eigenvalue problems of the Helmholtz equation with a circular outer and a number of eccentric circular inner boundaries,” *J. Acoust. Soc. Am.,* vol. 85, no. 2, pp. 576-581, 1989.

[92] O. Kopmaz and S. Telli, “Free vibration of a rectangular plate carrying a distributed mass,” *Journal of Sound and Vibration,* vol. 251, no. 1, p. 3957, 2002.

[93] Y. Zhang, J. Wen, Y. Xiao, X. Wen and J. Wang, “Theoretical investigation of the sound attenuation of membrane-type acoustic metamaterials,” *Physics Letter A,* vol. 376, pp. 1489-1495, 2012.

[94] L. Sun, K. Au-Yeung, M. Yang, S. Tang, Z. Yang and P. Sheng, “Membrane-type resonator as an effective miniaturized tuned vibration mass damper,” *AIP Advances* , vol. 6, p. 085212, 2016.

[95] L. Sun, “Experimental investigation of vibration damper composed of acoutic metamterials,” *Applied Acoustics,* vol. 119, pp. 101-107, 2017.

[96] P. Pai, “Metamaterial-based broadband elastic wave absorber,” *Journal of Intelligent Material Systems and Structures,* vol. 21, pp. 517-528, 2010.

[97] F. Ma, M. Huang, Y. Xu and J. Wu, “Bi-layer plate-type acoustic metamaterials with Willis coupling,” *Journal of Applied Physics,* vol. 123, p. 035104, 2018.

[98] J. Mei, G. Ma, M. Yang, Z. Yang, W. Wen and P. Sheng, “Dark acoustic metamaterials as super absorbers for low-frequency sound,” *Nature communications,* vol. 3, p. 756, 2012.

[99] N. Gao, H. Hou and Y. Mu, “Low frequency acoustic properties of bilayer membrane acoustic metamaterial with magnetic oscillator,” *Theoretical & Applied Mechanics Letters,* vol. 7, no. 4, pp. 252-257, 2017.

[100] F. Casadei, T. Delpero, A. Bergamini, P. Ermanni and M. Ruzzene, “Piezoelectric resonator arrays for tunable acoustic waveguides and metamaterials,” *Journal of Applied Physics,* vol. 112, p. 064902, 2012.

[101] P. Wang, F. Casadei, S. Shan, J. Weaver and K. Bertoldi, "Harnessing buckling to design tunable locally resonator acoustic metamaterials," *Physics Review Letters,* vol. 113, p. 014301, 2014.

[102] Z. Wang, Q. Zhang, K. Zhang and G. Hu, "Tunable digital metamaterial for broadband vibration isolation at low frequency," *Advanced Materials,* vol. 28, pp. 9857-9861, 2016.

[103] C. Nimmagadda and K. Matlack, "Thermally tunable band gaps in architected metamaterial structures," *Journal of Sound and Vibration,* vol. 439, pp. 29-42, 2019.

[104] Y. Cheng, X. Liu and D. Wu, "Temperature effects on the band gaps of Lamb waves in a one-dimensionnal phononic-crystal plate," *Journal of Acoustic Society of America,* vol. 129, no. 3, pp. 1157-1160, 2011.

[105] K. Jim, C. Leung, S. Lau, S. Choy and H. Chan, "Thermal tuning of phononic bandstructure in ferroelectric ceramic/epoxy phononic crystal," *Applied Physics Letters,* vol. 94, no. 19, p. 193501, 2009.

[106] C. Du, A. Plummer and D. Johnston, "Performance analysis of a new energy-efficient variable supply pressure electro-hydraulic motion control method," *Control Engineering Practice,* vol. 60, pp. 87-98, 2017.

[107] F. Langfeldt, J. Riecken, W. Gleine and O. von Estorff, "A membrane-type acoustic metamaterial with adjustable acoustic properties," *Journal of Sound and Vibration,* vol. 373, pp. 1-18, 2016.

[108] S. Xiao, G. Ma, Y. Li, Z. Yang and P. Sheng, "Active control of membrane-type acoustic metamaterial by electric field," *Applied Physics Letters,* vol. 106, no. 9, p. 091904, 2015.

[109] G. Ma, X. Fan, P. Sheng and M. Fink, "Shaping reverberating sound fields with an actively tunable metasurface," *Proceedings of the National Academy of Sciences of the United States of America,* vol. 115, pp. 6638-6643, 2018.

[110] X. Chen, X. Xu, S. Ai, H. Chen, Y. Pei and X. Zhou, "Active acoustic metamaterials with tunable effective mass density by gradient magnetic fields," *Applied Physics Letters,* vol. 105, p. 071913, 2014.

[111] W. Zhou, B. Wu, Muhammad, Q. Du, G. Huang, C. Lu and W. Chen, "Actively tunable transverse waves in soft membrane-type acoustic metamaterials," *Journal of Applied Physics,* vol. 123, p. 165304, 2018.

[112] X. Zhao and Z. Suo, "Theory of dielectric elastomers capable of giant deformation of actuation," *Physics Review Letters,* vol. 104, p. 178302, 2010.

[113] R. Karsten and H. Schlaak, “Adaptive absorber based on dielectric elastomer stack actuator with variable stiffness,” in *International Society for Optics and Photonics*, 2012.

[114] Z. Lu, Y. Cui, M. Debiasi, Z. Zhao and T. Laboratories, “A tunable dielectric elastomer acoustic absorber,” *ACTA ACUSTICA UNITED WITH ACUSTICA,* vol. 101, pp. 863-866, 2015.

[115] X. Yu, Z. Lu, F. Cui, L. Cheng and Y. Cui, “Tunable acoustic metamaterialwith an array of resonators actuated by dielectric elastomer,” *Extreme Mechanics Letters,* vol. 12, pp. 37-40, 2016.

[116] M. Debiasi, Z. Lu and Y. Cui, “Active membrane-based silencer and its acoustic characteristics,” *Applied Acoustics,* vol. 111, pp. 39-48, 2016.

[117] X. Yu, Z. Lu, L. Cheng and F. Cui, “Vibroacoustic modeling of an acoustic resonator tuned by dielectric elastomer membrane with voltage control,” *Journal of Sound and Vibration,* vol. 387, pp. 114-126, 2017.

[118] F. Casadei, M. Ruzzene, L. Dozio and K. Cunefare , “Broadband vibration control through periodic arrays of resonant shunts: experimental investigation on plates,” *Smart materials and structures,* vol. 19, no. 1, p. 015002, 2009.

[119] A. L. Goldstein, “Self-Tuning multimodal piezoelectric shunt damping,” *Journal of the Brazilian Society of Mechanical Sciences and Engineering,* vol. 33, no. 4, pp. 428-436, 2011.

[120] O. Heuss, R. Salloum, D. Mayer and T. Melz, “Tuning of a vibration absorber with shunted piezoelectric transducers,” *Arch Appl Mech,* vol. 86, pp. 1715-1732, 2016.

[121] A. Buhrdorf, O. Ahrens and J. Binder, “Capacitive micromachined ultrasonic transducers and their application,” *2001 IEEE Ultrasonics Symposium,* pp. 933-940, 2001.

[122] O. Umnova, K. Attenborough and C. Linton, “Effects of porous covering on sound attenuation by periodic arrays of cylinders,” *The Journal of the Acoustical Society of America,* vol. 119, no. 1, pp. 278-284, 2006.

[123] J. Sanchez-Perez, C. Rubio, R. Martinez-Sala, R. Sanchez-Grandia and V. Gomez, “Acoustic barriers based on periodic arrays of scatterers,” *Applied Physics Letters,* vol. 81, pp. 5240-5242, 2002.

[124] Y. Liao, Y. Chen, G. Huang and X. Zhou, “Broadband low-frequency sound isolation by lightweight adaptive metamaterials,” *Journal of Applied Physics,* vol. 123, p. 091705, 2018.

[125] H. Peng and P. Pai, “Acoustic metamaterial plates for elastic wave absorption and structural vibration suppression,” *International Journal of Mechanical Sciences,* vol. 89, pp. 350-361, 2014.

[126] K. Li, P. Rizzo and A. Bagheri, “A parametric study on the optimization of a metamaterial-based energy harvester,” *Smart materials and structures,* vol. 24, p. 115019, 2015.

[127] 韩雅娟 和 褚文博, “超材料发展现状及应用前景分析,” *新材料产业,* 卷 09, pp. 2-4, 2014.

[128] J.-S. Wu, Analytical and Numberical Methods for Vibration Analyses, John Wiley & Sons Singapore Pte. Ltd., 2013.

[129] Y. Zhang, “Research on the sound insulation properties of membrane-type acoustic metamaterials,” National University of Defense Technology, Changsha, 2014.

[130] Y. Zhang, J. Wen, Y. Xiao, X. Wen and J. Wang, “Theoretical investigation of the sound attenuation of membrane-type acoustic metamaterials,” *Physics Letters A,* vol. 376, pp. 1489-1494, 2012.

[131] C. Jung-San, Y. Huang and I. Chien, “Flexural wave propagation in metamaterial beams containing membrane-mass structures,” *International Journal of Mechanical Sciences,* Vols. 131-132, pp. 500-506, 2017.

[132] Y. Xiao, J. Wen and X. Wen, “Flexural wave band gaps in locally resonant thin plates with periodically attached spring-mass resonators,” *J. Phys. D: Appl. Phys.,* vol. 45, no. 19, p. 195401, 2012.

[133] S. Zhang, J. Wu and Z. Hu, “Low-frequency locally resonant band-gaps in phononic crystal plates with periodic spiral resonators,” *Journal of Applied Physics,* vol. 113, p. 163511, 2013.

[134] L. Shen and J. Wu, “Extremely low-frequency Lamb wave band gaps in a sandwich phononic crystal thin plate,” *International Journal of Modern Physics B,* vol. 29, p. 1550027, 2015.

[135] F. Ma, J. Wu, M. Huang, W. Zhang and S. Zhang, “A purely flexible lightweight membrane-type acoustic metamaterial,” *Journal of Physics D: Applied Physics,* vol. 48, p. 175105, 2015.

[136] L. Liu and M. Hussein, “Wave Motion in Periodic Flexural Beams and Characterization of the Transition Between Bragg Scattering and Local Resonance,” *Journal of Applied Mechanics,* vol. 79, no. 1, p. 011003, 2012.

[137] Z. Cheng, Y. Xu and L. Zhang, “Analysis of flexural wave bandgaps in periodic plate structures using differential quadrature element method,” *Internatioanl Journal of Mechanical Science,* vol. 100, pp. 112-125, 2015.

[138] C. Sugino, M. Ruzzene and A. Erturk, “Merging mechanical and electromechanical bandgaps in locally resonant metamaterials and metastructures,” *Journal of the Mechanics and Physics of Solids,* vol. 116, pp. 323-333, 2018.

[139] P. García and J. Fernández-Álvarez, “Floquet-Bloch Theory and Its Application to the Dispersion Curves of Nonperiodic Layered Systems,” *Mathematical Problems in Engineering,* vol. 12, p. 475364, 2015.

[140] G. Floquet, “Sur les équations différentielles linéaires à coefficients périodiques,” *Annales scientifiques de l'École Normale Supérieure,* vol. 12, pp. 47-88, 1883.

[141] Z. Lu, Y. Cui and M. Debiasi, “Active membrane-based silencer and its acoustic characteristics,” *Applied Acoustics,* vol. 111, pp. 39-48, 2016.

[142] C. Naify, C. Chang, G. McKnight and S. Nutt, “Transmission loss of membrane-type acoustic metamaterials with coaxial ring masses,” *Applied Physics,* vol. 110, p. 12490, 2011.

[143] L. Raghavan and S. Phani, “Local resonance bandgaps in periodic media: Theory and experiment,” *Journal of Acoustic Society America,* vol. 134, no. 3, pp. 1950-1959, 2013.

[144] J. Yang, An introduction to the theory of piezoelectricity, New York: Springer, 2005.

[145] Standards Committee of the IEEE Ultrasonics, Ferroelectrics, and Frequency Control Society, “IEEE Standard on Piezoelectricity,” IEEE, New York, 1987.

[146] A. Erturk and D. Inman, “Appendix A: piezoelectric constitutive equations,” *Piezoelectric Energy Harvesting,* pp. 343-348, 2011.

[147] C. Yang, “Dynamic Analysis of a Plate Incorporating DVAs and Tunable DVA Design,” The Hong Kong Polytechnic University, Hong Kong, 2009.

[148] J. Hartog and J. Ormondroyd, “Theory of the dynamic vibration absorber,” *ASME Journal of Applied Mechanics,* vol. 50, pp. 11-22, 1928.

[149] H. Peng, P. Pai and H. Deng, “Acoustic multi-stopband metamaterial plates design for broadband elastic wave absorption and vibration

suppression," *International Journal of Mechanical Sciences,* vol. 103, pp. 104-114, 2015.

PUBLISHED WORK DURING PHD STUDY

[1] C. Gao, D. Halim and X. Yi, "Study of bandgap property of a bilayer membrane-type metamaterial applied on a thin plate," International Journal of Mechanical Sciences, 2020.

[2] C. Gao, D. Halim and C. Rudd, "Prediction of bandgaps in membrane-type metamaterial attached to a thin plate," in INTER-NOISE and NOISE-CON Congress and Conference Proceedings, Madrid, 2019.

[3] C. Gao, D. Halim and C. Rudd, "Vibration absorption performance of membrane-type metamaterial on a thin plate," in INTER-NOISE and NOISE-CON Congress and Conference Proceedings, Madrid, 2019.

[4] C. Gao, D. Halim and C. Rudd, "Study of vibration absorption characteristics of membrane-type resonators with varying membrane configurations," in Internoise 2018 Proceedings, Chicago, 2018.